

Energy and System Size Dependence of Ξ^- and Ξ^+ Production in Relativistic Heavy-Ion Collisions at the CERN SPS

Dissertation
zur Erlangung des Doktorgrades
der Naturwissenschaften

vorgelegt beim Fachbereich Physik
der Johann Wolfgang Goethe-Universität
in Frankfurt am Main

von

Michael K. Mitrovski
aus Frankfurt am Main

Frankfurt am Main, 2007
(D 30)

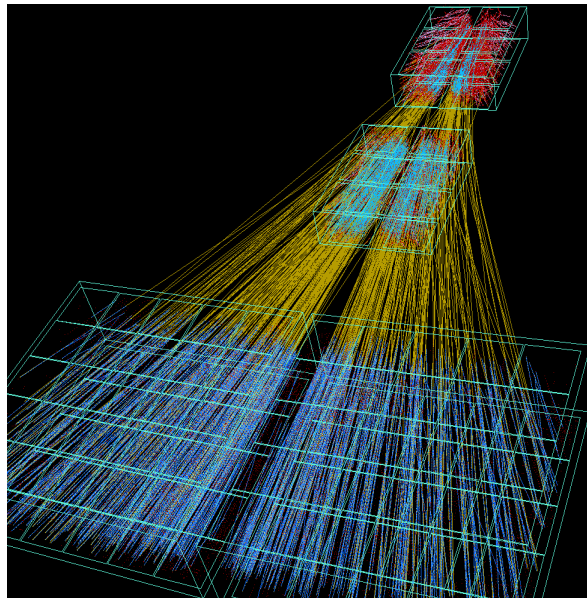
Vom Fachbereich Physik der Johann Wolfgang Goethe-Universität als Dissertation angenommen.

Dekan: Prof. Dr. Wolf Aßmus

Gutachter: Prof. Dr. Christoph Blume
Prof. Dr. Dr. h.c. Reinhard Stock

Datum der Disputation: 11.06.2007

Energy and System Size Dependence of Ξ^- and Ξ^+ Production in Relativistic Heavy-Ion Collisions at the CERN SPS



A Dissertation
Presented to the Faculty of
Johann Wolfgang Goethe-University
in Frankfurt/Main
for the Degree of
Doctor of Philosophy

By

Michael K. Mitrovski

Frankfurt am Main, 2007

*Der Mensch hat dreierlei Wege klug zu handeln:
erstens durch Nachdenken, das ist der edelste,
zweitens durch Nachahmen, das ist der leichteste,
und drittens durch Erfahrung, das ist der bitterste.*

(Konfuzius)

Die Wahrheit triumphiert nie, ihre Gegner sterben nur aus.

(Max Planck)

Zusammenfassung

Quarks sind die elementaren Bestandteile, aus denen Hadronen (Baryonen und Mesonen) aufgebaut sind. Zusammen mit den Leptonen und den Eichbosonen gelten sie heute als die fundamentalen Bausteine, aus denen alle Materie aufgebaut ist (siehe Kapitel 1). Im Standardmodell der Teilchenphysik werden diese Ergebnisse zusammengefasst.

Es gibt sechs verschiedene Quark-Arten (flavours): up, down, strange, charm, bottom und top. In der Natur kommen keine isolierten Quarks vor, sondern nur Kombinationen aus z.B. einem Quark-Antiquark Paar (Meson) oder aus drei Quarks (Baryon).

Die Quantenchromodynamik (QCD) beschreibt die starke Wechselwirkung zwischen Quarks und Gluonen. Quarks bauen unter anderem Protonen und Neutronen auf. Gluonen vermitteln die Wechselwirkung zwischen den Quarks. Konzeptionell ist die QCD an die Quantenelektrodynamik (QED) angelehnt, die die Wechselwirkung elektrisch geladener Teilchen (z.B. Elektron oder Positron) durch den Austausch von Photonen beschreibt. Analog wirkt die Kraft, die durch den Austausch von Gluonen beschrieben wird, zwischen Teilchen, die eine Farbladung (rot, grün, blau) tragen. Im Vergleich zur QED, wo das Photon neutral ist, trägt das Gluon selbst Farbe und wechselwirkt daher mit anderen Gluonen. Bei kleinen Quarkabständen und hohen Energien bzw. hohen Impulsüberträgen, fällt die Kopplungskonstante der starken Wechselwirkung (α_s) ab. Bei kleinem α_s sind Quarks und Gluonen schwach gebunden (*Asymptotische Freiheit*). Bei grossen Abständen bzw. kleinen Impulsüberträgen ist α_s gross. Die Zunahme von α_s bewirkt, dass unendlich viel Energie benötigt wird, um Quarks aus Hadronen herauszulösen. Dies hat die Folge, dass es günstiger ist ein neues Quark-Antiquark Paar zu erzeugen. Das erklärt, warum Quarks immer in Hadronen (Mesonen und Baryonen) gebunden sind und nie isoliert beobachtet werden können (*Confinement*).

Wenn Kernmaterie stark komprimiert wird, steigen Energiedichte und Temperatur, und möglicherweise erfährt die Kernmaterie einen Phasenübergang zu einem Zustand der als Quark Gluon Plasma (QGP) bezeichnet wird (Abbildung 1.4). Das QGP ist ein Zustand der Materie, in dem das Confinement der Quarks und Gluonen aufgehoben ist (*Deconfinement*). Dieser Zustand ist gekennzeichnet durch ein quasi-freies Verhalten der Quarks und Gluonen.

Man nimmt an, dass das Universum ungefähr 10^{-6} Sekunden nach dem Urknall, als die Energiedichte hoch genug war, diesen Zustand durchlief. Bei der Expansion des Universums kühlte das QGP ab, und die starke Kraft schloss

Quarks und Gluonen in Hadronen ein. Im heutigen Universum existiert das QGP höchstens noch im Zentrum von Neutronensternen und explodierenden schwarzen Löchern.

Es wird angenommen, dass durch ultrarelativistische Schwerionenkollisionen ein Zustand von sehr hohen Temperaturen und Energiedichten ($1 \text{ GeV}/\text{fm}^3$) im Labor erzeugt werden kann (Abbildung 1.5). Gitter-QCD-Rechnungen (Lattice QCD) deuten darauf hin, dass die Dichte, die gegenwärtig in Schwerionenkollisionen erreicht werden kann, hoch genug ist, um einen Übergang von Kernmaterie in einen Plasmazustand zu erreichen (Abbildung 1.4). Im weiteren Verlauf der Kollision kühlt der expandierende Feuerball ab. Nachdem die Produktion von neuen Quarks abgeschlossen ist, erreicht das System ein chemisches Gleichgewicht. Dabei hadronisieren die Quarks in Mesonen und Baryonen. Das immer noch expandierende System kühlt weiter ab. Die Hadronen wirken nur noch elastisch miteinander, wobei sich nur ihre Impulse, aber nicht die Identität ändert. Sobald auch die elastische Wechselwirkung zwischen den Hadronen endet (thermisches Ausfrieren), verlassen die Teilchen die Reaktionszone.

Die Interpretation solcher Experimente wird dadurch erschwert, dass das Quark Gluon Plasma eine Lebensdauer von nur einigen Fermi/c (10^{-23} Sekunden) hat und die räumliche Ausdehnung in der Größenordnung von 10^{-15} Meter liegt. Deshalb beobachtet man im Experiment nur den hadronischen Endzustand der Kollision, aus dem man dann Rückschlüsse auf den Materiezustand in den frühen Phasen der Kollision ziehen muss. Aufgrund von Modellrechnungen wurden einige Observablen vorgeschlagen, die einen Phasenübergang kennzeichnen. Eine Observable ist die Seltsamkeitsproduktion.

Seltsame (s) und Antiseltsame (\bar{s}) Quarks werden in der Kollision neu produziert und können deshalb Aufschluss über den Anfangszustand geben. Eine Überhöhung der Seltsamkeit in Schwerionenkollisionen im Vergleich zu elementaren Nukleon-Nukleon Kollisionen wurde als Signatur für ein QGP vorhergesagt. Es ist bis jetzt noch nicht klar, ob dieser Effekt auch auf hadronische Effekte zurückgeführt werden kann. Deshalb untersucht man die Energie- und Systemgrößenabhängigkeit von seltsame Hadronen, um einen Aufschluss vom Anfangszustand zu gewinnen.

Es gibt verschiedene Möglichkeiten um seltsame Quarks zu erzeugen. In einem Hadronen Gas muss ein gewisser Energie-Schwellenwert erreicht werden, um seltsame Hadronen zu produzieren. Dieser wird durch die Massendifferenz des Anfangs- und Endzustandes bestimmt. In der starken Wechselwirkung ist die Seltsamkeit eine Erhaltungsgröße, was heisst, dass ein Teilchen und Antiteilchen, die jeweils ein s bzw. \bar{s} enthalten, gleichzeitig in der Reaktion erzeugt werden müssen. Im Unterabschnitt 1.5.1 kann gesehen werden, dass die Energieschwellenwerte relativ hoch sind um Seltsamkeit in der Anfangsreaktion zu erzeugen.

Im Gegensatz zum Hadronengas müssen in einem *deconfined* Zustand nur seltsame und Antiseltsame Quarks erzeugt werden. Es gibt verschiedene Möglichkeiten in einem QGP ein $s\bar{s}$ Paar zu erzeugen. Zum einen können durch Gluon

Fusion ($g + g \rightarrow s\bar{s}$) und zum anderen durch leichte Quark-Anti-Quark Paarvernichtung ($q\bar{q} \rightarrow s\bar{s}$) seltsame und Antiseltsame Quarks erzeugt werden. Außerdem ist der Energie-Schwellenwert in einem QGP, um ein $s\bar{s}$ Paar zu erzeugen, einfach nur die bloße Masse der beiden seltsame Quarks. Deshalb ist es möglich bei den hohen Temperaturen die in einem QGP existieren, thermisch $s\bar{s}$ Paare zu erzeugen. Eine weitere Quelle überhöhter $s\bar{s}$ Paarproduktion resultiert aus dem Pauli-Prinzip. Da alle Quarks Fermionen sind, gilt unter der Annahme des Paulischen Ausschlussprinzips, dass zwei Fermionen nicht den gleichen quantenmechanischen Zustand annehmen können. Das führt dazu, dass die in der Kollision vermehrt produzierten leichten Quarks den gleichen Raum belegen und es deshalb energetisch einfacher wird $s\bar{s}$ Paare zu erzeugen. Diese Gründe führen dazu, dass es im Vergleich zu einem Hadronengas eine überhöhte Produktion von seltsame Hadronen gibt, wenn das System einen *deconfined* Zustand durchquert. Erste Messungen vom NA35 Experiment zeigten, dass das Kaon zu Pion Verhältnis in centralen S+S-Kollisionen bei 200 AGeV ungefähr ein Faktor zwei höher ist, als die die in N+N Wechselwirkungen gemessen wurden. Darüber hinaus wird keine weitere Seltsamkeitsüberhöhung von S+S zu Pb+Pb Kollisionen gemessen (Abbildung 1.8). Eine größere Seltsamkeitsüberhöhung wurde bei niedrigeren AGS-Energien vom E802 Experiment gemessen. Abbildung 1.9 zeigt das gemessene Doppelverhältnis in zentralen Pb+Pb/Au+Au Kollisionen von AGS, über SPS zu RHIC Energien im Vergleich zu p+p Wechselwirkungen. Bei niedrigen AGS-Energien, wo erwartet wird, dass kein QGP gebildet wird und deshalb es auch keine Seltsamkeitsüberhöhung geben sollte, wird tatsächlich eine größere Seltsamkeitsüberhöhung gemessen als bei RHIC-Energien. Dies steht im Widerspruch zu der oben genannten Hypothese. Deshalb kann man zusammenfassend sagen, dass das Konzept von Seltsamkeitsüberhöhung als Signal für das QGP in frage gestellt werden kann. Das Modell *Statistical Model Of The Early Stage* schlägt vor sich die Energieabhängigkeit des Verhältnisses von Seltsamkeit zu Pion sich anzuschauen. Dieses Modell macht eine Vorhersage, dass es einen Phasenübergang zwischen AGS- und SPS-Energien gibt, der sich in einem scharfen Maximum widerspiegelt, welche auch tatsächlich gemessen wurde (Abbildung 1.10). Das Problem dieses Modells ist, dass es keine wirkliche Aussage über die Produktion einzelnen von identifizierte Teilchen macht, wie z.B. das Ξ Hyperon.

In dieser Arbeit wird die experimentelle Analyse der Energie- und Systemgrößenabhängigkeit der Produktion von Ξ -Hyperonen am CERN SPS untersucht. Dazu wurden mit dem NA49 Detektor zentrale Blei-Blei-Kollisionen bei einer Energie von 20 – 158 AGeV, minimum bias Blei-Blei-Kollisionen bei 40 und 158 AGeV und semi-zentrale Silizium-Silizium-Kollisionen bei 158 AGeV aufgenommen. Im Folgenden wird das NA49 Experiment am CERN SPS vorgestellt, mit dem die Daten aufgezeichnet wurden, die die Grundlage für diese Analyse sind.

Am SPS Beschleuniger im CERN (Abbildung 2.1) werden Pb+Pb Kollisionen bis zu einer Strahlenergie von 158 AGeV erzeugt. Die hier analysierten Datensätze wurden in einem Zeitraum von 1999 bis 2002 aufgezeichnet. Das NA49 Experiment ist ein Hadronen-Spektrometer, welches geladene Hadronen

mit einer sehr großen Akzeptanz misst. Der schematische Aufbau des NA49 Detektorsystems ist in Abbildung 2.2 dargestellt. Die Hauptkomponenten sind die vier TPCs (Time Projection Chamber).

Die beiden Vertex-TPCs befinden sich jeweils in einem Magneten. Bei 158 AGeV beträgt die Magnetfeldstärke 1.5 Tesla in Vertex-TPC-1 und 1.1 Tesla in Vertex-TPC-2. Die Aufgabe der Magnete ist es, den Kegel produzierter Teilchen zu erweitern, um so auch in Bereichen mit hoher Spurdichte messen zu können. Die Vertex-TPCs dienen zur Impulsmessung der Hadronen. Die beiden Main-TPCs, die ein grosses Volumen besitzen, dienen zur Teilchenidentifikation. Dies geschieht durch die Messung des spezifischen Energieverlustes, dE/dx , der Hadronen im TPC-Gas. Die TPC basiert darauf, dass geladene Teilchen beim Durchgang durch ein Gas eine Spur ionisierter Gasatome hinterlassen. In einem elektrischen Feld driften die Elektronen, die bei der Ionisation freigesetzt wurden, zu einer Ausleseebene. Der Punkt, an dem die Elektronen auf der Ausleseebene ein Signal erzeugen, entspricht der Projektion des Ionisationspunktes auf die Ausleseebene. Die dritte Komponente, die den Raumpunkt der Ionisation festlegt, ist durch die Driftzeit bei bekannter Driftgeschwindigkeit gegeben. So erscheint eine Teilchenspur als eine Kette von Ionisationspunkten im Detektorgas. Der spezifische Energieverlust eines Teilchens beim Durchgang durch das Gas hängt ausschließlich von der Geschwindigkeit β ab. Die Stärke des auf der Ausleseebene induzierten Signals erlaubt den spezifischen Energieverlust zu bestimmen. Da der Impuls durch die Krümmung der Spur bekannt ist, kann so die Masse und damit die Identität des Teilchens bestimmt werden.

Kern-Kern-Kollisionen unterschiedlicher Zentralität können durch die Messung der nicht an der Kollision beteiligten (Spektator-) Nukleonen selektiert werden. Das zur Zentralitätsbestimmung verwendete Veto-Kalorimeter ist in einen Blei-Szintillator und einen Eisen-Szintillator Abschnitt unterteilt. Um nun die Detektorauslese und Selektion von zentralen Kollisionen zu starten, werden eine Reihe von Detektoren im Strahl benutzt. Zur Identifikation der einzelnen Strahlteilchen werden Čerenkov-Zähler (S1, S2') und Beam Positions-Detektoren (BPD-1/2/3) verwendet. Kollisionen im Target werden über den S3-Zähler selektiert, welcher in Anti-Koinzidenz mit S1 geschaltet ist. Mit den BPDs lässt sich durch die Höhe der von den Strahlteilchen erzeugten Pulse auch Rückschlüsse auf die Ladung des Strahlteilchens führen. Dies ist besonders für den Siliziumstrahl wichtig, da dieser nicht primär erzeugt wird, sondern durch die Fragmentation eines Bleistrahls.

Die NA49-Rekonstruktionskette verwandelt die aufgenommenen Rohdaten in ein Format, das später analysiert werden kann. Aus den gemessenen ADC-Werten wird in der Pad-Zeit-Ebene die Position des Clusters definiert. Diese Cluster werden dann in der Rekonstruktionskette zu globalen Spuren verbunden und deren Impule anhand der Krümmung im Magnetfeld bestimmt. Hiermit wird der Weg der Teilchen zur Targetebene zurück extrapoliert. Durch die Extrapolation der Spuren in Richtung des Targets, wird der Hauptvertex (der Interaktionspunkt im Target) bestimmt. Wenn alle Hauptvertexspuren gefunden wurden, wird nach Sekundärvertices von V0- (siehe Unterabschnitt 2.3.2) und

Ξ -Kandidaten (siehe Unterabschnitt 2.3.5) gesucht. Die Analyse beruht auf der Rekonstruktion der invarianten Masse der $V0$ - und Ξ -Kandidaten in einzelnen Bereichen des Phasenraums aus den Zerfallsprodukten. Das Ξ -Hyperon zerfällt in einer Kaskade in ein $V0$ -Teilchen und ein geladenes Pion. Das $V0$ -Teilchen zerfällt wiederum in zwei geladene Spuren. Für die Ξ -Rekonstruktion müssen dann alle drei geladenen Spuren kombiniert werden. Für die Ξ -Suche werden $V0$ -Kandidaten verwendet, die die $V0$ -Suchkriterien überstanden haben und durch die Kombination von passenden $V0$ s mit einer geladenen Spur rekonstruiert man das Ξ . In der $V0$ und Ξ -Suche wurden die Suchkriterien so gewählt, dass möglichst viele wahre $V0$ - und Ξ -Kandidaten gefunden werden und dennoch der Untergrund der zufälligen Paare reduziert wird. Später wird durch enger gewählt Qualitätskriterien das Signal zu Untergrund-Verhältnis optimiert (siehe Abschnitt 3.3). Bei der verwendeten Analyse waren diverse Qualitätskriterien nötig, um ein vernünftiges Signal zu erhalten. Neben den Verlusten durch die Qualitätskriterien, muß auch auf die endliche geometrische Akzeptanz und die hohe Spurdichte korrigiert werden. Deshalb mussten für jeden Bereich des Phasenraums Korrekturfaktoren ermittelt werden, um die gemessenen Rohdaten zu korrigieren (siehe Abschnitt 3.5).

Abschnitt 5.1 zeigt den Vergleich der Ergebnisse dieser Arbeit mit denen anderer Experimente. Ξ -Hyperonen in mittlerer Rapidität wurden bei einer Laborenergie von 40 und 158 AGeV auch von der NA57 Kollaboration gemessen. Bei zentralen Kollisionen wurde bei 40 AGeV eine Abweichung von 67% für das Ξ^- (2.6 Standardabweichungen) und 14% (0.3 Standardabweichungen) für das Ξ^+ Hyperon festgestellt. Bei 158 AGeV ist der Unterschied für das Ξ^- Hyperon 33% (5.8 Standardabweichungen) und 55% (4.5 Standardabweichungen) für das Ξ^+ (siehe Abbildung 5.1). Eine Diskrepanz wurde auch beim inversen Steigungsparameter festgestellt. Diese beträgt bei 40 AGeV 14% für die Ξ^- und 8% für die Ξ^+ und bei 158 AGeV 12% und 20% für die Ξ^- und Ξ^+ Hyperonen. Diese Unstimmigkeit setzt sich auch in der Zentralitätsabhängigkeit für Ξ^- bei 40 und 158 AGeV fort. Bei 40 AGeV gibt es eine gute Übereinstimmung in peripheren und semi-zentralen Kollisionen. Für zentrale Kollisionen ist ein grosser Unterschied zu beobachten. Der Unterschied ist auch bei 158 AGeV zu beobachten (siehe Abbildung 5.2).

Bei SPS Energien wird für das Ξ eine schwache Energieabhängigkeit des inversen Steigungsparameters sowie der mittleren transversalen Masse beobachtet (siehe Abbildung 5.3). Bei den höheren RHIC Energien steigen beide Meßgrößen wieder an. Das gleiche Verhalten wird auch für Pionen, Kaonen und Protonen gesehen. In einem thermischen Modell wird der inverse Steigungsparameter einer transversalen Massenverteilung als Ausfrieretemperatur der Teilchen interpretiert. Deshalb würde man erwarten, dass jeder Teilchensorte die gleiche Temperatur zugeordnet wird, wie in elementaren Nukleon-Nukleon-Reaktionen. In Kern-Kern-Kollisionen wurde zusätzlich noch eine kollektive transversale Expansion beobachtet. Der Unterschied zwischen dem inversen Steigungsparameter in p+p und Pb+Pb-Kollisionen, resultiert aus dieser kollektiven transversalen Expansion in Pb+Pb Kollisionen. Das gleiche Verhalten wird auch für schwerere Teilchen beobachtet, wie das Ξ - und Ω -Baryon. Es wird angenom-

men, dass mehrfach seltsame and Hadronen mit schweren Quarks früher vom Feuerball ausfrieren, als Teilchen mit leichteren Quarks, und deshalb ihre kollektive Bewegung von der partonischen Phase herrühren kann.

Abbildung 5.5 zeigt die Λ - und Ξ^- -Multiplizität, gemessen in minimum bias Blei-Blei-Reaktionen und kleineren Systemen, im Vergleich zu Λ - und Ξ^- -Yields in Proton-Proton-Kollisionen bei einer Schwerpunktsenergie von 17.3 GeV und 200 GeV. Es kann eine Seltsamkeitsüberhöhung beobachtet werden, die für Ξ^- stärker ist als für Λ -Hyperonen. Wird der Seltsamkeitsüberhöhungsfaktor von NA49 mit dem von STAR verglichen, wird erkannt, dass ersterer höher ist, was in Abbildung 5.6 gezeigt wird. Dass die Seltsamkeitsüberhöhung mit ansteigender Energie kleiner wird wurde bereits vorher beim K^+/π^+ Verhältnis gesehen.

Zusammen mit Ergebnissen bei AGS- und RHIC-Energien lässt sich die Anregungsfunktion der Ξ^- - und Ξ^+ -Hyperonen studieren. Die totale Multiplizität und die Rapiditätsdichte bei mittlerer Rapidität steigt mit der Schwerpunktsenergie an (siehe Abbildung 5.13). Das Ξ^-/π -Verhältnis in Kern-Kern Kollisionen zeigt einen Anstieg im AGS Energiebereich mit einem Maximum und einem Abfall bei SPS Energien. Im Gegensatz dazu steigt das Ξ^+/π -Verhältnis mit der Schwerpunktsenergie an. Der gleiche Trend wird auch bei mittlerer Rapidität beobachtet (siehe Abbildung 5.14).

Das Ξ^+/Ξ^- Verhältnis bei mittlerer Rapidität steigt von SPS zu RHIC Energien an, was auch für andere Baryonen beobachtet wird. Die Energieabhängigkeit für mehrfach seltsame Hyperonen ist schwächer als für Protonen und Λ . Dies kann dadurch erklärt werden, dass die Netto-Baryondichte bei mittlerer Rapidität stark von der Laborenergie abhängt.

Die hier präsentierten Messungen, wurden auch mit theoretischen Modellvorhersagen verglichen. Abbildung 5.12 zeigt die gemessene Seltsamkeitsüberhöhung, welche mit einer statistischen Modellrechnung (Redlich et al.) bei SPS- und RHIC-Energien verglichen wurde. Die Modellrechnungen liegen klar unter den gemessenen Resultaten von der NA49, NA57 und STAR Kollaboration. Eine möglich bessere Beschreibung der Messungen könnte das Perkulationsmodell bieten (Höhne et al.). Dieses Modell beschreibt besser die Form der gemessenen seltsame Mesonen als Funktion der Systemgröße und Zentralität, als das vorhergenannte einfache statistische Modell (Redlich et al.). Das Problem am Perkulationsmodell ist, das es im Moment noch keine Rechnungen für Mehrfachseltsame Hyperonen liefert. Ein weiterer Verbesserungsvorschlag für beide Modelle wäre, dass man die Annahme für eine totale Sättigung (entsprechend $\gamma_s = 1$) fallen lässt, was Ergebnisse der STAR Kollaboration nahegelegt haben, da ein Faktor kleiner eins kleine Systemen besser beschreibt. Abbildung 5.13 zeigt den Vergleich der gemessenen Anregungsfunktion der Ξ^- - und Ξ^+ -Hyperonen mit String-Hadronischen Modellen (RQMDv2.3, UrQMDv1.3) und einem statistischen Modell (γ_s frei wählbar). UrQMD unterschätzt nicht nur die Messung, sondern gibt auch den Trend nicht wieder. Etwas anders sieht das mit dem Modell RQMD aus, welches in sehr guter Übereinstimmung mit dem Messungen liegt. Im Vergleich dazu, liefert das statistische Modell nur eine qualitative Be-

schreibung der Messungen. In Abbildung 5.14 wird das Ξ/π -Verhältniss wiederum mit String-Hadronischen Modellen und statistischen Modellen verglichen. Wieder unterschätzt UrQMD die Messungen. Das Modell RQMD liefert auch hier eine gute Beschreibung der Daten bei 158 AGeV, aber keine Rechnungen über die Energieabhängigkeit. Dies gilt nicht für die statistischen Modelle. Das statistische Modell mit dem frei wählbaren γ_s unterschätzt die Messungen, wobei das Modell mit $\gamma_s = 1$ sie überschätzt. Das Maximum im Ξ^-/π -Verhältniss ist schärfer als es vom statistischen Modell mit $\gamma_s = 1$ vorhergesagt wurde. Gemeinsam ist, dass alle keine Kenntnis von einem Phasenübergang besitzen. Ein offener Punkt ist wie man die überlappenden Strings in dem RQMD Modell interpretiert. Eine mögliche Interpretation wäre, dass die Strings sich über den Perkolationsprozess zu einem QGP entwickeln. In dem Modell *Statistical Model Of The Early Stage* ist hingegen ein Phasenübergang eingebaut. In diesem Modell wird beschrieben, dass ein Phasenübergang Anomalien in der Energieabhängigkeit in der Produktion von Pion und Seltsamkeit bewirkt. Diese nicht monotone Struktur wird bei der Energieabhängigkeit des inversen Steigungsparameter und der mittleren transversalen Masse beobachtet und desweiteren in der Energieabhängigkeit Ξ^-/π -Verhältnisses. Es scheint tatsächlich, dass es einen Phasenübergang bei SPS-Energien vorhanden ist.

Die Ergebnisse dieser Arbeit wurden auf der Strange-Quark-Matter Konferenz 2006 in Los Angeles (USA) [91] vorgestellt und diskutiert.

Contents

1. Introduction	1
1.1. Hadronic Matter	1
1.1.1. Quark Combinations	2
1.1.2. Color Charge	3
1.2. The Strong Interaction: Confinement	4
1.2.1. Chiral Symmetry Restoration	6
1.3. The Phase Diagram of Strongly Interacting Matter	7
1.4. Relativistic Heavy Ion Collisions	7
1.5. Strangeness	11
1.5.1. Strangeness Production in a Hadronic Gas	11
1.5.2. Strangeness Production in a Quark Gluon Plasma	12
2. The NA49 Experiment at CERN SPS	17
2.1. The NA49 Detector Layout	18
2.2. Time Projection Chambers	20
2.2.1. The NA49 TPCs	21
2.3. Event Reconstruction	22
2.3.1. V0 Reconstruction	25
2.3.2. V0 Finding	25
2.3.3. V0 Fitting	26
2.3.4. Multi-Strange Hyperon Reconstruction	26
2.3.5. Ξ Finding	26
3. Data Analysis	31
3.1. Data sets	31
3.2. Event Cuts	32
3.2.1. Central Pb+Pb	32
3.2.2. Minimum Bias Pb+Pb	33

Contents

3.2.3. Semi-Central Si+Si	34
3.3. Analysis Cuts	36
3.3.1. Cuts on the Ξ Candidate	38
3.3.2. Cuts on the Daughter π of the Ξ Candidate	39
3.3.3. Cuts on the Daughter Λ Candidate	40
3.4. Invariant mass method	44
3.5. Correction	46
3.5.1. Geometrical Acceptance	47
3.5.2. Reconstruction Efficiency	48
3.5.3. Centrality Bin Size Effect	52
3.5.4. Influence of δ Electrons	54
4. Extraction of Spectra, Yields and Systematic Error	57
4.1. Transverse Momentum and Transverse Mass Spectra	57
4.1.1. Extrapolation of the Transverse Momentum Spectra	59
4.2. Rapidity Spectra and 4π Yields	60
4.3. Stability Checks of the Results and the Systematic Error	62
4.4. Lifetime	65
4.5. Comparison with another Ξ Analysis at 158 AGeV	66
5. Discussion	69
5.1. Comparison with Other Experiments	69
5.2. Energy Dependence	72
5.2.1. Inverse Slope Parameter and Mean Transverse Mass of the Ξ Hyperon	72
5.2.2. Strange Hadron Yield Enhancement	75
5.2.3. Excitation Function of Ξ production	76
5.2.4. Antibaryon/Baryon Ratio	78
5.3. Theoretical Models	79
5.3.1. Spectator-Participant Model	79
5.3.2. RQMD v2.3	80
5.3.3. UrQMD v1.3	81
5.3.4. Statistical Hadron Gas Models	82
5.3.5. Comparison to Models	83
6. Summary and Conclusion	87

A. Relativistic Kinematics and Lorentz-Transformation	91
A.1. Four Vector and Lorentz Transformation	91
A.2. Rapidity and Transverse Momentum	92
A.3. Pseudorapidity	92
A.4. Center of Mass Energy	94
B. Eventcuts	95
B.1. Central Pb+Pb	95
B.2. Minimum Bias Pb+Pb	100
C. Invariant Mass Distribution and Efficiency	103
D. Invariant Mass Distribution for p_t and $m_t - m_0$ Spectra and Numerical Values	107
D.1. Central Pb+Pb	107
D.2. Minimum Bias Pb+Pb	121
D.3. Semi-Central Si+Si	129
E. Invariant Mass Distribution for y Spectra and Numerical Values	133
E.1. Central Pb+Pb	133
F. Systematic Errors	141
G. Inverse Slope Parameter versus Particle Mass	145

Contents

1. Introduction

The goal of relativistic heavy ion collisions is to explore strongly interacting matter under extreme conditions. At high temperature and baryon density, nuclear matter is expected to melt into a state of free quarks and gluons, known as the Quark Gluon Plasma (QGP).

The study of deconfined matter is of interest not only in nuclear physics, but also in cosmology and astrophysics. The Universe (see Figure 1.1) itself existed in a similar state approximately 10^{-6} seconds after the big bang [1] before it expanded and cooled sufficiently for quarks and gluons to hadronize into nucleons and other hadrons. Even today, large volumes of deconfined quark matter might exist in the dense cores of neutron stars [2] and exploding black holes.

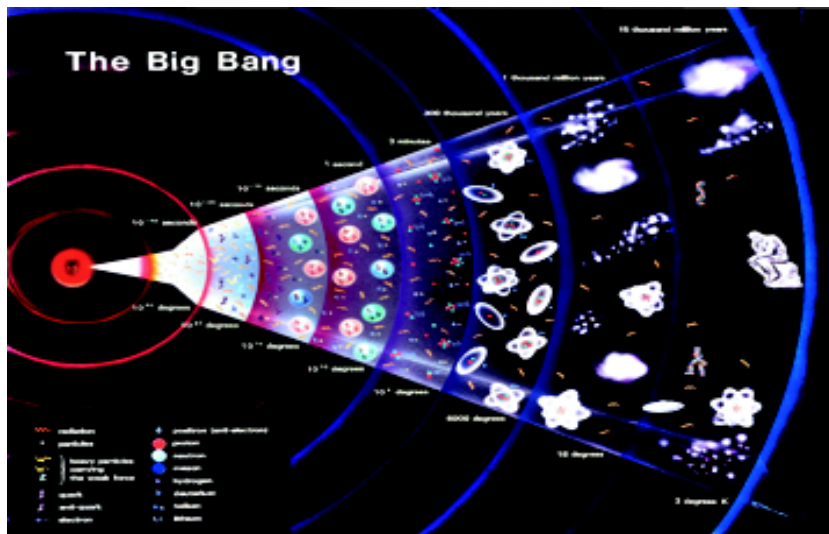


Figure 1.1.: The history of the Universe.

1.1. Hadronic Matter

Until the early 1960s, baryons and mesons were considered to be the building blocks for hadronic matter. Together with leptons, they were thought to

1. Introduction

constitute all the material in the known Universe. However, through deep inelastic electron-nucleon scattering experiments [3], it was eventually discovered that baryons and mesons must have substructure. A model based around such sub-particles, named quarks (q), was introduced independently by Zweig and Gell-Mann and developed by Gell-Mann in the 1960s [4]. It is believed that six types of flavors of quark named up (u), down (d), strange (s), charm (c), bottom (b) and top (t), and their corresponding anti-quarks ($\bar{u}, \bar{d}, \bar{s}, \bar{c}, \bar{b}, \bar{t}$), grouped into three generations, constitute the total number of quarks.

Flavor	Symbol	Mass (MeV)	Charge (e)	Quantum Number
up	u	1.5 – 4.0	+2/3	Isospin = +1/2
down	d	4.0 – 8.0	-1/3	Isospin = -1/2
strange	s	80.0 – 130.0	-1/3	Strangeness = -1
charm	c	1150.0 – 1350.0	+2/3	Charm = +1
bottom	b	4100.0 – 4400.0	-1/3	Bottom = -1
top	t	174300 ± 5100	+2/3	Top = +1

Table 1.1.: The properties of the 6 known quarks.

Table 1.1 shows properties of quarks [5] which all have spin $\frac{1}{2}\hbar$, including the approximate mass, fractional charge and relevant quantum number. In addition to the quantum numbers associated with quark flavour (isospin, strangeness, charm, bottom and top), each quark has the baryon number, $B = \frac{1}{3}$. Anti-quarks, which are the antiparticle equivalent of quarks, have the same mass as their quark counterparts but opposite charge and quantum numbers.

1.1.1. Quark Combinations

Quarks themselves are never seen in isolation, but always form strongly interacting particles, referred to as hadrons. The simplest combinations allowed are integer spin ($0\hbar, 1\hbar$) mesons or half integer spin ($\frac{1}{2}\hbar, \frac{3}{2}\hbar$) baryons formed respectively by a quark-antiquark ($q\bar{q}$) pair or three quarks (qqq). Some of the family of baryons that form the (spin^{parity}) $J^\pi = \frac{1}{2}^+$ octet, the $J^\pi = 0^-$ nonet and the $J^\pi = \frac{3}{2}^+$ decuplet are illustrated in Figure 1.2. The 3rd component of isospin, I_3 , is assigned to light quarks ($u = \frac{1}{2}, d = -\frac{1}{2}$) and S is the strangeness of the hadron. Any baryon with non-zero strangeness, is generically referred to as a hyperon. The two hyperons with $S = -1, I_3 = 0$ in Figure 1.2a are different because the ud pair is in a spin 0 state for the Λ , but is in spin 1 state for the Σ^0 . Properties of some of the strange hadrons encountered in this thesis are given in Table 1.2. Strange quarks decay via the weak interaction in which quark flavor is not conserved. Also given in the table are the principle decay channels and branching ratio for decaying strange hadrons, along with the mean lifetime, c . Lifetimes are often given as $c\tau$ in units of cm. All values are taken from the particle data book [5].

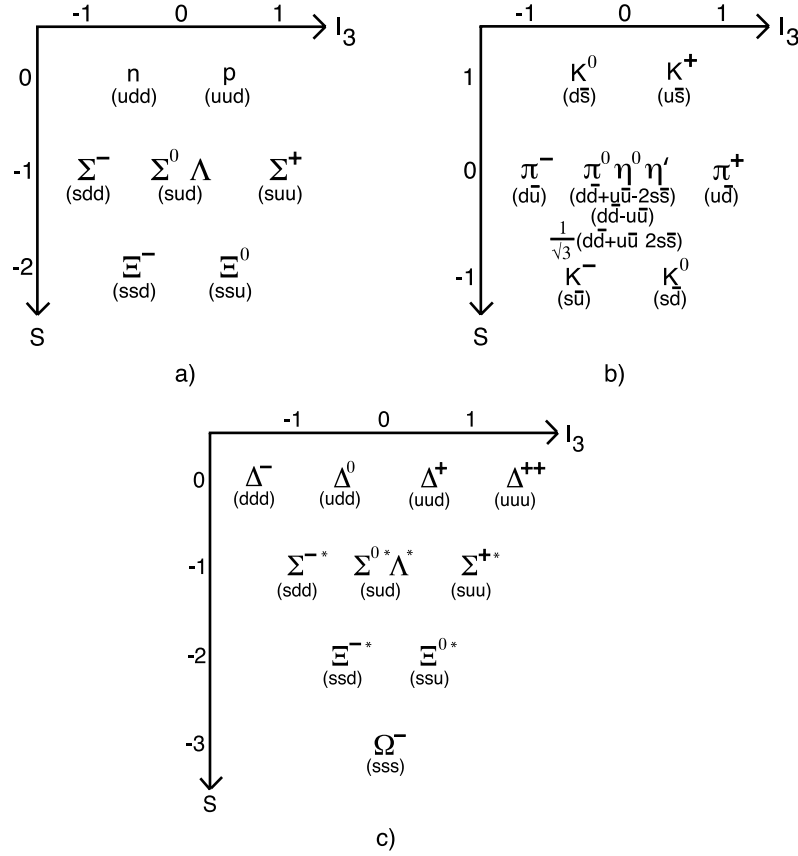


Figure 1.2.: a) The octet of spin 1/2 even parity baryons, b) The nonet of spin 0 odd parity mesons, c) The decuplet of spin 3/2 even parity baryons.

	S	Mass (MeV/c ²)	Decay	Branching Ratio (%)	$c\tau$ (cm)
K_s^0	+1	493.677	$\pi^+ + \pi^-$	68.6	2.6842
Λ	-1	1115.683	$p + \pi^-$	63.9	7.89
$\bar{\Lambda}$	+1	1115.683	$\bar{p} + \pi^+$	63.9	7.89
Ξ^-	-2	1314.83	$\Lambda + \pi^-$	99.522	4.91
$\bar{\Xi}^+$	+2	1314.83	$\bar{\Lambda} + \pi^+$	99.522	4.91
Ω^-	-3	1672.45	$\Lambda + K^-$	67.8	2.461
$\bar{\Omega}^+$	+3	1672.45	$\bar{\Lambda} + K^+$	67.8	2.461

Table 1.2.: The mass and strangeness of some of the predominant decay strange hadrons, where the branching ratios and lifetimes are given.

1.1.2. Color Charge

Quarks are assigned a color charge, either red, green or blue, and antiquarks either antired, antigreen or antiblue. However, as individual quarks have never been observed in nature, it is postulated that the color charge itself is confined,

1. Introduction

and hence all baryons and mesons must be colorless objects. Mesons are formed by a color-anticolor $q\bar{q}$ pairs, for example $s_{\text{blue}}\bar{s}_{\text{antiblue}}$, with baryons formed from three quarks with one of each color, for example $s_{\text{red}}s_{\text{blue}}d_{\text{green}}$.

The introduction of color is necessary in order not to contravene the Pauli exclusion principle, which forbids two fermions from occupying the same quantum state. The need for this is seen when examining particles such as the Δ^- (ddd), Δ^{++} (uuu) and Ω^- (sss). Each particle consists of three identical quarks leading to a symmetric spatial wavefunction, Ψ_{total} . The spin part of the wavefunction, ψ_{spin} must also be symmetric because the total spin is $\frac{3}{2}\hbar$ which means that all three quarks must have parallel spin. In order to satisfy the Pauli exclusion principle in the cases of the Δ^- , Δ^{++} and Ω^- , each quark in the baryon must carry a different color charge.

1.2. The Strong Interaction: Confinement

The strong nuclear force is described by Quantum Chromodynamics (QCD), the parallel field theory to Quantum Electrodynamics (QED) that describes the electromagnetic force. It is propagated by gluons analogously to photons in the electromagnetic force, but unlike photons, which do not carry electric charge, gluons carry color, and they can self-interact. The fact that gluons are not color neutral is an important difference between the strong and electromagnetic forces, which is manifested in the behaviour of the strong force potential. The potential between a quark and antiquark with a distance r apart is of the form

$$V(r) \sim -\frac{4}{3} \frac{\alpha_s(r)}{r} + kr, \quad (1.1)$$

where $\alpha_s(r)$ is the strong coupling constant, k is a constant of the order of 1 GeV/fm and r is the separation of the quarks. The $\frac{1}{r}$ term determines the potential at short distances, where the gluon distribution from a quark is radial, as shown in Figure 1.3a. Between any two separating (q or \bar{q}) quarks, for $r \geq 1$ fm, the second term in equation 1.1 dominates and $V(r) \rightarrow \infty$. Here, the constant k can be thought of as a spring constant providing the tension in the string. The self coupling of gluons causes the color field lines between the quarks to form a tube (Figure 1.3b). Therefore, the potential at large distances increases linearly with the separation of the quarks as the density of field lines remains constant. One implication of equation 1.1 is that an infinite amount of energy is required to separate two color charges. However, in practice, if the color flux tube is stretched enough, it becomes energetically favorable to rupture the tube and terminate the field lines with a $q\bar{q}$ pair created out of the QCD vacuum. Therefore it is not possible to separate two quarks on a large distance scale.

Equation 1.1 also implies, that on the small distance scale which is governed by the term proportional to $\frac{1}{r}$, deconfinement is possible if α_s tends to 0 faster than r .

1.2. The Strong Interaction: Confinement

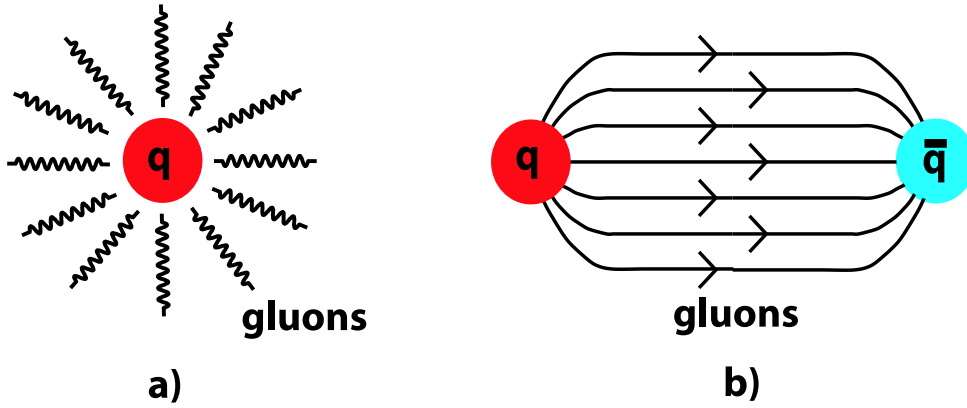


Figure 1.3.: The gluon distribution of a quark. a) Near the quark, they form a radial distribution, b) Further from the quark, they form a flux tube.

There are two phenomena which can lead to quark deconfinement at short distance scales. At very high energies, the bare quark itself can be probed and it is found that its effective color charge tends to zero as the energy with which it is probed increases. This process is called *asymptotic freedom*. At high hadronic density, quarks can interact with quarks from other hadrons. In this process, they lose their memory as to which hadron they are associated with. This is known as *Debye screening*.

Gluons carry both color and anticolor. Quarks are constantly emitting and reabsorbing virtual gluons according to the Heisenberg uncertainty principle. Consequently the net color of the system is not on the quark but rather surrounds it in the cloud of gluons. This has the effect of shielding the amount of original quark color seen by an approaching parton. In other words, the potential felt by a parton will decrease as the parton and quark separation decreases. From the first term in equation 1.1 it may be expected that $V(r) \rightarrow -\infty$ as $r \rightarrow 0$ [6, 7]. However at short distances, the strong coupling constant $\alpha_s(r)$ has a large dependence on Q^2 (and also r). The dependence is shown in equation 1.2

$$\alpha_s(Q^2) = \frac{12\pi}{(33 - 2n_f) \ln(Q^2/\Lambda_{\text{QCD}}^2)}, \quad (1.2)$$

where n_f is the number of quark flavors and Q^2 is the Lorentz invariant squared momentum transfer, and is only valid for $Q^2 \gg \Lambda_{\text{QCD}}^2$. The variable Λ_{QCD} can be thought of as the energy scale at which the strong force becomes strong. At distance of the order of the size of a nucleon (about 1 fm), over which confinement occurs, $\Lambda_{\text{QCD}} \approx 213$ MeV. At small distances, $\alpha_s(r) \rightarrow 0$, quicker than $r \rightarrow 0$ and so consequently $V(r) \rightarrow 0$. Quarks are then said to be free within the proximity of a nucleon, an effect which is known as asymptotic freedom.

An alternative consideration, which is applicable to bulk matter and also results in deconfinement of quarks and gluons, is that of Debye screening, analogous

1. Introduction

to the same effect in QED. In dense matter, the Coulomb potential felt by an orbiting electron is modified according to the formula

$$V'(r) = V(r) \exp\left(\frac{-r}{r_D}\right) = \frac{-e^2}{4\pi\epsilon_0 r} \left(\frac{-r}{r_D}\right), \quad (1.3)$$

where the electron binding radius is r , and the Debye screening radius, r_D is related to the number density of atoms, n_D by

$$r_D \sim \frac{1}{\sqrt[3]{n_D}}. \quad (1.4)$$

As the number density is increasing, r_D becomes smaller than the electron binding radius, and the exponential term in equation 1.1 tends to zero. As a result of Debye screening, the outermost electrons are freed from their host atom and the material becomes an electrical conductor. For the strong force equivalent, compression of quark matter is expected to give rise to a color conducting system of deconfined quarks and gluons.

1.2.1. Chiral Symmetry Restoration

At usual temperature and pressure, our world implies broken chiral symmetry. A transition into a chirally symmetric phase can occur at temperatures approximately the same as those required for a deconfined transition [8]. Chiral symmetry is related to the helicity of quarks. Particles whose spin vectors are aligned to their momentum vector are said to be *right handed*, while particles whose spin vectors are anti-parallel to the momentum vectors are referred to as being *left handed*. In any interaction with massless particles, the helicity of the particles is conserved.

At temperatures below this transition, quarks are massive particles. As α_s is greater than zero, quarks can interact and these interactions have the effect of increasing their mass so that it is greater than the *current* masses listed in Table 1.1. This is known as their *dynamical* mass and can be calculated from the hadronic masses using phenomenological models. This leads to light quark (u and d) masses of approximately 300 MeV, and a strange quark (s) mass of approximately 500 MeV. It is the easy to see why chiral symmetry is broken at these lower temperatures. As a quark with mass cannot travel at the speed of light, it is always possible to transform to a frame of reference where, in the case of a right handed particle, the momentum vector is no longer aligned to the spin vector, but anti-parallel to it. This situation, where quarks may appear to be either *left handed* or *right handed* depending on the frame of reference, clearly breaks chiral symmetry.

At temperatures above the chiral transition, α_s tends to zero and the interactions between quarks are reduced. Therefore, their effective mass is no longer given by their *dynamical* mass, but by their *current* value. As these values are still greater than zero, chiral symmetry can not be restored completely, only partially.

1.3. The Phase Diagram of Strongly Interacting Matter

The manifestation of a restoration of chiral symmetry in relativistic heavy ion collisions, where quark masses are given by their *current* value, rather than their *dynamical* value, may be two-fold. Firstly, the hadronic masses may be lower than expected, which could be visible in the lowering and broadening of resonance masses. Secondly, an increase in production rates of the heavier quarks may be seen. This should be most notable for the strange quark as the temperature of the system becomes comparable to the mass of the $s\bar{s}$.

1.3. The Phase Diagram of Strongly Interacting Matter

The sketch of the phase diagram of strongly interacting matter as a function of the temperature, T , and of the baryonic chemical potential (related to the net baryon density), μ_B as suggested by QCD-based considerations [9, 10] is shown in Figure 1.4. To a large extent these predictions are qualitative, as QCD at finite temperature and baryon number is one of the least explored domains of the theory. Three different states of matter are indicated: hadronic matter, QGP and color superconductor.

More quantitative results come from lattice QCD calculations which can be performed at $\mu_B = 0$. They strongly suggest a rapid crossover from the hadron gas to the QGP at the temperature $T_c = 170 - 190$ MeV [8, 11], which seems to be somewhat higher than the chemical freeze-out temperatures of central Pb+Pb/Au+Au collisions ($T = 150 - 170$ MeV) [12] at the top SPS and RHIC energies.

The nature of the transition to a QGP is expected to change with the increasing baryonic chemical potential. At high potential the transition may be of first order, with the end point of the first order transition domain, marked E in Figure 1.4 and calculated from [11] (2 + 1 flavors with physical quark masses), being the critical point of the second order.

Relativistic heavy ion collisions are a useful tool to explore the phase diagram of strongly interacting matter experimentally.

1.4. Relativistic Heavy Ion Collisions

To study nuclear matter under extreme conditions, it is necessary to create hot and dense nuclear matter in the laboratory. This can be achieved by colliding nuclei, either by shooting accelerated ions at a stationary target, or by head-on collisions of two ion beams. In order to achieve the biggest volume of excited nuclear matter, very heavy nuclei such as lead (Pb) or gold (Au) are used.

Therefore experiments beginning at Bevalac in Berkeley and continuing at the Joint Institute for Nuclear Research (JINR), at CERN SPS, the Schwerionen-Synchrotron (SIS) at the Gesellschaft für Schwerionenforschung (GSI), Alternating Gradient Synchrotron (AGS) and the Relativistic Heavy Ion Collider

1. Introduction

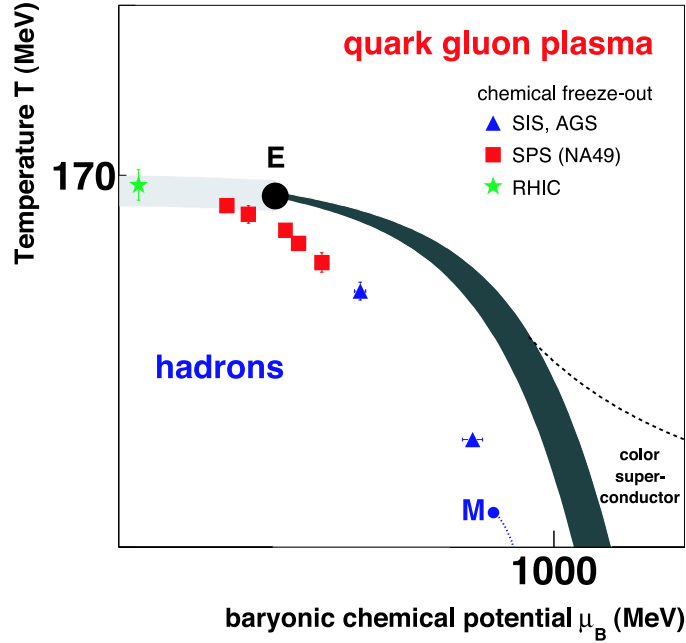


Figure 1.4.: The phase diagram of strongly interacting matter as a function of the temperature T and of the baryonic chemical potential μ_B . The chemical freeze-out points of hadrons produced in central Pb+Pb (Au+Au) collisions are taken from [12] and the critical point and the crossover curves for 2 + 1 flavors with physical quark masses from [11].

(RHIC) at the Brookhaven National Laboratory (BNL) and CERN LHC (Large Hadron Collider) are done. Presently this is the only way to search and confirm the existence of the QGP. Many nucleons are participating in nucleus-nucleus collisions compared to elementary proton-proton collisions, which are making multiple collisions in the reaction zone. The number of collisions as well as deposited energy depends on the size of the nucleus. The yield of secondary particles is much higher in Pb+Pb than in proton-proton collisions, so that there is a possibility of re-scattering between the produced hadrons.

There are different idealized pictures to describe heavy ion collisions. In the **Landau picture** [13] the interacting Lorentz contracted nuclei are fully stopped creating a baryon rich region in the center of mass of the interaction which is shown in Figure 1.5a. At the end, a hydrodynamically expanding fireball is left, which expands faster longitudinally than transversal due to the higher pressure gradient in longitudinal direction. The non-participating nuclei are flying without decelerate forward. In the laboratory frame, the initial energy density of the target nucleus is $\epsilon_0 = E/V$, where E and V are the energy and volume respectively. This is also the energy density of the beam ion in its rest

1.4. Relativistic Heavy Ion Collisions

frame. As the ion moves relativistically, the energy becomes $E' = E\gamma$ and the volume $V' = V/\gamma$, where γ is the relativistic factor equal to $1/\sqrt{1 - \frac{v^2}{c^2}} \approx \frac{\sqrt{s_{NN}}}{2m_n}$. As the two ions are completely stopped, they occupy the same physical space, so the energy density is given by equation:

$$\epsilon_{Landau} = 2\gamma^2 \frac{E}{V}. \quad (1.5)$$

In the **Bjorken picture** [1], the initial baryon charge of the target and projectile is so far apart in phase space that it cannot be slowed down completely during the heavy ion collision. In this so-called transparent energy regime the quanta carrying the baryon charge will essentially keep their initial velocities, i.e., the center of the reaction zone will be almost baryon free, which is shown in Figure 1.5b. However, much energy will be deposited in this baryon free region.

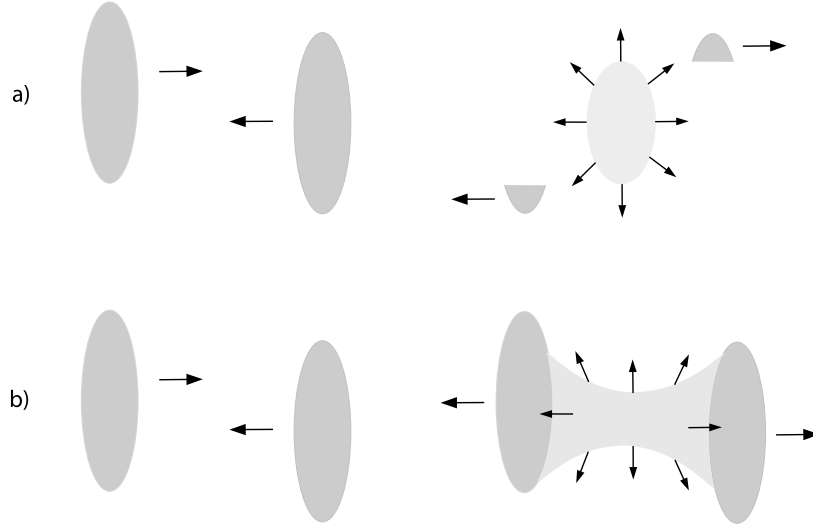


Figure 1.5.: Illustration of the Landau a) and Bjorken b) picture of nucleus+nucleus collisions.

Bjorken [1] has given a simple estimate of the initial energy density reached in central A+A collisions

$$\epsilon_{Bjorken} = \frac{1}{\tau \mathcal{A}} \frac{dE_t}{dy} \Big|_{y=y_{cm}}, \quad (1.6)$$

where \mathcal{A} is the transverse area of the incident nuclei, $\frac{dE_t}{dy}$ denotes the transverse energy of the collision product per unit of rapidity and the hadron formation time (assumed to be $\tau = 1$ fm/c). In both approaches the energy density increases with collision energy and thus at high enough energy a QGP should be formed.

1. Introduction

The space-time evolution of a heavy ion collision in the center of mass frame with and without formation of a QGP is shown in Figure 1.6. The situation before the collision is shown in a). The nuclei are accelerated to relativistic speed, which is why they appear Lorentz contracted. In b) the initial conditions are illustrated.

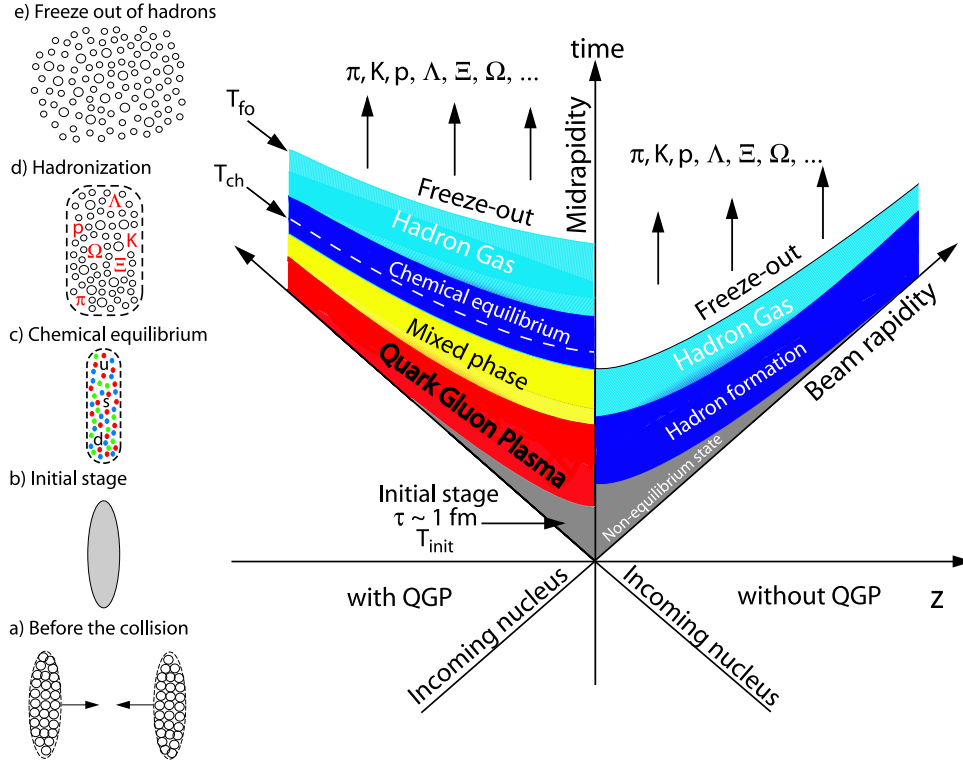


Figure 1.6.: Space-time evolution of the high-energy nuclear collisions with and without formation of a QGP.

The nuclei collide and interactions at small distances between quarks (partons) of the participating nucleons take place in a small volume. In both cases first a formation time is needed before either a hadron gas or a QGP is created. First the case QGP creation will be explained. In the following stage c), the QGP fireball is expanding due to internal pressure and cools down rapidly. Particle interactions become much softer, and processes at low transverse momentum play a dominant role. With the end of the production of new quarks, the system approaches chemical equilibrium. In d), the hadronization phase is represented. In this stage a QGP is transformed into mesons and baryons. Inelastic processes are stopped at a given temperature T_{ch} , this is known as chemical freeze out. The expansion and cooling continues until elastic collisions between particles stop at the thermal freeze out temperature T_{fo} , when momenta of the particles are fixed, which is shown in e). The freeze out times might be different for various particle species because of the different cross-section.

The emitted particles move freely towards the detectors, where they are finally measured.

On the right hand side of Figure 1.6 the evolution of a heavy ion collision is presented without quark gluon plasma phase transition. Characteristic for the hadron gas are frequent interactions (rescattering) which can change the kinetic properties via elastic and the particle composition of the system via inelastic interactions.

1.5. Strangeness

The strange (s) and anti-strange (\bar{s}) quarks are not contained in the colliding nuclei, but are newly produced and show up in the strange hadrons in the final state. Rafelski and Müller suggested that strange particle production is enhanced in the QGP with respect to that in a hadron gas [14] – [16]. This enhancement is relative to a collision where a transition to a QGP phase does not take place, such as p+p collisions where the system size is very small. The enhancement occurs because different channels are available for the production of strange quarks, as well as a difference in threshold energies due to the fact that in a deconfined state, only the strange quarks have to be produced, rather than strange hadrons themselves.

1.5.1. Strangeness Production in a Hadronic Gas

The hadronic interactions which create strange hadrons have a high energy threshold, which is calculated from the difference in masses between the initial and final state particles. Two such typical reactions involving nucleons (N) are given in equations 1.7 and 1.8. As strangeness is conserved in the strong interaction, a hadron containing a \bar{s} quark must be produced in the same reaction as a hadron containing a s quark. An example of a production reaction for Λ hyperons in a Hadronic Gas is presented in equation 1.7 and 1.8, where the threshold energy of 700 MeV and 2200 MeV, respectively:

$$N + N \rightarrow \Lambda + K^+ + N, \quad E_{\text{thresh}} \approx 700 \text{ MeV}, \quad (1.7)$$

$$N + N \rightarrow N + N + \Lambda + \bar{\Lambda}, \quad E_{\text{thresh}} \approx 2200 \text{ MeV}. \quad (1.8)$$

These threshold energies are quite large to produce strangeness in an initial collision. More realistically, the production of strange quarks is dominated by the re-scattering of particles as the fireball is dominated by produced pions, except when the net baryon density is large. The principal channels for strangeness production are given by equations 1.9 – 1.16, which have lower energy thresholds than strangeness production in primary interactions:

$$\pi + \pi \rightarrow K + \bar{K}, \quad E_{\text{thresh}} \approx 720 \text{ MeV}, \quad (1.9)$$

1. Introduction

$$\pi + N \rightarrow \Lambda + K, \quad E_{\text{thresh}} \approx 540 \text{ MeV}, \quad (1.10)$$

$$\pi + \bar{N} \rightarrow \bar{\Lambda} + \bar{K}, \quad E_{\text{thresh}} \approx 540 \text{ MeV}, \quad (1.11)$$

$$K + \pi \rightarrow \bar{\Lambda} + N, \quad E_{\text{thresh}} \approx 1420 \text{ MeV}, \quad (1.12)$$

$$\pi + \Lambda \rightarrow \Xi + K, \quad E_{\text{thresh}} \approx 560 \text{ MeV}, \quad (1.13)$$

$$\pi + \bar{\Lambda} \rightarrow \bar{\Xi} + \bar{K}, \quad E_{\text{thresh}} \approx 560 \text{ MeV}, \quad (1.14)$$

$$\pi + \Xi \rightarrow \Omega + K, \quad E_{\text{thresh}} \approx 705 \text{ MeV}, \quad (1.15)$$

$$\pi + \bar{\Xi} \rightarrow \bar{\Omega} + \bar{K}, \quad E_{\text{thresh}} \approx 705 \text{ MeV}. \quad (1.16)$$

Although the threshold energy for production of the Λ and $\bar{\Lambda}$ are the same, (as given by equations 1.10 and 1.11), dependent upon the amount of stopping, strange baryons are produced more readily due to the absence of anti-nucleons (\bar{N}). This is because there already are protons and neutrons present from the colliding ions while anti-nucleons have to be produced. Consequently, the Hadronic Gas phase has to be long lived to enable an equilibration of strangeness.

1.5.2. Strangeness Production in a Quark Gluon Plasma

For almost 25 years, it has been expected that the production of strange particles in a QGP phase would be enhanced with respect to a Hadron Gas [14, 16]. Strangeness is a good quantum number because it is conserved in strong interactions. Strange quarks (and therefore strange hadrons) decay via the weak interaction, where decay lifetimes of 10^{-10} s are typical and so these decays are not important on the time scale of a hadronizing QGP.

The production mechanisms for strange quarks in a QGP are different from a Hadronic Gas. They are produced due to gluon fusion ($g + g \rightarrow s\bar{s}$), as well as the annihilation of light $q\bar{q}$ pairs ($q\bar{q} \rightarrow s\bar{s}$) which are shown in Figure 1.7. As the plasma is expected to be initially gluon rich, and the equilibration of quarks takes time compared to the gluon equilibration time, the gluonic channels contribute more than 80 % to the total production rate of strange quarks.

The threshold energy required to create a pair of $s\bar{s}$ quarks in the QGP is just the bare mass of the two strange quarks ($E_{\text{thresh}} \approx 2m_s \approx 300 \text{ MeV}$). This means that due to the high temperatures involved in the QGP phase, the thermal production of $s\bar{s}$ pairs is possible. A further source of enhancement of $s\bar{s}$ pairs comes from the process of Pauli blocking of the light quarks. As all quarks are fermions, they obey the Pauli Exclusion Principle which states that no two fermions can be in the same quantum mechanical state. Therefore, as more and more light quarks are produced in the collision, they fill up the available energy levels and it becomes energetically favourable to create $s\bar{s}$ pairs. It is expected that the extra mechanisms for $s\bar{s}$ production in a QGP should lead to a production rate which is 10 to 30 times higher than in a Hadronic

Gas, and this should allow equilibration of strangeness even in the short lifetime of the fireball [16].

It therefore follows that the production of anti-strange and multi-strange baryons at freeze-out will be enhanced if the system passes through a deconfined phase, than if it remains in the Hadronic Gas phase only.

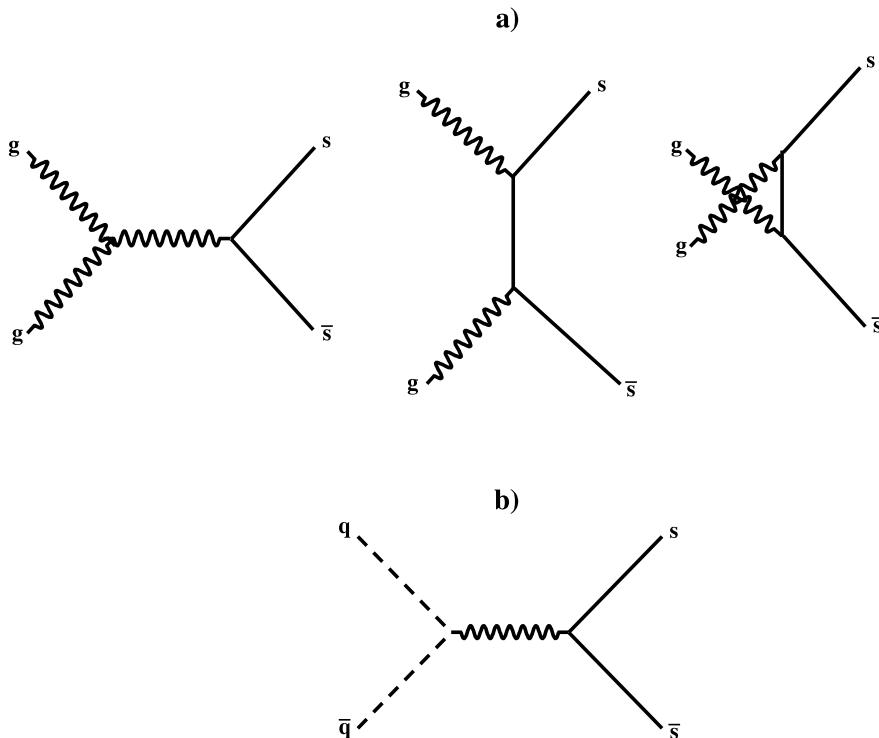


Figure 1.7.: Leading order QCD Feynman diagrams for $s\bar{s}$ production by gluon fusion and pairs of light quarks : a) $gg \rightarrow s\bar{s}$, b) $q\bar{q} \rightarrow s\bar{s}$.

Even if an enhancement of strangeness occurs in a QGP, there are still difficulties in quantifying the magnitude of this enhancement. As the lifetime of the QGP phase (or even the fireball in general) is unknown, it is impossible to compute the actual values of particle production in the two different scenarios. An enhancement is expected to occur ordinarily in A+A collisions compared to scaled p+p collisions, as strangeness will be produced in the secondary collisions indicated in equations 1.9 – 1.12. Another useful way to study strangeness enhancement is by using the ratio of strange quark pairs with respect to the produced non-strange quark pairs before resonance decays, the so-called strangeness suppression factor [17] defined as:

$$\lambda_s = \frac{2\langle s\bar{s} \rangle}{\langle u\bar{u} \rangle + \langle d\bar{d} \rangle}. \quad (1.17)$$

This ratio is strongly dominated by the most abundant strange and non-strange particles, kaons and pions. Kaons carry most of the produced (anti-) strangeness,

1. Introduction

the ratio $\langle K + \bar{K} \rangle / \langle \pi \rangle$ is often used to quantify relative strangeness production:

$$\langle K + \bar{K} \rangle = \frac{K^+ + K^- + 2K_s^0}{4}, \quad (1.18)$$

$$\langle \pi \rangle = \frac{\pi^+ + \pi^-}{2}. \quad (1.19)$$

An increase in the $\langle K + \bar{K} \rangle / \langle \pi \rangle$ ratio in A+A collisions compared to p+p or p+A collisions could then indicate an increase in the production of strangeness. The K^+/π^+ ratio is often used as a measurement of strangeness enhancement rather than the $\langle K + \bar{K} \rangle / \langle \pi \rangle$ ratio. The reason is that K^+ carry about 50% of all \bar{s} -quarks independent of the energy.

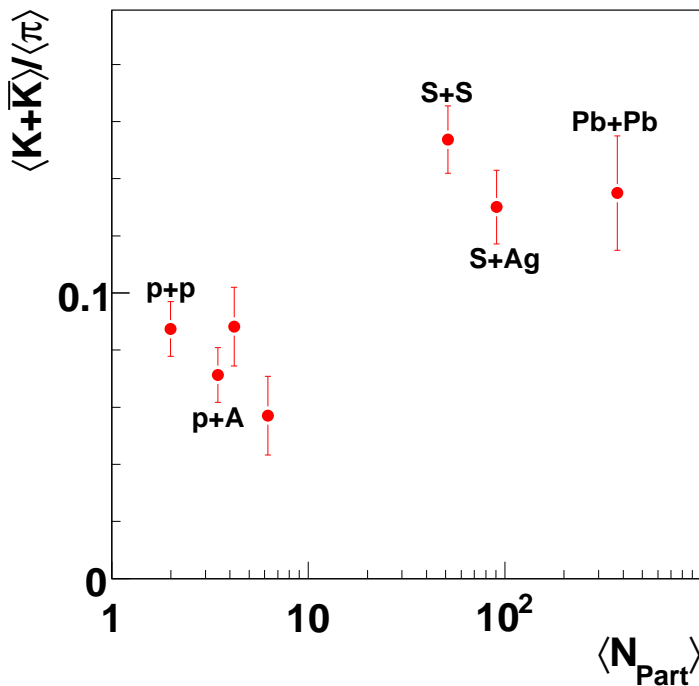


Figure 1.8.: The dependence of the K/π ratio, defined as the sum of the total kaon multiplicity (K^+ , K^- , $2K_s^0$) divided by all pions (π^+ , π^- , π^0), on the number of participant nucleons at 158 AGeV.

The first possibility to compare the above expectations with the data was in 1988 when the preliminary results from sulfur and silicon beams at SPS and AGS became available. The NA35 experiment reported [18, 19] that in central S+S collisions at 200 AGeV the kaon to pion ratio is approximately two times higher than in N+N interactions at the same energy per nucleon (see Figure 1.8). The results for $\langle K + \bar{K} \rangle / \langle \pi \rangle$ is obtained by using the pion multiplicities measured in the same data sample [20] and are not just compared to S+S but also to S+Ag [21], N+N and p+A data [22, 23].

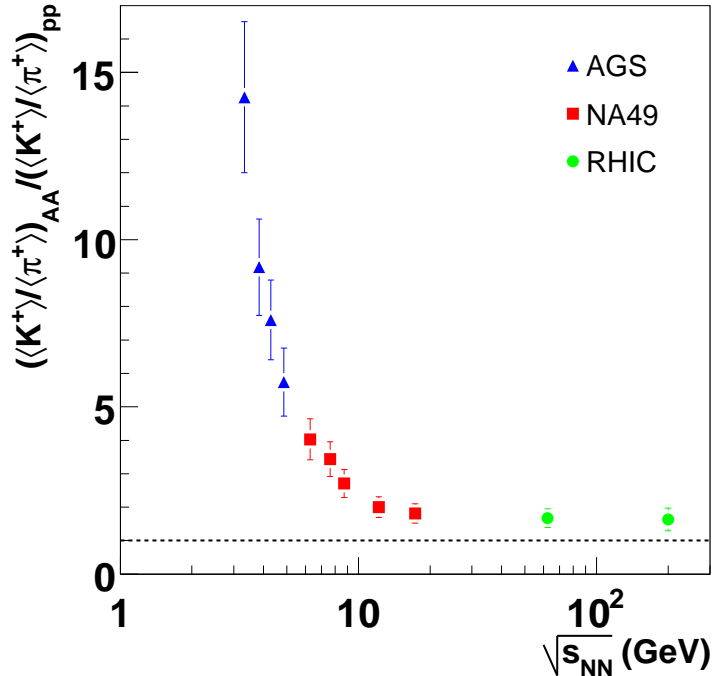


Figure 1.9.: The double ratio $\langle K^+\rangle/\langle\pi^+\rangle$ from central Pb+Pb and Au+Au reactions divided by $\langle K^+\rangle/\langle\pi^+\rangle$ from p+p reactions as a function of the initially available energy. The errors include statistical and a 15% uncertainty in the parametrization of the $\langle K^+\rangle/\langle\pi^+\rangle$ from p+p reactions.

A suppression with respect to p+p interactions is observed in p+A collisions. An enhancement is observed going to S+S collisions. No further enhancement is visible going from S+Ag to Pb+Pb collisions. An even larger enhancement was measured by the E802 collaboration [24]. Recent data on central Pb+Pb/Au+Au collisions from low AGS to RHIC [25] – [31] energies complete this picture. Figure 1.9 shows the $\langle K^+\rangle/\langle\pi^+\rangle$ ratio measured in Pb+Pb/Au+Au collisions divided by the corresponding ratio in p+p interactions [32, 33]. It is visible that a strangeness enhancement is observed at all energies and the enhancement is even stronger at lower AGS energies than at RHIC energies. Thus an interpretation following the original concept that strangeness enhancement is a signature for the QGP [14] – [16] is questionable. At low AGS energies due to lower energy density formation of a QGP is not expected and therefore no strangeness enhancement should be observed. Quite contrary a larger strangeness enhancement is seen at AGS energies than at RHIC energies. Therefore one can conclude that the concept of strangeness enhancement as a signal of QGP is incorrect [34]. It is argued that the strangeness production mechanism in p+p is different than in A+A. Thus it was suggested

1. Introduction

in [35] to analyze the energy dependence of strangeness to pion ratio in A+A collisions. Furthermore the model predicts a transition to a QGP between AGS and SPS energies to be indicated by a "horn" like structure in strangeness to entropy ratio (see Figure 1.10). The model predicts energy dependence of total strangeness and entropy production but gives no specific predictions concerning production of identified hadrons, e.g. Ξ hyperons considered in this thesis.

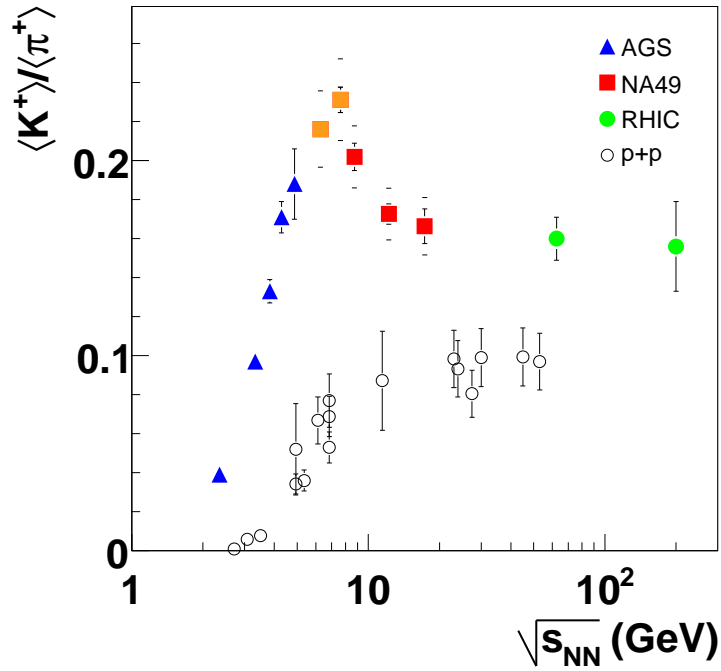


Figure 1.10.: Energy dependence of full phase space $\langle K^+ \rangle / \langle \pi^+ \rangle$ ratio in central Pb+Pb and Au+Au collisions from AGS to RHIC energies [25] – [31]. The data for p+p interactions are shown by open circles for comparison [32, 33].

This prediction motivated the energy scan program of NA49. The experiment registered central Pb+Pb collisions at 20, 30, 40, 80 and 158 AGeV, semi-central Si+Si collisions at 158 AGeV and minimum bias Pb+Pb collisions at 40 and 158 AGeV. In this work the energy and system size dependence of Ξ^- and $\bar{\Xi}^+$ production is studied.

2. The NA49 Experiment at CERN SPS

The measurements described in this thesis are part of the experimental program of the NA49 collaboration. The NA49 experiment is located in the North Area of the European Center for Nuclear Research (CERN) at the H2-Beamline. Figure 2.1 illustrates the layout of the CERN accelerator complex. Since 1994 it has been possible to accelerate lead ions with a momentum of 158 GeV per nucleon. Ions are first produced by an Electron Cyclotron Resonance (ECR) source and separated with a spectrometer. Then Pb^{25+} ions are accelerated with a Radio Frequency Quadrupole (RFQ) and Linear Accelerator (LINAC). The ions are then stripped to the Pb^{53+} state and enter the Proton Synchrotron Booster ring (Booster). After being accelerated to 94 MeV per nucleon, the ions are injected into the Proton Synchrotron (PS). Following a further acceleration, the ions are injected into the Super Proton Synchrotron (SPS) via a second stripper foil. In the SPS, fully stripped Pb^{82+} ions are accelerated to their final energy [37]. With the current configuration it is just possible to accelerate (anti-)protons and lead ions. The study of silicon+silicon reactions is possible through the generation of a secondary fragmentation beam which is produced by a primary target (1 cm carbon) in the extracted lead-beam. With the proper setting of the beam line magnets a large fraction of all $Z/A = 1/2$ fragments at ≈ 158 AGeV are transported to the NA49 experiment.

For central lead+lead interactions at top SPS energies (158 GeV per nucleon) about 1600 charged particles have to be detected to study heavy ion collisions. It is desirable to measure as many as possible of the produced particles, and extract the maximum information of the collision. With this assumption, a detector has to be designed with a large acceptance, good momentum resolution, good two-track resolution and particle identification. This condition is fulfilled in NA49 with four Time Projection Chambers (see section 2.1) as primary detectors for charged particles, Time of Flight walls and two Calorimeters. NA49 can be operated with different target configurations (lead-, carbon- and siliconfoil, liquid hydrogen) to analyze a multitude of diverse collisions, from elementary hadron-hadron collisions over hadron-nucleus to collisions of light nuclei to lead-lead collisions.

2. The NA49 Experiment at CERN SPS

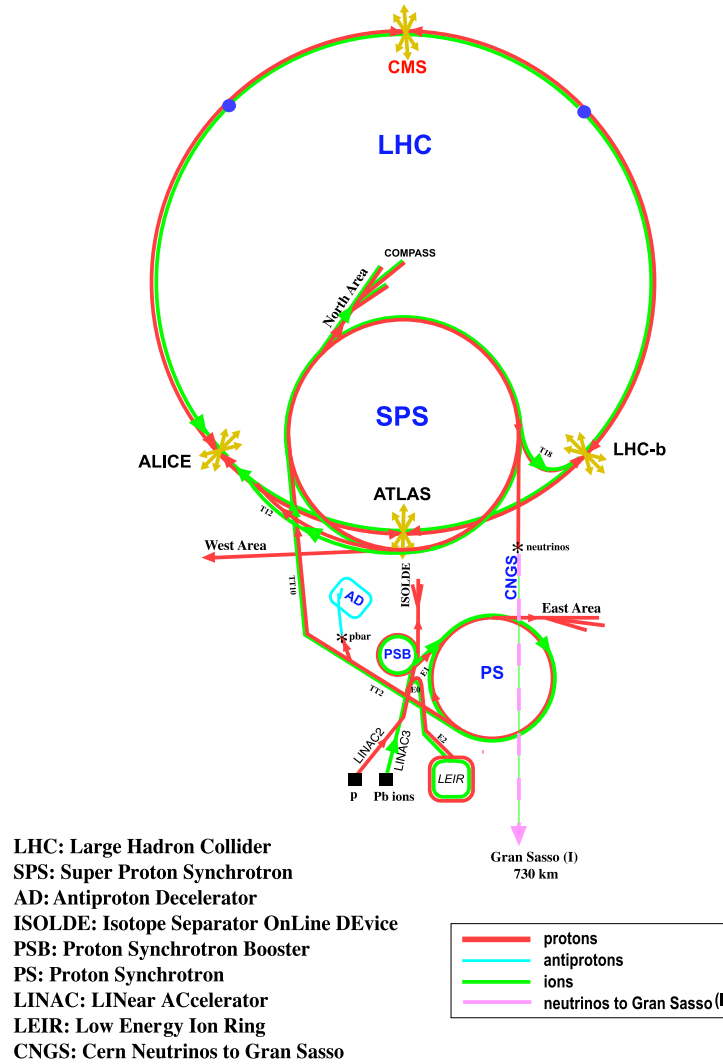


Figure 2.1.: Layout of the CERN accelerator complex.

2.1. The NA49 Detector Layout

The NA49 experiment [36] is a large acceptance spectrometer for charged hadrons. In a central lead-lead collision 1600 charged particles are produced. Because of the high track density, a detector is needed with good space- and two track resolution and a minimum of material in the acceptance in order to minimize the rate of secondary interactions and multiple scattering. Therefore *Time Projection Chambers* (TPC) were selected, which are the main components in NA49. Figure 2.2 shows a detailed layout of the NA49 experimental apparatus.

The first two Vertex TPCs (VTPC-1 and VTPC-2) are located each in one superconductive dipole magnet (VTX-1 and VTX-2). At 158 AGeV the magnetic field is 1.5 Tesla for VTX-1 and 1.1 Tesla for VTX-2. The total bending power

2.1. The NA49 Detector Layout

for the magnets is 7.8 Tm for a length of 7 m. It is possible to operate the magnet in two polarizations (std \pm). The job of the magnets is to expand the reaction cone to measure particle tracks in high track density regions. It is possible to determine the momentum p of charged particles from the deflection in the magnetic field B [38]:

$$p = 0.3 \cdot q [e] \cdot B [T] \cdot R [m] \cdot \frac{1}{\cos\lambda} \quad (2.1)$$

where q is the charge of the particle, R the radius of curvature of the particle and λ the track angle in y -direction. The exact knowledge of the magnetic field is needed to determine the momenta and therefore two methods independent of each other have been used. On the one hand the magnetic field is calculated with the program TOSCA and on the other hand it is measured in 4 cm^3 steps with a Hall probe [39]. The deviation between both methods is 0.5%.

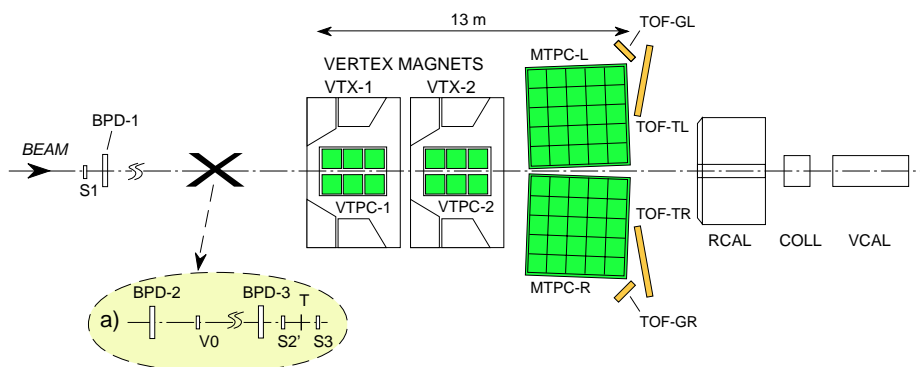


Figure 2.2.: Set-up of the NA49 experiment at the CERN SPS.

Dependent on particle topology the track momenta can be determined up to $dp/p^2 = 0.3 \cdot 10^{-4} \frac{1}{\text{GeV}}$.

Downstream of VTPC-2 are two large volume Main TPCs (MTPC-L and MTPC-R) positioned on either side of the beam in a field-free area. In the Main TPCs the particle identification is done via the specific energy loss dE/dx . The resolution of the specific energy loss is in the range of 3–4%. Beyond the Main TPCs are the *Time-of-Flight* (TOF) walls. The TOF acceptance is at midrapidity and it supports the particle identification in the TPCs. The flight time measurement starts as soon as the projectile passes the Quartz-Čerenkov-counter $S1$. The time between the start time and the end time defines the flight time, where the height of the signal is the dimension of the particle charge. The particle identification with the Time-of-Flight measurement is based on the relativistic relation $pc = \beta\gamma m_0 c^2$, with $\gamma = \frac{1}{\sqrt{1-\beta^2}}$ and $\beta = \frac{v}{c}$:

$$(m_0 c^2)^2 = (pc)^2 \cdot \left(\frac{c^2 t^2}{s^2} - 1 \right) \quad (2.2)$$

It is now possible to determine the mass m of the particle from the flight time and the momentum p , which is determined in the TPC.

2. The NA49 Experiment at CERN SPS

Two downstream calorimeters complete the setup. The opening of the *Collimator* (COLL) is adjusted such that beam particles, projectile fragments and spectator neutrons and protons can reach the Veto-Calorimeter (VCAL) [36]. The Veto-Calorimeter is 20 meters behind the target and after the Collimator. The Veto-Calorimeter, constructed originally for the NA5 experiment [40], consists of lead scintillators and iron scintillators. The energy resolution can be parametrized by :

$$\sigma(E)/E = 1.0/\sqrt{E(\text{GeV})} \quad (2.3)$$

Central collisions can be selected by discriminating the analog energy sum signal. A typical threshold setting at $E_{\text{veto}} \leq 8$ TeV corresponds to about 4 % of the Pb+Pb interaction cross section and an impact parameter below 3 fm.

A series of *Beam Position Detectors* (BPD) and Čerenkov-counters are used for the data acquisition. The BPD is a two dimensional multi-wire proportional counter with a area of 3×3 cm² giving x and y coordinates of the beam. Two orthogonal sense wire planes with a 2 mm pitch are sandwiched between three cathode planes. Each lead ion passing through the three BPDs can be projected to the target z position giving an independent measurement of the primary interaction vertex. The resulting precision of the beam position extrapolated to the target is 40 μm for Pb beams.

In order to select central lead-lead events and to trigger the read-out, a combination of the signals of the Čerenkov-counters S1, S2', S3 and the Veto-Calorimeter is used. It is possible to determine the charge of the beam particles with the Čerenkov-counters. Therefore the signals of S1 and S2 are used to select the lead-ions. The lead target is actually contained within the counter S3 and has a thickness of 207 μm and an interaction rate of about 1%. Čerenkov light is reflected towards a photomultiplier tube by a mylar strip with a thickness of 25 μm , which ensures that no more extra material is placed in the beamline than necessary. For lead-lead collisions the interaction in the target is selected with the S3 counter, which is switched in anti-coincidence with S1 and S2.

2.2. Time Projection Chambers

The majority of particle detection in NA49 is done with the four large volume TPCs. These devices combine technology of drift chambers and multi-wire proportional counters. The TPC is capable of recording the trajectory of charged particles in three dimensions.

A TPC consists of a gas filled box lain in an electric field (E) with one face chosen as the readout plane. The basic idea behind TPC operation is illustrated in figure 2.3. A charged particle passing the gas box will interact with the gas causing it to be ionized. Electrons from this ionization drift (upwards) towards the readout plane under the influence of the field. The field is maintained by a potential difference between the bottom of the TPC and a gating grid of wires near the cathode plane and this defines the drift region. Beyond the gating grid lies a series of sense wires held at a high voltage. When the

drifting electrons pass the gating grid, they are rapidly accelerated towards the sense wires until they have sufficient energy to cause secondary ionization. If the accelerating potential is held constant, the amount of secondary ionization produced is proportional to the original number of drifting electrons. This is the principle behind the proportional counter.

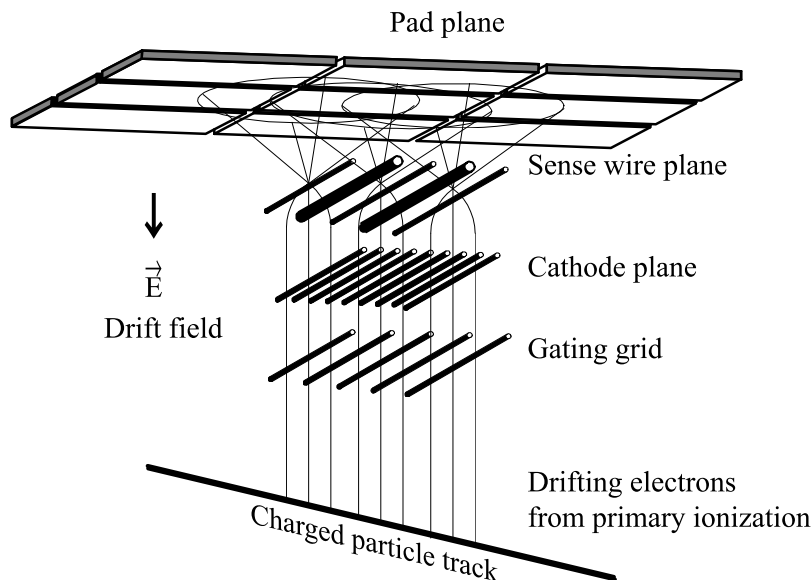


Figure 2.3.: Schematic layout of the TPC readout chambers.

When electrons from the secondary ionization reach the sense wires, the total charge can be read out. By providing several such wires along the top plane of a TPC, the location of the original ionization in the two dimensions orthogonal to the drift direction can be obtained. An alternative approach is to use a plane of pads situated just above the sense wires. Movement of the positive ions from the secondary ionisation induces charge on the pads which are then read out. In principle, covering the detection plane with rows of these pads gives position information in the two directions orthogonal to the drift direction. The location of the original ionization in the drift direction is obtained from the product of the drift time and drift velocity. Thus, determination of the original particle ionization in all three spatial dimensions is possible with a TPC.

2.2.1. The NA49 TPCs

Table 2.1 shows the physical properties of the NA49 TPCs [41]. Both Main TPCs (MTPC) consist of 25 (5×5) sectors and the VTTPCs consist of 6 (2×3) sectors as shown in figure 2.2. Generally, each MTPC sector is subdivided into 18 rows of 128 pads and is correspondingly classified as standard resolution (SR). However, the five sectors closest to the beamline are higher resolution (HR) sectors and contain 192 pads per padrow. Furthermore, all sectors in the

2. The NA49 Experiment at CERN SPS

VTPCs consist of 24 rows of 192 pads. Increased resolution is desirable close to the beamline because the track density is higher there. Both of the VTPCs are split into two equal halves on either side of the beamline, with a separation gap of 20 cm. This space is to avoid deposition of charge in the sensitive volume by the beam. This problem is also avoided with the MTPCs since they are situated on either side of the beamline. The choice of gas used in the TPCs is a critical design consideration. Both the velocity and diffusion of the drifting electrons depend on the mixture and pressure of the selected gas [42]. The chosen gas mixture is Ne/CO₂ (90/10) for the VTPCs and Ar/CH₄/CO₂ (90/5/5) for the MTPCs. With the selected gas mixture the FWHM of the charge distribution can be limited to about 5 mm both in transverse and longitudinal drift direction after 60 cm.

	VTPC-1	VTPC-2	
Volume [m ³]	2 · 2,5 · 0,98	2 · 2,5 · 0,98	
Gas	Ne/CO ₂ (90/10)	Ne/CO ₂ (90/10)	
Sectors	6	6	
Padrows per sector	24	24	
Pads per padrow	192	192	
Channels (pads)	27648	27648	
Pad length [mm]	16/28	28	
Pad width [mm]	3,5	3,5	
Angle [°]	12-55	3-20	

	MTPC-L/R		
Volume [m ³]	3,9 · 3,9 · 1,8		
Gas	Ar/CH ₄ /CO ₂ (90/5/5)		
Sectors	25		
Padrows per sector	18		
Channels (pads)	63360		
Sectortyp	HR	SR	SR'
Pads per padrow	192	128	128
Pad length [mm]	40	40	40
Pad width [mm]	3,6	5,5	5,5
Angle [°]	0	0	15

Table 2.1.: Physical properties of the NA49 TPCs.

2.3. Event Reconstruction

During the production of data, which was carried out at CERN for the analysis described in this thesis, raw events are processed through the NA49 reconstruction chain which reconstructs each event. The reconstruction chain itself consists of a series of software packages which process this data performing a

2.3. Event Reconstruction

variety of different tasks, such as cluster finding, track finding and fitting, primary vertex location, $\frac{dE}{dx}$ determination, TOF information and strange particle reconstruction.

Before the first event of raw data is read in, other information is also loaded. These constants comprise the magnetic field maps, detector geometry information and program parameters which are used by the software packages in the production. Once completed, the reconstructed event is written to an output Data Summary Tape (DST). Typically three Mbytes of DST data are written per event. The information which is saved in the DSTs is important for the calculation of the track information, but too much for the analysis especially for the analysis of millions of events. Because of this reason, miniDSTs are used for the analysis, which implies the subset of all information that is really needed.

The miniDSTs are saved as ROOT-Trees [43]. ROOT [44] [45] is an object orientated analysis environment which is based on the programming language C++. Adapted classes to the detector are developed in NA49 to save event and track information [43]. These classes are used for the analysis in this thesis.

Details of the reconstruction chain are already discussed in different diploma and Ph.D. theses (e.g. [46]). Therefore just the important aspects of the reconstruction, which are used for the analysis, will be discussed. In order to make the maximum use of the available information it is necessary to combine the data measured by the four local TPCs and treat the whole NA49 setup as one *global* detector system. The analysis software providing the unification of the detector system will thus be referred to as the *Global Tracking Chain* [47].

This serves the approach to combine the superior momentum determination of the VTPCs+MTPCs (with a momentum resolution of $dp/p^2 = 0.3 \times 10^{-4} (\text{GeV}/c)^{-1}$) with the excellent particle identification capabilities of the large volume MTPCs and it also facilitates the pattern recognition by extrapolating well separated tracks in one detector to the high track density region of another.

The NA49 global tracking is based on a strategy of data reduction by first translating the hits in the detector into space points and then connecting these by pattern recognition algorithmus. The space points are generated by identifying continous regions of charge pixels above threshold, so called "clusters", which are then connected to "tracks". The algorithmus used are set up to search for tracks oncoming from the main vertex first, because they offer the best constraints for momentum reconstruction and are thus easiest to find. Removing the easy and well defined tracks from the sample leaves a moderate multiplicity of special cases.

The MTPCs have a simple track model (straight-lines) which eases pattern recognition. Due to the absence of a magnetic field in the detector only tracks originating from the main vertex can be assigned a momentum that defines a unique trajectory. The VTPCs have a good momentum resolution ($dp/p^2 = 7.0 \times 10^{-4} (\text{GeV}/c)^{-1}$) independent of the main vertex because of the direct

2. *The NA49 Experiment at CERN SPS*



Figure 2.4.: The NA49 reconstruction chain.

measurement of the track bending, but suffer from a high track density and a complex track model of a helix distorted by inhomogenities in the magnetic field. Figure 2.4 shows the NA49 reconstruction chain.

2.3.1. V0 Reconstruction

Three neutral single strange hadrons (Λ , $\bar{\Lambda}$ and K_s^0) can be studied at NA49. These particles are uncharged and therefore do not cause ionisation in the TPC gas themselves. Instead, they are recognized by their weak decay into two oppositely charged daughters in a characteristic "v" shape. They are collectively referred to as V0s. Table 1.2 shows the properties of the V0 candidates. The weakly decaying charged hyperons Σ^+ and Σ^- are not reconstructable due to the fact that only one daughter is charged. Neutral Σ^0 hyperons decay electromagnetically via $\Sigma^0 \rightarrow \Lambda + \gamma$ and, because of the shorter time scale of the electromagnetic interaction, it is experimentally indistinguishable from the weakly decaying Λ hyperon. Consequently, measurements of Λ and $\bar{\Lambda}$ hyperons represent the summed contribution from $\Lambda + \Sigma^0$ and $\bar{\Lambda} + \bar{\Sigma}^0$ respectively.

2.3.2. V0 Finding

V0 candidates are found from particle tracks by taking each positively charged track in combination with each negative track and tracking them through the NA49 magnetic field. In the V0 finding software, *v0find*, particles are tracked from the first measured point in the TPC in the direction towards the target to the minimum allowed z position in steps of 2 cm. The separation of each positive-negative pair in x and y are compared at each z position and a minimum is found if one exists. At the minimum, the distance of closest approach (DCA) of the pair in x and y ($dcax$ and $dcay$) is found. If the DCA is smaller than 0.5 cm in x and 0.25 cm in y , the pair are considered as a V0 candidate. For kinematic analysis of V0s, it is important to know the momentum of the daughter tracks, so *v0find* insists the global tracks has a minimum of 10 points in VT1 or 20 points in VT2.

The following, basically geometrical, V0 finding criteria are selected in such a way to find as many V0 candidates as possible but still reduce the combinatorial background. The first geometrical criterion is the z position of the determined V0 vertex. This quantity has to be larger than -555 cm for all V0 candidates. If the crossing point of a track pair is before this point it will be rejected. It is also requested that the extrapolated daughter track has a minimum distance in the target plane. The distance in y direction is larger than 0.75 cm. This cut makes sure that both tracks are not from the main vertex.

The extrapolated track of the mother particle has to be in a certain range of the main vertex in x and y direction. Detailed descriptions about the ϕ angle, dip-cut and the armenteros criteria can be found here [48, 49]. Table 2.2 shows a summary of the used cuts in the V0 finder. These cuts are referred as the *GSIttype* and are used for the further analysis.

2. The NA49 Experiment at CERN SPS

Variable	Cut
Measured Points in the TPC	≥ 10 (VTPC-1) ≥ 20 (VTPC-2)
dca _x	≤ 0.5 cm
dca _y	≤ 0.25 cm
Z_{Vertex}	≥ -555 cm
$ X_{\text{Target}} $	≤ 25 cm
$ Y_{\text{Target}} $	≤ 25 cm
ϕ	≥ 0.2 rad ≤ 2.9 rad
$ x1minx2 $	≥ 0 cm
$ y1miny2 $	≥ 0.75 cm
dip-cut	$= 1$
p_t^{Arm}	≤ 0.35 GeV/c

Table 2.2.: V0 cuts (for lead-lead-collisions) of the Λ hyperons.

2.3.3. V0 Fitting

Found V0 candidates are presently fitted geometrically with the client *v0fit*. Each V0 daughter track is associated with one extra point (the V0 decay vertex). From this additional constraint a better determination of the true V0 momentum is expected if the V0 candidate is really a decaying particle. V0s are fitted with a nine parameter Levenburgh-Marquardt fitting procedure [50]. The nine variables are the three coordinates of the decay vertex and three momentum components from each of the two charged daughters.

2.3.4. Multi-Strange Hyperon Reconstruction

In addition to singly strange V0s, there are multi-strange hyperons which can be reconstructed additionally in NA49. Properties of the doubly strange Ξ , triply strange Ω s and their antiparticles are shown in Table 1.2. It is not possible to measure the uncharged Ξ^0 . The π^0 is uncharged and cannot be detected in the NA49 TPCs. Thus, only the charged Ξ s in the decay modes shown in Table 1.2 can be considered. As an example, the topology of the decay process for the Ξ is illustrated in figure 2.5.

2.3.5. Ξ Finding

The Ξ reconstruction is performed with the program *xi_find* and is based on locating the decay vertices in an analogous way to V0 finding (see subsection 2.3.2). Here, V0 candidates are reconstructed first from global tracks and V0 vertices are obtained. Ξ candidates are found by taking suitable V0s in

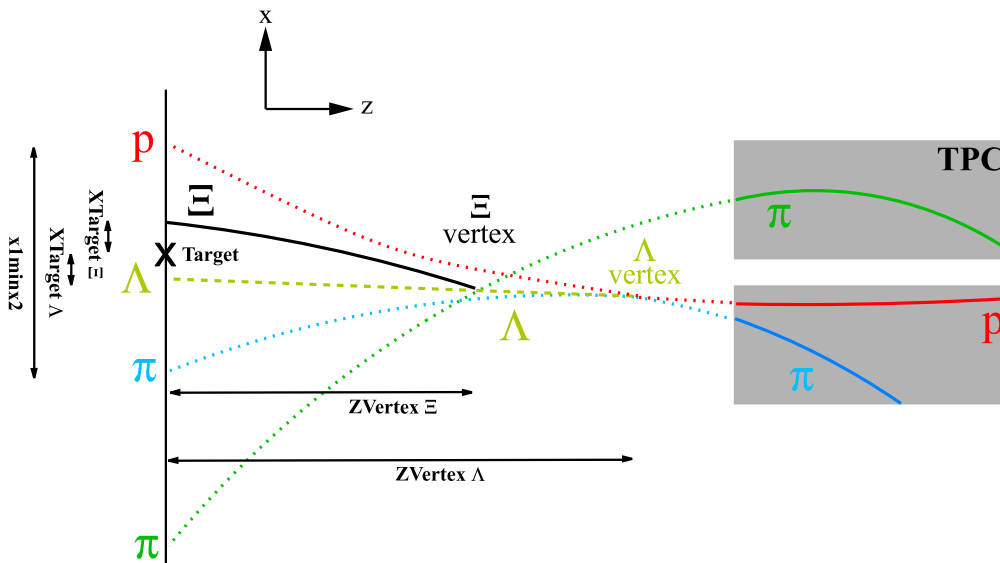


Figure 2.5.: Decay topology of the Ξ hyperon and definition of target and decay length which are applied in the analysis.

combination with charged tracks. From table 1.2, a charged Ξ will decay into Λ and $\bar{\Lambda}$ and a charged pion. The distance of every pion and V0 candidate in x - and y -direction will be compared at every z position to find the distance of closest approach (dc_{ax} , dc_{ay}). The two-dimensional separation is deduced in the plane orthogonal to the beam direction and consecutive steps are compared in the search for a minimum and hence a DCA. If a minimum is located and the x and y separation components are both less than 1 cm, the V0 and charged track are considered as a Ξ candidate.

The minimum number of reconstructed points, n_{point} , is applied to all three reconstructed tracks in either VTPC (see Fig. 2.6). If desired, three different n_{point} parameters can be applied to the separate daughter tracks, but for the current cuts used these values are kept the same.

A further cut is applied to select only those V0s which appear to be Λ or $\bar{\Lambda}$ particles. For Ξ candidates the V0 invariant mass under the Λ hypothesis (M_{Λ}) must be in the range $1.101 \leq M_{\Lambda} \leq 1.131 \text{ GeV}/c^2$.

In the rest frame of the decaying parent particle, conservation of momentum dictates that the daughters are emitted back-to-back. For the case of a relativistic particle traveling through a TPC, the decay frame is not stationary in the laboratory frame and a transformation must be made between the two. Specifically, in the laboratory frame there will be a Lorentz boost in the direction given by the parents velocity just before decay.

Podolanski and Armenteros [51] calculated the transverse momentum, p_t^{Arm} as:

$$p_t^{\text{Arm}} = p_{1,2} \cdot \sin \phi_{1,2}, \quad (2.4)$$

2. The NA49 Experiment at CERN SPS

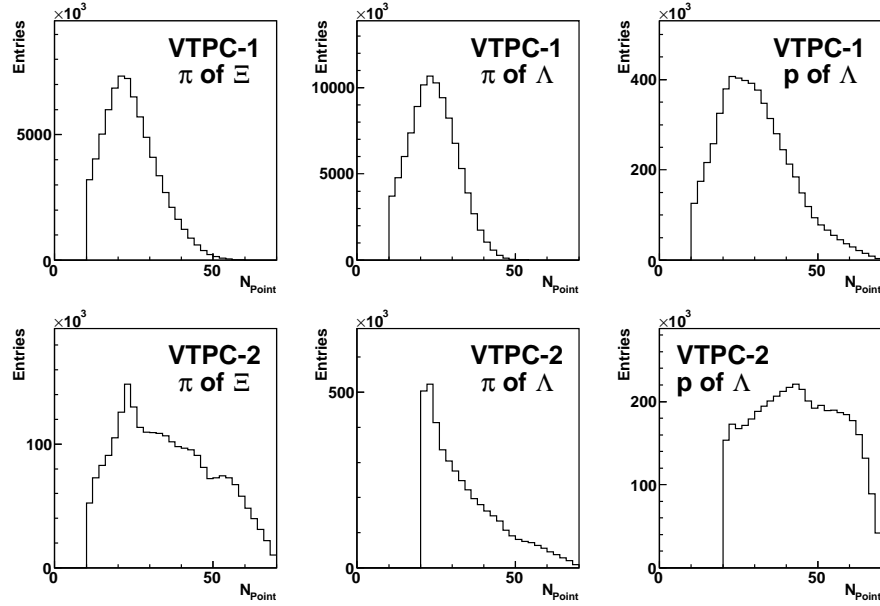


Figure 2.6.: The number of reconstructed points distribution for the three different daughter tracks in either VTPC.

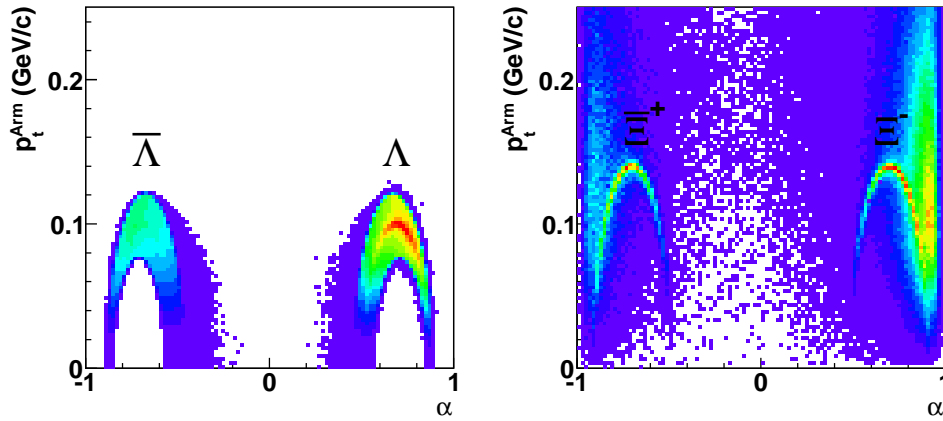


Figure 2.7.: The Armenteros-Podolanski plot for V0s candidates (left) and Ξ candidates (right) after V0 finder, Ξ finder and analysis cuts.

where a daughter with respect to the parent's momentum vector and a variable is defined as:

$$\alpha = \frac{p(1)_{\parallel} - p(2)_{\parallel}}{p(1)_{\parallel} + p(2)_{\parallel}}, \quad (2.5)$$

with the fractional difference of longitudinal momentum shared between the daughters. Here, p_{\parallel} is the component of the daughter's momentum along the original direction of the parent. Particle (1) is customarily chosen as the most

2.3. Event Reconstruction

positively charged daughter. Plots of p_t^{Arm} against α describe ellipses which are unique for different decaying systems. Figure 2.7 shows the Armenteros-Podolanski plot for V0s (left) and Ξ , Ω (right) after V0 finder, Ξ finder and analysis cuts. Table 2.3 summarize the used cuts in the Ξ finder.

Variable	Cut
Measured Points in the TPC	≥ 10 (VTPC-1)
	≥ 20 (VTPC-2)
dcax	≤ 1.0 cm
dca _y	≤ 1.0 cm
M_Λ	$1.101 \leq M_\Lambda \leq 1.131$ GeV/ c^2
Z_{Vertex}	≥ -560 cm
$ X_{\text{Target}} $	≤ 3 cm
$ Y_{\text{Target}} $	≤ 3 cm
$p_t^{\text{Arm V0}}$	≤ 0.25 GeV/ c
p_t^{Arm}	≤ 0.3 GeV/ c

Table 2.3.: Ξ finder cuts (for lead-lead-collisions) of the Ξ hyperons.

2. *The NA49 Experiment at CERN SPS*

3. Data Analysis

3.1. Data sets

To study the energy and system size dependence of the Ξ production, 5 different data sets in the beam energy range 20 – 158 AGeV were analyzed for the energy dependence in Pb+Pb collisions and two minimum bias Pb+Pb data sets with a beam energy of 40 and 158 AGeV. At 40 AGeV both polarities of the magnetic field are available. Besides Pb+Pb NA49 took also Si+Si collisions at 158 AGeV. The magnetic field configuration is denoted with std+, respectively std–, where std refers to the magnetic field at 158 AGeV. The corresponding number of wounded nucleons $\langle N_W \rangle$ (see subsection 5.3.1) for the 7.2 % most central data set is $\langle N_W \rangle = 349$. For the 23.5 % most central data set $\langle N_W \rangle$ is 262, whereas the 10% selection has a $\langle N_W \rangle$ of 335. For the semi-central Si+Si data set $\langle N_W \rangle$ is 37. The system, number of events, the magnetic field configuration, the centrality and the production key for the different data sets are shown in Table 3.1.

System	Beam Energy	Magnetic Field	$\sigma/\sigma_{\text{tot}}$ (%)	N_{evt}	Prod. Key
Pb	20 AGeV	20G+	7.2 %	357416	03A
Pb	30 AGeV	30G+	7.2 %	418408	02J
Pb	40 AGeV	1/4 std+	7.2 %	362337	00W
Pb	40 AGeV	1/4 std–	7.2 %	217110	00C
Pb	80 AGeV	1/2 std+	7.2 %	303989	01E
Pb	158 AGeV	std+	23.5 %	2911405	01I
Pb	158 AGeV	std+	10 %	1238236	01I
Si	158 AGeV	std+	12.2 %	384553	00X
Pb	40 AGeV	1/4 std+	min.bias	390583	02C
Pb	40 AGeV	1/4 std–	min.bias	360210	01D
Pb	158 AGeV	std+	min.bias	338163	01J

Table 3.1.: Data sets on nucleus-nucleus collisions used for this thesis.

3. Data Analysis

3.2. Event Cuts

The determination of the main vertex is not possible for some reconstructed events, in others, the determination of the vertex is questionable. This can result from non-target interactions or other error sources. Also interactions of several beam particles recorded as one event can cause problems with the main vertex reconstruction. The following subsections will discuss the event cuts which are applied for the different systems and centralities.

3.2.1. Central Pb+Pb

The main vertex position in x - and y -direction is determined by the Beam Position Detectors (BPD). Another determination of the main vertex position is the fit-method. In this method all tracks are fitted back to the vertex to determine the main vertex position. For this analysis the z -position is determined with this method. Figure 3.1 shows the difference between the BPD- and Fit-method for the x - and y -position. Ideally the difference between both methods is zero, but experimentally a smearing ($\sigma_x = 0.25$ mm, $\sigma_y = 0.15$ mm, $\sigma_z = 1.1$ mm) is observed. The shift in x - and y -direction could be explained with a not perfect residual correction.

Too large differences indicate a failed main vertex fit and are therefore excluded. The dashed lines in Figure 3.1 indicate the values of the event cuts in x - and y -direction. Additionally the z_{Fit} distribution is shown. For the z coordinate, the real target position is known to be at $z = -581.0$ cm. A cut around this value on the fitted z -position rejects possible non-target interactions.

Cut	Removed Events [%]
$vertex.iflag = 0$	0.35
$-0.05 < x_{\text{BPD}} - x_{\text{Fit}} < 0.16$	0.11
$-0.06 < y_{\text{BPD}} - y_{\text{Fit}} < 0.07$	0.29
$-581.6 < z_{\text{Fit}} < -580.5$	0.04
Total	0.78

Table 3.2.: The event cuts and the fraction of events failing the cut if applied separately for the 20 AGeV central Pb+Pb data set.

The other quantity is a flag that has been set to each event during the reconstruction. If the fit on all tracks to determine the main vertex position converges, the $vertex.iflag$ is set to 0. In the case that the fit diverges or other problems occur during the reconstruction, it is set to non-zero values. Only events with $vertex.iflag = 0$ are analyzed here. The cut values and the removed events of the individual cuts as well as the total loss of the cuts for the 20 AGeV central Pb+Pb data set are summarized in Table 3.2. A summary

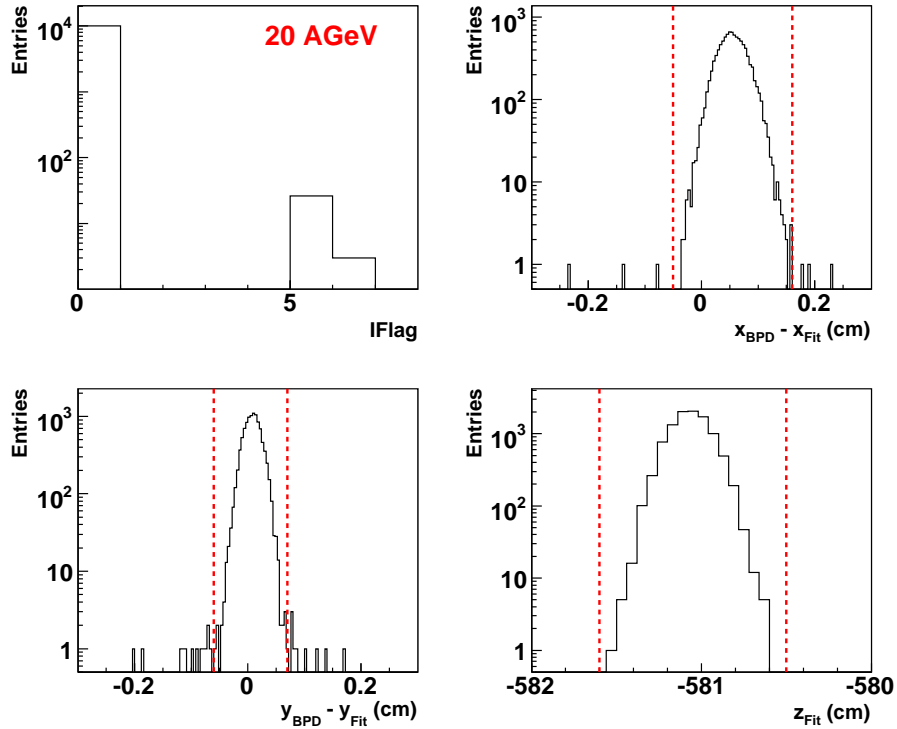


Figure 3.1.: The event properties for the 20 AGeV central Pb+Pb data set. Dashed lines indicate the values of the event cuts.

for the event cuts at 30, 40, 80 and 158 AGeV central Pb+Pb can be found in Appendix B.1.

3.2.2. Minimum Bias Pb+Pb

Event cuts are also applied for the minimum bias data sets at 40 and 158 AGeV. For these data sets just the fit-method is used to determine the main vertex position. Figure 3.2 shows the fit-method for the x -, y - and z -position and the *vertex.iflag*. The high background in Figure 3.2d results from non-target interactions from the beam particle with the target or detector gas.

The dashed lines indicate the values of the event cuts. The cut values and the percentage of removed events by the individual cuts as well as all cuts together for the 40 AGeV (std-) minimum bias Pb+Pb data set are summarized in Table 3.3. To study the centrality dependence of the Ξ -production, it is important to find an experimental quantity, which describes the centrality of the collision. A measure of the centrality of a reaction is the E_{Veto} energy. The Veto-Calorimeter is placed in such a way that it measures the energy of the particles in the beam direction. Figure 5.10 shows the impact parameter of the collision, defined as the separation of the two nuclei orthogonal to the direction

3. Data Analysis

Cut	Removed Events [%]
$vertex.iflag = 0$	0.57
$-0.28 < x_{Fit} < 0.22$	0.37
$-0.40 < y_{Fit} < 0.405$	0.12
$-581.58 < z_{Fit} < -580.6$	43.8
Multiplicity cut	2.14
Total	47.0

Table 3.3.: The event cuts and the fraction of events failing the cut if applied separately for the 40 AGeV (std-) minimum bias Pb+Pb data set.

of the beam (see subsection 5.3.1). Spectator nucleons from the projectile Pb ion which do not suffer any interactions will pass directly through the experiment and deposit their energy in the veto calorimeter. The nuclei which participate in the reaction are called participant nucleons. Events in which the energy of the spectator is below a certain threshold are selected as central events. More central events show not only less energy deposited in the veto calorimeter but also a higher multiplicity (see Figure 3.2g). The E_{Veto} energy and the charged-particle multiplicity exhibit approximately a linear relationship. A clear second branch is visible with a lower slope as the main branch. The second branch is produced from reaction at the S2-Counter and from reactions of the projectile Pb ion with nuclei of the helium gas, which surrounds the target.

For a given impact parameter it is possible to calculate $\langle N_W \rangle$ with the aid of the Glauber model (see subsection 5.3.1). The binning of the event samples in centrality was done on the basis of energy measurements in the Veto-Calorimeter (see section 2.1). Its distribution was divided into 6 bins with varying widths. Each bin has a mean energy and corresponds in a Glauber-like picture to an impact parameter range (b) with an appropriate mean, the mean number of wounded nucleons $\langle N_W \rangle$ and the mean number of participants $\langle N_{part} \rangle$ (see subsection 5.3.1). Details of the binning are given in Table 3.4. A summary for the event cuts at 40 (std+) and 158 AGeV minimum bias Pb+Pb can be found in Appendix B.2.

3.2.3. Semi-Central Si+Si

For the semi-central Si+Si data set the same procedure as for the minimum bias data sets (see subsection 3.2.2) is used to determine the main vertex position. Figure 3.4 shows the Fit-method for the x -, y - and z -position. The dashed lines indicate the values of the event cuts. The cut values and the removed events of the individual cuts as well as the total loss of the cuts for the 158 AGeV semi-central Si+Si data set are summarized in Table 3.5. The lead ions from the SPS can be fragmented by directing the beam to a conversion target (10 mm carbon) immediately after extraction from the SPS. The BPDs deliver not only the position of the beam but also its energy loss which allows to distinguish

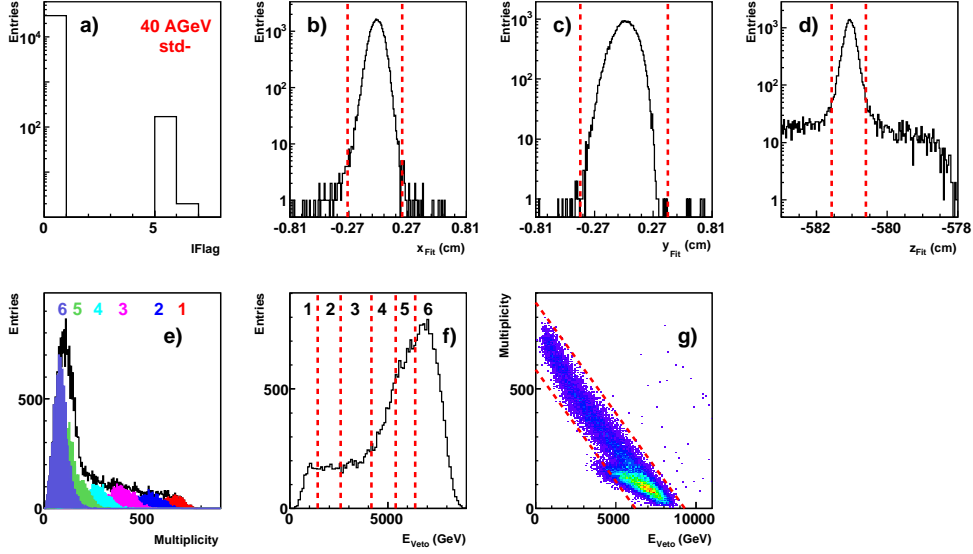


Figure 3.2.: The event properties used in event cuts for the studied 40 AGeV (std-) minimum bias Pb+Pb data set: a) *vertex.i.flag*, b) x_{Fit} position, c) y_{Fit} position, d) z_{Fit} position, e) Multiplicity distribution, f) E_{Veto} energy and g) Multiplicity vs. E_{Veto} . Dashed lines indicate the values of the event cuts.

Centrality [%]	$\langle b \rangle$ (fm)	$\langle N_W \rangle$	$\langle N_{\text{part}} \rangle$
0 – 5	2.5	347	378
5 – 12.5	4.8	276	333
12.5 – 23.5	6.9	193	263
23.5 – 33.5	8.7	126	193
33.5 – 43.5	10.0	82	140
43.5 – ∞	11.8	42	79
Centrality [%]	$\langle b \rangle$ (fm)	$\langle N_W \rangle$	$\langle N_{\text{part}} \rangle$
0 – 5	2.4	351	386
5 – 12.5	4.3	290	351
12.5 – 23.5	6.3	210	291
23.5 – 33.5	8.1	142	222
33.5 – 43.5	9.4	93	164
43.5 – ∞	12.7	43	88

Table 3.4.: Listed for the 158 (top) and 40 (bottom) AGeV Pb+Pb minimum bias data sets and six centralities are: $\langle b \rangle$, the estimated mean impact parameter; $\langle N_W \rangle$, the estimated number of wounded nucleons, and $\langle N_{\text{part}} \rangle$, the estimated mean number of participants [52].

3. Data Analysis

different masses at the same momentum.

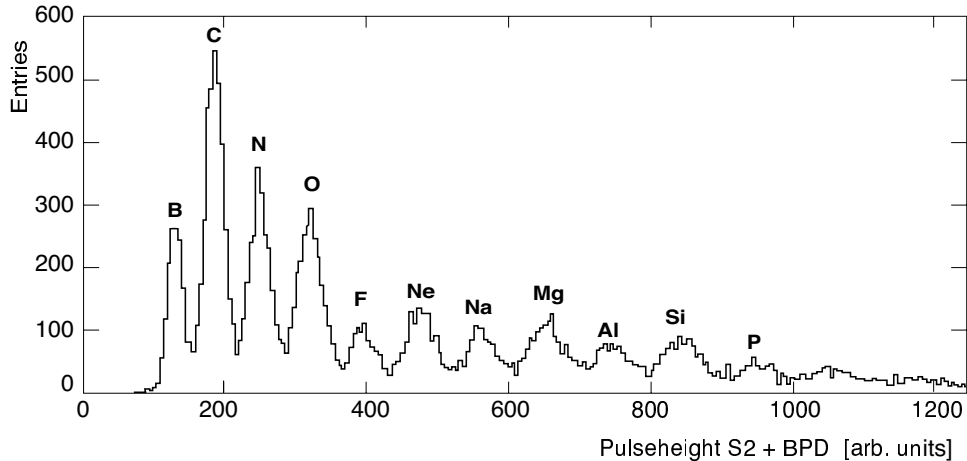


Figure 3.3.: Spectrum of fragments produced from the fragmentation of a 158 AGeV lead beam momentum combining the charge sum signal of the BPDs with the information from S2 [36].

The pulse height of the signal in the beam counter S2 gives information about the charge. Combining both measurements therefore allows for a clean selection of one specific nucleus (see figure 3.3). In practice, a window on the S2 pulse height is set, which limits the spectrum of nuclei to be recorded online (see figure 3.4). Offline, the BPD information can be used to select only one type of nuclei. For silicon beams the S2 detector was used for the beam definition.

Figure 3.4e demonstrates that the trigger selected not only silicon projectiles, but also nuclei with similar atomic mass. Offline the charge is precisely calculated allowing for a clean identification. Using only silicon projectiles would reduce the event sample for analysis by 70%. To avoid this strong reduction of the event sample, in this analysis aluminium, silicon and phosphor nuclei were selected as beam particle.

3.3. Analysis Cuts

The cuts applied in the V0 finder (see subsection 2.3.2) and Ξ finder (see subsection 2.3.5) have been chosen relatively loose to keep most of the signal and to reduce a part of *combinatorial background* in the invariant mass spectra. The background consists of combinations of primary charged tracks or wrong combinations with secondary particles which passed the criteria of the V0 finder and Ξ finder. A high background makes the signal extraction more difficult and increases the statistical error on the yield. The cuts are stricter in the analysis

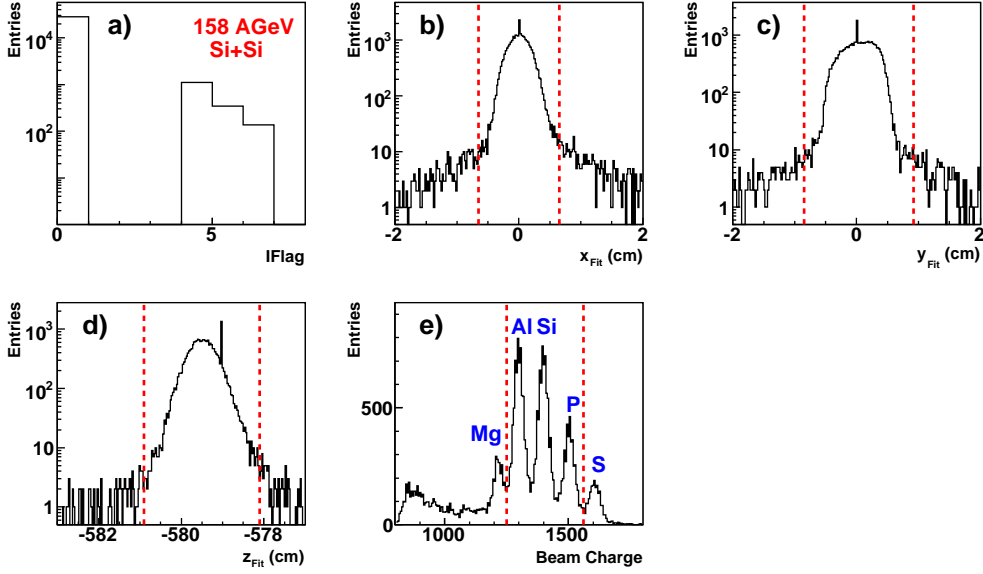


Figure 3.4.: The event properties used in event cuts for the studied 158 AGeV semi-central Si+Si data set: a) $vertex.i\text{flag}$, b) x_{Fit} position, c) y_{Fit} position, d) z_{Fit} position, e) Beam charge distribution (Pulseheight S2 + BPD). Dashed lines indicate the values of the event cuts.

Cut	Removed Events [%]
$vertex.i\text{flag} = 0$	5.3
$-0.65 < x_{\text{Fit}} < 0.65$	2.9
$-0.85 < y_{\text{Fit}} < 0.92$	0.8
$-580.9 < z_{\text{Fit}} < -578.1$	31.2
$1250 < \text{Beam charge} < 1560$	18.9
Total	59.1

Table 3.5.: The event cuts and the fraction of events failing the cut if applied separately for the 158 AGeV semi-central Si+Si data set.

to reduce the combinatorial background and improve the signal to background ratio. The $X_{\text{Target-}}$, $Y_{\text{Target-}}$ and Z_{Vertex} -position and the same side criteria belongs to these cuts for the Ξ candidate. Furthermore a cut on the daughter pion (b_y cut) of the Ξ candidate decay and a Z_{Vertex} cut on the V0 candidate is applied. Additionally, a cut on the daughter pion (b_y cut) of the V0 candidate is applied. The particle identification for the daughter proton of the daughter Λ is done by measuring the energy loss dE/dx of the particles (see subsection 3.3.3). All applied cuts will be explained in the following.

3. Data Analysis

3.3.1. Cuts on the Ξ Candidate

The variable X_{Target} and Y_{Target} is the distance in x - and y -direction of the extrapolated Ξ track in the target plane:

$$X_{\text{Target}} = X_{\Xi\text{-track}} - X_{\text{main vertex}}, \quad (3.1)$$

$$Y_{\text{Target}} = Y_{\Xi\text{-track}} - Y_{\text{main vertex}}. \quad (3.2)$$

The Ξ candidate is extrapolated back to the main vertex through the magnetic field. Strong target cuts offer good selection criteria for real Ξ , because primary particles originate from the main vertex, but wrong combinations would not necessarily appear to point back to the main vertex.

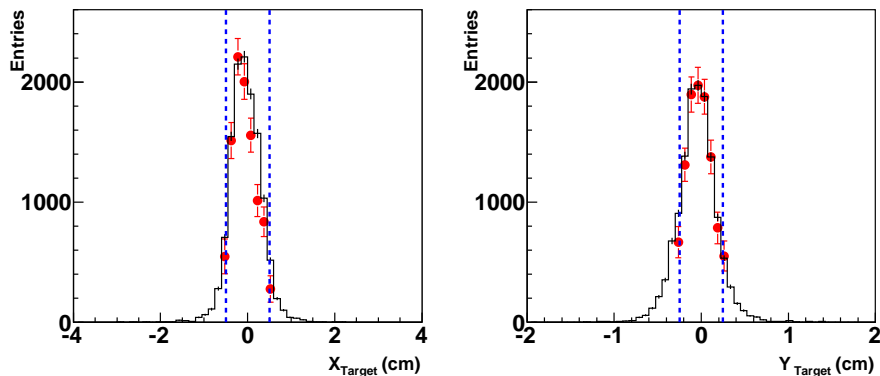


Figure 3.5.: X_{Target} (left) and Y_{Target} (right) distribution of the Ξ candidate at midrapidity in central Pb+Pb collisions at 30 AGeV. The dashed lines indicate the different cuts applied in the analysis, the points the measured distribution and the histogram the distribution determined from an embedding simulation.

Figure 3.5 shows the X_{Target} and Y_{Target} distribution of the Ξ candidate as determined from the embedding simulation. The points represent the measured distribution, where the dashed lines represent the cuts applied in this analysis:

$$|X_{\text{Target}}| \leq 0.5 \text{ cm},$$

$$|Y_{\text{Target}}| \leq 0.25 \text{ cm}.$$

If the decay vertex of the Ξ candidate is close to the target, the probability is high that one of the tracks is not a secondary track. The fraction of random combinations which causes combinatorial background are caused from primary tracks. A tighter cut is selected ($Z_{\text{Vertex}} \geq -555 \text{ cm}$) in this analysis. Figure 3.6

shows the Z_{Vertex} distribution of the Ξ candidate as determined from the embedding simulation. The points represent the measured distribution, where the dashed lines represent the cuts applied in the analysis.

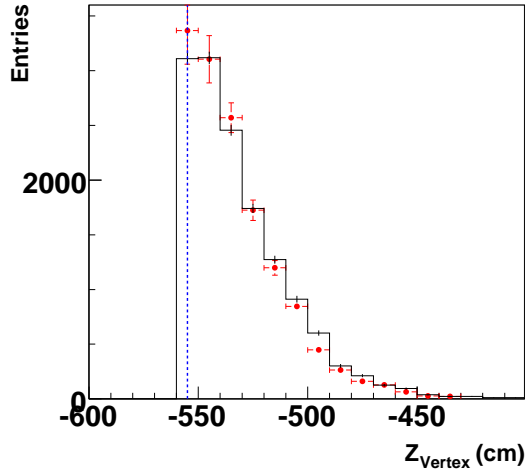


Figure 3.6.: The decay vertex distribution of the Ξ candidate at midrapidity in central Pb+Pb collisions at 30 AGeV. The dashed line indicate the different cuts applied in the analysis, the points the measured distribution and the histogram the distribution determined from an embedding simulation.

Another criterion in the analysis is the *same side* condition. There are two different possibilities. Tracks are called *opposite side* tracks if the daughter tracks of the Ξ candidate are lying on different sides of the TPC or, if lying on the same side of the TPC they are called *same side* tracks. Figure 3.7 clearly demonstrates both criteria. The *same side* condition as determined from the embedding simulation is shown in Figure 3.8, where the points represent the measured distribution. In this analysis only daughters are used which are on the same side of the TPC, which reduces the combinatorial background. It is clearly visible that the simulation reproduces the data.

3.3.2. Cuts on the Daughter π of the Ξ Candidate

The variable $b_y(\Xi)$ is the distance in y -direction of the extrapolated pion track from the main vertex in the target plane:

$$b_y(\Xi) = Y_{\pi\text{-track}} - Y_{\text{main vertex}}. \quad (3.3)$$

The pions are extrapolated back to the main vertex through the magnetic field and if they are particles from secondary decays they point on average away from

3. Data Analysis

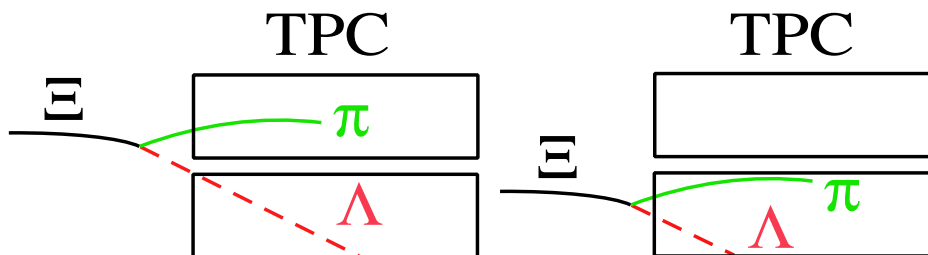


Figure 3.7.: *Same side* condition for the Ξ candidate. On the left side both daughters of the Ξ candidate are on different sides of the TPC (*opposite side*) and on the right hand side both daughters are on the same side of the TPC (*same side*).

the main vertex. Figure 3.9 shows the $b_y(\Xi)$ distribution of the daughter pion of the Ξ candidate as determined from the embedding simulation. The points represent the measured distribution, where the dashed lines represent the cut applied in this analysis:

$$|b_y(\Xi)| \geq 1.0 \text{ cm.}$$

It is clearly visible that the simulation reproduces also in this case of the $b_y(\Xi)$ distribution the data.

3.3.3. Cuts on the Daughter Λ Candidate

The amount of charge which is collected on the pads of the TPC is proportional to the specific energy loss $\frac{dE}{dx}$ of the particles. The atoms of the detector gas become ionized when charged particles cross the detector gas. The charged particles leave free electrons and ions along their tracks, which results in a reduction of the particle energy. The Bethe-Bloch formula is used to describe the mean specific energy loss (dE) per length unit (dx) as a function of the velocity β of the particle [53],[54] as:

$$-\left\langle \frac{dE}{dx} \right\rangle = \frac{4\pi N z^2 e^4 Z}{m_e \beta^2 c^2 A} \left(\ln \left[\frac{2m_e \beta^2 c^2}{I^2 (1 - \beta^2)} \right] - \beta^2 - \delta(\beta) \right), \quad (3.4)$$

where Z and A are the atomic number and the mass number of the gas, I the mean excitation energy which is estimated based on experimental stopping-power measurements, its determination is the main uncertainty in the calculation of the expected mean energy loss, N the Avogadro constant, m_e the electron mass, e the elementary charge, z and v the charge number and the velocity of the particle, $\delta(\beta)$ the density effect correction and $\beta = \frac{v}{c}$. For all practical purposes the energy loss $\frac{dE}{dx}$ is just a function of particle velocity β .

This function is characterized by the reciprocal-quadratic decrease with β and

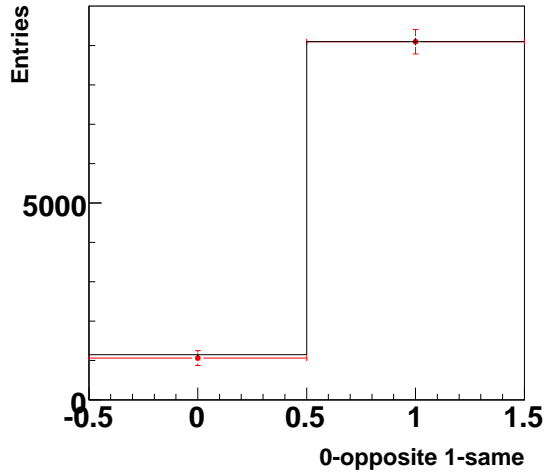


Figure 3.8.: *Same side* condition for the Ξ candidate at midrapidity in central Pb+Pb collisions at 30 AGeV. The points represent the measured data distribution and the histogram the distribution determined from embedding simulation.

the logarithmical increase for large velocities (*relativistic rise*) followed by the Fermi plateau (Figure 3.10). The NA49 measurements are in the range of the *relativistic rise*. Charged particles can be identified in the TPCs with the help of the specific energy loss.

A cut on the specific energy loss is applied to the protons (anti-protons) from Λ ($\bar{\Lambda}$). In the analysis no cut is used on the decay pions, because 90 % of the charged hadrons are pions. Figure 3.11 shows the specific energy loss $\frac{dE}{dx}$ for the positive daughter of the Λ candidate with a momentum of 7.5 GeV/c. It is clearly visible that the distributions of the protons and kaons are partially overlapping each other and therefore a clean selection of protons is not possible. The specific energy loss for a given momentum is characterized by the position $\frac{dE}{dx}_{\text{Mean}}$, the width σ and the height of the actual particle distribution and can be parameterized with a Gaussian distribution.

With this kind of parameterization every particle has three free parameter because the relative positions of the particles to each other should not change. The position of the $\frac{dE}{dx}_{\text{Mean}}$ distribution at NA49 can be parameterized. The resolution of the specific energy loss $\frac{\sigma_{\text{Mean}}}{\frac{dE}{dx}}$ is 3.0–5.0% for all data sets and the momentum dependence can be fitted by the following equation:

$$\frac{\sigma}{dE/dx}(p) = \frac{X_0}{\sqrt{X_1 + p}} + X_2. \quad (3.5)$$

This equation is used in the analysis to determine the actual width of the identification band σ for a given total momentum p of the particle. In the

3. Data Analysis

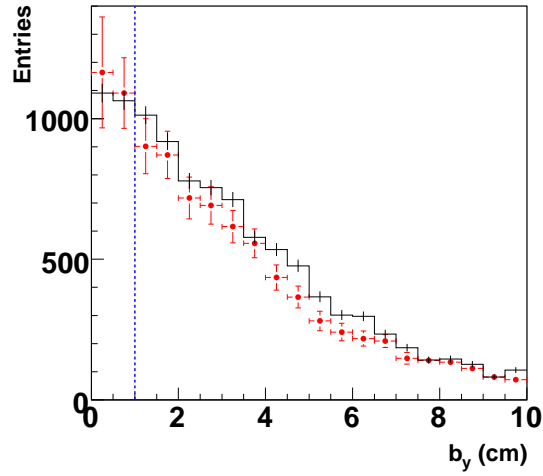


Figure 3.9.: $b_y(\Xi)$ distribution of the daughter π of the Ξ candidate at midrapidity in central Pb+Pb collisions at 30 AGeV. The dashed lines indicate the different cuts applied in the analysis, the points the measured distribution and the histogram the distribution determined from an embedding simulation.

analysis pions are accepted which fulfill the following condition:

$$\left| \frac{dE}{dx} - \frac{dE}{dx}_{\text{Mean}} \right| \leq 3.5 \cdot \sigma(p). \quad (3.6)$$

A large part of the pions and kaons is cut out by this criterion without losing any protons (anti-protons). Therefore no corrections need to be applied for this cut.

Figure 3.12 shows the Z_{Vertex} distribution of the Λ candidate as determined from the embedding simulation. The points represent the measured distribution, where the dashed lines represent the cuts applied in the analysis. To reduce combinatorial background candidates where the Z_{Vertex} position is bigger than -555 cm are rejected.

The variable $b_y(\Lambda)$ is the distance in y -direction of the extrapolated pion track from the daughter Λ from the main vertex in the target plane:

$$b_y(\Lambda) = Y_{\pi\text{-track}} - Y_{\text{main vertex}}. \quad (3.7)$$

The pions are extrapolated back to the main vertex through the magnetic field and if they are particles from secondary decays they point on average away from the main vertex. Figure 3.13 shows the $b_y(\Lambda)$ distribution of the daughter pion of the Λ candidate as determined from the embedding simulation. The points represent the measured distribution, where the dashed lines represent the cuts applied in the analysis:

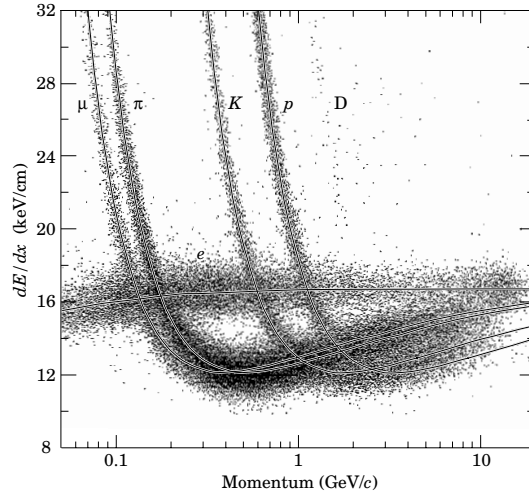


Figure 3.10.: The dependence of the mean energy loss on the momentum p of the particle (taken from [5]).

$$|b_y(\Lambda)| \geq 0.5 \text{ cm.}$$

The Z_{Vertex} distribution from the daughter Λ and the $b_y(\Lambda)$ distribution from the daughter π of the Λ can be also reproduced in the simulation. Table 3.6 summarizes the applied analysis cuts in this thesis.

Cuts on the Ξ candidate
$Z_{\text{Vertex}} \geq -555 \text{ cm}$
$ X_{\text{Target}} \leq 0.5 \text{ cm}$
$ Y_{\text{Target}} \leq 0.5 \text{ cm}$
$\pi + \Lambda$ vertex same side
Cuts on the daughter Λ candidate
GSI type
$Z_{\text{Vertex}} \geq -555 \text{ cm}$
dE/dx cut on the decay proton
Cuts on the daughter π of the Ξ candidate
$b_y(\Xi) \geq 0.5 \text{ cm}$
Cuts on the daughter π of the Λ candidate
$b_y(\Lambda) \geq 1.0 \text{ cm}$

Table 3.6.: Summary of the applied analysis cuts.

3. Data Analysis

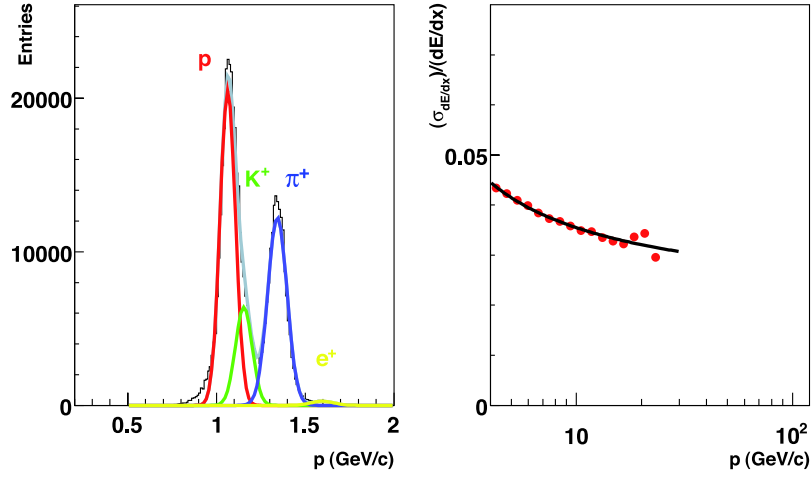


Figure 3.11.: The dE/dx distribution of secondary positive tracks (left) at a momentum of $7.5 \text{ GeV}/c$ for central Pb+Pb collisions at 30 AGeV . The distribution is parameterized with a fit of four overlapping Gauss curves. On the right side the extracted resolution from the Gauss fit for the specific energy loss as a function of the momenta is shown. The line represents equation 3.5 which is used to describe the momentum dependence resolution of the specific energy loss.

3.4. Invariant mass method

The sum of energy and momentum of the daughter particles is equal to the energy and the momentum of the mother particle due to conservation of energy and momentum:

$$m_{inv}^2 = m_\pi^2 + m_\Lambda^2 + 2 \cdot E_\pi \cdot E_\Lambda - (p_{x,\pi} \cdot p_{x,\Lambda}) \cdot (p_{y,\pi} \cdot p_{y,\Lambda}) \cdot (p_{z,\pi} \cdot p_{z,\Lambda}). \quad (3.8)$$

m_{inv} is the invariant mass. Invariant because it is unchanged with respect to Lorentz transformations. The invariant mass is calculated in the $V0$ reconstruction under the assumption that the particle is a Λ ($\bar{\Lambda}$) or K_s^0 and in the multi-strange hyperon reconstruction a Ξ or Ω . Table 1.2 shows the mass of the corresponding charged decay particles. Before a $V0$ and a pion are combined to a hypothetical Ξ , the Λ candidate is required to match the nominal Λ mass. If these particles are primary particles or from different decay channels the invariant mass is distributed differently. This distribution is called combinational background.

Figure 3.14 shows for illustration the invariant mass of the Ξ^- (upper row) and $\bar{\Xi}^-$ (lower row) candidates ($-0.5 < y < 0.5$, $p_t = 0.6 - 2.1 \text{ GeV}/c$) in central Pb+Pb collisions from $20 - 158 \text{ AGeV}$. The vertical lines represent the

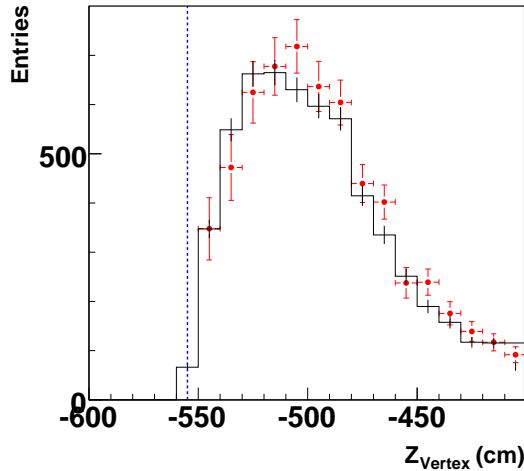


Figure 3.12.: The decay vertex distribution of the Λ candidate at midrapidity in central Pb+Pb collisions at 30 AGeV. The dashed line indicate the different cuts applied in the analysis, the points the measured distribution and the histogram the distribution determined from an embedding simulation.

mass position a determined in the Particle Physics Book [5]. The form and the amount of the background varies a lot between the different y - p_t bins and also beam energies. The typical mass resolution, as obtained from a fit with a Gaussian is $\sigma_m \approx 4 \text{ MeV}/c^2$ for all energies. For the quantitative determination of the Signal the expression *Signal to Background* is used which is defined in the following:

$$\frac{S}{B} = \frac{n_S - n_B}{n_B} \quad (3.9)$$

where n_S is the number of entries around the nominal mass in a window of 20 MeV/c^2 . The entries under the signal are called n_B (Background distribution). Here a polynominal of 7th order proved to be the most stable solution to fit the Ξ background :

$$f_B = \sum_{i=1}^7 a_i \cdot m_{\text{inv}} \quad (3.10)$$

A good approach to describe the invariant mass peak is to use the peak shape (f_S) obtained from the simulation in the same y - p_t bin. Figure 3.14 shows that this method perfectly reproduces the form of the measured mass peak. Only one fit parameter to scale the height is needed. An illustration for the minimum bias Pb+Pb data set at 40 and 158 AGeV and semi-central Si+Si data set at 158 AGeV can be found in Appendix C.

Fitting is carried out with the MINUIT package in ROOT [44] [45] through a χ^2 minimization while varying the parameters. Here, it is done in two steps : First, the background is fitted only by f_B , with the peak region being excluded.

3. Data Analysis

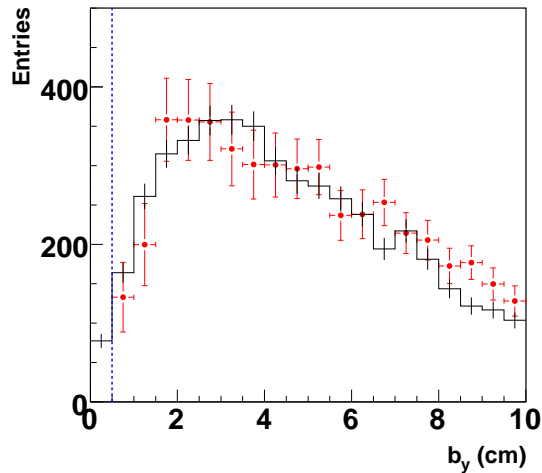


Figure 3.13.: $b_y(\Lambda)$ distribution of the daughter π of the Λ candidate at midrapidity in central Pb+Pb collisions at 30 AGeV. The dashed lines indicate the different cuts applied in the analysis, the points the measured distribution and the histogram the distribution determined from an embedding simulation.

The parameters found by this step are then taken as start parameters for the fit to the whole histogram with $f_B + f_S$. Now, the background can be described by f_B with the parameters resulting from the second fit.

The signal is extracted by integrating over the histogram that contains the measured signal and background and subtracting the integral of f_B in the same interval. The range of this interval was chosen large enough to accept most of the true particles in all phase space regions. On the other hand it should not be chosen bigger than necessary, as a window that is too large raises the statistical error on the background.

3.5. Correction

The goal of this analysis is to make a statement about the energy, centrality, and system size dependence of Ξ production. In the applied analysis different cuts are used to get an acceptable signal to background ratio. The NA49 detector also has a finite geometrical acceptance (see subsection 3.5.1). These reasons have to be taken into account and the measurement has to be corrected for this influence and in addition to receive corrected rapidity, transverse momentum and transverse mass spectra. Therefore the correction has to be done differentially in small phase space bins.

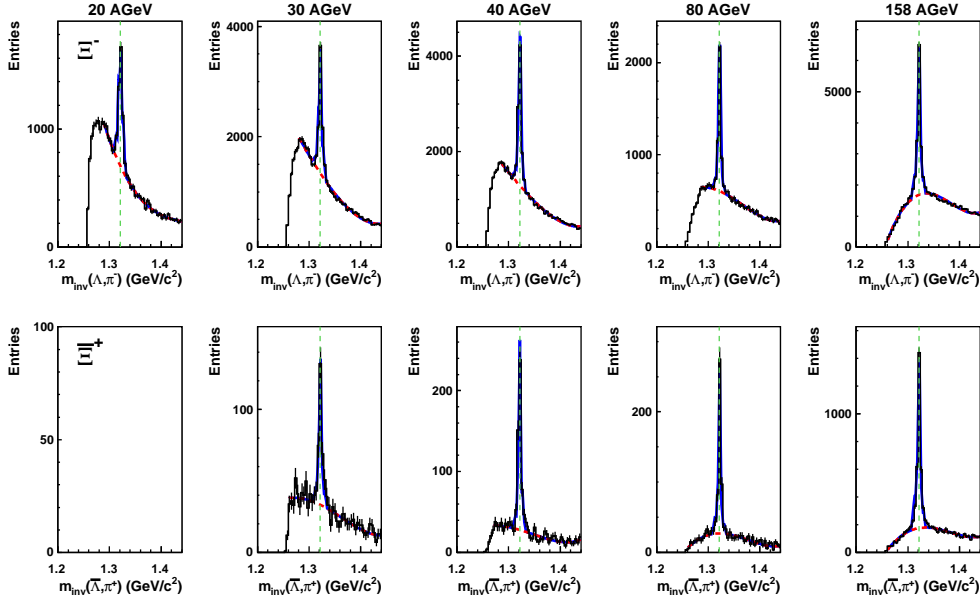


Figure 3.14.: The invariant mass distribution of Ξ^- (upper row) and $\bar{\Xi}^-$ (lower row) candidates ($-0.5 < y < 0.5$, $p_t = 0.6 - 2.1$ GeV/c) in central Pb+Pb collisions from 20 – 158 AGeV. The full curves (blue) represent a fit to signal and background as described in the text. The dashed curves show the background (red) contribution. The vertical lines represent the mass position from the Particle Physics Book [5].

3.5.1. Geometrical Acceptance

The NA49 detector does not cover the full phase space and therefore corrections have to be applied to the data. The geometrical acceptance correction accounts for those particles which do not enter the spectrometer. Efficiency correction factors take into account those which fail one or more of the selection cuts. Monte Carlo (MC) simulation plays an essential role in the calculation of acceptance and efficiency corrections. Any particle may be simulated provided the particle type and starting momenta at the primary vertex are given. For the case of the Ξ hyperon, knowledge of the particles lifetime, decay modes, and branching ratios allows simulation of how real hyperons decay. Each MC particle is decaying randomly according to these properties, a decay vertex is located and daughter tracks are assigned momenta. The first step is the MC generation of primary particles. Values for y , p_t and ϕ were randomized according to predefined distributions. The momenta are calculated such that the corresponding y and p_t values and the particles populate the $y-p_t$ phase space according to the thermal parameters. The thermal parameters define a Gaussian shape in y

3. Data Analysis

and a Boltzmann like form in p_t given by:

$$\frac{dN}{dp_t} = C \cdot p_t \cdot e^{-\frac{m_t}{T}}, \quad (3.11)$$

where C is the amplitude, T the inverse slope parameter and m_t the transverse mass. Differentiating the relation $m_t = \sqrt{m_0^2 + p_t^2}$ with respect to p_t and using the chain rule, equation 3.11 can be expressed in terms of m_t as:

$$\frac{1}{m_t} \frac{dN}{dm_t} = C \cdot e^{-\frac{m_t}{T}}, \quad (3.12)$$

which is the Boltzmann formula.

The input temperature parameter for generating MC Ξ^- and $\bar{\Xi}^+$ particles was chosen to be $T = 300$ MeV. A Gaussian form in rapidity was chosen, centered at midrapidity with a width, $\sigma_y = 1$. The same input temperature and rapidity width is chosen for all energies and centralities. It is visible that the inverse slope parameter is energy and centrality independent (Section 4.1 and 5.2.1). To leave the input temperature and the rapidity width constant has no big effect on the efficiency correction. For simplicity, only one MC hyperon was generated per event. The physics processes acting on MC particles as they are tracked through the NA49 experiment are simulated by the GEANT package [55]. GEANT accounts for interactions of the MC particles with detector material and decays of unstable particles, which includes assignment of momentum to the decay daughter products. A number of interaction processes are available with GEANT and those used for this analysis include hadronic multiple scattering and pair production. The GEANT description of the NA49 experiment includes details of the experimental apparatus and geometry, along with the same magnetic field map as used in data production. Of all produced particles $\approx 40\%$ of the Ξ fall into the acceptance of the detector, i.e. all three decay particles are seen in the sensitive detector volume.

3.5.2. Reconstruction Efficiency

The reconstruction efficiency correction includes the inefficiency of the single track and Ξ reconstruction, and the loss due to the high track density. Besides that also losses from analysis cuts are considered. For the efficiency correction, MC data is embedded into real data and run through the reconstruction chain. This method has the advantage that the simulated data is treated in the same way as real data (overlapping of tracks and cluster). MC points from tracks of accepted particles are used as input for the efficiency part of the simulation chain. MC points are defined as ideal single points situated below the middle of a TPC padrow. The TPC response simulator, *mtsim* [56], uses MC points to create TPC data in the digitized format of the readout electronics. In order to mimic the data as closely as possible, *mtsim* takes into account all the effects suffered by electrons as they drift through the TPC gas towards the readout plane including diffusion, pad crossing angle, charge loss and intrinsic detector resolution. However, *mtsim* does not use a detailed simulation of each effect

separately, but parametrized response functions which determine the shape and size of the charge clusters in the pad and time directions.

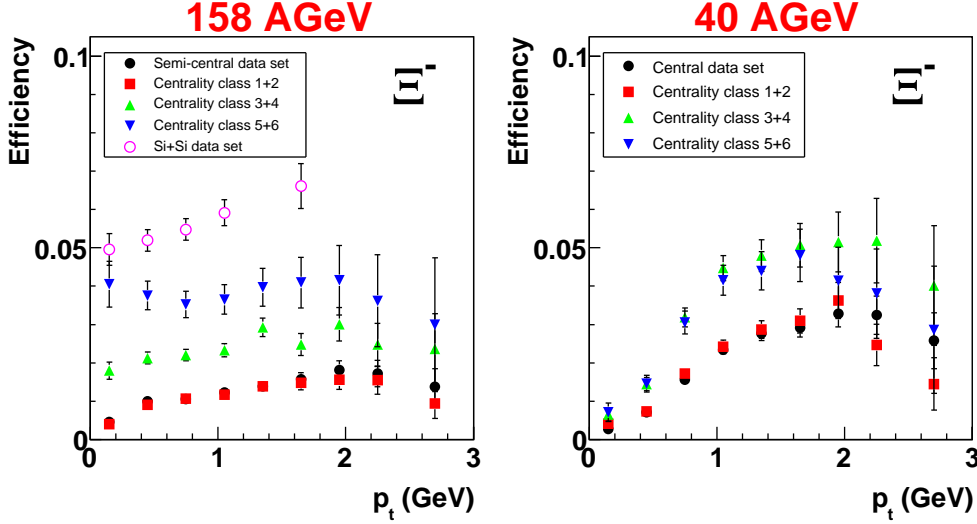


Figure 3.15.: p_t dependence of the total efficiency (geometrical acceptance and reconstruction efficiency) for Ξ^- at midrapidity ($|y| \leq 0.5$) for different centralities at 158 AGeV (left) and 40 AGeV (right).

These functions, which are different for the bending plane (x, y) and time direction (t), are of the same form as seen for drifting charge in real data [56, 57]. The centre of each MC point is moved randomly to simulate the momentum resolution of the TPCs. Once the MC data has been transformed into raw data format, it is combined with raw data from a real event by the program *gembed*. The combined event is ready to be passed to the global reconstruction chain, which reconstructs the whole event now including the embedded MC particles.

To determine the efficiency, a procedure evaluates which simulated particles have been reconstructed. This procedure is called *matching* and done by the *gmatch* client. It starts with the *point matching*, where for each GEANT generated phase space point corresponding reconstructed points in proximity are searched. In each plane spanned by a pad row and the drift direction, the distance is evaluated both in y direction and perpendicular to it. Two points match if they lie within a rectangle of $0.5 \times 0.5 \text{ cm}^2$. This criterion is loose enough that the matching also works in areas of the detector where distortions prevail. The point matching may be ambiguous. This is reduced in the *trackmatching*. A reconstructed track is accepted as a match to a simulated track, when a minimum of 5 of its measured points in a VTTPC (or 10 in a MTTPC) match to the according simulated point. For a simulated Ξ , the condition is even stricter, as all three daughter tracks have to be matched. The same analysis cuts have to be applied in the determination of the efficiency. At the end the efficiency is

3. Data Analysis

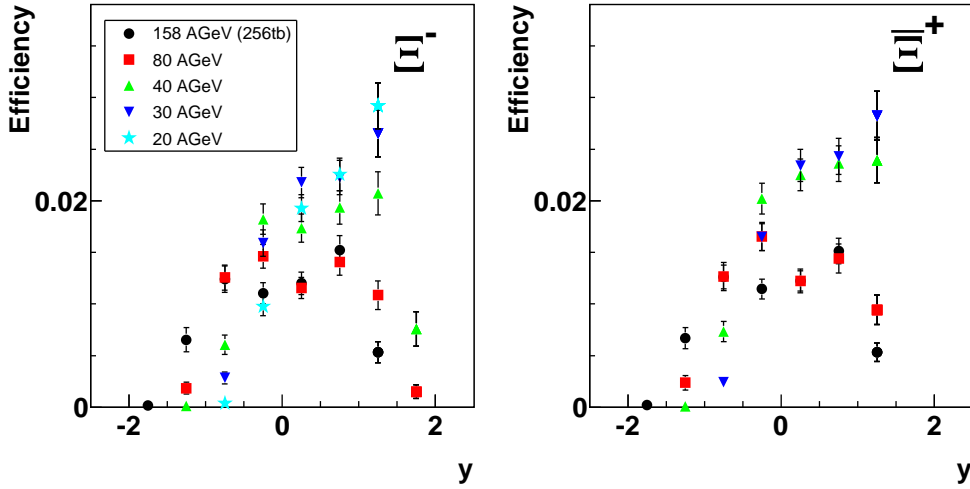


Figure 3.16.: Rapidity dependence of the total efficiency (geometrical acceptance and reconstruction efficiency) for Ξ^- (left) and Ξ^+ (right) at midrapidity ($|y| \leq 0.5$) in central Pb+Pb collisions from 20 – 158 AGeV.

defined with the formula as:

$$C_{\text{efficiency}} = \frac{N_{\text{matched}}}{N_{\text{geant}}}, \quad (3.13)$$

where N_{geant} is the number of generated Ξ and N_{matched} the number of Ξ after matching. Figure 3.15 shows the p_t dependence of the total efficiency for Ξ^- at midrapidity ($|y| \leq 0.5$) for different centralities at 158 AGeV (left) and 40 AGeV (right). As can be clearly seen, the efficiency in all centrality classes depends on p_t . As expected, the efficiency decreases with increasing centrality. The p_t ($|y| \leq 0.5$) of the total efficiency in central Pb+Pb collisions from 20 – 158 AGeV is shown in C.3. The rapidity dependence of the total efficiency in central Pb+Pb collisions is shown in Figure 3.16. It can be seen that for lower energies the efficiency is better at forward rapidity. The reason is again the lower track density. For the 80 and 158 AGeV data set a poor efficiency is visible in backward and in forward rapidity which results from a high track density. Figure 3.17 (left) shows the integrated efficiency in the full NA49 acceptance as a function of the particle multiplicity for Ξ^- in central Pb+Pb collisions at 20, 30, 40, 80 and 158 AGeV. It can be clearly seen that the integrated efficiency increases with decreasing energy which can be explained with the lower track density at lower energies. At 158 AGeV the integrated efficiency is $\approx 1\%$, whereas at 20 AGeV it is $\approx 2\%$.

On the right hand side of Figure 3.17 the system size dependence of the integrated efficiency for Ξ^- plotted versus the particle multiplicity at 158 AGeV is shown. It is visible that the integrated efficiency is increasing with decreasing

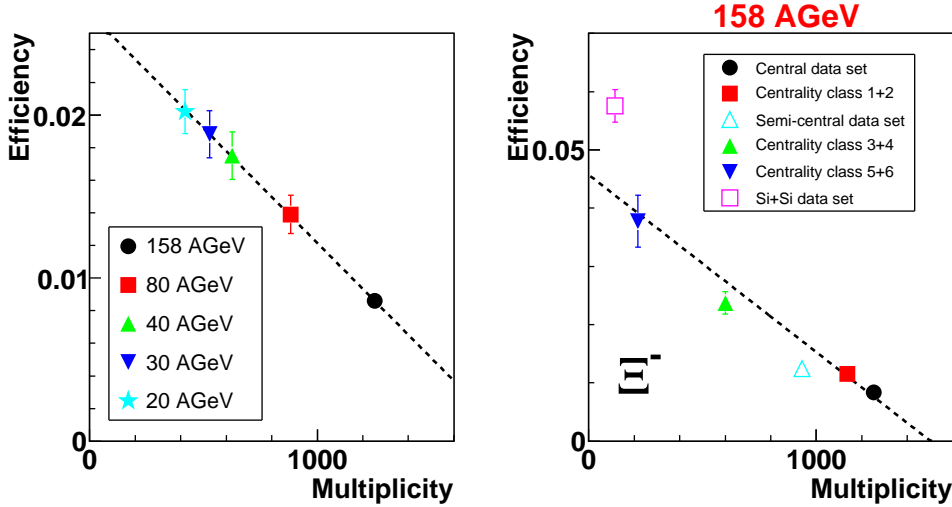


Figure 3.17.: The integrated efficiency for Ξ^- in the full NA49 acceptance as a function of the particle multiplicity for central Pb+Pb collisions at different energies (left) and for different system sizes at 158 AGeV (right) as a function of the particle multiplicity.

centrality. One remark has to be done for the Si+Si data set at 158 AGeV. For the Si+Si efficiency show here no embedding simulation was used. Therefore just the geometrical and reconstruction efficiency is shown and used for corrections. Following the trend of the integrated efficiency in Figure 3.17 (right) an estimate can be done about the efficiency after embedding simulation. It seems that the integrated efficiency could be $\approx 4.5\%$ but this has to still be verified with an embedding simulation. To check how much the high track density affects the resolution a look will be taken at some important variables as the transverse momentum, rapidity, invariant mass and the decay vertex position of the Ξ^- . The resolution is calculated as:

$$\delta X_{\text{Resolution}} = A_{\text{matched}} - B_{\text{Input}}, \quad (3.14)$$

where B_{Input} is the input distribution and A_{matched} the one determined after embedding and matching.

Figure 3.18 (top left) shows the resolution of the transverse momentum as a function of the transverse momentum at midrapidity ($|y| \leq 0.5$) at 158 AGeV. It can be seen that the transverse momentum resolution for the Ξ^- is $\delta p_t(\Xi^-) \approx 1.0 \cdot 10^{-2}$ GeV and does not depend on transverse momentum. No dependence is also seen for the Ξ^- invariant mass (top middle) and the Ξ^- decay vertex position (top right) at midrapidity as a function of the transverse momentum. The invariant mass resolution as a function of the transverse momentum is $\delta m_{\text{inv}}(\Xi^-) \approx 3-4$ MeV/ c^2 , in accordance with the fits to the measured m_{inv} spectra (see Figure 3.14). The resolution for the Ξ^- decay vertex position $\delta Z_{\text{Vertex}}(\Xi^-)$ is ≈ 3 cm. A different dependence is observed for the rapidity

3. Data Analysis

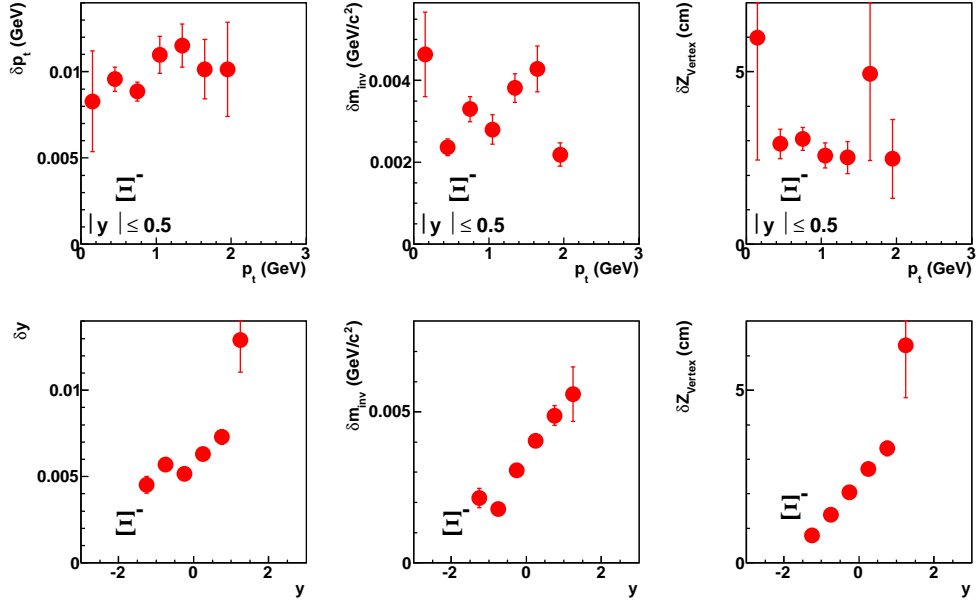


Figure 3.18.: Resolutions of the transverse momentum (top left), the invariant mass of the Ξ^- (top middle) and the Ξ^- decay vertex position (top right) as a function of the transverse momentum at midrapidity ($|y| \leq 0.5$) and the rapidity (bottom left), the invariant mass of the Ξ^- (bottom middle) and the Ξ^- decay vertex position (bottom right) as a function of the rapidity.

resolution which is shown in Figure 3.18 (bottom left). The resolution becomes poorer because the opening angle for faster particles is smaller than for slower ones. This is also reflected in the Ξ^- invariant mass (bottom middle) and decay vertex position (bottom right) resolution as a function of the rapidity. Looking on the values for invariant mass resolution it can be seen that it is in the range between 2–6 MeV/c² which is still a good mass resolution.

A good cross-check for the simulation is to compare the distribution of the variables used for analysis cut to the distributions determined from the data. As can be seen in section 3.3, the simulation describes the data well for the distributions e.g. of $b_y(\Xi)$ (see Figure 3.9) and $b_y(\Lambda)$ (see Figure 3.13). This supports the claim that the simulation is of sufficient quality for calculating correction factors.

3.5.3. Centrality Bin Size Effect

In the data and embedding analysis of the minimum bias data sets big centrality bins are selected which include a 10%–20% variation in the centrality and therefore also in the number of charged particles. In an event with a low track density, the probability is higher to find a Ξ and therefore the correction factor

is smaller than for events with a high track density. At the same time in an event with low multiplicity the mean number of produced Ξ s has to be smaller than in a event with high multiplicity (see Figure 3.19 (left)). As a result the correction factor for events with higher multiplicity has to have a higher weight than events with lower multiplicity.

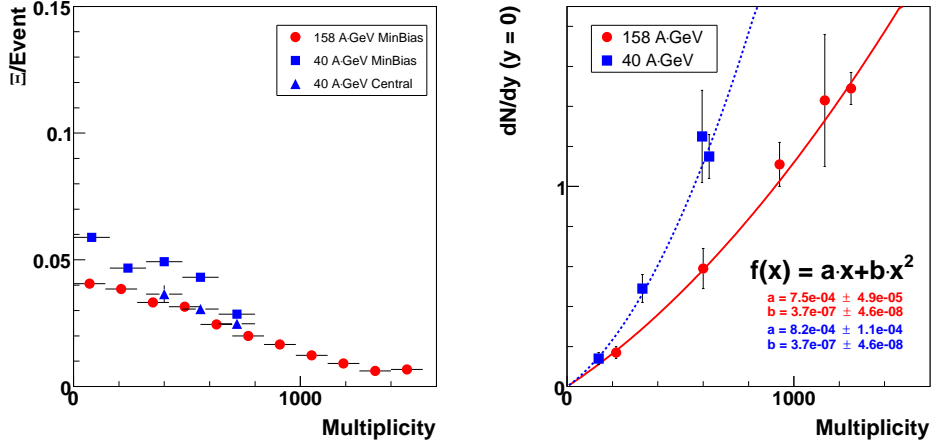


Figure 3.19.: The number of matched Ξ^- (left) and the corrected yield (right) as a function of the particle multiplicity.

The weighted total number of matched Ξ^- is defined as:

$$N_{\text{gmatched}}(y, p_t) = \frac{\sum f_g(\text{mult})(y, p_t) \cdot N_{\text{matched}}(y, p_t)}{\sum f_{\text{mult}}(y, p_t)}, \quad (3.15)$$

where N_{matched} is the not weighted number of matched Ξ^- in an event and $f_g(\text{mult})$ the weighting factor for every event, where mult is the multiplicity of the event. With the weighting factor $f_g(\text{mult})$ it is now taken into account that events with a higher multiplicity have on the average more Ξ^- . The minimum bias results of Ξ^- at 40 and 158 AGeV are used to calculate $f_g(\text{mult})$ (see Figure 3.19 (right)). To fit the data a second order polynomial is used with the resulting parameters a and b to determine the weighting factor for every embedded event as:

$$f_g(\text{mult}) = a \cdot \text{mult} + b \cdot \text{mult}^2. \quad (3.16)$$

After applying the weight in the correction a mean difference of 13% for the 158 AGeV (see Figure 3.20 (left)) and 10% for the 40 AGeV (see Figure 3.20 (right)) data sets is visible between weighted and not weighted midrapidity Ξ^- yields. The difference observed between for the number of matched Ξ as a function of the particle multiplicity at 40 AGeV results from missing parts in the multiplicity distribution which was used for the embedding simulation. This also contributes to the systematic error.

3. Data Analysis

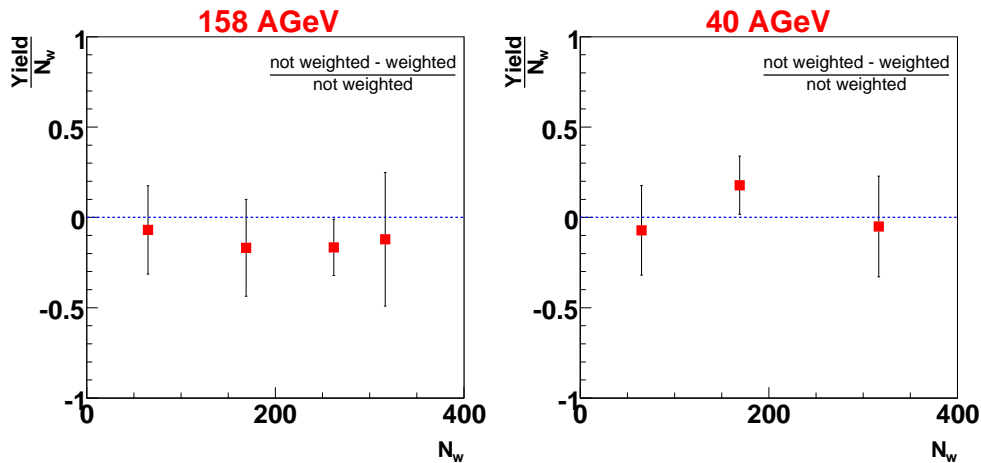


Figure 3.20.: Comparison between weighted and not weighted midrapidity Ξ^- yields ($|y| \leq 0.5$) at 158 AGeV (left) and 40 AGeV (right).

3.5.4. Influence of δ Electrons

Another possible effect, which could influence the efficiency correction of the spectra, is the event dependence on the number of beam particles travelling through the detector during the TPC readout [58]. Normally one event is excluded for data taking if additional beam particles are making inelastic interactions with the target in a certain time interval. However, it is possible that beam particles pass the detector which do not interact inelastically with the target. The inelastic interaction between the gas molecules in the target or detector gas with the beam particles can create δ electrons. The δ electrons have a low transverse momentum and longitudinal momenta in the order of 100 MeV. They are bent in the VTPC by the magnetic field, spiraled to the left and could influence the reconstruction efficiency.

The Wave Form Analyzer (WFA) collects information for the beam counters to determine the number of beam particles (N_{Beam}) that cross the detector during TPC readout. The ideal situation is $N_{Beam} = 1$. This means that only one lead ion that interacted with the target traverses the experiment during readout. In the current analysis no cut was applied on N_{Beam} . Figure 3.21 shows the N_{Beam} distribution (left) for the 158 AGeV (258tb) data set. Its mean value is $\langle N_{Beam} \rangle = 4.8$ and approximately 10% of all events possess a value of $N_{Beam} = 1$. The Ξ efficiency as a function of N_{Beam} is shown in Figure 3.21 (right). It is visible that the Ξ efficiency depends on N_{Beam} . Beside this high intensity run NA49 took also a low intensity minimum bias run at 158 AGeV. For the low intensity run the mean value of N_{Beam} is between 1 and 2. On the left hand side of Figure 3.15 the total reconstruction efficiency at 158 AGeV is shown. If one compares now the total reconstruction efficiency for the centrality class 1+2 (low intensity run) with the one of the semi-central data set (high inten-

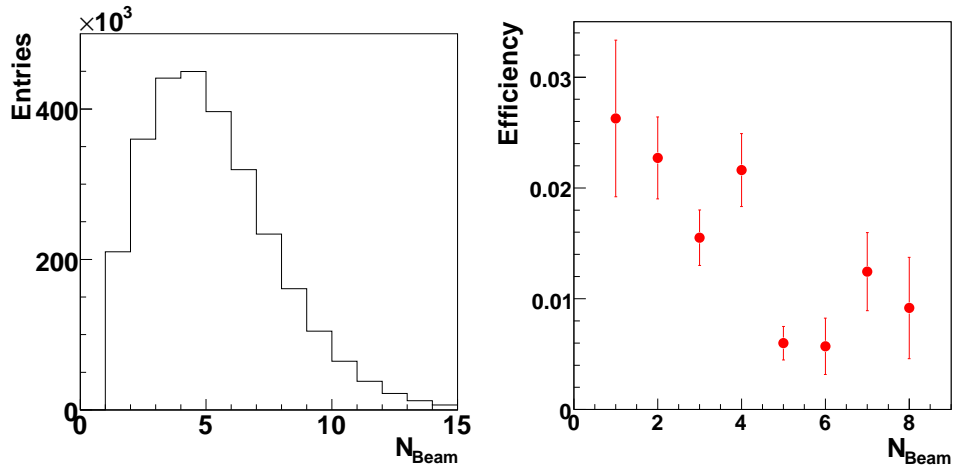


Figure 3.21.: N_{Beam} distribution (left) and the Ξ efficiency as a function of N_{Beam} (right) in central Pb+Pb collisions at 158 AGeV (256tb).

sity run), which are in a similar centrality range, it is clearly visible that the δ electrons are not making a big influence in the Ξ analysis and therefore no cut on the beam particles is necessary.

3. *Data Analysis*

4. Extraction of Spectra, Yields and Systematic Error

The *bin-by-bin* method is used in this analysis. In this method, the background subtracted raw data are separated into discrete bins of rapidity and transverse momentum. Acceptance and efficiency corrections are also computed in each of these y - p_t bins which are then applied to the data to determine the corrected yield. Final distributions are obtained by projecting and extrapolating the corrected distribution on the y or p_t axes separately. The *bin-by-bin* correction method has the advantage that it is to first order independent of the spectral shape of the assumed input distribution, compared to the *averaging* method. In the latter approach, the background subtracted raw data are projected, separately, along the y and p_t axes first. The resulting one-dimensional distributions are then corrected for acceptance and efficiency and final spectra are created. The *averaging* method suffers from the fact that the applied correction factors (and therefore the final results) are slightly dependent on the input distribution used to generate the initial MC particles. However, statistical errors for the *bin-by-bin* method are generally larger, since it requires higher MC statistics.

Results are presented for the Ξ^- in central and minimum bias Pb+Pb and semi-central Si+Si collisions and Ξ^+ for central Pb+Pb collisions. The Ξ^- and Ξ^+ are reconstructed with the global tracking chain and corrected with the *bin-by-bin* correction method. For the final distributions, the corrected y - p_t data were normalized by dividing by the bin size and the number of events taken. Then the corrected data were projected on the p_t and y axes by summing over other variables like the invariant mass and lifetime.

4.1. Transverse Momentum and Transverse Mass Spectra

Initially the corrected, normalized data are projected onto the p_t axis (summing over one unit in rapidity). The transverse mass distribution is computed with $m_t - m_0 = \sqrt{m_0^2 + p_t^2} - m_0$. The resulting p_t and $m_t - m_0$ spectra measured at midrapidity ($|y| \leq 0.5$) are presented in Figure D.21 and 4.2 at different energies in central Pb+Pb collisions. The corresponding fits to the invariant mass spectra can be found in Appendix D. Using Equations 3.11 and 3.12 to fit either the p_t or the $m_t - m_0$ distribution has to result in the same temperature parameter T . Indeed in the analysis presented, temperature parameters are

4. Extraction of Spectra, Yields and Systematic Error

obtained from fits to equation 3.11 and the equation is used to extrapolate over the full p_t range (see subsection 4.1.1).

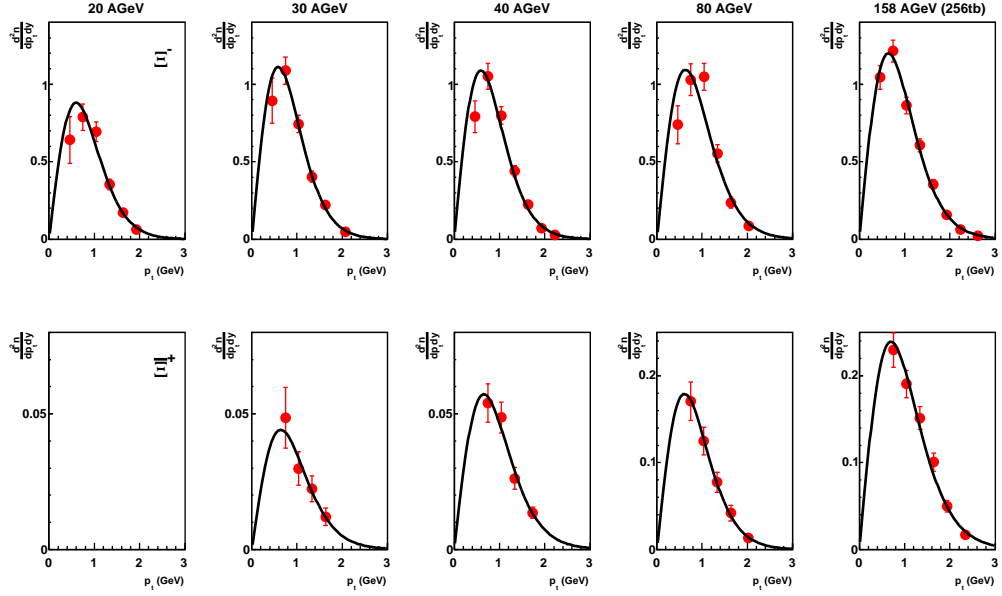


Figure 4.1.: Transverse momentum spectra for Ξ^- (top) and Ξ^+ (bottom) at midrapidity ($|y| \leq 0.5$) for different collision energies corrected with the *bin-by-bin* method. The lines represent Boltzmann fits with equation 3.11.

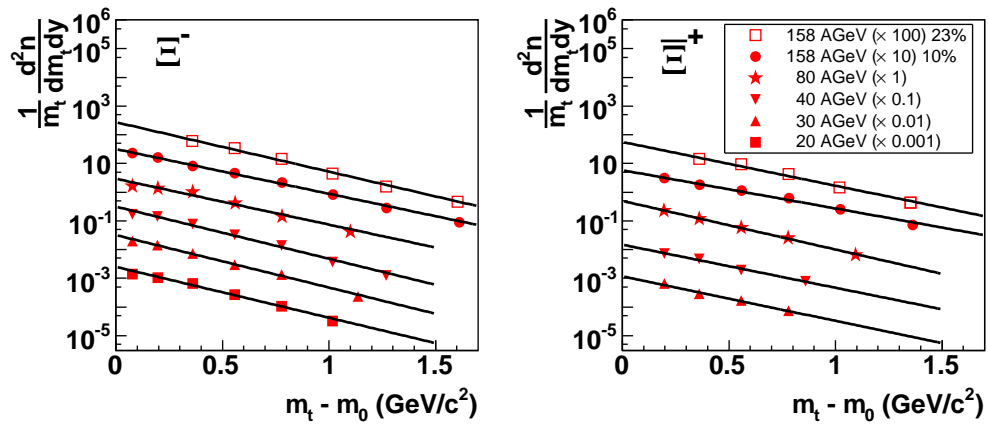


Figure 4.2.: Transverse mass spectra for Ξ^- (left) and Ξ^+ (right) at midrapidity ($|y| \leq 0.5$) for different collision energies corrected with the *bin-by-bin* method. The lines represent Boltzmann fits with equation 3.12.

4.1. Transverse Momentum and Transverse Mass Spectra

Figure 4.2 shows the transverse mass spectra at midrapidity ($|y| \leq 0.5$) for different energies in central Pb+Pb collisions. The transverse momentum and mass spectra for the minimum bias Pb+Pb and semi-central Si+Si data can be found in Appendix D.2 and D.3. The numerical values of all p_t - and $m_t - m_0$ -bins can be found in Appendix D. The inverse slope as a function of the centrality is shown in Figure 4.3. At 40 AGeV no centrality dependence of the inverse slope is visible. At 158 AGeV the inverse slope is increasing from light systems and stays constant for minimum bias Pb+Pb collisions.

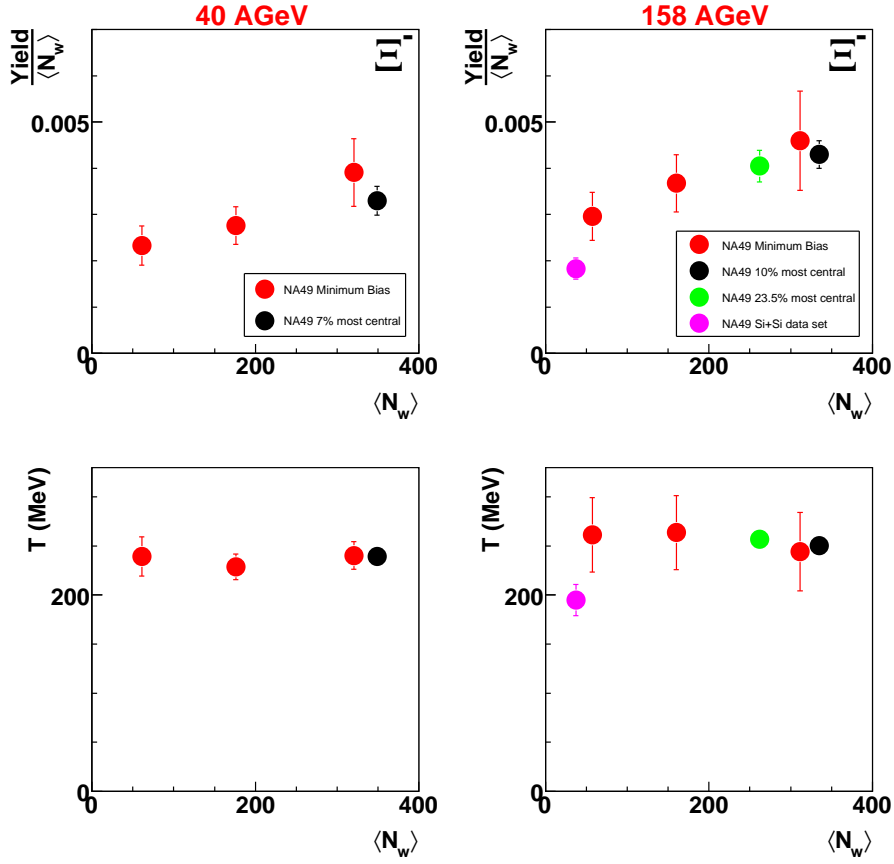


Figure 4.3.: The Ξ^- yield at midrapidity as a function of the centrality at 40 AGeV (top left) and 158 AGeV (top right). Inverse slope parameter T as a function of the centrality at 40 AGeV (bottom left) and 158 AGeV (bottom right). The fit range at 40 AGeV is $m_t - m_0 > 0.08$ GeV and at 158 AGeV $m_t - m_0 > 0.31$ GeV.

4.1.1. Extrapolation of the Transverse Momentum Spectra

Because of finite geometrical acceptance, NA49 is only sensitive in a certain p_t range. However, with the fitted temperature parameters now known, the yield

4. Extraction of Spectra, Yields and Systematic Error

can be extrapolated over the full transverse momentum range $0 < p_t < \infty$, assuming the distribution is thermal over the whole range. To determine the rapidity density for a current rapidity interval, the following equation has to be integrated:

$$\frac{dn}{dy} = \int_0^{+\infty} \frac{d^2n}{dp_t dy} dp_t = \int_0^{+\infty} C \cdot p_t \cdot e^{-\frac{m_t}{T}} dp_t, \quad (4.1)$$

where C and T are the fit parameters. In this method the integral and the resulting rapidity density is very dependent on the quality of the fit. Instead the measured data points of the p_t spectra are summed up and the fit function is used to make an extrapolation into the range not measured. The extrapolation factors, C_{p_t} , are computed by integrating equation 4.1 with the fitted T over the whole range and dividing by the integral over the experimentally sensitive range $p_t \text{ min} - p_t \text{ max}$:

$$C_{p_t} = \frac{\int_0^{+\infty} \frac{d^2n}{dp_t dy} dp_t}{\int_{p_t \text{ min}}^{p_t \text{ max}} \frac{d^2n}{dp_t dy} dp_t}. \quad (4.2)$$

Table D.23, D.36 and D.39 summarizes the central rapidity densities calculated from equation 4.1 and 4.2, the extrapolation factor C_{p_t} (from eq. 4.2) and inverse slope parameter T which are obtained after applying corrections for the central Pb+Pb, minimum bias Pb+Pb and semi-central Si+Si data sets. Figure 4.3 shows the centrality dependence of the Ξ^- midrapidity yields at 40 (top left) and 158 AGeV (top right). At both energies a clear centrality dependence is visible.

4.2. Rapidity Spectra and 4π Yields

Figure 4.4 shows the rapidity distributions, where the dN/dy values have been obtained by integrating over the full p_t range for the Ξ^- and Ξ^+ for different collision energies. The resulting distributions and extrapolation factors are given in Table E.23 (the rapidity distribution for the Ξ^- at 158 AGeV (256tb) is shown in Figure E.1). Symmetric reflection at midrapidity is possible because the beam and target ions are identical in Pb+Pb collisions. The y distributions are well described by a sum of two Gaussians, displaced relative to midrapidity by y_0 :

$$\frac{dN}{dy} = A \cdot \left[\exp\left(-\frac{(y - y_0)^2}{2\sigma^2}\right) + \exp\left(-\frac{(y + y_0)^2}{2\sigma^2}\right) \right], \quad (4.3)$$

where A is the height, y_0 the centroid and σ_y the width of the distribution. Gaussian fits (see equation 4.3) are superimposed on the data points shown in Figure 4.4. To extract the 4π yield, the measured data points of the rapidity spectra are summed up and equation 4.3 is used to make an extrapolation in the range not measured.

4.2. Rapidity Spectra and 4π Yields

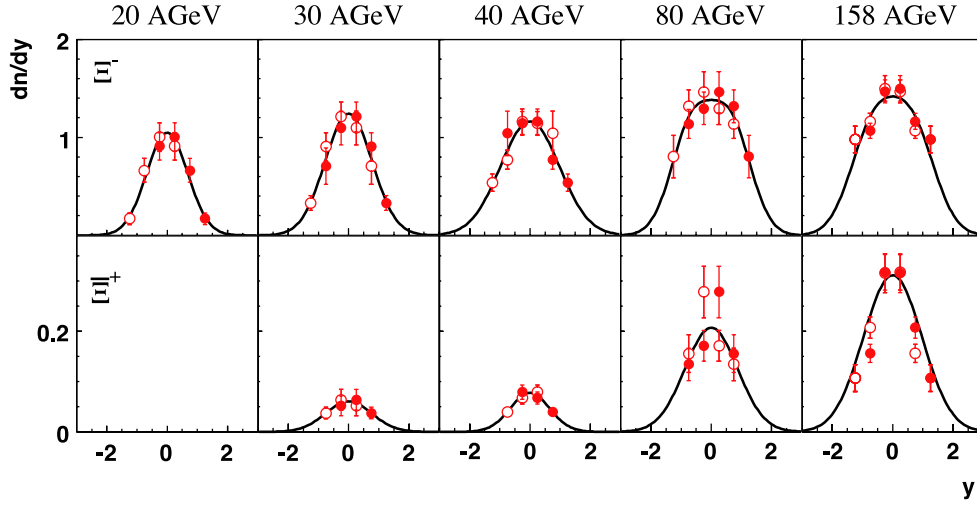


Figure 4.4.: Rapidity distributions for Ξ^- (top) and Ξ^+ (bottom) at different collision energies corrected with the *bin-by-bin* method and extrapolated with equation 4.3. Solid points show measurements, open symbols were obtained by reflection at midrapidity.

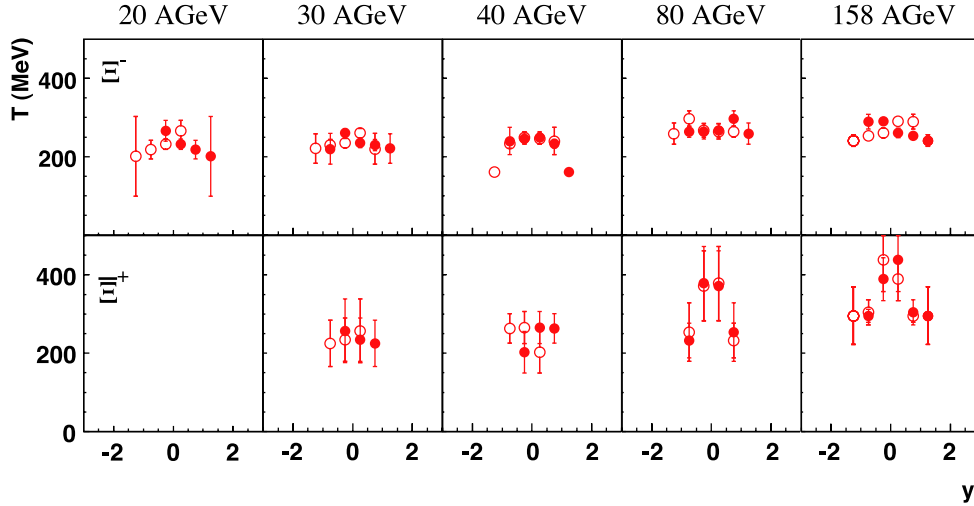


Figure 4.5.: The inverse slope as a function of the rapidity for Ξ^- (top) and Ξ^+ (bottom) at different collision energies. Solid points show measurements, open symbols were obtained by reflection at midrapidity.

The extrapolation factors C_y , are computed by integrating equation 4.3 over the whole range and dividing by the integral within the experimentally sensitive

4. Extraction of Spectra, Yields and Systematic Error

range:

$$C_y = \frac{\int_0^{+\infty} \frac{dn}{dy} dy}{\int_{y_{\min}}^{y_{\max}} \frac{dn}{dy} dy}. \quad (4.4)$$

The inverse slope as a function of rapidity is shown in Figure 4.5. Table E.23 summarizes the energy, 4π yields calculated from equation 4.4, extrapolation factors C_y and RMS widths of the y-distributions which are obtained after applying corrections for the central Pb+Pb data set. The numerical values of all y-bins for the data sets, analyzed in this thesis, can be found in the appendix E. There is an indication that a rapidity dependence of the inverse slope exist. Due to limited acceptance the measurement of the centrality dependence of the rapidity spectra is not possible.

4.3. Stability Checks of the Results and the Systematic Error

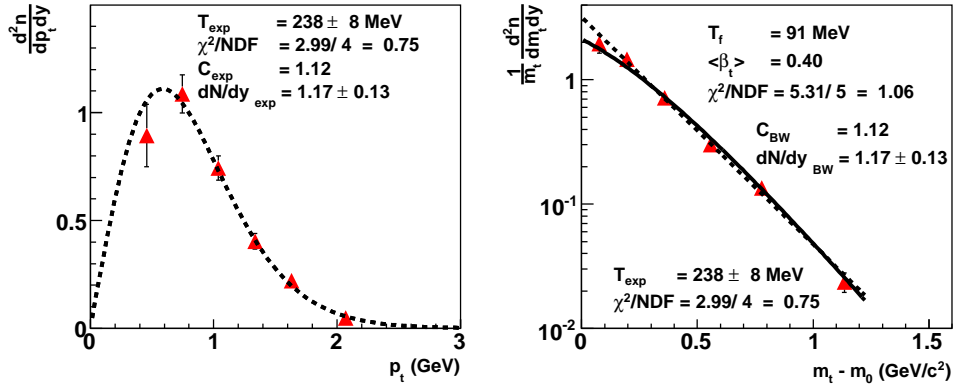


Figure 4.6.: Transverse mass spectra of the Ξ^- at midrapidity at 30 AGeV. The dashed curve shows the exponential fit and the solid line shows a model including transverse expansion [60].

The error of a measurement consists of the statistical error, which results from statistical fluctuations of the measurement and the systematic error. There are different sources which define the systematic error. One source is the determination of the extrapolation factor. Another way to estimate the systematic error is the variation of the cuts which are used in the analysis which were discussed in section 3.3.

Like already discussed in subsection 4.1.1, NA49 is only sensitive in a limited p_t range due to its finite geometrical acceptance. An extrapolation over the full transverse momentum range $0 < p_t < \infty$ was done with equation 4.1. As a

4.3. Stability Checks of the Results and the Systematic Error

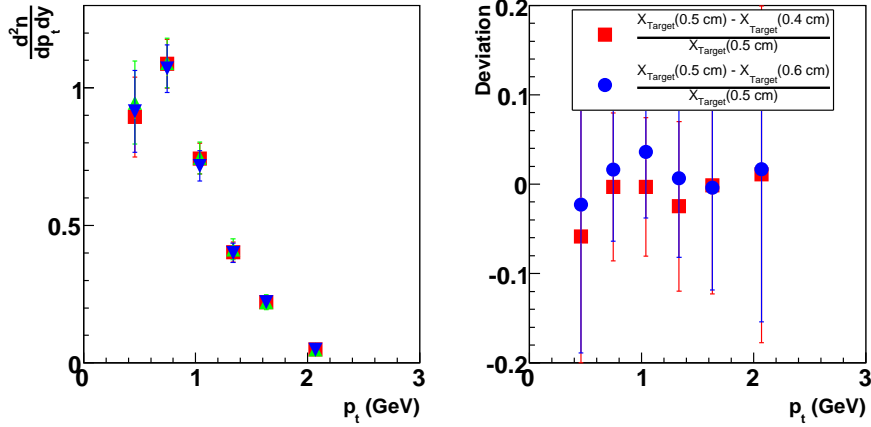


Figure 4.7.: Comparison of the stability with changes of the cut X_{Target} of the Ξ^- at 30 AGeV illustrated at the transverse momentum spectra (top left) and $m_t - m_0$ spectra (top right) respectively at midrapidity and the deviation of the changes of the cut X_{Target} of the Ξ^- (bottom left).

comparison to the Boltzmann fit (equation 4.1), the blast wave approach [60] is used. In this model thermal sources expanding with a collective velocity are assumed and is defined as:

$$\frac{dN}{m_t dm_t dy} \propto \int_0^R r dr m_t I_0 \left(\frac{p_t \sinh \rho}{T_f} \right) K_1 \left(\frac{m_t \cosh \rho}{T_f} \right), \quad (4.5)$$

where the parameters of the model are the freezeout temperature T_f and the transverse flow velocity β_s at the surface. In this model a linear radial velocity profile $\beta_t(r) = \beta_r(r/R)$ is assumed, which is motivated by hydrodynamical calculations (where R is the radius of the source and $\rho = \tanh^{-1} \beta_t$ the boost angle). To illustrate the deviations of the two different fit methods and the variation of the cuts the 30 AGeV central Pb+Pb data set is used as in the following. Figure 4.6 shows both fit methods, the extrapolation factors and the extracted dN/dy at midrapidity. The extrapolation factor C_{exp} , which results from the Boltzmann fit (see equation 3.11) is the same as the extrapolation factor from the blast wave fit (see equation 4.5). Therefore no difference between the two fit functions occurs at all energies.

The investigated effect is the stability with respect to changes of the cuts. Figure 4.7 shows the difference by changing the cut X_{Target} of the Ξ^- at 30 AGeV. Here the standard value, which is 0.5 cm, is varied to 0.6 cm and 0.4 cm. The same procedure as for the p_t spectra is used to check the stability for the rapidity spectra. Figure 4.8 shows the difference after changing the X_{Target} cut of the Ξ^- .

Appendix F shows the stability check for the Y_{Target} -cut, the b_y -cut of the pion

4. Extraction of Spectra, Yields and Systematic Error

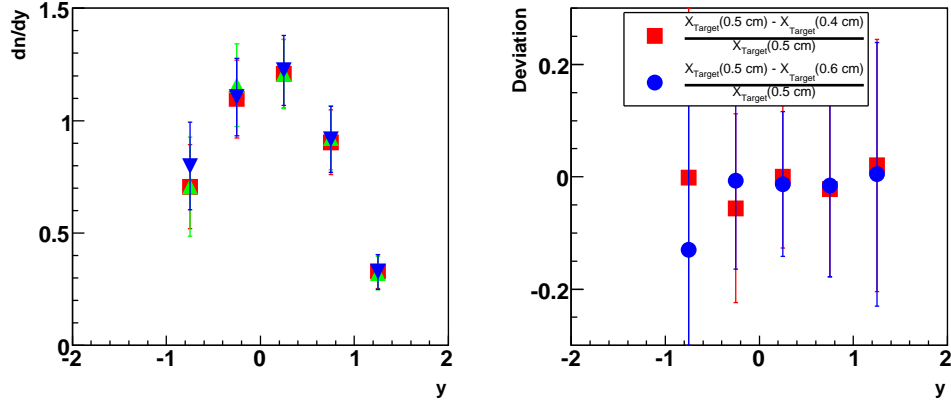


Figure 4.8.: Comparison of the stability with changes of the cut X_{Target} of the Ξ^- at 30 AGeV illustrated at the rapidity spectra (left) and the deviation of the changes of the cut X_{Target} of the Ξ^- (right).

of the mother Ξ^- and the b_y -cut of the pion of the daughter Λ for the transverse momentum- and rapidity spectra.

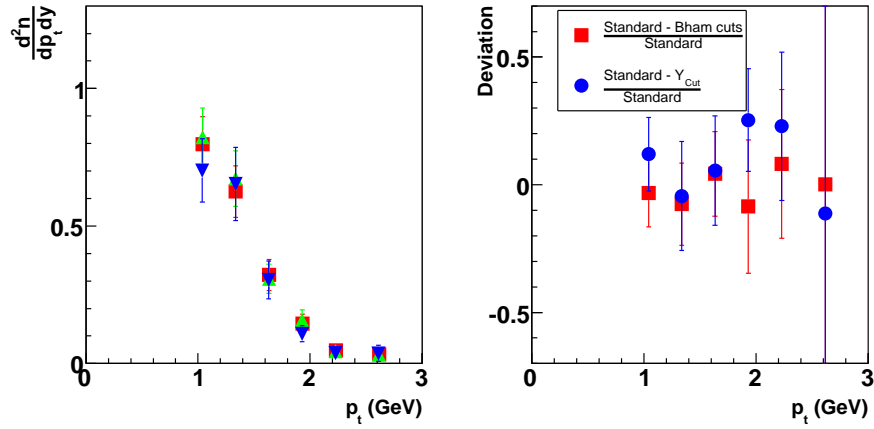


Figure 4.9.: Comparison of the stability with two different analysis strategies for the Ξ^- at 158 AGeV illustrated at the transverse momentum spectra (left) at midrapidity and the deviation of the different analysis strategies (right).

At 158 AGeV a high track density exists. Therefore another cut can be applied to cut-off tracks, which have many points in the high track density region which is called the y_{cut} . In the y_{cut} two parallel planes are defined vertical to the y -axis with a distance symmetric to the beam axis. More details about the y_{cut} can be found in [48]. Another method to check the systematic error is to use the *Birmingham cuts* in the V0 finder [61]. The difference between the Birmingham

and GSI cuts is that in the Birmingham method no uniform cuts are used for the V0 search. In this method three types of V0s exists (VT1/VT2/Combi). Is the first point of both daughter tracks from a V0 on opposite sides in the VTPC-1, the V0s are calles VT1. The same case is also for VT2 V0s but additionally to it the tracks can lie on both sides of VTPC-2. In the Combi type V0s one of the daughter tracks is on a different side and VTPC than the other one. Figures 4.9 and 4.10 shows the difference as a function of p_t and rapidity for the different analysis strategies with the standard method.

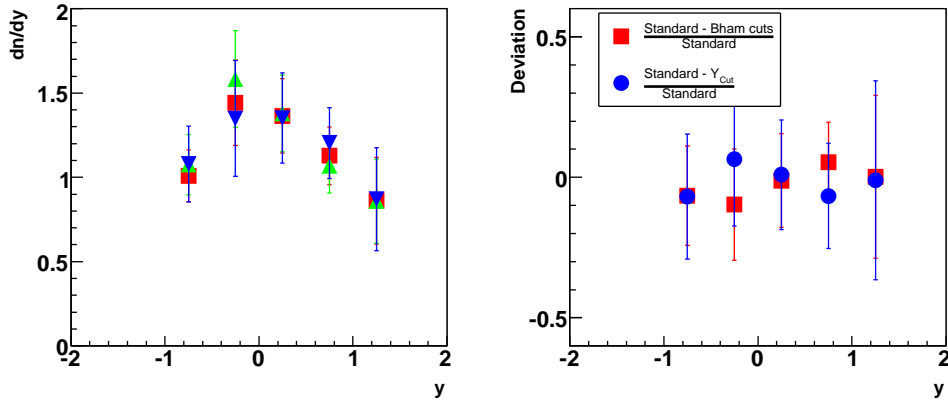


Figure 4.10.: Comparison of the stability with two different analysis strategies for the Ξ^- at 158 AGeV illustrated at the rapidity spectra (left) and the deviation of the different analysis strategies (right).

This stability checks to determine the systematic error is done for all data sets which are used in this thesis. The systematic error for the inverse slope parameter is 6% for the Ξ^- and 10% for the Ξ^+ . For the midrapidity a systematic of 11% ist determined for the Ξ^- and Ξ^+ . For the total multiplicity the systematic error depends on the extrapolation described in section 4.2 and is summarized in Table E.23.

4.4. Lifetime

Another consistency check for the employed reconstruction method that can be performed is a lifetime calculation. This involves a full correction for acceptance and efficiency and has the advantage that the mean lifetimes of all the particles are known [5]. Here the lifetime, τ , is expressed as $c\tau$ and measured in the center of mass of the Ξ . Figure 4.11 shows the corrected lifetime distribution at midrapidity for Ξ^- (left) and Ξ^+ (right) hyperons at 30 AGeV. The lifetimes τ_0 is extracted from the data for both Ξ^- and Ξ^+ using the following equation:

$$\frac{dN}{d\tau} = C \cdot \exp\left(\frac{-\tau}{\tau_0}\right), \quad (4.6)$$

4. Extraction of Spectra, Yields and Systematic Error

where C is the initial number of hyperons and τ_0 is the lifetime.

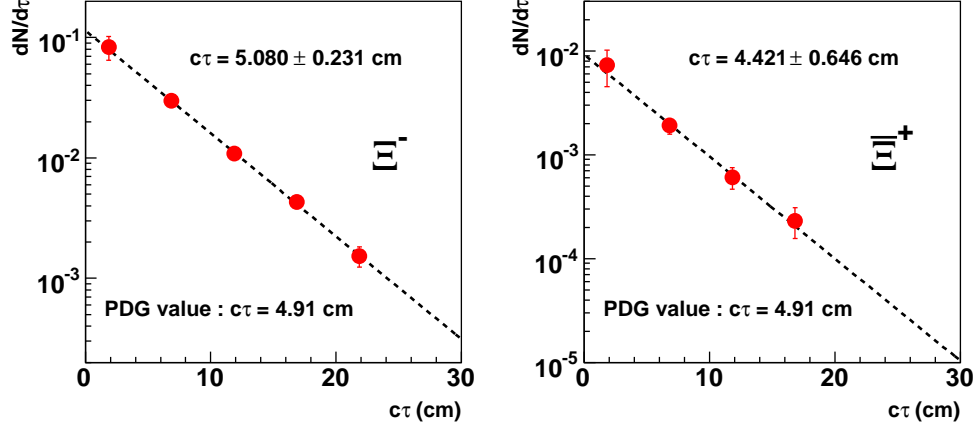


Figure 4.11.: Lifetime distribution at midrapidity ($|y| \leq 0.5$) for Ξ^- (left) and Ξ^+ (right) hyperons at 30 AGeV.

In both cases, the data are well described by the exponential in equation 4.6. The Particle Physics Book mean lifetime value for the Ξ^- , and therefore also the Ξ^+ , is given as $c\tau_0 = 4.91$ cm [5]. The values extracted from this analysis are for the Ξ^- $c\tau_0 = 5.080 \pm 0.231$ cm and for the Ξ^+ $c\tau_0 = 4.421 \pm 0.646$ cm and are in good agreement with this value.

4.5. Comparison with another Ξ Analysis at 158 AGeV

The Ξ results of this analysis are compared with the result of an already published one at 158 AGeV. Therefore a cut to the 10% most central events is applied for the 158 AGeV (256tb) data set to be in the same centrality range as the analysis by R. Barton [59].

	My Analysis	R. Barton Analysis [1pt]
$\frac{dN}{dy} _{y=0} (\Xi^-)$	1.44 ± 0.10	1.49 ± 0.08
$\frac{dN}{dy} _{y=0} (\Xi^+)$	0.31 ± 0.03	0.33 ± 0.04
$4\pi (\Xi^-)$	4.04 ± 0.16	4.12 ± 0.20
$4\pi (\Xi^+)$	0.66 ± 0.04	0.77 ± 0.04

Table 4.1.: Comparison of the midrapidity ($|y| \leq 0.5$) and 4π yields of the Ξ^- and Ξ^+ hyperon at 158 AGeV (10% most central) with the results by R. Barton [59].

Figure 4.12 shows the comparison of Ξ^- (left) and Ξ^+ (right) rapidity spectra

4.5. Comparison with another Ξ Analysis at 158 AGeV

at 158 AGeV with the analysis from R. Barton. In the analysis of R. Barton different analysis cuts were used [61]. It is visible that that the new analysis is compatible with the old one. Also the extracted midrapidity and 4π yields shown in Table 4.1 are in good agreement.

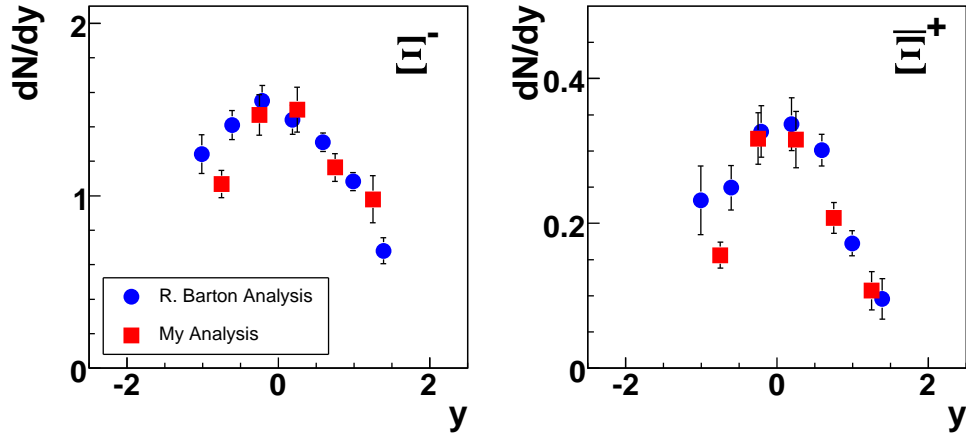


Figure 4.12.: Comparison of Ξ^- (left) and Ξ^+ (right) rapidity spectra at 158 AGeV (10% most central) with the analysis by R. Barton [59].

4. *Extraction of Spectra, Yields and Systematic Error*

5. Discussion

In this chapter the results on Ξ^- and Ξ^+ production for central and minimum bias Pb+Pb as well as semi-central Si+Si collisions are discussed. In the first section the results on the inverse slope parameter, the rapidity distributions and the Ξ^+/Ξ^- ratios are compared to the measurements from the NA57 collaboration. In the next sections the energy dependence of Ξ^- and Ξ^+ production and the strangeness enhancement of Ξ^- is shown. The chapter closes with the comparison to statistical and microscopic models.

5.1. Comparison with Other Experiments

The NA57 collaboration also has measured Ξ^- and Ξ^+ hyperons in Pb+Pb collisions at 40 and 158 AGeV [62] – [67]. The NA57 detector [68] has been designed to accept particles produced one unit around midrapidity. Due to this limited acceptance a comparison of the central rapidity densities, slope parameter and ratios is possible, but not of the integrated yields. For a comparison, the NA49 yields of Ξ^- and Ξ^+ hyperons at midrapidity in central Pb+Pb collisions need to be scaled, because the centrality selection is different between the two experiments. NA57 selected 5% for most central collisions, whereas the corresponding NA49 numbers are 7% at 40 AGeV and 10% at 158 AGeV (see [69]).

	NA49		NA57	
	40 AGeV	158 AGeV	40 AGeV	158 AGeV
$T(\Xi^-)$ (MeV)	239±6	267±9	206±22	299±12
$T(\Xi^+)$ (MeV)	286±7	296±17	308±63	356±31
$\frac{dN}{dy} _{y=0}(\Xi^-)$	1.19±0.11	1.56±0.11	1.99±0.31	2.08±0.09
$\frac{dN}{dy} _{y=0}(\Xi^+)$	0.07±0.01	0.33±0.03	0.08±0.03	0.51±0.04

Table 5.1.: Comparison of the inverse slope parameters and the central rapidity densities of the Ξ^- and Ξ^+ hyperon (NA49 results on dN/dy scaled up to 5% most central) with measurements by the NA57 collaboration. Shown are the statistical errors.

It can be assumed that in this small centrality range a scaling with $\langle N_W \rangle$ holds. The mean number of wounded nucleons per collision is different for the two data sets used in this analysis ($\langle N_W \rangle(7\%) = 349$ and $\langle N_W \rangle(10\%) = 335$, respectively)

5. Discussion

and smaller than for the 5% most central ($\langle N_W \rangle (5\%) = 362$). For this comparison, the NA49 yields at midrapidity were scaled by a factor of $362/349 = 1.04$ at 40 AGeV and $362/335 = 1.08$ at 158 AGeV. Table 5.1 summarizes the comparison of the inverse slope parameters and the midrapidity yields with the measurements of NA57. A discrepancy of 67% is visible for Ξ^- (2.6 standard deviations) and 14% for Ξ^+ (0.3 standard deviations) at 40 AGeV. At 158 AGeV the difference for Ξ^- is about 33% (5.8 standard deviations) and 55% (4.5 standard deviations) for Ξ^+ .

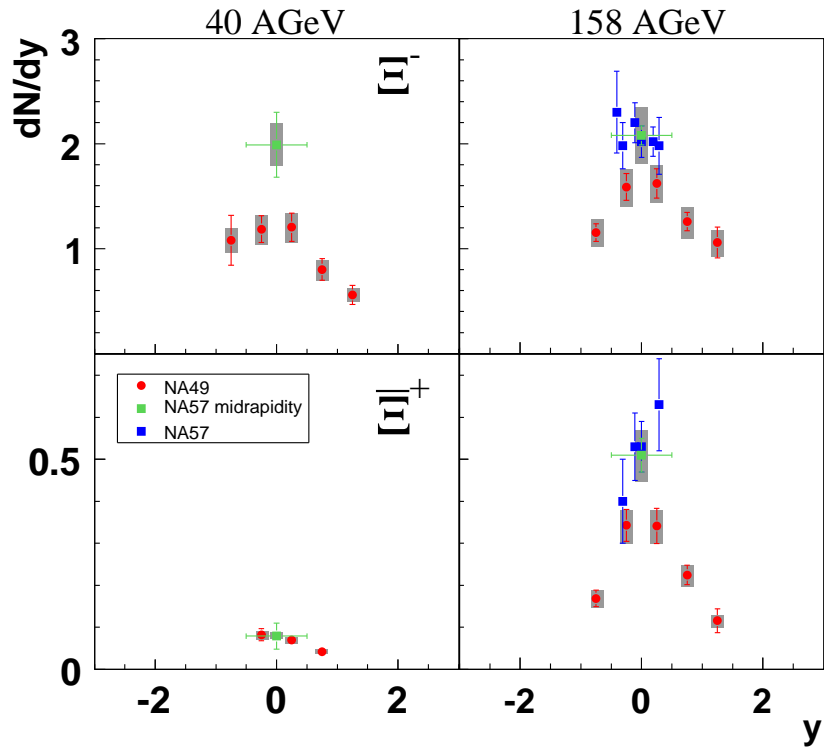


Figure 5.1.: Comparison of Ξ^- (top) and Ξ^+ (bottom) rapidity spectra at 40 and 158 AGeV (scaled up to 5% most central) with measurements from the NA57 collaboration. The systematic errors are represented by the grey areas.

Figure 5.1 shows the comparison of the Ξ^- (top) and Ξ^+ (bottom) rapidity spectra at 40 and 158 AGeV with results from NA57. The green squares represent the yields integrated in one unit around midrapidity and the blue squares the rapidity distributions from NA57. The discrepancy between NA49 and NA57 is clearly visible.

The slope parameters for Ξ^- and Ξ^+ hyperons are also in disagreement with the results from NA57. The discrepancy is 14% for the Ξ^- and 8% for the Ξ^+ at 40 AGeV. At 158 AGeV the difference for the Ξ^- is 12% and 20% for the

5.1. Comparison with Other Experiments

Ξ^- . This difference is not only visible for the Ξ hyperon yields, also for the Λ , Ω and K_s^0 . Nevertheless, the Ξ^+/Ξ^- ratios at midrapidity shown in Table 5.2 are consistent with the ones from NA57. Also for the other hyperons the ratios are in a good agreement with the measurements from NA57.

	Ξ^+/Ξ^- ($ y < 0.5$)	
	40 AGeV	158 AGeV
NA49	0.06 ± 0.01	0.22 ± 0.03
NA57	0.07 ± 0.01	0.25 ± 0.01

Table 5.2.: Comparison of the Ξ^+/Ξ^- ratio at midrapidity with measurements from the NA57 collaboration. The errors shown are statistical only.

It is also possible to compare the centrality dependence of Ξ^- production one unit around midrapidity at 40 AGeV and 158 AGeV. This is shown in Figure 5.2. For both energies the Ξ^- yield is rising from peripheral to central collisions. At 40 AGeV a good agreement is observed between NA49 and NA57 for peripheral and semi-central collisions. For central collisions a discrepancy is visible. At 158 AGeV the very peripheral bin agrees with NA57 but for semi-central and central collisions a difference is observed.

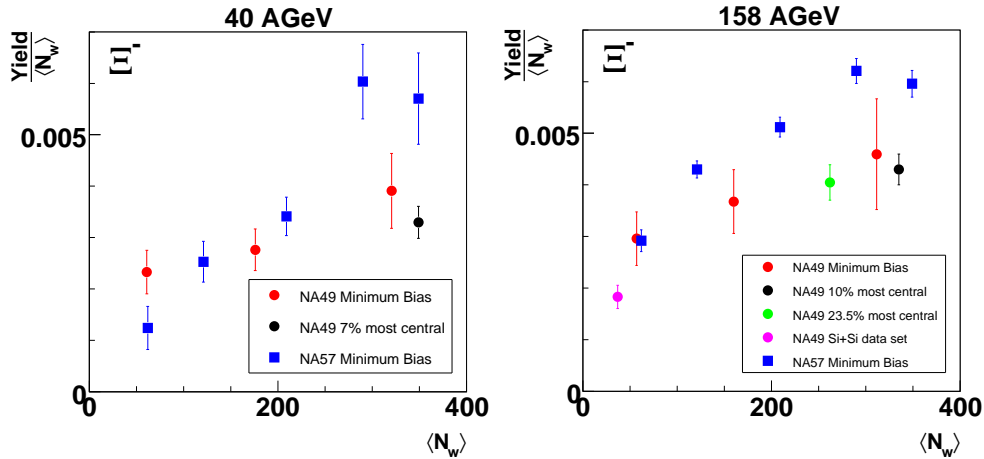


Figure 5.2.: Comparison of the Ξ^- yield at midrapidity as a function of the centrality at 40 AGeV (left) and 158 AGeV (right) with results from NA57. The errors shown are statistical only.

The disagreement between NA57 and NA49 is still an open issue. A couple of meetings and discussions with the NA57 collaboration could not solve this problem. Measurements by STAR in a low energy run at RHIC might unravel this puzzle in the near future.

5.2. Energy Dependence

In the following, the energy dependence of the observables inverse slope parameter T , mean transverse mass $\langle m_t \rangle - m_0$, the midrapidity and total yields and the Ξ^+/Ξ^- ratios are shown. The results of Ξ^- and Ξ^+ production in central Pb+Pb collisions at 20, 30, 40, 80 and 158 AGeV beam energy at the CERN SPS from this thesis are compared to measurements at different energies. For the lower energies (6 AGeV) a measurement at the Alternating-Gradient-Synchrotron (AGS) exists. At the Relativistic-Heavy-Ion-Collider (RHIC), heavy-ion collisions at a center of mass energy of 62.4, 130 and 200 GeV per nucleon-nucleon pair are performed. To compare the results from fixed-target and collider experiments with each other, the center of mass energy is used instead of the kinetic energy E_{kin} , which is defined in Appendix A.4. The conversion between both energies is shown in Table A.1. Also the midrapidity values is shown in Table A.1 for the different beam energies.

The results from the AGS accelerator are from the E895 experiment. The E895 collaboration measured Ξ^- in Au+Au collisions at 6 AGeV beam energy in a rapidity window $|y| \leq 0.5$. The total multiplicity is taken from reference [70].

The STAR collaboration provides measurements of Ξ production at 62.4, 130 and 200 GeV in Au+Au collisions at midrapidity ($|\eta| \leq 0.5$) [71, 72].

5.2.1. Inverse Slope Parameter and Mean Transverse Mass of the Ξ Hyperon

The m_t spectra were fitted by a Boltzmann like function (see equation 3.12) to extract the inverse slope parameters of Ξ^- and Ξ^+ . In order to compare the NA49 inverse slope parameter T with the ones from the NA57 and STAR experiments the m_t fitting range is $m_t - m_0 > 0.19 \text{ GeV}/c^2$.

The left hand side of Fig. 5.3 shows the inverse slope parameter at midrapidity as a function of the center of mass energy $\sqrt{s_{NN}}$. A weak energy dependence at SPS energies is observed for the inverse slope parameter of the Ξ^- . At RHIC energies higher values are observed. The Ξ^+ (open symbols) shows the same energy dependence. Measurements of Ξ hyperons at lower energies would be needed to fully study their energy dependence. This might be done by the CBM² experiment at FAIR³.

The inverse slope parameter provides in the case of kaons a good characterization of the spectra. For heavier particles like the Ξ , however, the local slope of the spectra depends on m_t . Instead, the first moment of the m_t -spectra can be used to study their energy dependence. On the right hand side of Fig. 5.3 the energy dependence of the mean transverse mass, $\langle m_t \rangle - m_0$, is shown for the Ξ . The mean transverse mass was calculated by fitting the measured data (see section 4.1) with three different fit functions: A double exponential and a blast

²The Compressed Baryonic Matter experiment

³Facility for Antiproton and Ion Research

wave function (see 4.5). The difference between these three methods represents the systematic error.

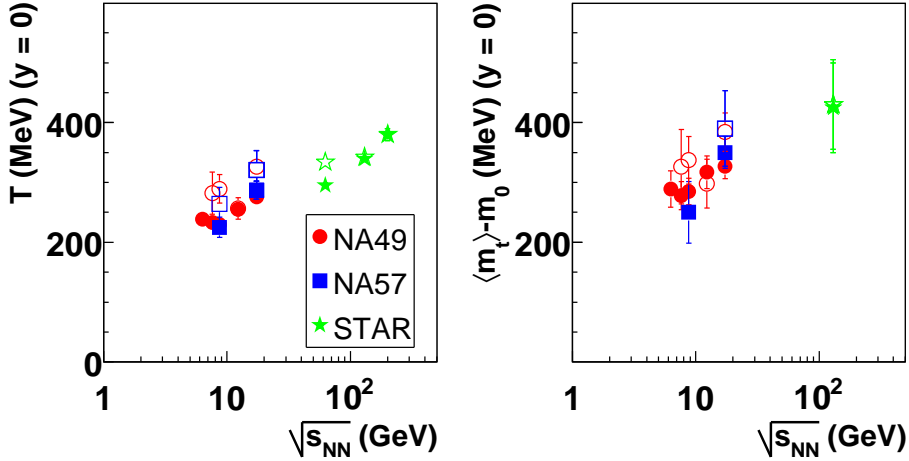


Figure 5.3.: Energy dependence of the inverse slope parameter T (left) and mean transverse mass $\langle m_t \rangle - m_0$ (right) of Ξ at midrapidity in central Pb+Pb/Au+Au collisions from SPS to RHIC energies. Filled symbols represent the Ξ^- and open symbols indicate the Ξ^+ .

Within a static fireball model the inverse slope parameter of a m_t distribution gives the temperature of the particles. In this, all particle species have the same temperature. The m_t -spectra in nucleus-nucleus collisions are additionally affected by a collective transverse expansion. If the energy density and hence the initial pressure increases with beam energy, an increase of transverse expansion is expected. Assuming that the strength of the transverse expansion is reflected in the inverse slope parameter or the mean transverse mass, a rise with $\sqrt{s_{NN}}$ is expected. Both, the inverse slope parameter, as well as the mean transverse mass show a weak energy dependence at SPS energies. At RHIC energies even higher values are observed. The same behaviour is also seen for pions, kaons and protons [73].

In a hydro-dynamical model, flow develops because of pressure gradients which are generated in the nuclear or the partonic medium, and hence the inverse slope parameter T does not reflect the true freeze-out temperature of each particle species. This is illustrated in Figure 5.4 which shows the masses of various particles along with their corresponding inverse slope parameters in central Pb+Pb collisions at 40 AGeV (left) and 158 AGeV (right) (the corresponding plots for 20, 30 and 80 AGeV can be found in Appendix G.). The behaviour shown in Figure 5.4 can be explained by the notion that if the fireball is expanding with a certain velocity, and all particles freeze-out at approximately the same temperature, the inverse slope parameter should increase with the mass of the particle. Therefore, the temperature at thermal freeze-out T_{fo} can be obtained

5. Discussion

by extrapolating to zero mass assuming the parameterization given in equation 5.1, where T_{fo} is the thermal freeze-out temperature of the fireball, $\langle\beta_t\rangle$ is the mean transverse velocity of the particles in the fireball and m_i is the mass of particle i [60] :

$$T = T_{fo} + m_i \cdot \langle\beta_t\rangle^2. \quad (5.1)$$

As can be seen in Figure 5.4 the dependence predicted by equation 5.1 is borne out by the data, if only pions, kaons, protons, and deuterons are considered. However, all other heavier particles do not follow this trend but have approximately the same inverse slope parameter. In [75] it is argued that is due to the fact that heavy particles, like the Ω , do not participate in hadronic rescattering and the collective motion can only be developed in the pre-hadronic stage, i.e. partonic stage for these hadrons.

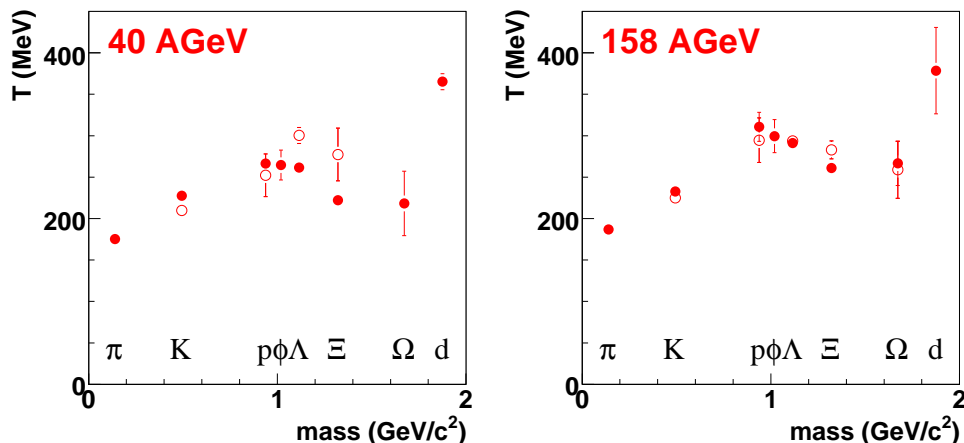


Figure 5.4.: Midrapidity hadron slope parameter T as a function of particle mass in central Pb+Pb collisions at 40 AGeV (left) and 158 AGeV (right). The open symbols represent the antiparticles.

If one omits the pions and deuterons from these considerations, it is maybe even fair to say that all particles exhibit the same inverse slope parameter. Most of the known resonances are decaying into pions (in low p_t) and influence the measured pion inverse slope parameter and therefore they can not be considered. The deuterons can also not be taken into account. It is believed that the deuterons are created by coalescence of protons and neutrons at freeze-out [74]. Thus, the inverse slope parameter of pions and deuterons is difficult to interpret and they should not be taken into account. Therefore, it might even be argued that maybe all particles reflect only the collective motion that is developed in the partonic stage and that the influence in the subsequent hadronic phase is marginal.

5.2.2. Strange Hadron Yield Enhancement

The Λ and Ξ^- yields in Pb+Pb collisions at $\sqrt{s_{NN}} = 17.3$ GeV measured by the NA49 experiment are compared with p+p [76] yields to derive an enhancement factor E defined as :

$$E = \left(\frac{\text{Yield}}{\langle N_W \rangle} \right)_{A+A} / \left(\frac{\text{Yield}}{\langle N_W \rangle} \right)_{p+p}, \quad (5.2)$$

where $\langle N_W \rangle$ is the number of wounded nucleons. The resulting enhancement factors are displayed in Figure 5.5. The measurements are compared to results from the NA57 and STAR collaboration at $\sqrt{s_{NN}} = 200$ GeV [77, 78]. An enhancement is observed, with the doubly strange Ξ^- being enhanced more than the Λ s, in accordance with the original prediction [14] – [16]. The same trend is also measured by the NA57 collaboration at $\sqrt{s_{NN}} = 17.3$ GeV. But instead of p+p NA57 uses p+Be as reference [65].

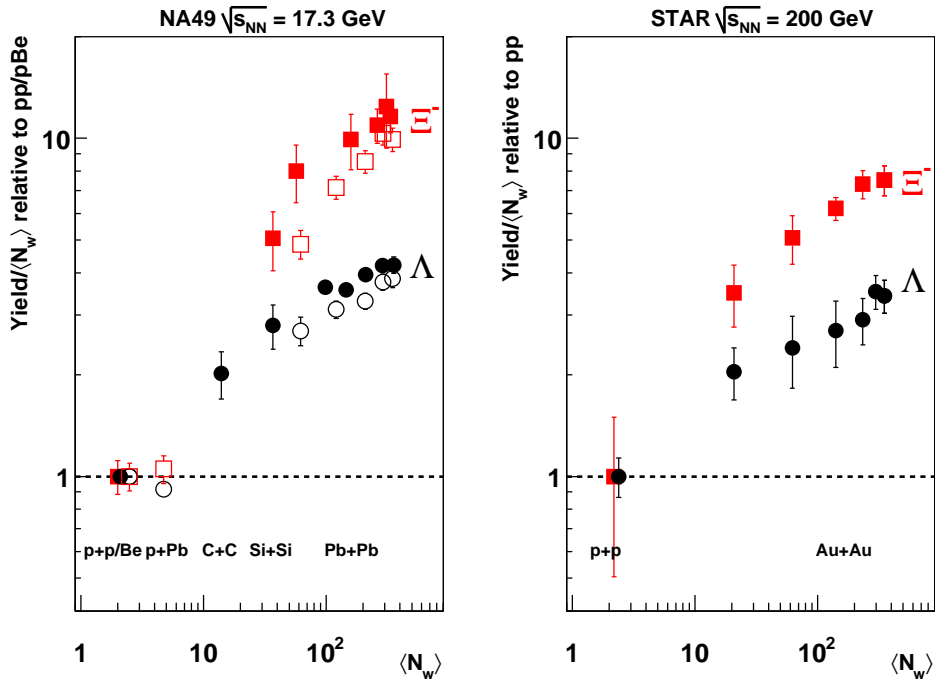


Figure 5.5.: Hyperon enhancement as a function of the number of wounded nucleons at $\sqrt{s_{NN}} = 17.3$ GeV (left) from NA49 (filled symbols), $\sqrt{s_{NN}} = 17.3$ GeV from NA57 (left) (open symbols) and $\sqrt{s_{NN}} = 200$ GeV from STAR (right).

Since already in p+A reactions a slight enhancement for hyperons is observed [76], the enhancement relative to p+Be is less. However, when the enhancement at SPS is compared to the one measured by STAR at $\sqrt{s_{NN}} = 200$ GeV, it is found that the enhancement at RHIC energies is actually less than at SPS

5. Discussion

energies. The enhancement for the most central bin is shown in Figure 5.6 as a function of the strangeness content $|s|$ of the particle. A clear hierarchy of the enhancements is visible, which increases with the strangeness content of the particle.

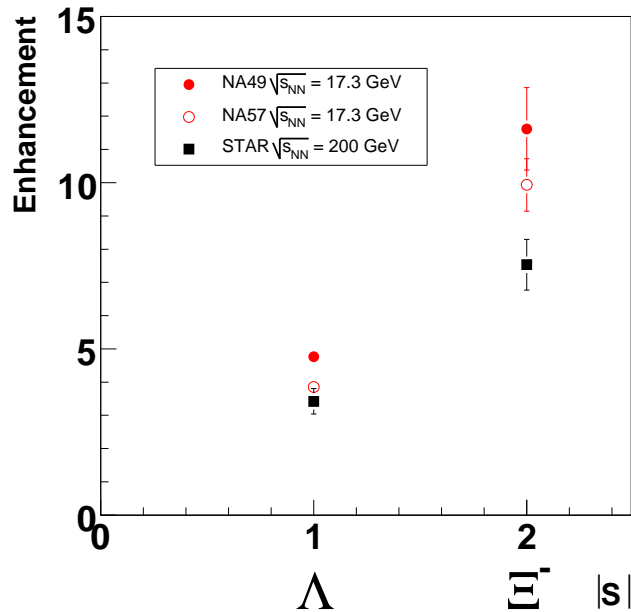


Figure 5.6.: Strangeness enhancement for Λ and Ξ^- at $\sqrt{s_{NN}} = 17.3$ GeV (filled symbols NA49 and open symbols NA57) and $\sqrt{s_{NN}} = 200$ GeV (STAR) in the most central bin.

It has been shown that increasing the collision energy, also increases the available phase space for particle production in small systems such as p+p [77, 78]. Thus the enhancement is predicted to decrease with increasing $\sqrt{s_{NN}}$, as the baseline measured (p+p) becomes less canonically suppressed with respect to the larger Pb+Pb (Au+Au) system. In fact, the enhancement is greater at $\sqrt{s_{NN}} = 17.3$ GeV than at $\sqrt{s_{NN}} = 200$ GeV and it is similar to what was seen for kaons (see Figure 1.9).

5.2.3. Excitation Function of Ξ production

For AGS energies an almost complete stopping of the target and projectile nucleons exists [13] leading to a baryon rich region at midrapidity. At RHIC energies the colliding nuclei are almost transparent (no complete stopping) [1] and the center of the reaction zone is almost net baryon free. In the SPS energy range a mixture of both scenarios exists (see section 1.4). Figure 4.4 shows the rapidity distribution of Ξ^- and Ξ^+ hyperons from 20 AGeV – 158 AGeV. At low SPS energies the production of particles is concentrated at central rapidity

5.2. Energy Dependence

and the distribution gets broader for higher energies. The Ξ^- still can include a valence quark from the target or projectile nucleons. This effect is visible in the rapidity distribution of the Ξ^- which is broader than the one from the Ξ^+ . Figure 5.7 shows the energy dependence of midrapidity and total Ξ^- and Ξ^+ yields. A clear energy dependence is visible for Ξ^- and Ξ^+ .

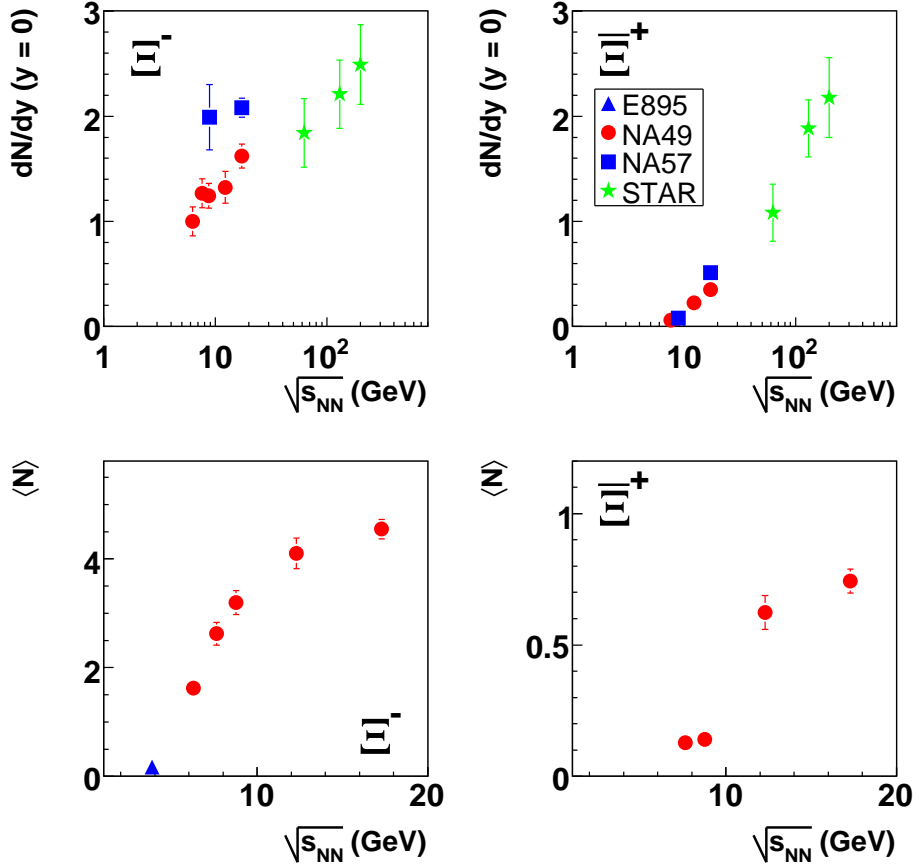


Figure 5.7.: The energy dependence of Ξ^- (top left) and Ξ^+ (top right) yields at midrapidity and of the total Ξ^- (bottom left) and Ξ^+ (bottom right) yields from AGS to RHIC energies.

Figure 5.8 shows the energy dependence of the midrapidity and total Ξ^- (Ξ^+) yields from AGS to RHIC energies, normalized to midrapidity and total pion yields. The total pion multiplicity is calculated as:

$$\pi = 1.5 \cdot (\pi^- + \pi^+). \quad (5.3)$$

Here the factor 1.5 takes into account the π^0 mesons. While Ξ^+/π and $\langle \Xi^+ \rangle / \langle \pi \rangle$ ratios rise continuously with energy, a distinct maximum is visible in the energy dependence of the ratios Ξ^-/π and $\langle \Xi^- \rangle / \langle \pi \rangle$.

5. Discussion

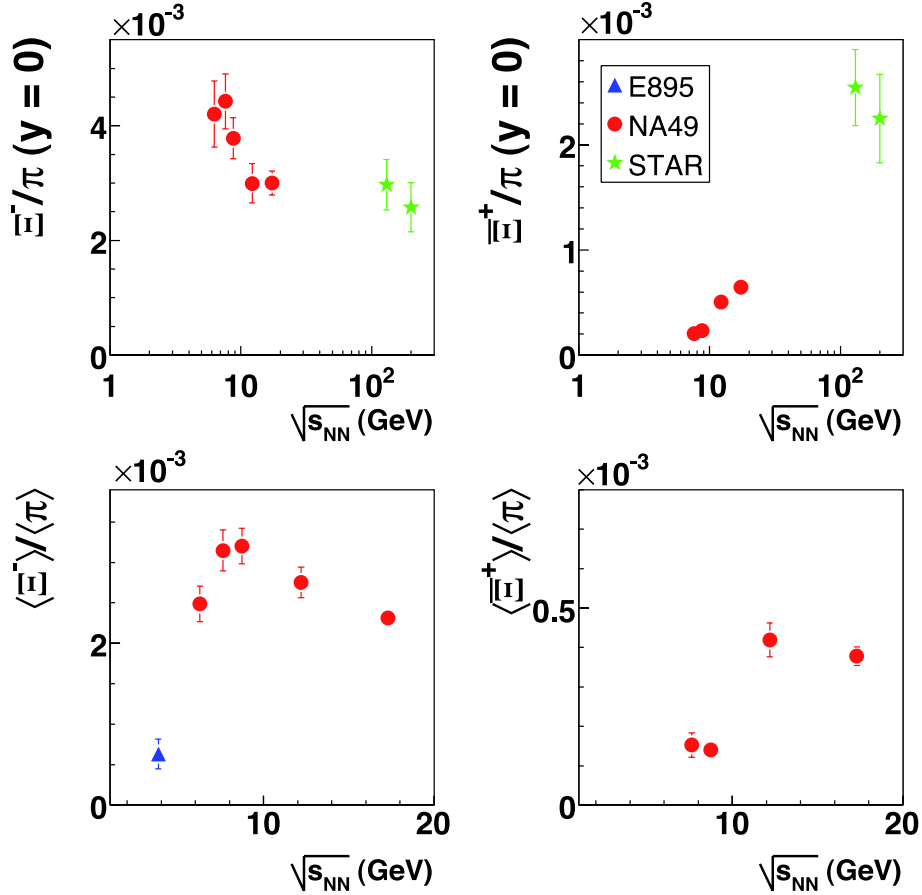


Figure 5.8.: The energy dependence of Ξ^- (top left) and Ξ^+ (top right) yields at midrapidity and of the total Ξ^- (bottom left) and Ξ^+ (bottom right) yields from AGS to RHIC energies, normalized to midrapidity and total pion yields ($\pi = 1.5 (\pi^+ + \pi^-)$) [82] – [85]).

5.2.4. Antibaryon/Baryon Ratio

The $\bar{\Xi}^+/\Xi^-$ ratio at midrapidity are compared to other \bar{B}/B ratios from NA49 [86] – [90] and RHIC experiments [72]. These ratios are shown in Figure 5.9 as a function of the center of mass energy. The ratios increase with increasing strangeness content of the baryons at a given energy. The energy dependence of the ratio for multiply strange hyperons is weaker than that for protons and Λ . Because the net baryon density at midrapidity is a strong function of the beam energy, the antibaryon to baryon ratio strongly depends on the number of valence up and down quarks in the hadron. For Ω with no valence up/down quarks the energy dependence of the ratio is the weakest. The ratio at SPS energies is not one for the Ω because it carries baryon number. The open symbols represent measurements from the NA57 collaboration [62] which are in good agreement with the NA49 data.

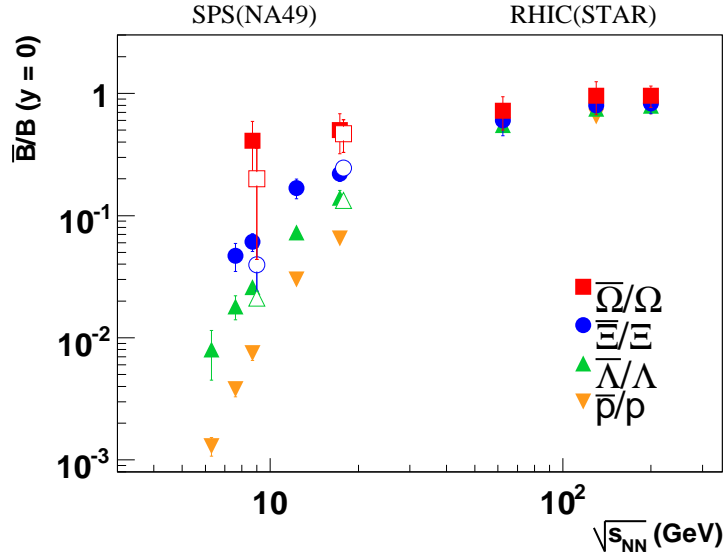


Figure 5.9.: The antibaryon/baryon ratio (\bar{B}/B) at midrapidity from SPS to RHIC energies. Open symbols represent measurements from the NA57 collaboration.

5.3. Theoretical Models

In order to understand and interpret the experimental data, they are compared to theoretical models. As described in section 1.4, the different stages of the collision have disparate processes which involve either hadronic or quark and gluon degrees of freedom. It becomes very difficult to model the whole collision within one model. Therefore many models are developed which deal with one particular stage of the collision. There are two types of models. Microscopic models which attempt to explain the details of particle production by a sequence of interactions between particles. Secondly there are statistical models which assumes that a matter at equilibrium is formed at a given stage of the collision.

5.3.1. Spectator-Participant Model

The Glauber model [92] describes an initial stage of p+A and A+A collisions as a sequence of N+N interactions. The model is based on three assumptions: a) the colliding nucleons have straight trajectories, b) a constant nucleus-nucleus cross-section is assumed for every nucleus-nucleus collision (typically 30 mb at SPS energies) and c) the density distribution is described by a nuclear density function. A schematic view of a nucleus-nucleus collision is shown in Figure 5.10. Two classes of nucleons can be distinguished: nucleons which undergo inelastic

5. Discussion

interactions, so called participants and nucleons which do not suffer any inelastic interactions, spectators.

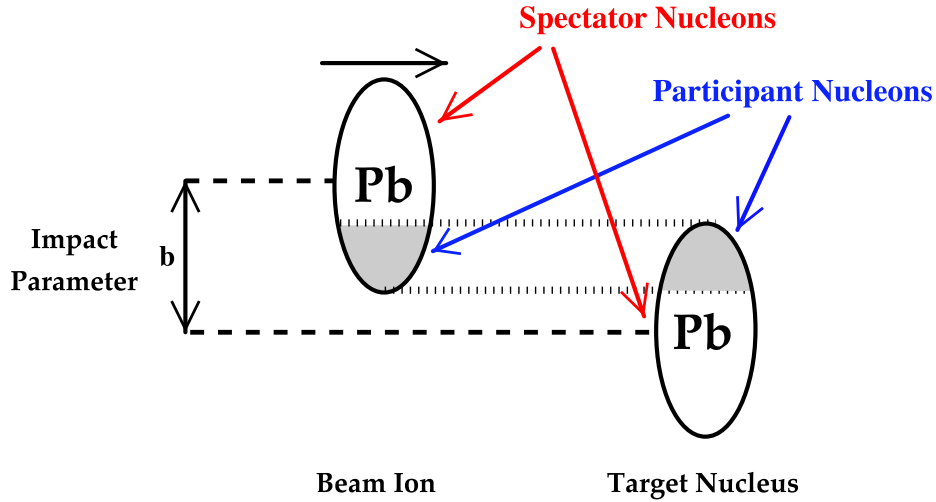


Figure 5.10.: Definition of impact parameter.

The distance between the trajectories which describes the center of the nucleus, is characterized by the impact parameter b . The size and the structure of the region, where the nucleons of the two nucleus collide, is defined by this parameter. Collisions with $b \approx 0$ are called central interactions and those with $b \approx A^{1/3}$ are called peripheral collisions. There are different ways to characterize A+A collisions: number of wounded nucleons ($\langle N_W \rangle$), number of participants ($\langle N_{\text{part}} \rangle$) and number of collisions ($\langle N_{\text{coll}} \rangle$). To determine the number of wounded nucleons just the initial collision of the nucleons calculated with Glauber model are taken into account. Secondary interactions are neglected. One step further is the determination of the number of participants. Participants are all nucleons which suffered inelastic interaction either in initial stage or in the course of expansion of the system. Normally the calculation is done by a string hadronic Monte Carlo generator. Therefore the quantity $\langle N_{\text{part}} \rangle$ is a little bit bigger than $\langle N_W \rangle$. The maximum value of both quantities $\langle N_W \rangle$ and $\langle N_{\text{part}} \rangle$ is the number of nuclei of the participating nucleus in a reaction. A given nucleon can suffer many collisions and the total number of all nucleon-nucleon collisions is defined as $\langle N_{\text{coll}} \rangle$. This number can be much bigger than the maximum value of $\langle N_W \rangle$ and $\langle N_{\text{part}} \rangle$.

5.3.2. RQMD v2.3

RQMD (Relativistic Quantum Molecular Dynamics) [93, 94] is a microscopic model to simulate heavy ion collisions.

In general, transport models propagate the colliding nucleons through phase-space. Interaction probabilities are calculated using published interaction cross-

sections of free hadrons and the relative phase space proximity of pairs of particles at each time step of the reaction. Inelastic collisions may produce new particles, such as pions, which are also propagated through phase space along with the nucleons. The reaction ends when the phase space density reaches a low enough threshold such that the probability of further interactions is small - the freeze-out point. No post freeze-out effects, such as Coulomb interaction, are included in this model. All final-state particle distributions are frozen at the end of the reaction.

In-medium effects for nucleon-nucleon interactions can be included by using the mean field setting, which scales the free nucleon cross-sections to mock up the in-medium dependence of the interaction probabilities.

The string, representing the color field, describes the strong interaction between quarks. Hadrons are produced when strings decay. The model assumes that the exchanging momentum is absorbed from a quark between the colliding nucleons. This causes new quark and anti-quark pairs to be created. The probability of creating a light quark anti-quark pair is higher than a strange anti-strange pair. This probability does not depend on the total energy of the string, but on the energy density in the string and the quark mass. The ratio between the production of strange and non-strange quarks in the string fragmentation is an important parameter. It determines the kaon to pion ratio in the final state. If two particles are close enough to each other there is a probability that they will interact with each other. The interaction cross-section for rescattering based on relative simple resonance model calculations, which is verified from experimental data (e.g. pion-nucleon and kaon-pion scattering). Overlapping strings do not fragment independently from each other but form *color ropes*.

5.3.3. UrQMD v1.3

UrQMD (Ultrarelativistic Quantum Molecular Dynamics) [95] is a microscopic model based on a phase space description of the reaction with transport theory. Particle production takes place via excitation, coalescence, resonance decay or string fragmentation.

The propagation of all particles is simulated numerically according to equations of motion. Cross-sections are interpreted geometrically providing an interaction of two particles. Therefore rescattering of particles is included by construction of the model. The essential cross-section inputs are two body potentials and decay widths. No in-medium properties different from those in the vacuum are assumed.

In UrQMD cross-sections are a function of the incoming and outgoing particle types, their isospins and their center of mass energy. They may either be tabulated, parameterized according to an algebraic function or extracted from other cross-sections via general principles, such as detailed balance or the additive quark model (AQM). The principle of detailed balance is based on the time-reversal invariance of the matrix element of the reaction.

5. Discussion

5.3.4. Statistical Hadron Gas Models

For systems involving large numbers of produced particles, statistical models can be considered within the context of the grand canonical ensemble. Statistical models of strong interactions were proposed more than 50 years ago by Landau [13] and Fermi [96]. The Hadron gas description of the final state was developed by Hagedorn [97, 98]. No statement is made in this kind of model about how the system arrives to statistical equilibrium. Depending on the hadron gas model version hadron yields [12] or yield ratios [99, 100] are described. These models work quite well over a broad energy range (see Figure 5.11). The basic parameters are, volume V , a temperature T and chemical potentials (μ_Q, μ_s, μ_B). The extracted parameters T and μ_B show a systematic energy dependence, where the baryonic chemical potential μ_B is decreasing with energy while the chemical freeze-out temperature is increasing (see Figure 1.4). It is visible that the extracted hadronization temperature is close to the phase transition temperature calculated for lattice QCD. It is argued that the system is *born into* equilibrium out from a partonic state [101]. It is furthermore supported by calculations showing that the time to reach an equilibrium in a pure hadronic medium, considering collision rates and time scales of the hadronic fireball expansion, is longer than the lifetime of the fireball [102].

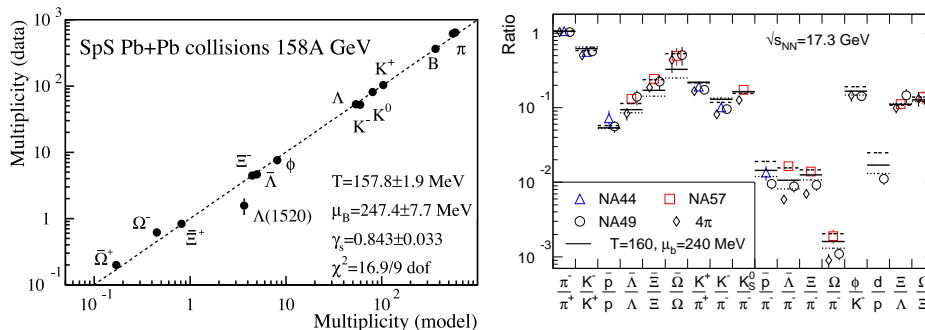


Figure 5.11.: The measured versus fitted yields [12] (left) and the fitted ratios of hadron yields at 158 A GeV [99] (right).

The problem with these models is that they do not describe the collision dynamics, i.e. how the system arrives into equilibrium. One explanation could be that the success of the statistical models can be understood as a result of *phase-space dominance* [103]. The other would be that it is not clear whether the success of the statistical models means that the system has been equilibrated via a thermodynamic process in the sense of Boltzmann. The statistical model fits work also remarkably well in the canonical formulation for particle ratios in p+p and $e^+ + e^-$ collisions [104]. It could mean that *statistical* does not always mean *thermodynamic* in the sense of matter in thermal equilibrium.

A statistical model predicts mean particle multiplicities, $\langle n_i \rangle$, of type i as:

$$\langle n_i \rangle = \frac{(2J_i + 1) V}{(2\pi)^3} \int d^3p \frac{1}{\gamma_s^{-S_i} \exp[(E_i - (\mu_B + \mu_S + \mu_Q))/T] \pm 1}. \quad (5.4)$$

For final particle numbers the contribution from decays of unstable resonances is included. The γ_s was introduced in order to account for a deviation of strangeness from chemical equilibrium (strangeness suppression factor), where γ_s can be between 0 and 1, and full strangeness equilibration is represented by $\gamma_s = 1$. This parameter is used in different statistical models [12, 99, 100].

5.3.5. Comparison to Models

The strange hadron yield enhancement is shown in figure 5.12. It is argued that strangeness enhancement may be explained by the different ways in which statistical model calculations have to be approached. For small systems, such as p+p, the canonical ensemble must be used. This means that the exact conservation of quantum numbers reduces the phase space available for particle production. The correlation volume V of the system created by collisions at constant $\sqrt{s_{NN}}$ is assumed to be proportional to $\langle N_W \rangle$: ($V = \frac{V_0}{2} \langle N_W \rangle$ in [79], where V_0 is the volume of the nucleon). However, when a comparison of the shape of the measured enhancement as a function of $\langle N_W \rangle$ to that predicted by the model assuming a linear dependence on $\langle N_W \rangle$ is made the measured functional form is not well represented. Furthermore the model underpredicts the measurements by NA49, NA57 and STAR. However, in the model the expected enhancement rapidly increases with the volume (N_W), and for the Λ and Ξ^- saturates for $N_W > 30$. Conversely, as shown in Figure 5.12, the data is not reproduced by the statistical model. A different approach to determine the correlation volume is the percolation model [80]. In this model the fireball volume is segmented into smaller sub-volumes (clusters). These clusters are formed when strings statistically overlap. While in smaller systems multiple clusters are formed in central Pb+Pb collisions a single cluster is formed. All clusters hadronize independently and the overall hadronization volume V_h is calculated as

$$V_h = A_c \frac{V_0}{\pi r_s^2} \quad (5.5)$$

Here A_c is the cluster size, V_0 the hadronization volume for p+p collisions and r_s the effective string radius. This segmentation leads to a smaller correlation volume for the onset of grand canonical strangeness production. The shape of strange meson production as a function of the system size and centrality is better described than in the simple model. For multistrange hyperons no predictions from this model are available. Both models have the assumption of an overall saturation of strangeness in common ($\gamma_s = 1$). On the other hand results from STAR [81] point to a strangeness undersaturation in small systems requiring a factor $\gamma_s < 1$. This could be one more important aspect to be considered in both models. Figure 5.13 shows the energy dependence for the

5. Discussion

midrapidity and total Ξ^- (Ξ^+) yields starting from AGS to RHIC energies. The results are compared to string-hadronic models [95, 94] and a statistical hadron gas model [12]. The midrapidity and total yields are clearly underpredicted by the string-hadronic model UrQMD.

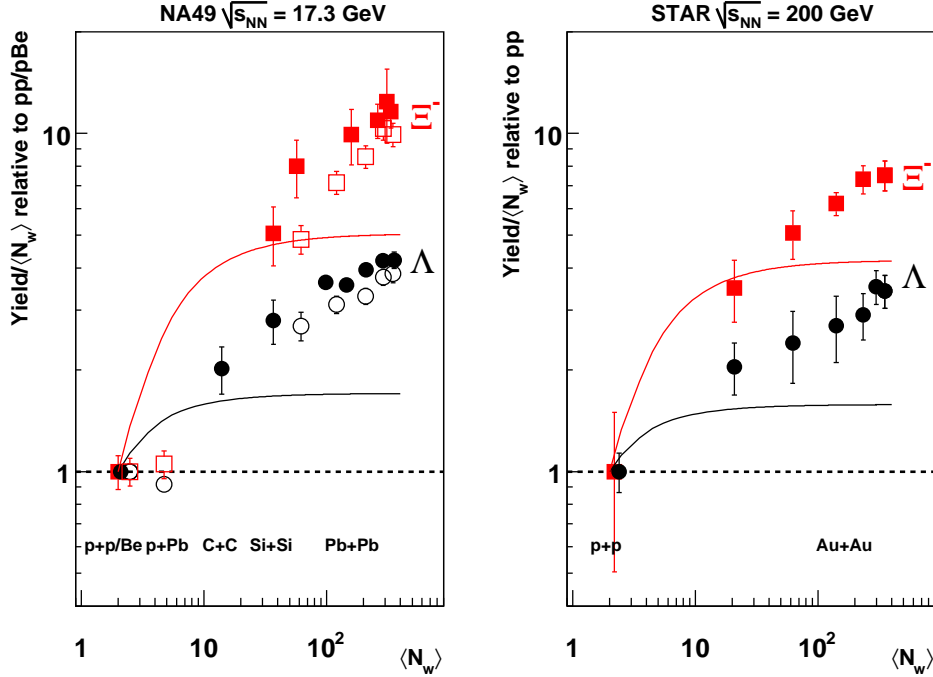


Figure 5.12.: Hyperon enhancement as a function of the number of wounded nucleons at $\sqrt{s_{NN}} = 17.3$ GeV (left) from NA49 (filled symbols), $\sqrt{s_{NN}} = 17.3$ GeV from NA57 (left, open symbols) and $\sqrt{s_{NN}} = 200$ GeV from STAR (right). The lines represent the corresponding calculations with the statistical model [79].

A better description is provided by RQMD version 2.3, including the color rope mechanism. On the other hand, the statistical hadron gas model which uses a grand canonical ensemble underpredicts the data as well but describes better the trend of the data. In this model, the chemical freeze-out temperature, the baryonic chemical potential are fitted to all yields of the measured hadrons. The hadron gas model (labeled A in Figure 5.13) introduces in addition a strangeness undersaturation parameter $\gamma_s =$ free in the fits, which have been performed at each energy separately. Figure 5.14 shows the energy dependence of the midrapidity and total Ξ^- (Ξ^+) yields from AGS to RHIC energies, normalized to midrapidity and total pion yields. The observed energy dependence is compared with predictions from the string-hadronic models [94, 95] and statistical hadron gas models [12, 100]. It is again visible that the string-hadronic model UrQMD underpredicts the measurements whereas RQMD version 2.3 provides a better description. The hadron gas model with $\gamma_s =$ free (labeled A in Figure 5.13)

underpredicts the data.

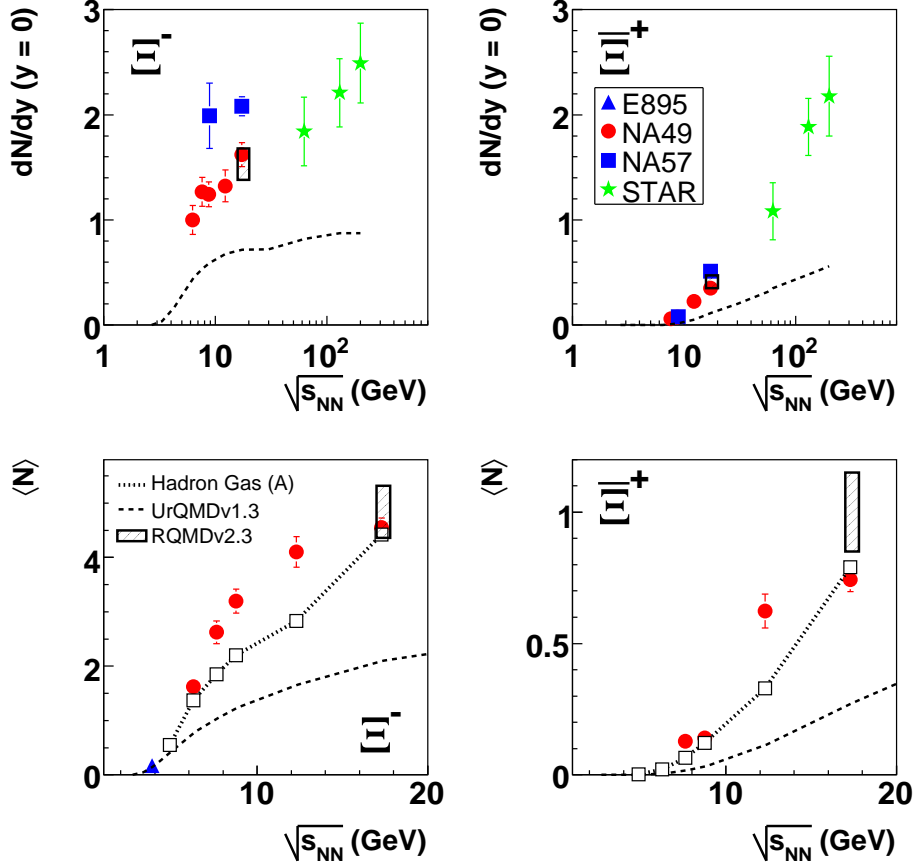


Figure 5.13.: The energy dependence of Ξ^- (top left) and Ξ^+ (top right) yields at midrapidity and of the total Ξ^- (bottom left) and Ξ^+ (bottom right) yields from AGS to RHIC energies. The data are compared to string-hadronic models [94, 95] and statistical hadron gas model [12].

On the other hand the hadron gas model which uses $\gamma_s = 1$ (labeled B in Figure 5.14) overpredicts the data. Another difference is that hadron gas model B is using a parametrization of T and μ_B as a function of energy. As mentioned above, hadron gas model B fits every energy separately and is not using a parametrization for T and μ_B as hadron gas model A. None of the two hadron gas models perfectly describe the Ξ^- and Ξ^+ results. It seems that the truth has to be somewhere in-between. One statement can be made about the string-hadronic model UrQMD (see subsection 5.3.3). This model fails to describe the data assuming a hadronic scenario. A better description of the data is presented by RQMD version 2.3 (see subsection 5.3.2) which includes the color rope mechanism. The open question is how to interpret the overlapping strings

5. Discussion

which form color ropes.

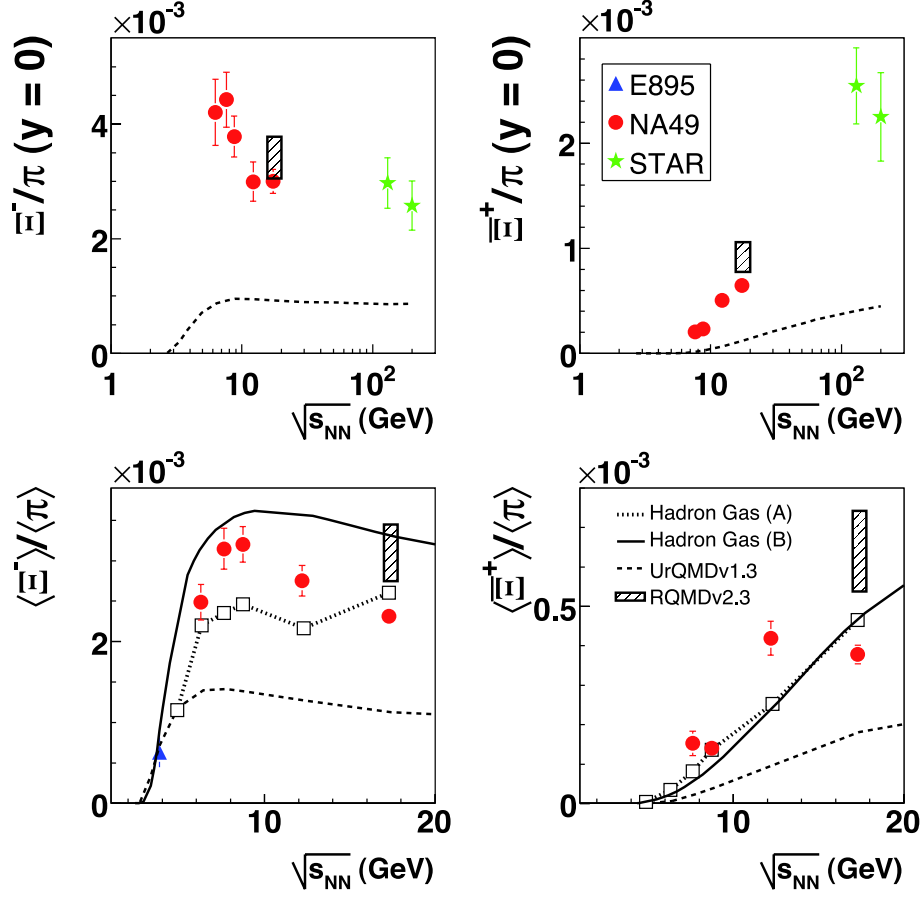


Figure 5.14.: The energy dependence of Ξ^- (top left) and Ξ^+ (top right) yields at midrapidity and of the total Ξ^- (bottom left) and Ξ^+ (bottom right) yields from AGS to RHIC energies, normalized to midrapidity and total pion yields ($\pi = 1.5 (\pi^+ + \pi^-)$ [82] – [85]). The data are compared to string-hadronic models [94, 95] and statistical hadron gas models [12, 100].

6. Summary and Conclusion

Results on Ξ^- and $\bar{\Xi}^+$ hyperon production in central Pb+Pb collisions at 20, 30, 40, 80 and 158 AGeV have been presented. Furthermore, the centrality dependence of Ξ^- production in minimum bias Pb+Pb collisions at 40 and 158 AGeV was studied. For the first time Ξ^- at 158 AGeV in semi-central Si+Si interactions were measured. All measurements were performed with the NA49 detector at the CERN SPS.

Ξ^- and $\bar{\Xi}^+$ candidates were identified via the decay channel $\Xi^- \rightarrow \Lambda + \pi^-$ ($\bar{\Xi}^+ \rightarrow \bar{\Lambda} + \pi^+$). The Λ vertex is identified by selecting positive and negative tracks that are consistent with an origin at the decay of a hyperon some distance from the primary collision point. The secondary vertex of the decay is located in a similar way by combining the previously identified Λ with a charged particle. The typical mass resolution, as obtained from a fit with a Gaussian is $\sigma_m = 4 \text{ GeV}/c^2$. The acceptance and efficiency were calculated in bins of p_t and y . The total efficiency at 158 AGeV is $\approx 1\%$, whereas it increases at 20 AGeV to $\approx 2\%$.

Results on transverse mass spectra of Ξ^- (left) and $\bar{\Xi}^+$ (right) integrated over the rapidity range $-0.5 < y < +0.5$ in central Pb+Pb collisions from 20 – 158 AGeV are obtained. The shape of the spectra is approximately exponential in $m_t - m_0$. No centrality dependence of the inverse slope is visible. At 158 AGeV the inverse slope is increasing from light systems and stays constant for minimum bias Pb+Pb collisions. A clear centrality dependence is visible for the Ξ^- midrapidity yields at 40 and 158 AGeV which is shown in Figure 4.3.

The NA49 experiment features a large acceptance in the forward hemisphere allowing for measurements of Ξ^- and $\bar{\Xi}^+$ rapidity spectra. The rapidity spectra are well described by the sum of two Gaussians at all energies. For the first time the total multiplicity of $\langle \Xi^- \rangle$ and $\langle \bar{\Xi}^+ \rangle$ was measured in central Pb+Pb reactions. Due to limited statistics no rapidity spectra could be measured for the minimum bias Pb+Pb data sets at 40 and 158 AGeV as well as for the semi-central Si+Si data set at 158 AGeV.

Measurements on Ξ^- and $\bar{\Xi}^+$ production at 40 and 158 AGeV exists also from the NA57 collaboration. A discrepancy is observed between the results measured in this thesis and the ones from NA57. The difference of 67% is visible for Ξ^- (2.6 standard deviations) and 14% for $\bar{\Xi}^+$ (0.3 standard deviations) at 40 AGeV. At 158 AGeV the discrepancy for Ξ^- is about 33% (5.8 standard deviations) and 55% (4.5 standard deviations) for $\bar{\Xi}^+$. A deviation is also visible in the centrality dependence of the midrapidity yields at 40 and 158 AGeV.

6. Summary and Conclusion

To make an overall conclusion the results in this thesis are compared to results at higher and lower energies. For lower energies, results from the E895 collaboration and at higher energies measurements from the STAR collaboration are used. The inverse slope parameter T and the mean transverse mass $\langle m_t \rangle - m_0$ for Ξ^- and $\bar{\Xi}^+$ stay at an approximately constant value through the SPS energy range and ends up slightly higher at RHIC energy. Similar behavior is seen for pions, kaons and protons. The inverse slope parameter of the measured hadrons can also be used to indicate the existence of radial flow in the collision. The inverse slope parameter as a function of the particle mass is approximately constant for $m > 0.5$ GeV. The difference between the inverse slope parameter measured in p+p interactions and Pb+Pb collisions results from the collective expansion which occurs in Pb+Pb collisions. However, the same trend is also visible for heavier strange baryons like the Ξ and Ω . It is assumed that multi-strange and heavy flavored hadrons are freezing out earlier than lighter quark particles and their collective motion can only be developed at the pre-hadronic stage, i.e. partonic stage for these hadrons.

The study of strangeness is motivated by its role as a signature for the Quark Gluon Plasma. Any enhancement in the yield must be with respect to a 'normal' yield, where a QGP is not formed. This is usually taken to mean suitably scaled p+p collisions, where the volume of the system created is too small for a QGP to occur. The results at SPS and RHIC energies show an enhancement, with the doubly strange Ξ^- being enhanced more than the Λ , in accordance with the original prediction. However, the enhancement decreases with increasing $\sqrt{s_{NN}}$, which is similar to the K^+/π^+ ratio.

The midrapidity and total Ξ^- and $\bar{\Xi}^+$ yields increases with the collision energy from AGS to RHIC energies (see Figure 5.7). A monotonic increase with the collision energy of the $\langle \Xi^+ \rangle / \langle \pi \rangle$ and Ξ^+/π ratio is visible. The $\langle \Xi^- \rangle / \langle \pi \rangle$ and Ξ^-/π ratio shows a steep rise from AGS energies, a maximum around the lowest SPS energy and a decrease to top SPS energy (see Figure 5.8). The measurement at RHIC indicates that the $\langle \Xi^- \rangle / \langle \pi \rangle$ and Ξ^-/π ratio stays nearly constant from the top SPS energy.

The antibaryon over baryon ratios are enhanced at RHIC energies over the SPS results, indicating the approach to zero net baryon density at midrapidity for higher energy collisions. At lower energies the ratio is not one due to the fact that the net baryon density at midrapidity is a strong function of the beam energy, the antibaryon to baryon ratio strongly depends on the number of valence up and down quarks in the hadron.

The measured results are also compared to published model predictions. The strange hadron yield enhancement is compared to statistical model calculations which is shown in Figure 5.12. The measured form of the enhancement is not well represented by the statistical model. Furthermore the model underpredicts the measurements done by the NA49, NA57 and STAR collaborations. A different approach to explain the enhancement is the percolation model. This model describes the shape of strange meson production as a function of the system size and centrality better than the simple statistical model. At the moment

no predictions are made for multistrange hyperons. One possible improvement for both models would be to drop the assumption of an overall saturation of strangeness (corresponding to $\gamma_s = 1$). The STAR collaboration showed results that the strangeness undersaturation factor for small systems is < 1 . Figure 5.13 shows the energy dependence of midrapidity and total Ξ^- and Ξ^+ yields compared to string-hadronic models (RQMDv2.3, UrQMDv1.3) and to a statistical hadron gas model (γ_s free). The UrQMD model does not follow the trend and clearly underpredicts the data whereas RQMD with the color rope mechanism gives a good description of the data. The statistical hadron gas model provides a qualitative description of the measurements. The $\langle \Xi^- \rangle / \langle \pi \rangle$ (Ξ^-/π) and $\langle \Xi^+ \rangle / \langle \pi \rangle$ (Ξ^+/π) ratios are compared to string-hadronic models (RQMD, UrQMD) and statistical hadron gas models (see Figure 5.14). Again the UrQMD model underpredicts the measurements. A better description is provided by the RQMD model with the color rope mechanism. The statistical hadron gas model with $\gamma_s = \text{free}$ underestimates the ratio whereas the model with $\gamma_s = 1$ overpredicts the data. None of the used model predictions includes a phase transition. One open issue is how to interpret the overlapping strings in the RQMD model. A possible interpretation could be that the strings may evolve to the QGP via the percolation process. However, it is not clear how the percolation can be incorporated into a more general picture of string interaction (and fusion), and why it does not lead to a phase transition. A phase transition is included in the model of the early stage of A+A collisions. In this model, a transition to a deconfined state of matter may cause anomalies in the energy dependence of pion and strangeness production. This non-monotonic structure is observed in the energy dependence of the inverse slope parameter and $\langle m_t \rangle - m_0$ as well as in the energy dependence of the Ξ^-/π ratio. It seems that the phase transition is located at SPS energies.

6. *Summary and Conclusion*

A. Relativistic Kinematics and Lorentz-Transformation

A.1. Four Vector and Lorentz Transformation

The space-time coordinates of a point x are denoted by a contravariant vector with components x^μ :

$$x^\mu = \begin{pmatrix} x^0 \\ x^1 \\ x^2 \\ x^3 \end{pmatrix} = \begin{pmatrix} t \\ \vec{x} \end{pmatrix} = \begin{pmatrix} t \\ x \\ y \\ z \end{pmatrix}. \quad (\text{A.1})$$

The momentum-energy coordinate p is also denoted by a contravariant vector with components p^μ :

$$p^\mu = \begin{pmatrix} p^0 \\ p^1 \\ p^2 \\ p^3 \end{pmatrix} = \begin{pmatrix} E \\ \vec{p} \end{pmatrix} = \begin{pmatrix} E \\ \vec{p}_t \\ \vec{p}_z \end{pmatrix} = \begin{pmatrix} E \\ p_x \\ p_y \\ p_z \end{pmatrix}. \quad (\text{A.2})$$

The natural units $c = \hbar = 1$ are used. Thereby the equations can be written in a covariant form.

In any coordinate system Σ_i the momentum square is a conserved quantity, namely the mass of the particle:

$$p_\mu \cdot p^\mu = E^2 - |\vec{p}|^2 = m^2. \quad (\text{A.3})$$

A particle with the velocity β moving against the frame Σ in the z -direction of the moving coordinate system Σ' can be described with the four momentum $p'_\mu = (E', \vec{p}')$. With the Lorentz-Transformation of the inertial system Σ in an moving system Σ' takes place as:

$$\begin{pmatrix} E' \\ p'_z \end{pmatrix} = \begin{pmatrix} \gamma & -\gamma\beta \\ -\gamma\beta & \gamma \end{pmatrix} z \quad (\text{A.4})$$

with $\beta = \frac{v_z}{c}$, $\gamma = \frac{E}{m}$, $\gamma = \frac{1}{\sqrt{1-\beta^2}}$.

A.2. Rapidity and Transverse Momentum

Other useful variables used commonly to describe the kinematic condition of a particle is the rapidity variable y and the transverse momentum p_t . The rapidity of a particle is defined in terms of its energy-momentum components E and p_z :

$$y = \frac{1}{2} \ln \left(\frac{E + p_z}{E - p_z} \right). \quad (\text{A.5})$$

The transverse momentum is denoted as:

$$p_t = \sqrt{p_x^2 + p_y^2}. \quad (\text{A.6})$$

The transverse mass is Lorentz-invariant, whereas the rapidity is shifted linearly at the Lorentz-transformation:

$$y' = y + y_0. \quad (\text{A.7})$$

A.3. Pseudorapidity

To characterize the rapidity of a particle, it is necessary to measure two quantities of the particle, such as its energy and its longitudinal momentum. In many experiments, it is only possible to measure the angle of the detected particle relative to the beam axis. In that case, it is convenient to utilize this information by using the pseudorapidity variable η to characterize the detected particle. The pseudorapidity is defined as:

$$\eta = -\ln[\tan(\theta/2)], \quad (\text{A.8})$$

where θ is the angle between the particle momentum \vec{p} and the beam axis. In terms of the momentum, the pseudorapidity can be written as:

$$\eta = \frac{1}{2} \ln \left(\frac{|\vec{p}| + p_z}{|\vec{p}| - p_z} \right). \quad (\text{A.9})$$

By comparing equation A.5 and A.9, it is easy to see that the pseudorapidity coincides with the rapidity when the momentum is large, that is, when $|\vec{p}| \approx E$. We consider the change of variables from (y, \vec{p}_t) to (η, \vec{p}_t) . It is easy to express y as a function of η . From the definition of η , we have:

$$e^\eta = \sqrt{\frac{|\vec{p}| + p_z}{|\vec{p}| - p_z}}, \quad (\text{A.10})$$

$$e^{-\eta} = \sqrt{\frac{|\vec{p}| - p_z}{|\vec{p}| + p_z}}. \quad (\text{A.11})$$

Adding equation A.10 and A.11, we obtain the relation:

$$|\vec{p}| = p_t \cosh \eta. \quad (\text{A.12})$$

where p_t is the transverse momentum (see section A.2). Subtracting equation A.11 from A.10, we obtain:

$$p_z = p_t \sinh \eta. \quad (\text{A.13})$$

Using these results, we can express the rapidity in terms of the pseudorapidity as:

$$y = \frac{1}{2} \ln \left[\frac{\sqrt{p_t^2 \cosh^2 \eta + m^2} + p_t \sinh \eta}{\sqrt{p_t^2 \cosh^2 \eta + m^2} - p_t \sinh \eta} \right], \quad (\text{A.14})$$

where m is the rest mass of the particle. Conversely, the pseudorapidity can be expressed in terms of the rapidity by:

$$\eta = \frac{1}{2} \ln \left[\frac{\sqrt{m_t^2 \cosh^2 y - m^2} + m_t \sinh y}{\sqrt{m_t^2 \cosh^2 y - m^2} - m_t \sinh y} \right]. \quad (\text{A.15})$$

If the particle have a distribution $dN/dydp_t^{\vec{}}$ in terms of the rapidity, then the distribution in the pseudorapidity is:

$$\frac{dN}{d\eta d\vec{p}_t} = \sqrt{1 - \frac{m^2}{m_t^2 \cosh^2 y}} \frac{dN}{dy d\vec{p}_t}. \quad (\text{A.16})$$

In many experiments, only the pseudorapidity of the detected particle is measured to give $dN/d\eta$, which is the integral of $dN/d\eta d\vec{p}_t^{\vec{}}$ with respect to the transverse momentum. One can compare this quantity with dN/dy , which is the integral of $dN/dy d\vec{p}_t^{\vec{}}$ with respect to the transverse momentum. From equation A.16, we can infer that in the region of y much greater than zero, $dN/d\eta$ and dN/dy are approximately the same, but in the region of y close to zero, there is a small depression of the $dN/d\eta$ distribution relative to dN/dy due to the above transformation A.16. In experiments at high energies where dN/dy has a plateau shape, this transformation gives a small dip in $dN/d\eta$ around $\eta \approx 0$.

A. *Relativistic Kinematics and Lorentz-Transformation*

A.4. Center of Mass Energy

The center of mass energy $\sqrt{s_{\text{NN}}}$, or shortly \sqrt{s} , is the available energy per colliding nucleon pair. For a fixed-target experiment it is defined as the following as:

$$\sqrt{s_{\text{NN}}} = \sqrt{2 \cdot m_0^2 + 2 \cdot m_0 \cdot E_{\text{Proj}}}, \quad (\text{A.17})$$

where m_0 is the rest mass of the nuclei ($m_{\text{N}} = 938.27 \text{ MeV}/c^2$) and E_{Proj} the energy of the projectile. It is also possible to express $\sqrt{s_{\text{NN}}}$ by $E_{\text{Proj}} = E_{\text{kin}} + m_{\text{N}}$ (where E_{kin} is the kinetic energy):

$$\sqrt{s} = \sqrt{2 \cdot m_0} \sqrt{2 \cdot m_0 + E_{\text{kin}}}. \quad (\text{A.18})$$

Table A.1 shows the converted values of the kinematical quantities.

E_{kin} (GeV)	p_{Lab} (GeV/c)	\sqrt{s} (GeV)	y_{mid}
1.06	1.76	2.35	0.69
1.96	2.74	2.68	0.90
4.00	4.85	3.32	1.17
5.93	6.80	3.83	1.34
7.94	8.83	4.29	1.47
10.74	11.6	4.87	1.61
11.2	12.1	4.96	1.63
14.6	15.5	5.56	1.73
19.8	20	6.27	1.88
29.1	30	7.62	2.08
38.7	39.6	8.73	2.22
78.3	79.2	12.3	2.56
157.5	158.4	17.3	2.91
199.2	200	19.4	3.03

Table A.1.: Kinematical quantities.

B. Eventcuts

B.1. Central Pb+Pb

Cut	Removed Events [%]
$vertex.i\,flag = 0$	0.29
$-0.09 < x_{BPD} - x_{Fit} < 0.12$	0.15
$-0.065 < y_{BPD} - y_{Fit} < 0.08$	0.16
$-581.85 < z_{Fit} < -580.72$	0.10
Total	0.70

Table B.1.: The event cuts and the fraction of events failing the cut if applied separately for the 30 AGeV central Pb+Pb data set.

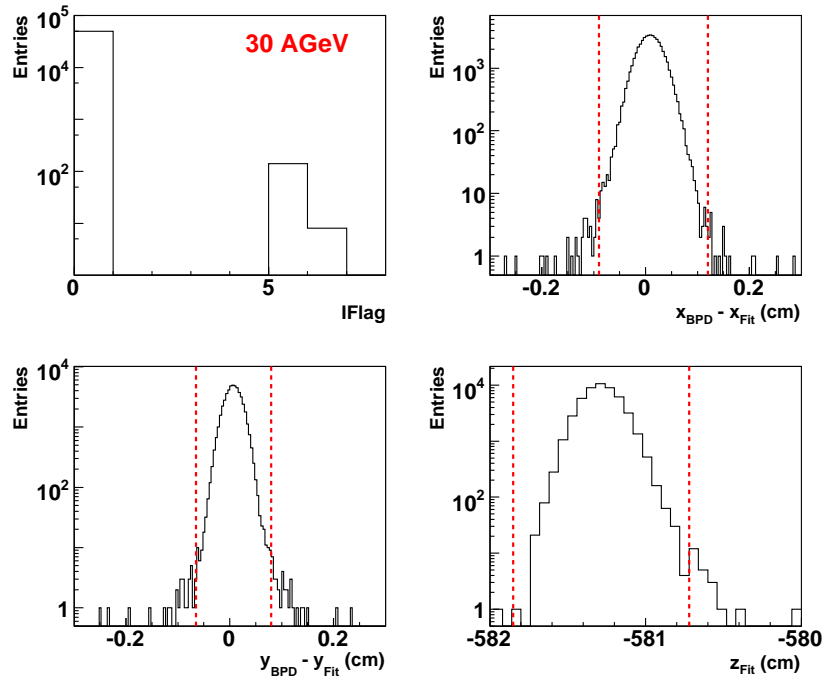


Figure B.1.: The event properties for the 30 AGeV central Pb+Pb data set. Dashed lines indicate the values of the event cuts.

B. Eventcuts

Cut	Removed Events [%]
$vertex.iflag = 0$	0.35
$-0.08 < x_{\text{BPD}} - x_{\text{Fit}} < 0.1$	0.04
$-0.082 < y_{\text{BPD}} - y_{\text{Fit}} < 0.041$	0.26
$-581.5 < z_{\text{Fit}} < -580.6$	0.04
Total	0.70

Table B.2.: The event cuts and the fraction of events failing the cut if applied separately for the 40 AGeV central Pb+Pb (std-) data set.

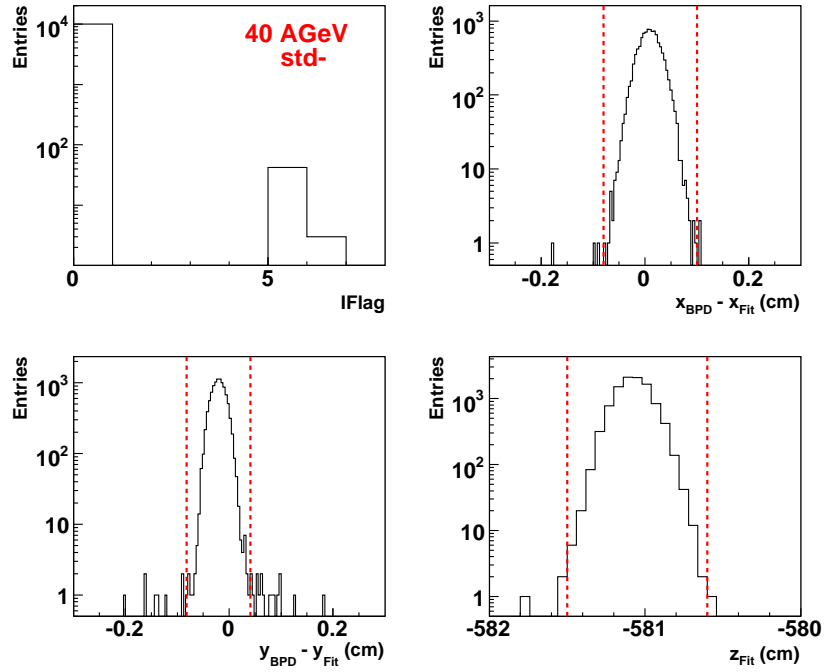


Figure B.2.: The event properties for the 40 AGeV central Pb+Pb data set (std-). Dashed lines indicate the values of the event cuts.

Cut	Removed Events [%]
$vertex.i\,flag = 0$	0.30
$-0.1 < x_{\text{BPD}} - x_{\text{Fit}} < 0.08$	0.03
$-0.06 < y_{\text{BPD}} - y_{\text{Fit}} < 0.041$	0.47
$-581.5 < z_{\text{Fit}} < -580.65$	0.07
Total	0.88

Table B.3.: The event cuts and the fraction of events failing the cut if applied separately for the 40 AGeV central Pb+Pb (std+) data set.

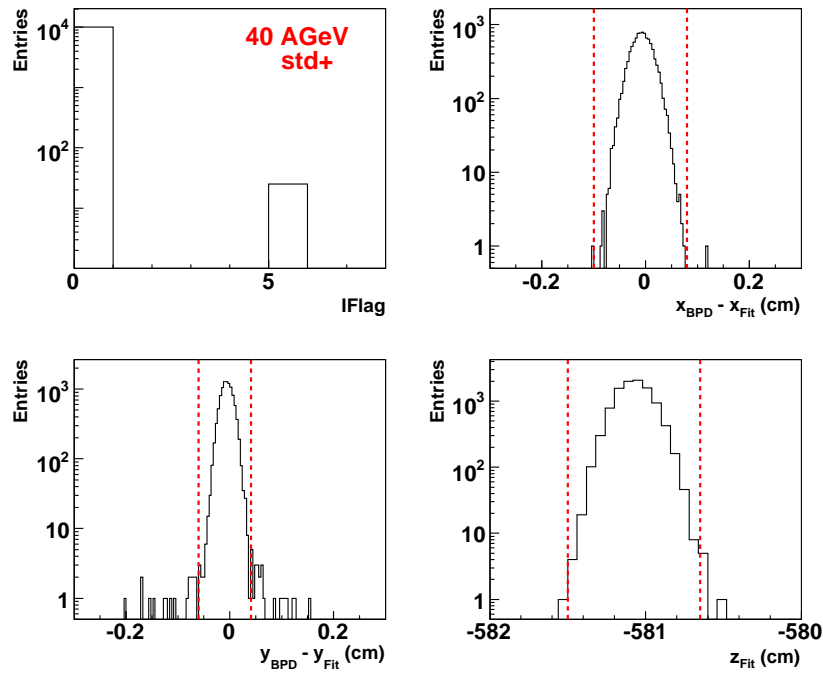


Figure B.3.: The event properties for the 40 AGeV central Pb+Pb data set (std+). Dashed lines indicate the values of the event cuts.

B. Eventcuts

Cut	Removed Events [%]
$vertex.iflag = 0$	0.42
$-0.12 < x_{\text{BPD}} - x_{\text{Fit}} < 0.06$	0.13
$-0.08 < y_{\text{BPD}} - y_{\text{Fit}} < 0.04$	0.31
$-581.8 < z_{\text{Fit}} < -580.6$	0.33
Total	1.19

Table B.4.: The event cuts and the fraction of events failing the cut if applied separately for the 80 AGeV central Pb+Pb data set.

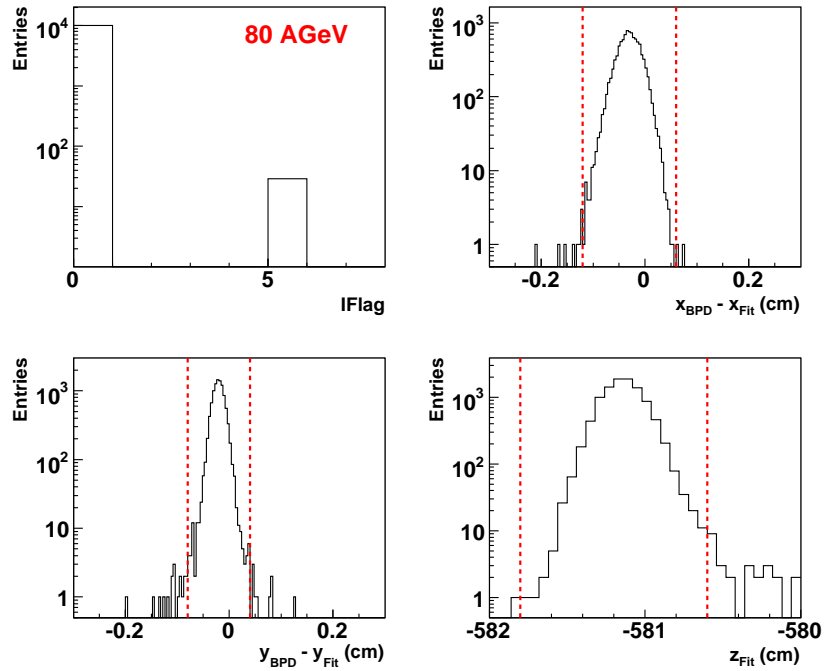


Figure B.4.: The event properties for the 80 AGeV central Pb+Pb data set. Dashed lines indicate the values of the event cuts.

Cut	Removed Events [%]
$vertex.i\text{flag} = 0$	0.54
$-0.1 < x_{\text{Fit}} < 0.16$	0.23
$-0.14 < y_{\text{Fit}} < 0.27$	0.13
$-581.74 < z_{\text{Fit}} < -580.36$	0.50
Total	1.4

Table B.5.: The event cuts and the fraction of events failing the cut if applied separately for the 158 AGeV central Pb+Pb data set.

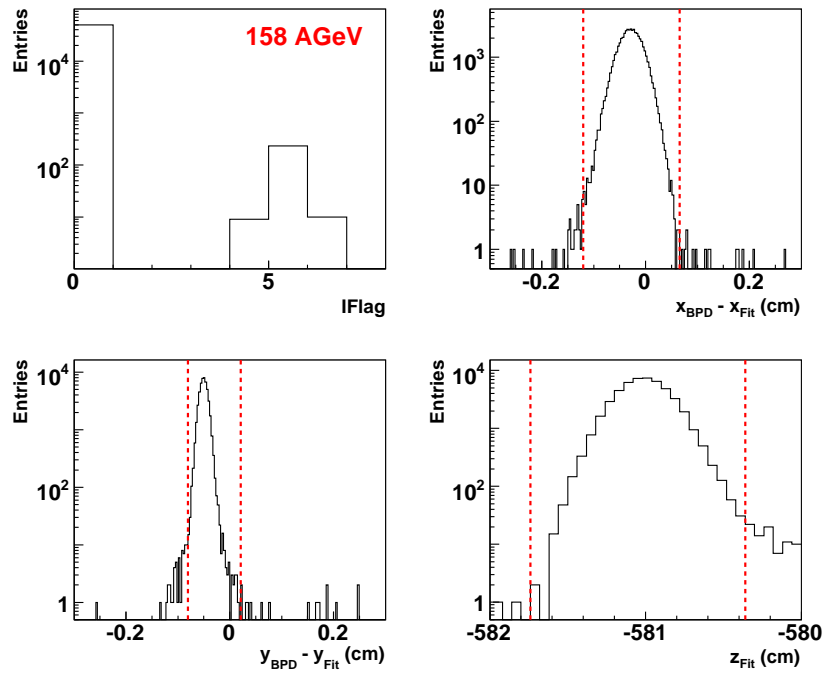


Figure B.5.: The event properties for the 158 AGeV central Pb+Pb data set. Dashed lines indicate the values of the event cuts.

B. Eventcuts

B.2. Minimum Bias Pb+Pb

Cut	Removed Events [%]
$vertex.iflag = 0$	0.56
$-0.285 < x_{Fit} < 0.27$	0.44
$-0.60 < y_{Fit} < 0.60$	0.07
$-581.7 < z_{Fit} < -580.63$	45.7
Multiplicity cut	3.21
Total	49.98

Table B.6.: The event cuts and the fraction of events failing the cut if applied separately for the 40 AGeV (std+) minimum bias Pb+Pb data set.

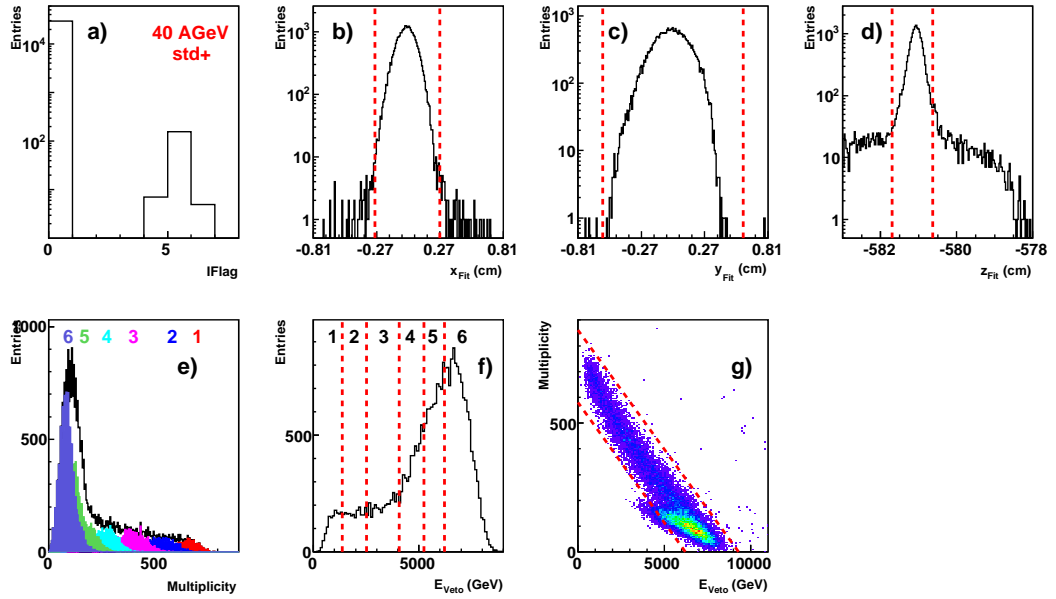


Figure B.6.: The event properties for the 40 AGeV (std+) minimum bias Pb+Pb data set: a) $vertex.iflag$, b) x_{Fit} position, c) y_{Fit} position, d) z_{Fit} position, e) Multiplicity distribution, f) E_{Veto} energy and g) Multiplicity vs. E_{Veto} . Dashed lines indicate the values of the event cuts.

B.2. Minimum Bias Pb+Pb

Cut	Removed Events [%]
$vertex.iflag = 0$	0.56
$-0.15 < x_{Fit} < 0.16$	0.22
$-0.20 < y_{Fit} < 0.18$	0.31
$-581.1 < z_{Fit} < -579.7$	40.6
Multiplicity cut	0.28
Total	41.97

Table B.7.: The event cuts and the fraction of events failing the cut if applied separately for the 158 AGeV (Run 4016 - 4019) minimum bias Pb+Pb data set.

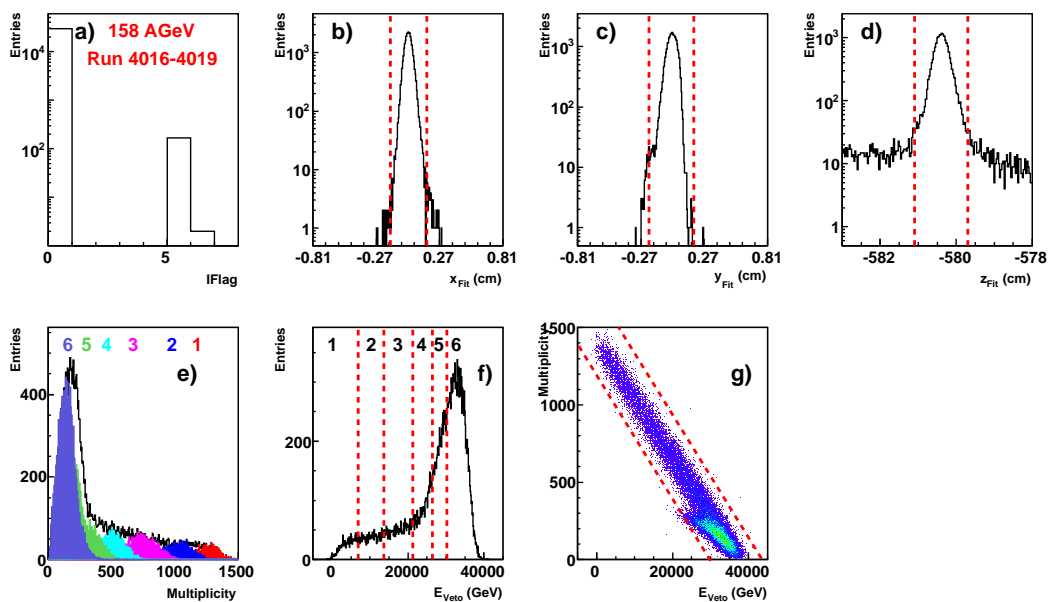


Figure B.7.: The event properties for the 158 AGeV (Run 4016 - 4019) minimum bias Pb+Pb data set: a) $vertex.iflag$, b) x_{Fit} position, c) y_{Fit} position, d) z_{Fit} position, e) Multiplicity distribution, f) E_{Veto} energy and g) Multiplicity vs. E_{Veto} . Dashed lines indicate the values of the event cuts.

B. Eventcuts

Cut	Removed Events [%]
$vertex.iflag = 0$	0.71
$-0.125 < x_{Fit} < 0.16$	0.77
$-0.16 < y_{Fit} < 0.14$	2.12
$-581.9 < z_{Fit} < -580.5$	44.64
Multiplicity cut	0.42
Total	48.66

Table B.8.: The event cuts and the fraction of events failing the cut if applied separately for the 158 AGeV (Run 4078 - 4102) minimum bias Pb+Pb data set.

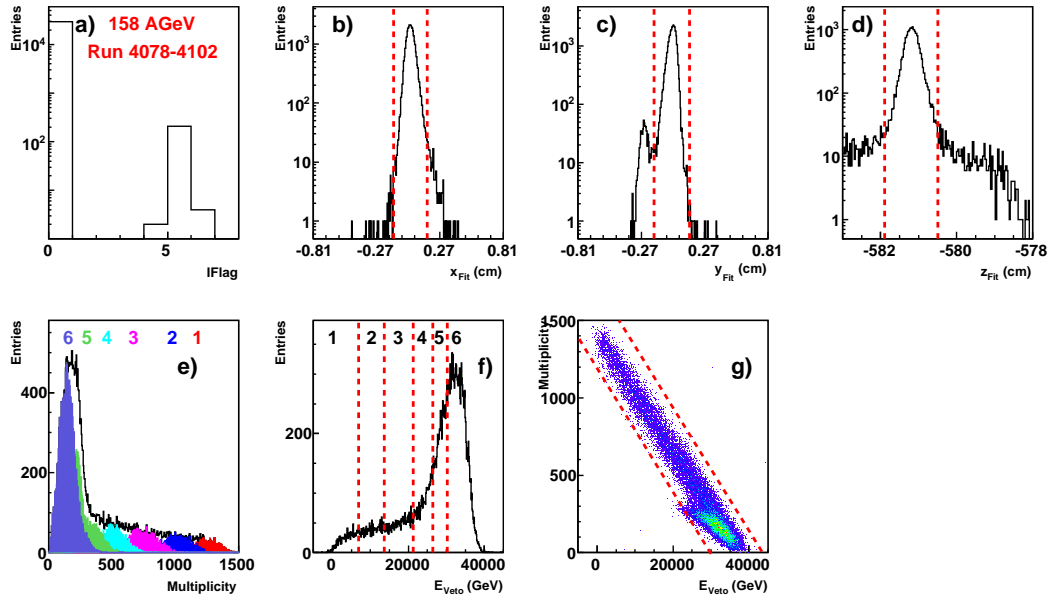


Figure B.8.: The event properties for the 158 AGeV (Run 4078 - 4102) minimum bias Pb+Pb data set: a) $vertex.iflag$, b) x_{Fit} position, c) y_{Fit} position, d) z_{Fit} position, e) Multiplicity distribution, f) E_{Veto} energy and g) Multiplicity vs. E_{Veto} . Dashed lines indicate the values of the event cuts.

C. Invariant Mass Distribution and Efficiency

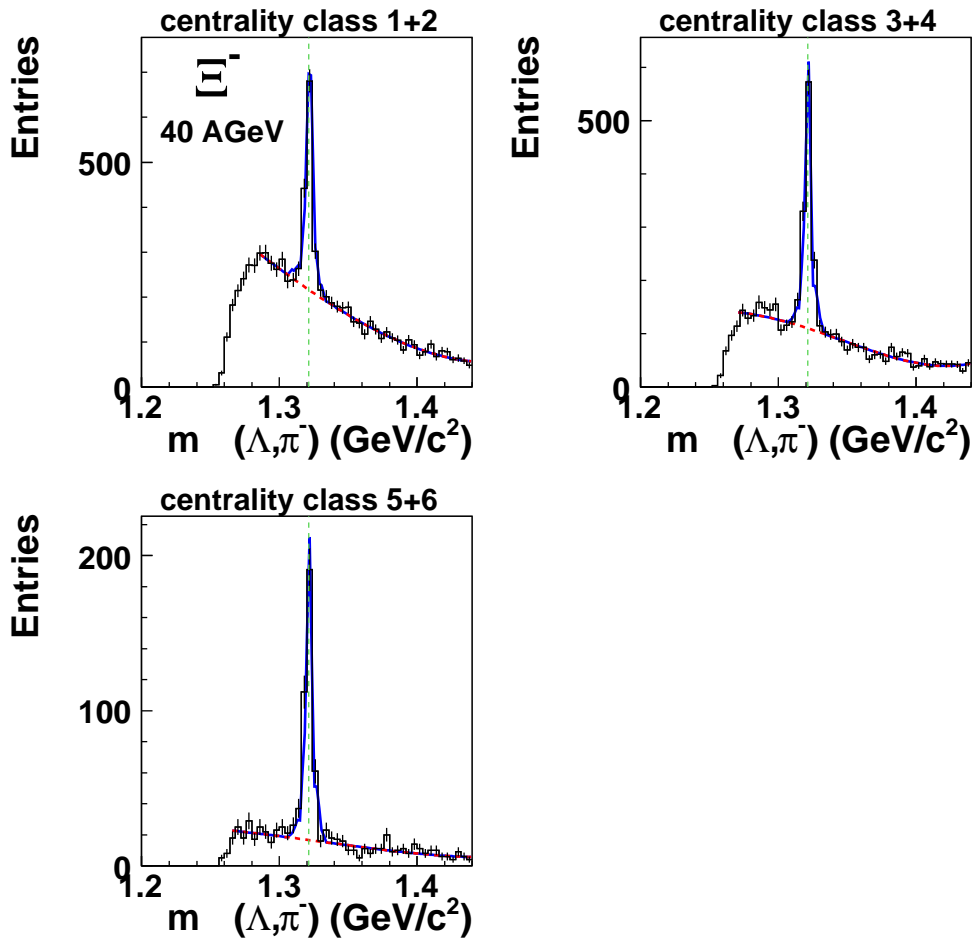


Figure C.1.: The invariant mass distribution of Ξ^- candidates ($-0.5 < y < 0.5$, $p_t = 0.6 - 2.1 \text{ GeV}/c$) in minimum bias Pb+Pb collisions at 40 AGeV. The full curves (blue) represent a fit to signal and background described in the text. The dashed curves show the background (red) contribution. The vertical lines represent the mass position from the Particle Physics Book [5].

C. Invariant Mass Distribution and Efficiency

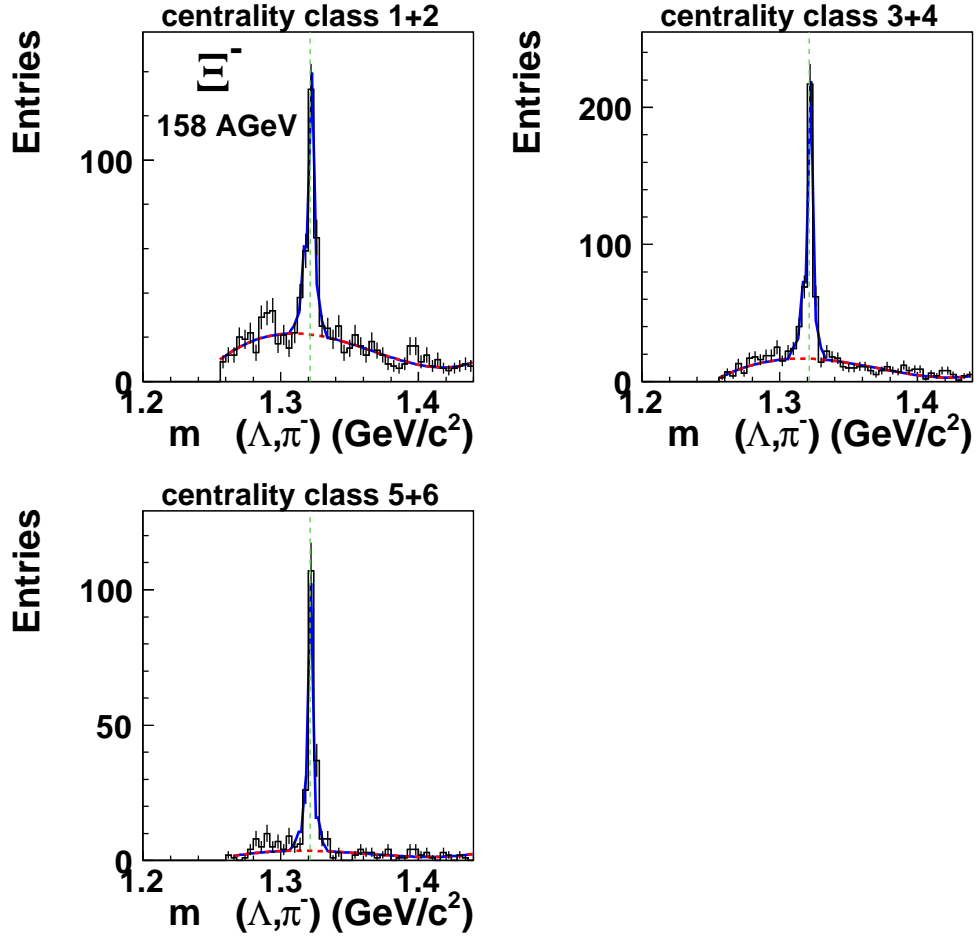


Figure C.2.: The invariant mass distribution of Ξ^- candidates ($-0.5 < y < 0.5$, $p_t = 0.6 - 2.1 \text{ GeV}/c$) in minimum bias Pb+Pb collisions at 158 AGeV. The full curves (blue) represent a fit to signal and background described in the text. The dashed curves show the background (red) contribution. The vertical lines represent the mass position from the Particle Physics Book [5].

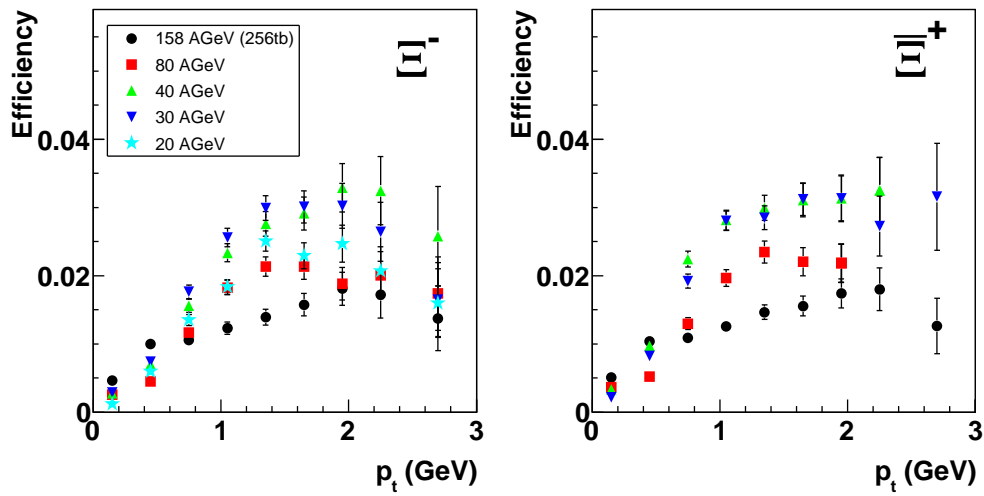


Figure C.3.: p_t dependence of the total efficiency (geometrical acceptance and reconstruction efficiency) for Ξ^- (left) and Ξ^+ (right) at midrapidity ($|y| \leq 0.5$) in central Pb+Pb collisions from 20 – 158 AGeV.

C. Invariant Mass Distribution and Efficiency

D. Invariant Mass Distribution for p_t and $m_t - m_0$ Spectra and Numerical Values

D.1. Central Pb+Pb

p_t (GeV)	dN/dp_t	stat. error	sys. error
0.4572	0.6407	0.1516	0.0705
0.7455	0.7885	0.0851	0.0867
1.0388	0.6933	0.0626	0.0762
1.3345	0.3542	0.0343	0.0390
1.6316	0.1718	0.0246	0.0189
1.9296	0.0624	0.0135	0.0069

Table D.1.: Numerical values for the 20 AGeV central Pb+Pb $\Xi^- p_t$ spectra.

$m_t - m_0$ (GeV/ c^2)	$1/m_t dN/dm_t$	stat. error	sys. error
0.0769	1.4011	0.3316	0.1541
0.1958	1.0577	0.1141	0.1163
0.3595	0.6674	0.0603	0.0734
0.5567	0.2654	0.0257	0.0292
0.7782	0.1053	0.0151	0.0116
1.0173	0.0323	0.0070	0.0036

Table D.2.: Numerical values for the 20 AGeV central Pb+Pb $\Xi^- m_t - m_0$ spectra.

D. Invariant Mass Distribution for p_t and $m_t - m_0$ Spectra and Numerical Values

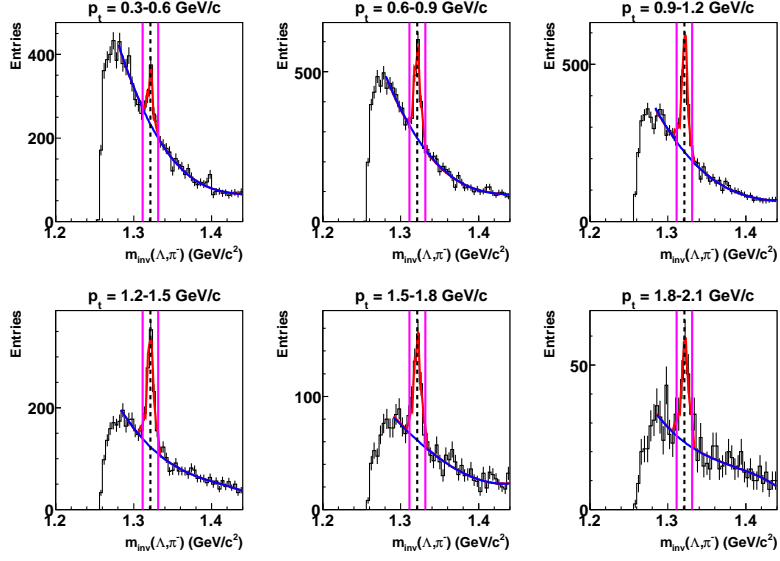


Figure D.1.: Invariant mass distribution of Ξ^- candidate at midrapidity ($|y| \leq 0.5$) in different p_t bins in central Pb+Pb collisions at 20 AGeV. A black dotted line indicates the nominal mass and the vertical purple lines show the integrated mass window (20 MeV).

p_t (GeV)	dN/dp_t	stat. error	sys. error
0.4571	0.8939	0.1451	0.0983
0.7452	1.0875	0.0884	0.1196
1.0385	0.7432	0.0561	0.0818
1.3342	0.4030	0.0361	0.0443
1.6312	0.2205	0.0255	0.0243
2.0706	0.0490	0.0087	0.0054

Table D.3.: Numerical values for the 30 AGeV central Pb+Pb Ξ^- p_t spectra.

$m_t - m_0$ (GeV/c ²)	$1/m_t dN/dm_t$	stat. error	sys. error
0.0768	1.9558	0.3175	0.2151
0.1957	1.4593	0.1186	0.1605
0.3593	0.7156	0.0540	0.0787
0.5564	0.3021	0.0270	0.0332
0.7779	0.1352	0.0156	0.0149
1.1350	0.0237	0.0042	0.0026

Table D.4.: Numerical values for the 30 AGeV central Pb+Pb Ξ^- $m_t - m_0$ spectra.

D.1. Central Pb+Pb

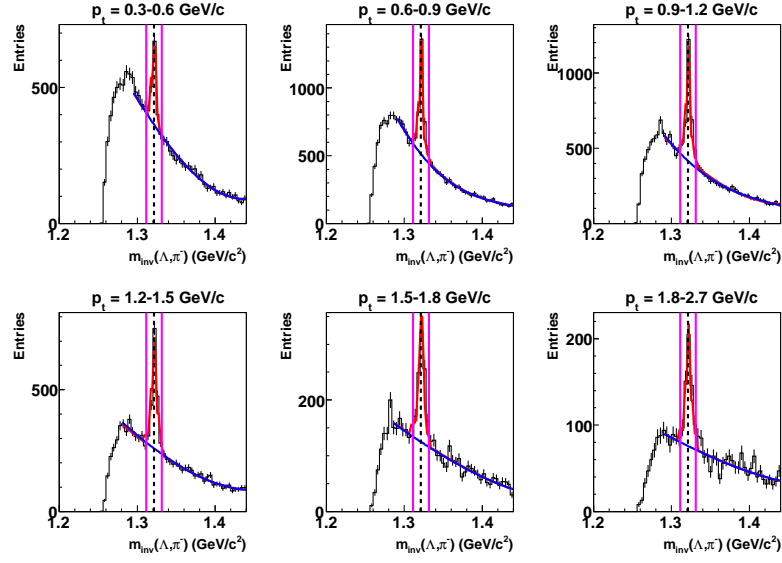


Figure D.2.: Invariant mass distribution of Ξ^- candidates at midrapidity ($|y| \leq 0.5$) in different p_t bins in central Pb+Pb collisions at 30 AGeV. A black dotted line indicates the nominal mass and the vertical purple lines show the integrated mass window (20 MeV).

p_t (GeV)	dN/dp_t	stat. error	sys. error
0.7461	0.0485	0.0111	0.0053
1.0397	0.0298	0.0062	0.0033
1.3355	0.0224	0.0047	0.0025
1.6327	0.0120	0.0032	0.0013

Table D.5.: Numerical values for the 30 AGeV central Pb+Pb Ξ^+ p_t spectra.

$m_t - m_0$ (GeV/c ²)	$1/m_t dN/dm_t$	stat. error	sys. error
0.1961	0.0650	0.0149	0.0072
0.3600	0.0287	0.0060	0.0032
0.5574	0.0167	0.0035	0.0018
0.7790	0.0074	0.0020	0.0008

Table D.6.: Numerical values for the 30 AGeV central Pb+Pb Ξ^+ $m_t - m_0$ spectra.

D. Invariant Mass Distribution for p_t and $m_t - m_0$ Spectra and Numerical Values

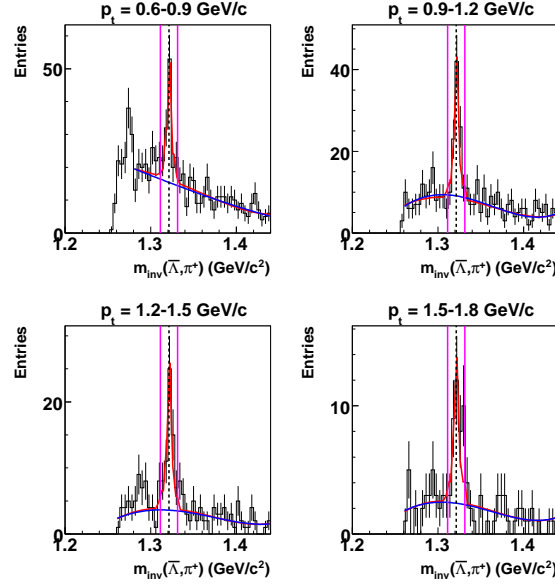


Figure D.3.: Invariant mass distribution of Ξ^+ at midrapidity ($|y| \leq 0.5$) in different p_t bins in central Pb+Pb collisions at 30 AGeV. A black dotted line indicates the nominal mass and the vertical purple lines show the integrated mass window (20 MeV).

p_t (GeV)	dN/dp_t	stat. error	sys. error
0.4571	0.7902	0.1031	0.0869
0.7452	1.0520	0.0832	0.1157
1.0385	0.7987	0.0564	0.0879
1.3341	0.4390	0.0361	0.0483
1.6312	0.2228	0.0236	0.0245
1.9291	0.0702	0.0111	0.0077
2.2276	0.0278	0.0069	0.0031

Table D.7.: Numerical values for the 40 AGeV central Pb+Pb Ξ^- p_t spectra.

$m_t - m_0$ (GeV/c ²)	$1/m_t dN/dm_t$	stat. error	sys. error
0.0768	1.7290	0.2255	0.1902
0.1956	1.4117	0.1116	0.1553
0.3592	0.7691	0.0543	0.0846
0.5564	0.3290	0.0271	0.0362
0.7779	0.1366	0.0145	0.0150
1.0169	0.0364	0.0057	0.0040
1.2687	0.0125	0.0031	0.0014

Table D.8.: Numerical values for the 40 AGeV central Pb+Pb Ξ^- $m_t - m_0$ spectra.

D.1. Central Pb+Pb

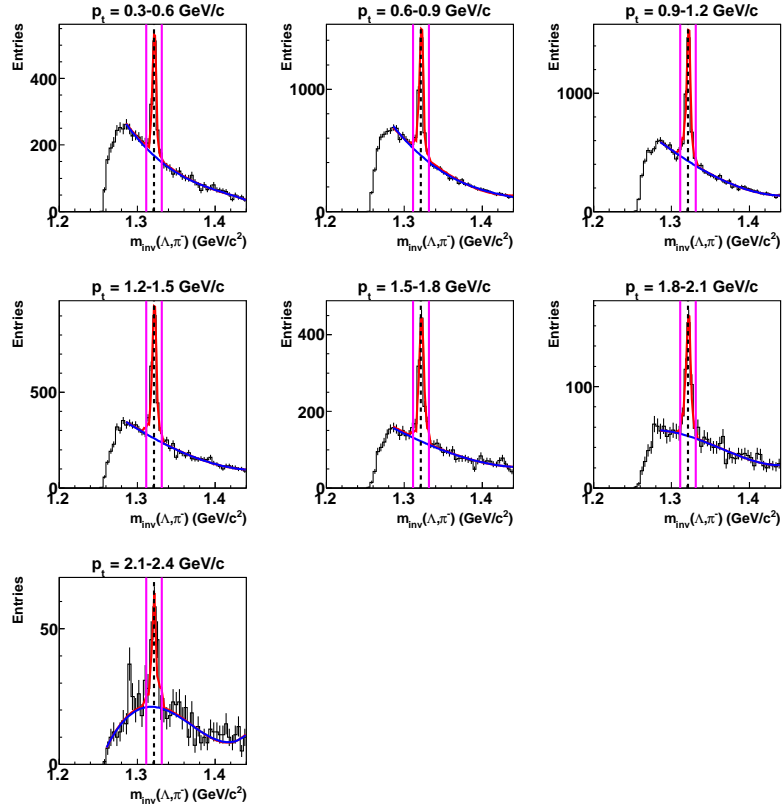


Figure D.4.: Invariant mass distribution of Ξ^- at midrapidity ($|y| \leq 0.5$) in different p_t bins in central Pb+Pb collisions at 40 AGeV. A black dotted line indicates the nominal mass and the vertical purple lines show the integrated mass window (20 MeV).

D. Invariant Mass Distribution for p_t and $m_t - m_0$ Spectra and Numerical Values

p_t (GeV)	dN/dp_t	stat. error	sys. error
0.7472	0.0540	0.0071	0.0059
1.0410	0.0486	0.0056	0.0053
1.3370	0.0262	0.0041	0.0029
1.7356	0.0135	0.0021	0.0015

Table D.9.: Numerical values for the 40 AGeV central Pb+Pb Ξ^+ p_t spectra.

$m_t - m_0$ (GeV/ c^2)	$1/m_t dN/dm_t$	stat. error	sys. error
0.1966	0.0723	0.0095	0.0080
0.3608	0.0467	0.0054	0.0051
0.5584	0.0196	0.0030	0.0022
0.8600	0.0078	0.0012	0.0009

Table D.10.: Numerical values for the 40 AGeV central Pb+Pb Ξ^+ $m_t - m_0$ spectra.

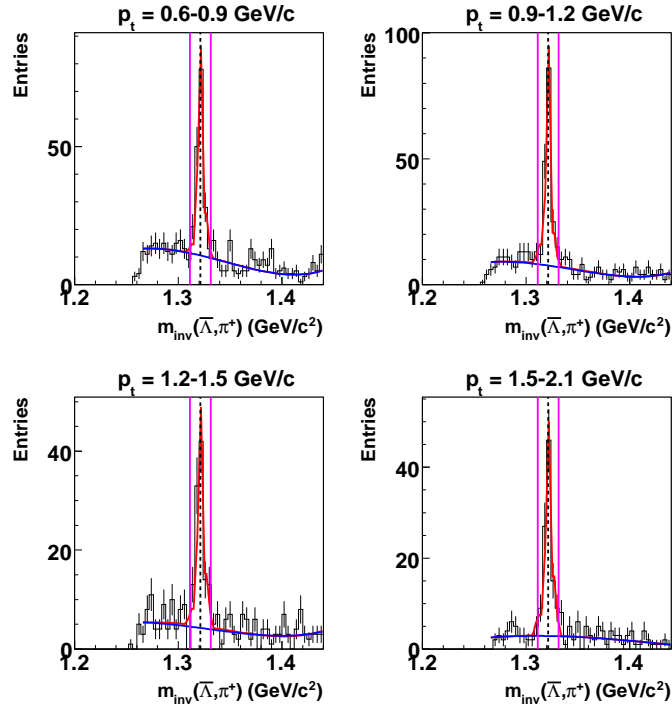
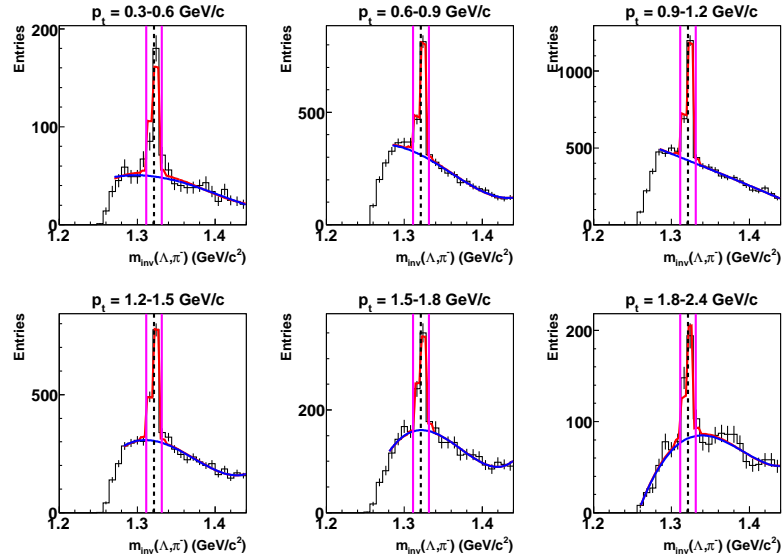


Figure D.5.: Invariant mass distribution of Ξ^+ candidates at midrapidity ($|y| \leq 0.5$) in different p_t bins in central Pb+Pb collisions at 40 AGeV. A black dotted line indicates the nominal mass and the vertical purple lines show the integrated mass window (20 MeV).

p_t (GeV)	dN/dp_t	stat. error	sys. error
0.4584	0.7391	0.1218	0.0813
0.7473	1.0293	0.1030	0.1132
1.0411	1.0482	0.0851	0.1153
1.3371	0.5539	0.0556	0.0609
1.6344	0.2363	0.0357	0.0260
2.0298	0.0868	0.0174	0.0095

 Table D.11.: Numerical values for the 80 AGeV central Pb+Pb Ξ^- p_t spectra.

$m_t - m_0$ (GeV/ c^2)	$1/m_t dN/dm_t$	stat. error	sys. error
0.0773	1.6122	0.2658	0.1277
0.1967	1.3774	0.1378	0.1515
0.3609	1.0069	0.0817	0.1108
0.5585	0.4142	0.0416	0.0456
0.7804	0.1445	0.0219	0.0159
1.1006	0.0428	0.0085	0.0047

 Table D.12.: Numerical values for the 80 AGeV central Pb+Pb Ξ^- $m_t - m_0$ spectra.

 Figure D.6.: Invariant mass distribution of Ξ^- at midrapidity ($|y| \leq 0.5$) in different p_t bins in central Pb+Pb collisions at 80 AGeV. A black dotted line indicates the nominal mass and the vertical purple lines show the integrated mass window (20 MeV).

D. Invariant Mass Distribution for p_t and $m_t - m_0$ Spectra and Numerical Values

p_t (GeV)	dN/dp_t	stat. error	sys. error
0.7458	0.1707	0.0299	0.0188
1.0393	0.1248	0.0154	0.0137
1.3351	0.0773	0.0088	0.0085
1.6322	0.0419	0.0055	0.0046
2.0211	0.0130	0.0018	0.0014

Table D.13.: Numerical values for the 80 AGeV central Pb+Pb Ξ^+ p_t spectra.

$m_t - m_0$ (GeV/ c^2)	$1/m_t dN/dm_t$	stat. error	sys. error
0.1960	0.2289	0.0299	0.0252
0.3598	0.1201	0.0154	0.0132
0.5571	0.0579	0.0088	0.0064
0.7787	0.0257	0.0055	0.0028
1.0933	0.0064	0.0018	0.0007

Table D.14.: Numerical values for the 80 AGeV central Pb+Pb Ξ^+ $m_t - m_0$ spectra.

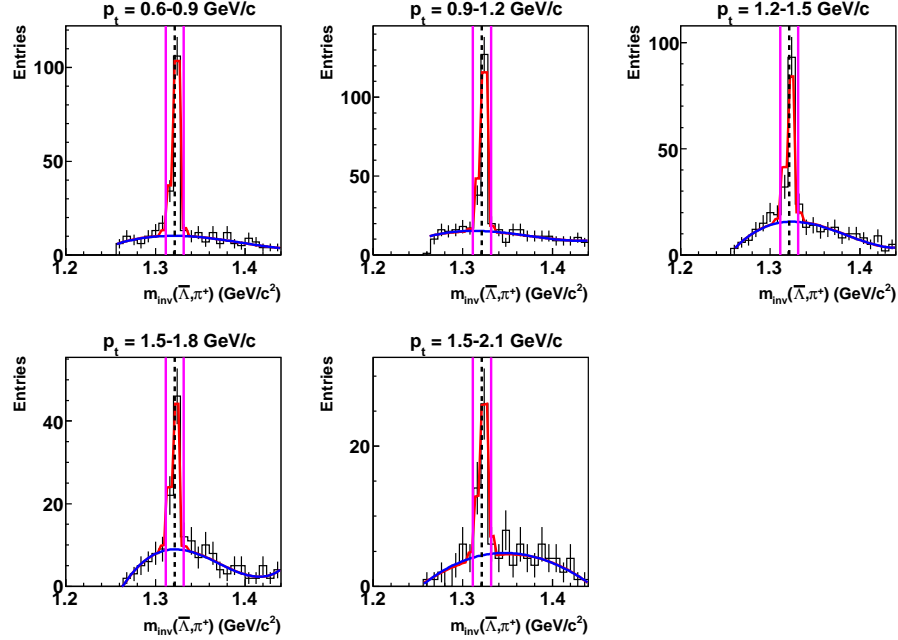


Figure D.7.: Invariant mass distribution of Ξ^+ candidates at midrapidity ($|y| \leq 0.5$) in different p_t bins in central Pb+Pb collisions at 80 AGeV. A black dotted line indicates the nominal mass and the vertical purple lines show the integrated mass window (20 MeV).

p_t (GeV)	dN/dp_t	stat. error	sys. error
1.0384	0.6352	0.0491	0.0699
1.3340	0.4572	0.0399	0.0503
1.6311	0.2342	0.0258	0.0258
1.9290	0.0848	0.0123	0.0093
2.2275	0.0353	0.0077	0.0039
2.6084	0.0123	0.0044	0.0014

Table D.15.: Numerical values for the 158 AGeV semi-central Pb+Pb (256tb) (23% most central) $\Xi^- p_t$ spectra.

$m_t - m_0$ (GeV/ c^2)	$1/m_t dN/dm_t$	stat. error	sys. error
0.3592	0.6117	0.0472	0.0673
0.5563	0.3427	0.0299	0.0377
0.7778	0.1436	0.0158	0.0158
1.0168	0.0439	0.0064	0.0048
1.2686	0.0159	0.0034	0.0017
1.6027	0.0047	0.0017	0.0005

Table D.16.: Numerical values for the 158 AGeV semi-central Pb+Pb (256tb) (23% most central) $\Xi^- m_t - m_0$ spectra.

D. Invariant Mass Distribution for p_t and $m_t - m_0$ Spectra and Numerical Values

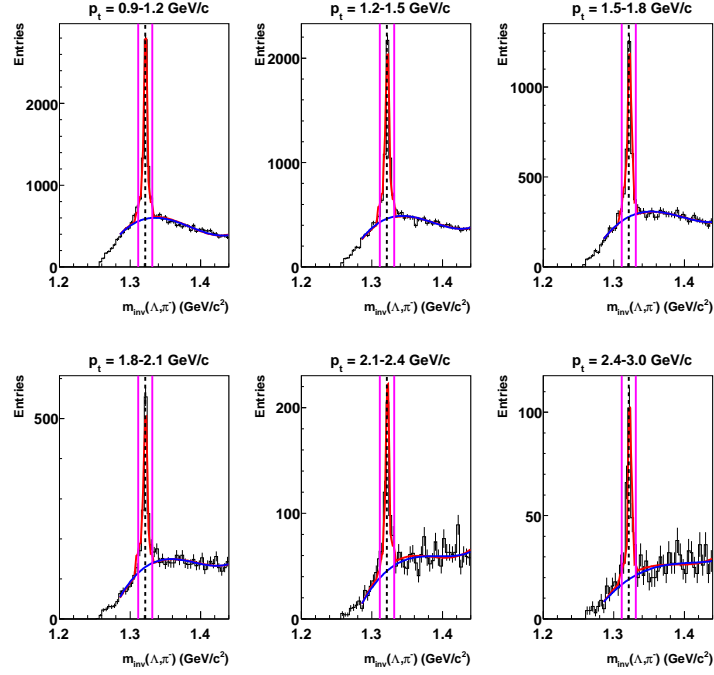


Figure D.8.: Invariant mass distribution of Ξ^- at midrapidity ($|y| \leq 0.5$) in different p_t bins in central Pb+Pb collisions at 158 AGeV (256tb) (23% most central). A black dotted line indicates the nominal mass and the vertical purple lines show the integrated mass window (20 MeV).

p_t (GeV)	dN/dp_t	stat. error	sys. error
1.0409	0.1499	0.0126	0.0165
1.3369	0.1258	0.0116	0.0138
1.6342	0.0701	0.0082	0.0077
1.9323	0.0279	0.0043	0.0031
2.3242	0.0102	0.0025	0.0011

Table D.17.: Numerical values for the 158 AGeV semi-central Pb+Pb (256tb) (23% most central) Ξ^+ p_t spectra.

$m_t - m_0$ (GeV/ c^2)	$1/m_t$ dN/dm_t	stat. error	sys. error
0.3607	0.1440	0.0121	0.0158
0.5583	0.0941	0.0087	0.0104
0.7802	0.0429	0.0050	0.0047
1.0195	0.0144	0.0022	0.0016
1.3522	0.0044	0.0011	0.0005

Table D.18.: Numerical values for the 158 AGeV semi-central Pb+Pb (256tb) (23% most central) Ξ^+ $m_t - m_0$ spectra.

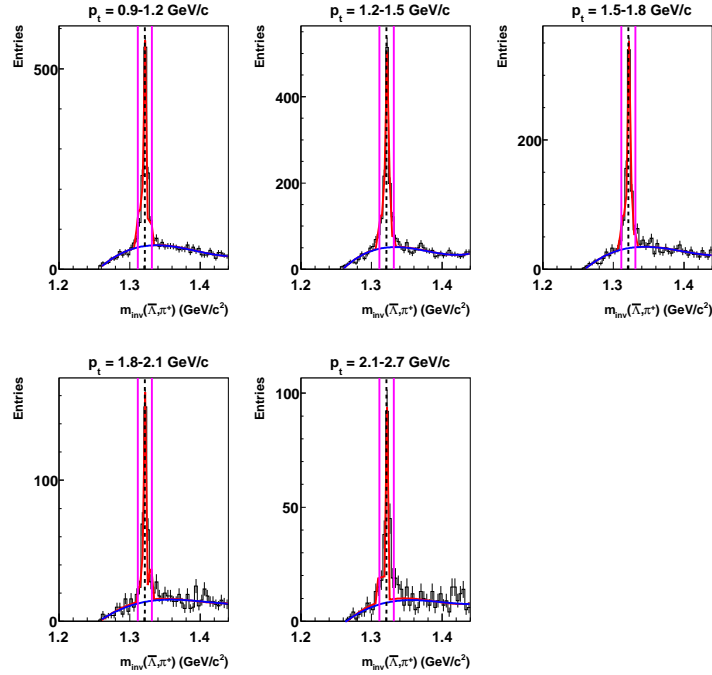


Figure D.9.: Invariant mass distribution of Ξ^+ at midrapidity ($|y| \leq 0.5$) in different p_t bins in central Pb+Pb collisions at 158 AGeV (256tb) (23% most central). A black dotted line indicates the nominal mass and the vertical purple lines show the integrated mass window (20 MeV).

D. Invariant Mass Distribution for p_t and $m_t - m_0$ Spectra and Numerical Values

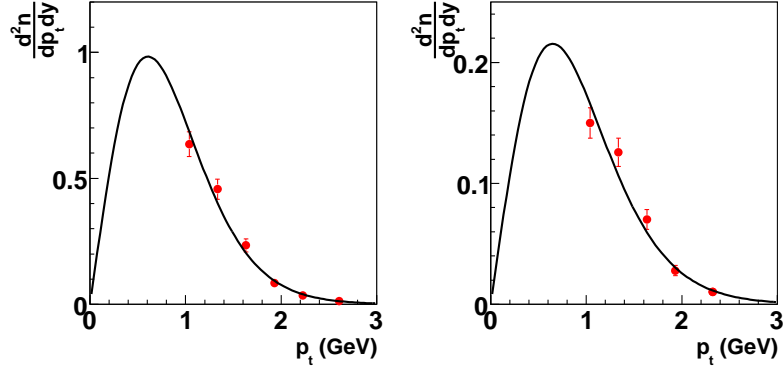


Figure D.10.: Transverse momentum spectra for Ξ^- at midrapidity ($|y| \leq 0.5$) for different centrality bins at 158 AGeV (256tb) (23% most central) corrected with the *bin-by-bin* method.

p_t (GeV)	dN/dp_t	stat. error	sys. error
0.4580	1.0441	0.0768	0.1149
0.7466	1.2147	0.0708	0.1336
1.0403	0.8624	0.0530	0.0949
1.3362	0.6059	0.0409	0.0666
1.6334	0.3547	0.0302	0.0390
1.9315	0.1580	0.0185	0.0174
2.2301	0.0620	0.0107	0.0068
2.6178	0.0232	0.0064	0.0026

Table D.19.: Numerical values for the 158 AGeV semi-central Pb+Pb (256tb) (10% most central) Ξ^- p_t spectra.

$m_t - m_0$ (GeV/ c^2)	$1/m_t dN/dm_t$	stat. error	sys. error
0.0771	2.2798	0.1676	0.2508
0.1964	1.6269	0.0949	0.1790
0.3604	0.8290	0.0509	0.0912
0.5579	0.4534	0.0306	0.0499
0.7796	0.2171	0.0185	0.0239
1.0189	0.0818	0.0096	0.0090
1.2708	0.0278	0.0048	0.0031
1.6111	0.0089	0.0025	0.0010

Table D.20.: Numerical values for the 158 AGeV semi-central Pb+Pb (256tb) (10% most central) Ξ^- $m_t - m_0$ spectra.

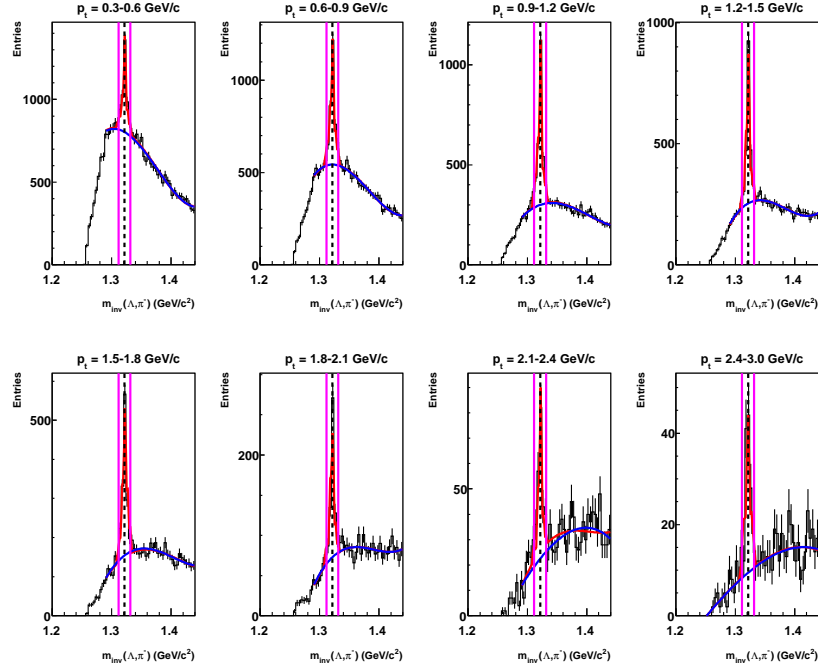


Figure D.11.: Invariant mass distribution of Ξ^- at midrapidity ($|y| \leq 0.5$) in different p_t bins in central Pb+Pb collisions at 158 AGeV (256tb) (10% most central). A black dotted line indicates the nominal mass and the vertical purple lines show the integrated mass window (20 MeV).

p_t (GeV)	dN/dp_t	stat. error	sys. error
0.7491	0.2297	0.0197	0.0253
1.0434	0.1906	0.0157	0.0210
1.3397	0.1513	0.0132	0.0166
1.6373	0.1006	0.0106	0.0111
1.9355	0.0498	0.0068	0.0055
2.3370	0.0166	0.0034	0.0018

Table D.21.: Numerical values for the 158 AGeV semi-central Pb+Pb (256tb) (10% most central) Ξ^+ p_t spectra.

D. Invariant Mass Distribution for p_t and $m_t - m_0$ Spectra and Numerical Values

$m_t - m_0$ (GeV/c ²)	$1/m_t$ dN/dm _t	stat. error	sys. error
0.1976	0.3066	0.0263	0.0337
0.3623	0.1827	0.0150	0.0201
0.5604	0.1130	0.0099	0.0124
0.7826	0.0614	0.0065	0.0068
1.0222	0.0257	0.0035	0.0028
1.3634	0.0071	0.0015	0.0008

Table D.22.: Numerical values for the 158 AGeV semi-central Pb+Pb (256tb) (10% most central) Ξ^+ $m_t - m_0$ spectra.

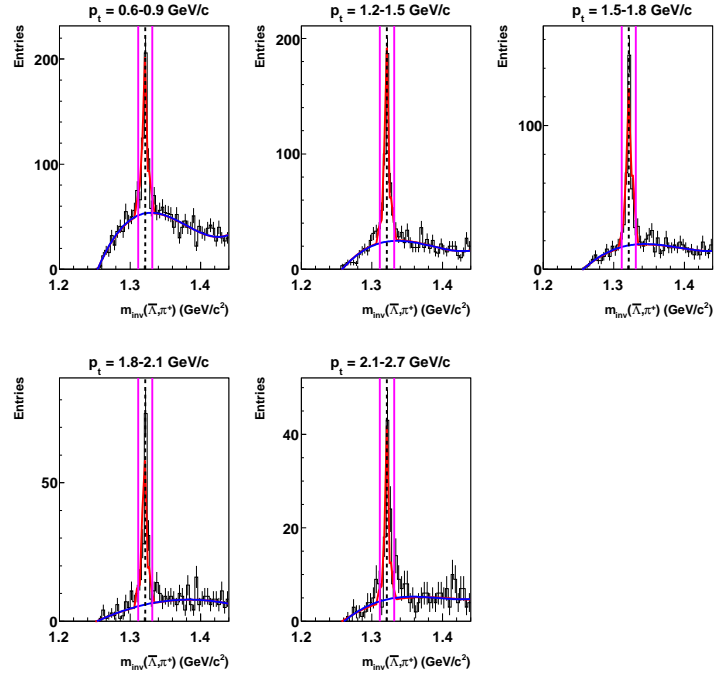


Figure D.12.: Invariant mass distribution of Ξ^+ at midrapidity ($|y| \leq 0.5$) in different p_t bins in central Pb+Pb collisions at 158 AGeV (256tb) (10% most central). A black dotted line indicates the nominal mass and the vertical purple lines show the integrated mass window (20 MeV).

D.2. Minimum Bias Pb+Pb

Energy (AGeV)		$\frac{dN}{dy} _{y=0}$ (Eq. 4.1)	$\frac{dN}{dy} _{y=0}$ (Eq. 4.2)	C_{p_t}	T (MeV)
20	Ξ^-	0.96 ± 0.13	$0.93 \pm 0.13 \pm 0.10$	1.14	$245 \pm 11 \pm 15$
30	Ξ^-	1.18 ± 0.13	$1.17 \pm 0.13 \pm 0.13$	1.12	$238 \pm 8 \pm 14$
	Ξ^+	0.05 ± 0.01	$0.05 \pm 0.01 \pm 0.006$	1.62	$280 \pm 47 \pm 28$
40	Ξ^-	1.17 ± 0.12	$1.15 \pm 0.11 \pm 0.13$	1.13	$239 \pm 6 \pm 14$
	Ξ^+	0.07 ± 0.01	$0.07 \pm 0.01 \pm 0.008$	1.50	$289 \pm 24 \pm 29$
80	Ξ^-	1.27 ± 0.15	$1.22 \pm 0.14 \pm 0.13$	1.11	$278 \pm 11 \pm 17$
	Ξ^+	0.20 ± 0.03	$0.21 \pm 0.03 \pm 0.02$	1.49	$266 \pm 18 \pm 27$
158 (23% most central)	Ξ^-	1.09 ± 0.10	$1.11 \pm 0.11 \pm 0.12$	2.53	$252 \pm 8 \pm 15$
	Ξ^+	0.26 ± 0.03	$0.26 \pm 0.03 \pm 0.03$	2.21	$285 \pm 12 \pm 29$
158 (10% most central)	Ξ^-	1.41 ± 0.10	$1.44 \pm 0.10 \pm 0.16$	1.10	$278 \pm 6 \pm 17$
	Ξ^+	0.31 ± 0.03	$0.31 \pm 0.03 \pm 0.03$	1.37	$326 \pm 13 \pm 33$
158 (from [59])	Ξ^-	–	$1.49 \pm 0.08 \pm 0.22$	1.51	–
	Ξ^+	–	$0.33 \pm 0.04 \pm 0.05$	1.45	–

Table D.23.: Summary of central Pb+Pb results showing energy, central rapidity densities calculated from equation 4.1 and 4.2, extrapolation factor C_{p_t} (from eq. 4.2) and inverse slope parameter T .

D.2. Minimum Bias Pb+Pb

p_t (GeV)	dN/dp_t	stat. error	sys. error
0.4572	0.9941	0.2545	0.1094
0.7454	1.0939	0.1652	0.1203
1.0388	0.7587	0.1121	0.0083
1.3345	0.5209	0.0789	0.0573
1.6316	0.2325	0.0483	0.0256
2.0186	0.0580	0.0175	0.0064

Table D.24.: Numerical values for the 40 AGeV minimum bias Pb+Pb Ξ^- (centrality class 1+2) p_t spectra.

$m_t - m_0$ (GeV/ c^2)	$1/m_t dN/dm_t$	stat. error	sys. error
0.0769	2.1741	0.5566	0.2392
0.1958	1.4675	0.2216	0.1614
0.3594	0.7304	0.1079	0.0803
0.5566	0.3903	0.0591	0.0429
0.7782	0.1425	0.0296	0.0157
1.0913	0.0287	0.0086	0.0032

Table D.25.: Numerical values for the 40 AGeV central Pb+Pb Ξ^- (centrality class 1+2) $m_t - m_0$ spectra.

D. Invariant Mass Distribution for p_t and $m_t - m_0$ Spectra and Numerical Values

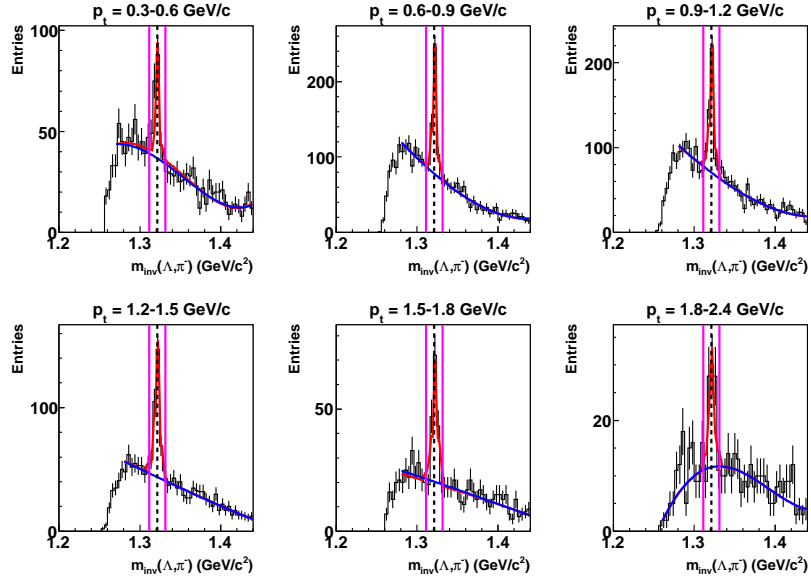


Figure D.13.: Invariant mass distribution of Ξ^- candidates at midrapidity ($|y| \leq 0.5$) in different p_t bins (centrality classes 1+2) in minimum bias Pb+Pb collisions at 40 AGeV. A black dotted line indicates the nominal mass and the vertical purple lines show the integrated mass window (20 MeV).

p_t (GeV)	dN/dp_t	stat. error	sys. error
0.4559	0.4629	0.0795	0.0509
0.7433	0.4193	0.0498	0.0461
1.0362	0.2628	0.0317	0.0289
1.3315	0.1664	0.0231	0.0183
1.6283	0.0660	0.0136	0.0073
2.0064	0.0232	0.0057	0.0026

Table D.26.: Numerical values for the 40 AGeV minimum bias Pb+Pb Ξ^- (centrality class 3+4) p_t spectra.

$m_t - m_0$ (GeV/c ²)	$1/m_t dN/dm_t$	stat. error	sys. error
0.0764	1.0153	0.1745	0.1117
0.1947	0.5640	0.0669	0.0620
0.3578	0.2537	0.0305	0.0279
0.5545	0.1250	0.0173	0.0138
0.7757	0.0406	0.0084	0.0045
1.0811	0.0116	0.0028	0.0013

Table D.27.: Numerical values for the 40 AGeV central Pb+Pb Ξ^- (centrality class 3+4) $m_t - m_0$ spectra.

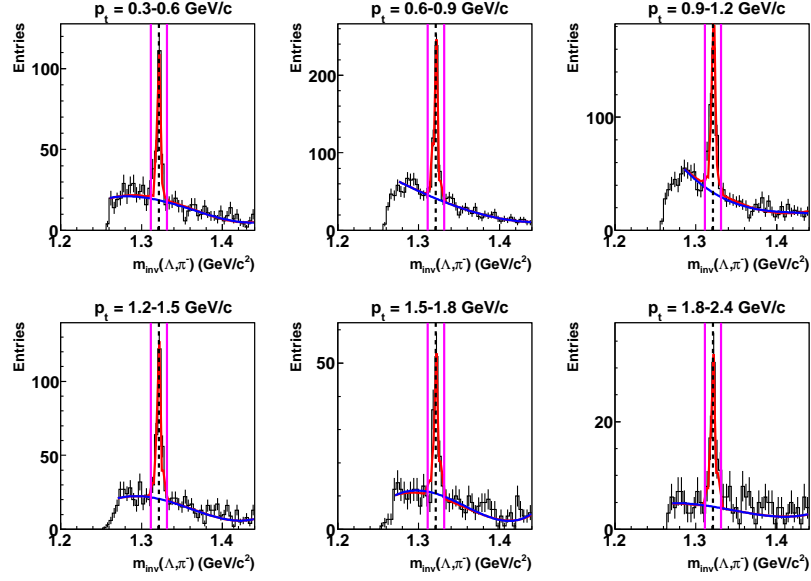


Figure D.14.: Invariant mass distribution of Ξ^- candidates at midrapidity ($|y| \leq 0.5$) in different p_t bins (centrality classes 3+4) in minimum bias Pb+Pb collisions at 40 AGeV. A black dotted line indicates the nominal mass and the vertical purple lines show the integrated mass window (20 MeV).

p_t (GeV)	dN/dp_t	stat. error	sys. error
0.4564	0.1193	0.0270	0.0131
0.7442	0.1289	0.0192	0.0142
1.0372	0.0816	0.0120	0.0090
1.3327	0.0441	0.0082	0.0049
1.7180	0.0202	0.0044	0.0022

Table D.28.: Numerical values for the 40 AGeV minimum bias Pb+Pb Ξ^- (centrality class 5+6) p_t spectra.

$m_t - m_0$ (GeV/ c^2)	$1/m_t dN/dm_t$	stat. error	sys. error
0.0766	0.2613	0.0592	0.0287
0.1952	0.1732	0.0258	0.0191
0.3585	0.0787	0.0116	0.0087
0.5554	0.0331	0.0061	0.0036
0.8460	0.0118	0.0025	0.0013

Table D.29.: Numerical values for the 40 AGeV central Pb+Pb Ξ^- (centrality class 5+6) $m_t - m_0$ spectra.

D. Invariant Mass Distribution for p_t and $m_t - m_0$ Spectra and Numerical Values

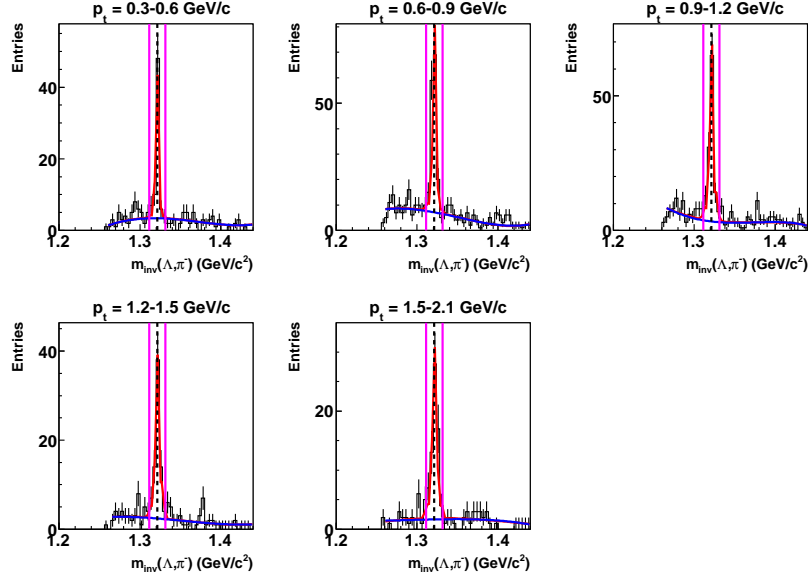


Figure D.15.: Invariant mass distribution of Ξ^- candidates at midrapidity ($|y| \leq 0.5$) in different p_t bins (centrality classes 5+6) in minimum bias Pb+Pb collisions at 40 AGeV. A black dotted line indicates the nominal mass and the vertical purple lines show the integrated mass window (20 MeV).

p_t (GeV)	dN/dp_t	stat. error	sys. error
0.4582	1.0828	0.2770	0.1191
0.7469	0.8578	0.2061	0.0944
1.0406	0.9267	0.1751	0.1019
1.3366	0.5149	0.1160	0.0566
1.7338	0.2016	0.0546	0.0222

Table D.30.: Numerical values for the 158 AGeV minimum bias Pb+Pb Ξ^- (centrality class 1+2) p_t spectra.

$m_t - m_0$ (GeV/c ²)	$1/m_t dN/dm_t$	stat. error	sys. error
0.0772	2.3632	0.6045	0.2600
0.1965	1.1484	0.2759	0.1263
0.3606	0.8905	0.1683	0.0980
0.5582	0.3852	0.0868	0.0424
0.8586	0.1163	0.0315	0.0128

Table D.31.: Numerical values for the 158 AGeV central Pb+Pb Ξ^- (centrality class 1+2) $m_t - m_0$ spectra.

D.2. Minimum Bias Pb+Pb

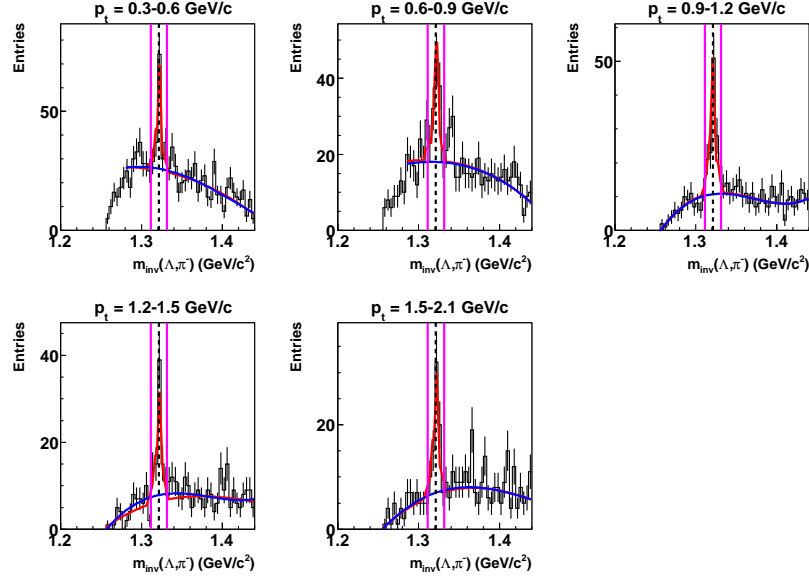


Figure D.16.: Invariant mass distribution of Ξ^- candidates at midrapidity ($|y| \leq 0.5$) in different p_t bins (centrality classes 1+2) in minimum bias Pb+Pb collisions at 158 AGeV. A black dotted line indicates the nominal mass and the vertical purple lines show the integrated mass window (20 MeV).

p_t (GeV)	dN/dp_t	stat. error	sys. error
0.4584	0.7111	0.1421	0.0782
0.7473	0.9188	0.1324	0.1011
1.0411	0.7703	0.1109	0.0847
1.3371	0.4027	0.0695	0.0443
1.7359	0.1973	0.0407	0.0217

Table D.32.: Numerical values for the 158 AGeV minimum bias Pb+Pb Ξ^- (centrality class 3+4) p_t spectra.

$m_t - m_0$ (GeV/c ²)	$1/m_t dN/dm_t$	stat. error	sys. error
0.0773	1.5513	0.3101	0.1706
0.1967	1.2295	0.1772	0.1352
0.3609	0.7399	0.1066	0.0814
0.5585	0.3012	0.0520	0.0331
0.8603	0.1137	0.0234	0.0125

Table D.33.: Numerical values for the 158 AGeV central Pb+Pb Ξ^- (centrality class 3+4) $m_t - m_0$ spectra.

D. Invariant Mass Distribution for p_t and $m_t - m_0$ Spectra and Numerical Values

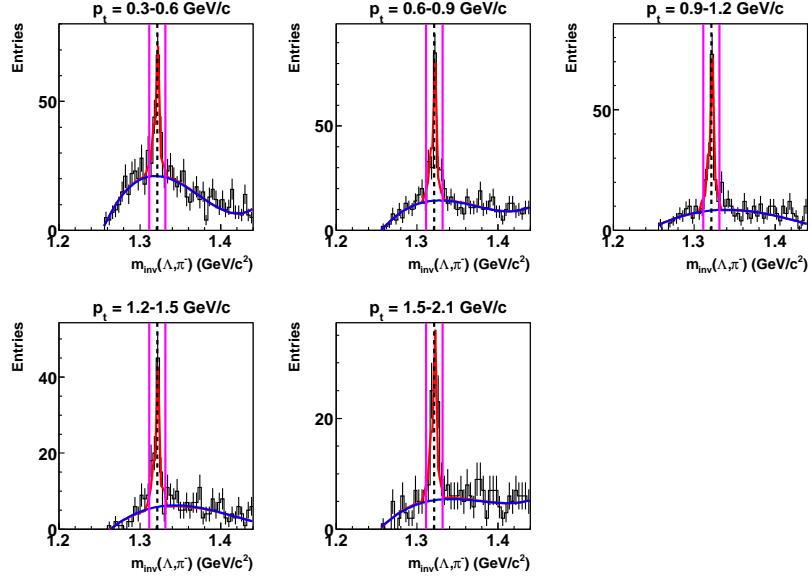


Figure D.17.: Invariant mass distribution of Ξ^- candidates at midrapidity ($|y| \leq 0.5$) in different p_t bins (centrality classes 3+4) in minimum bias Pb+Pb collisions at 158 AGeV. A black dotted line indicates the nominal mass and the vertical purple lines show the integrated mass window (20 MeV).

p_t (GeV)	dN/dp_t	stat. error	sys. error
0.1977	0.2140	0.0827	0.0235
0.4589	0.6500	0.1261	0.0715
0.7481	0.9423	0.1451	0.1037
1.0421	0.5781	0.1092	0.0636
1.3383	0.5994	0.1102	0.0659
1.7409	0.1342	0.0387	0.0043

Table D.34.: Numerical values for the 158 AGeV minimum bias Pb+Pb Ξ^- (centrality class 5+6) p_t spectra.

$m_t - m_0$ (GeV/c ²)	$1/m_t dN/dm_t$	stat. error	sys. error
0.0147	1.0824	0.4182	0.1191
0.0774	1.4163	0.2747	0.1558
0.1971	1.2596	0.1939	0.1386
0.3615	0.5547	0.1048	0.0610
0.5594	0.4479	0.0824	0.0493
0.8642	0.0771	0.0222	0.0085

Table D.35.: Numerical values for the 158 AGeV central Pb+Pb Ξ^- (centrality class 5+6) $m_t - m_0$ spectra.

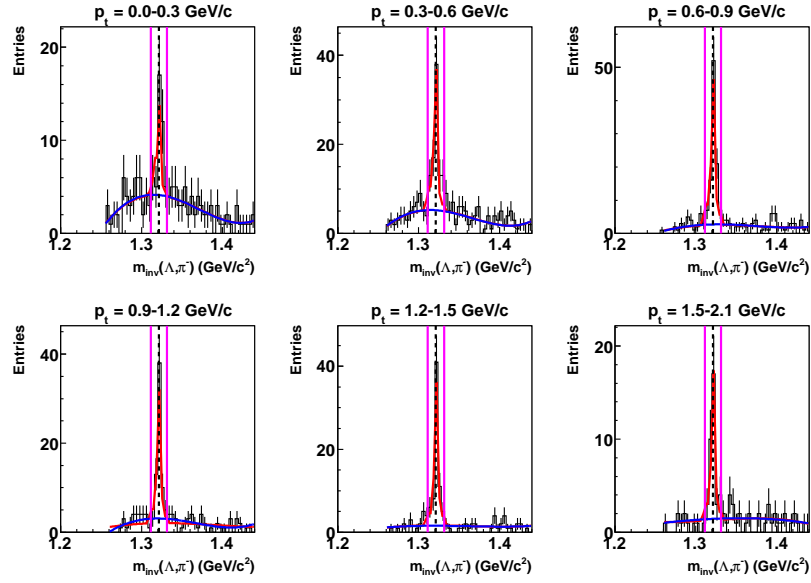


Figure D.18.: Invariant mass distribution of Ξ^- candidates at midrapidity ($|y| \leq 0.5$) in different p_t bins (centrality classes 5+6) in minimum bias Pb+Pb collisions at 158 AGeV. A black dotted line indicates the nominal mass and the vertical purple lines show the integrated mass window (20 MeV).

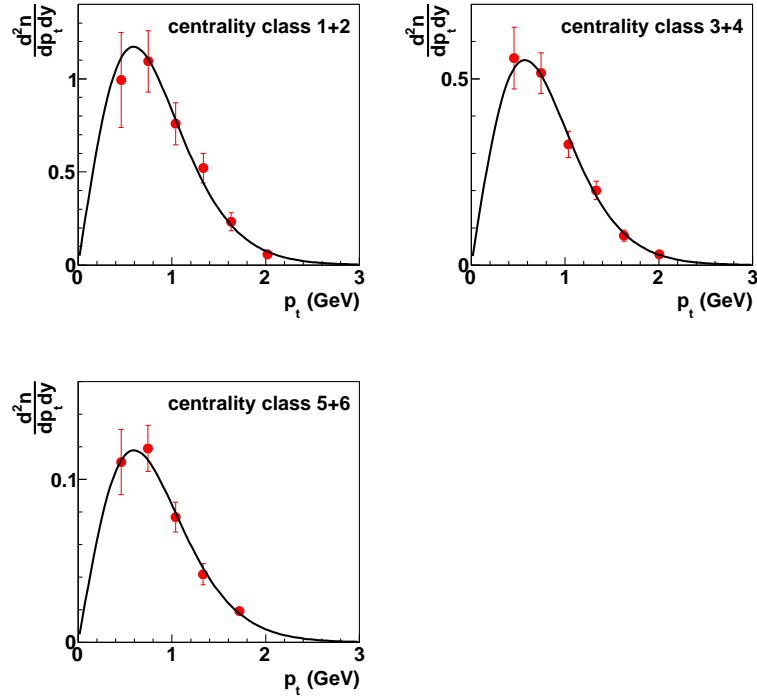


Figure D.19.: Transverse momentum spectra for Ξ^- at midrapidity ($|y| \leq 0.5$) for different centrality bins at 40 AGeV corrected with the *bin-by-bin* method.

D. Invariant Mass Distribution for p_t and $m_t - m_0$ Spectra and Numerical Values

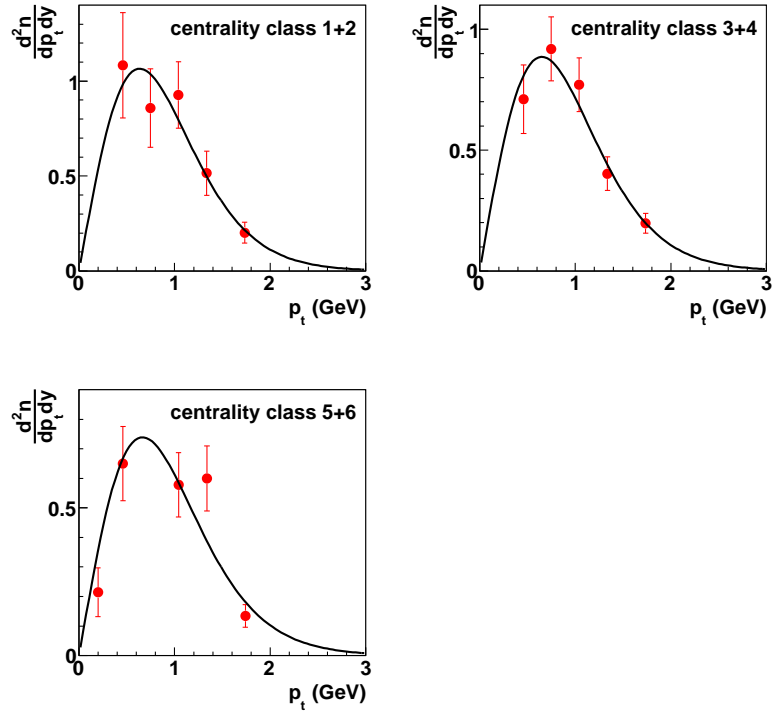


Figure D.20.: Transverse momentum spectra for Ξ^- at midrapidity ($|y| \leq 0.5$) for different centrality bins at 158 AGeV corrected with the *bin-by-bin* method.

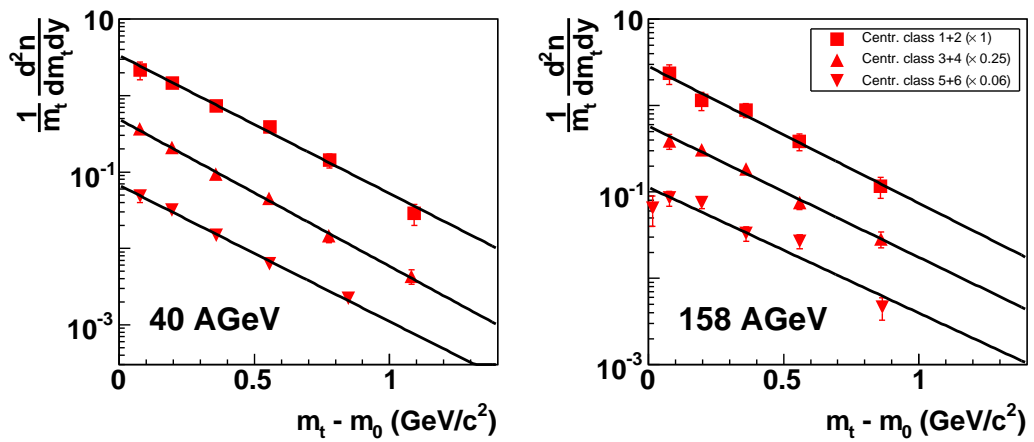


Figure D.21.: Transverse mass spectra for Ξ^- at midrapidity ($|y| \leq 0.5$) for different centrality bins at 40 AGeV (left) and at 158 AGeV (right) corrected with the *bin-by-bin* method.

40 AGeV					
Centrality Bin		$\frac{dN}{dy} _{y=0}$ (Eq. 4.1)	$\frac{dN}{dy} _{y=0}$ (Eq. 4.2)	C_{p_t}	T (MeV)
1+2	Ξ^-	1.26 ± 0.23	$1.25 \pm 0.23 \pm 0.14$	1.12	$240 \pm 14 \pm 14$
3+4	Ξ^-	0.46 ± 0.07	$0.49 \pm 0.07 \pm 0.05$	1.14	$226 \pm 12 \pm 14$
5+6	Ξ^-	0.14 ± 0.03	$0.14 \pm 0.03 \pm 0.02$	1.14	$243 \pm 18 \pm 15$
158 AGeV					
1+2	Ξ^-	1.38 ± 0.32	$1.43 \pm 0.33 \pm 0.16$	1.14	$274 \pm 30 \pm 16$
3+4	Ξ^-	0.57 ± 0.10	$0.59 \pm 0.10 \pm 0.06$	1.14	$286 \pm 24 \pm 17$
5+6	Ξ^-	0.15 ± 0.03	$0.17 \pm 0.03 \pm 0.02$	1.04	$299 \pm 25 \pm 18$

Table D.36.: Summary of minimum bias results showing energy, central rapidity densities calculated from equation 4.1 and 4.2, extrapolation factor C_{p_t} (from equation 4.2) and inverse slope parameter T .

D.3. Semi-Central Si+Si

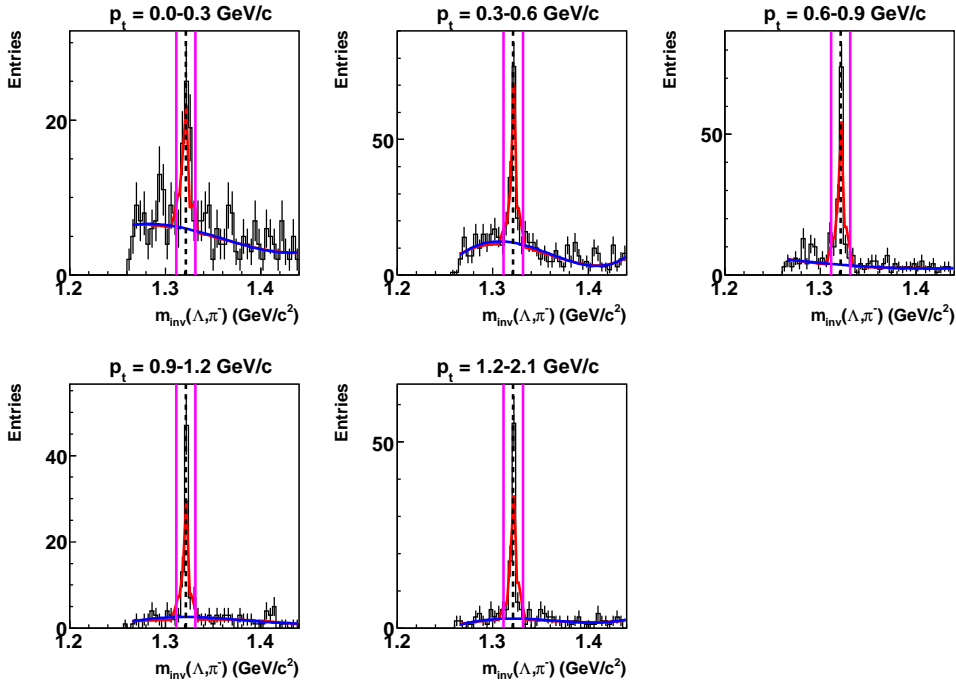


Figure D.22.: Invariant mass distribution of Ξ^- at midrapidity ($|y| \leq 0.5$) in different p_t bins in semi-central Si+Si collisions at 158 AGeV. A black dotted line indicates the nominal mass and the vertical purple lines show the integrated mass window (20 MeV).

D. Invariant Mass Distribution for p_t and $m_t - m_0$ Spectra and Numerical Values

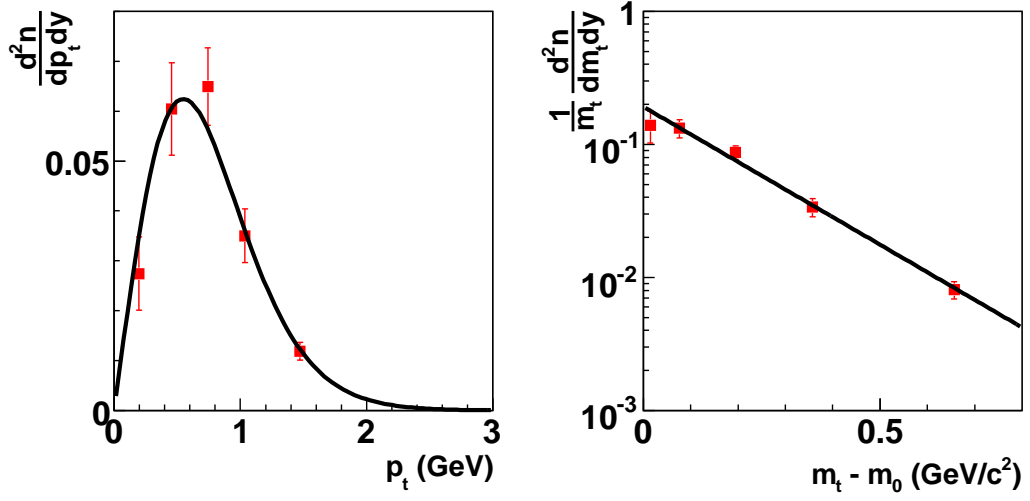


Figure D.23.: Transverse momentum (left) and transverse mass (right) distribution at midrapidity ($|y| \leq 0.5$) in semi-central Si+Si collisions at 158 AGeV.

p_t (GeV)	dN/dp_t	stat. error	sys. error
0.1967	0.0275	0.0074	0.0030
0.4555	0.0604	0.0093	0.0066
0.7427	0.0649	0.0077	0.0071
1.0354	0.0350	0.0054	0.0039
1.4721	0.0119	0.0018	0.0013

Table D.37.: Numerical values for the 158 AGeV semi-central Si+Si Ξ^- p_t spectra.

$m_t - m_0$ (GeV/c ²)	$1/m_t dN/dm_t$	stat. error	sys. error
0.0146	0.1395	0.0374	0.0153
0.0763	0.1327	0.0204	0.0146
0.1944	0.0874	0.0104	0.0096
0.3573	0.0338	0.0052	0.0037
0.6568	0.0081	0.0012	0.0009

Table D.38.: Numerical values for the 158 AGeV semi-central Si+Si Ξ^- $m_t - m_0$ spectra.

D.3. Semi-Central Si+Si

Energy (A GeV)		$\frac{dN}{dy} _{y=0}$ (Eq. 4.1)	$\frac{dN}{dy} _{y=0}$ (Eq. 4.2)	C_{p_t}	T (MeV)
158	Ξ^-	0.06 ± 0.01	$0.07 \pm 0.01 \pm 0.008$	1.01	$210 \pm 13 \pm 13$

Table D.39.: Summary of semi-central Si+Si results showing energy, central rapidity densities calculated from equation 4.1 and 4.2, extrapolation factor C_{p_t} (from eq. 4.2) and inverse slope parameter T .

D. Invariant Mass Distribution for p_t and $m_t - m_0$ Spectra and Numerical Values

E. Invariant Mass Distribution for y Spectra and Numerical Values

E.1. Central Pb+Pb

y	dN/dy	stat. error	sys. error
-0.25	0.9087	0.1383	0.1000
0.25	1.0026	0.1443	0.1103
0.75	0.6641	0.1215	0.0731
1.25	0.1705	0.0596	0.0188

Table E.1.: Numerical values for the 20 AGeV central Pb+Pb Ξ^- y spectra.

y	Slope (MeV)	stat. error (MeV)	sys. error (MeV)
-0.25	266	26	16
0.25	232	13	14
0.75	218	24	13
1.25	201	101	12

Table E.2.: Numerical values for the inverse slope parameter as a function of rapidity for the 20 AGeV central Pb+Pb Ξ^- .

E. Invariant Mass Distribution for y Spectra and Numerical Values

y	dN/dy	stat. error	sys. error
-0.75	0.7062	0.1870	0.0777
-0.25	1.0964	0.1728	0.1206
0.25	1.2090	0.1524	0.1330
0.75	0.9040	0.1437	0.0994
1.25	0.3284	0.0750	0.0361

Table E.3.: Numerical values for the 30 AGeV central Pb+Pb Ξ^- y spectra.

y	Slope (MeV)	stat. error (MeV)	sys. error (MeV)
-0.75	220	39	13
-0.25	260	12	29
0.25	235	12	14
0.75	229	14	14
1.25	221	37	13

Table E.4.: Numerical values for the inverse slope parameter as a function of rapidity for the 30 AGeV central Pb+Pb Ξ^- .

y	dN/dy	stat. error	sys. error
-0.25	0.0517	0.0199	0.0057
0.25	0.0636	0.0206	0.0070
0.75	0.0374	0.0114	0.0041

Table E.5.: Numerical values for the 30 AGeV central Pb+Pb Ξ^+ y spectra.

y	Slope (MeV)	stat. error (MeV)	sys. error (MeV)
-0.25	257	81	26
0.25	234	55	23
0.75	225	59	23

Table E.6.: Numerical values for the inverse slope parameter as a function of rapidity for the 30 AGeV central Pb+Pb Ξ^+ .

y	dN/dy	stat. error	sys. error
-0.75	1.0405	0.2281	0.1145
-0.25	1.1431	0.1228	0.1257
0.25	1.1612	0.1304	0.1277
0.75	0.7728	0.0980	0.0850
1.25	0.5392	0.0884	0.0593

Table E.7.: Numerical values for the 40 AGeV central Pb+Pb Ξ^- y spectra.

y	Slope (MeV)	stat. error (MeV)	sys. error (MeV)
-0.75	240	35	14
-0.25	246	14	15
0.25	248	15	15
0.75	233	11	14
1.25	161	10	10

Table E.8.: Numerical values for the inverse slope parameter as a function of rapidity for the 40 AGeV central Pb+Pb Ξ^- .

y	dN/dy	stat. error	sys. error
-0.25	0.0790	0.0139	0.0087
0.25	0.0672	0.0121	0.0074
0.75	0.0399	0.0082	0.0044

Table E.9.: Numerical values for the 40 AGeV central Pb+Pb Ξ^+ y spectra.

y	Slope (MeV)	stat. error (MeV)	sys. error (MeV)
-0.25	202	53	20
0.25	265	41	27
0.75	263	37	26

Table E.10.: Numerical values for the inverse slope parameter as a function of rapidity for the 40 AGeV central Pb+Pb Ξ^+ .

E. Invariant Mass Distribution for y Spectra and Numerical Values

y	dN/dy	stat. error	sys. error
-0.75	1.1359	0.1480	0.1249
-0.25	1.2954	0.1664	0.1425
0.25	1.4607	0.2114	0.1607
0.75	1.3172	0.1687	0.1449
1.25	0.8053	0.2162	0.0886

Table E.11.: Numerical values for the 80 AGeV central Pb+Pb Ξ^- y spectra.

y	Slope (MeV)	stat. error (MeV)	sys. error (MeV)
-0.75	269	16	16
-0.25	275	27	17
0.25	244	24	15
0.75	258	34	15
1.25	315	41	19

Table E.12.: Numerical values for the inverse slope parameter as a function of rapidity for the 80 AGeV central Pb+Pb Ξ^- .

y	dN/dy	stat. error	sys. error
-0.75	0.1337	0.0334	0.0147
-0.25	0.1854	0.0331	0.0204
0.25	0.2699	0.0522	0.0297
0.75	0.1527	0.0303	0.0168

Table E.13.: Numerical values for the 80 AGeV central Pb+Pb Ξ^+ y spectra.

y	Slope (MeV)	stat. error (MeV)	sys. error (MeV)
-0.75	270	57	27
-0.25	340	89	34
0.25	329	75	33
0.75	245	51	25

Table E.14.: Numerical values for the inverse slope parameter as a function of rapidity for the 80 AGeV central Pb+Pb Ξ^+ .

y	dN/dy	stat. error	sys. error
-1.25	0.4378	0.0697	0.0482
-0.75	0.6966	0.0674	0.0766
-0.25	0.9200	0.0890	0.1012
0.25	0.9240	0.0884	0.1016
0.75	0.8378	0.0712	0.0922

Table E.15.: Numerical values for the 158 AGeV (256tb) (23% most central) central Pb+Pb Ξ^- y spectra.

y	Slope (MeV)	stat. error (MeV)	sys. error (MeV)
-1.25	229	13	14
-0.75	255	9	15
-0.25	252	8	15
0.25	228	7	14
0.75	234	9	14

Table E.16.: Numerical values for the inverse slope parameter as a function of rapidity for the 158 AGeV (256tb) (23% most central) central Pb+Pb Ξ^- .

E. Invariant Mass Distribution for y Spectra and Numerical Values

y	dN/dy	stat. error	sys. error
-1.25	0.0567	0.0112	0.0062
-0.75	0.1335	0.0143	0.0080
-0.25	0.2812	0.0322	0.0309
0.25	0.2402	0.0258	0.0264
0.75	0.1728	0.0168	0.0190

Table E.17.: Numerical values for the 158 AGeV (256tb) (23% most central) central Pb+Pb Ξ^+ y spectra.

y	Slope (MeV)	stat. error (MeV)	sys. error (MeV)
-1.25	223	23	22
-0.75	265	17	27
-0.25	286	16	29
0.25	303	21	30
0.75	284	27	28

Table E.18.: Numerical values for the inverse slope parameter as a function of rapidity for the 158 AGeV (256tb) (23% most central) central Pb+Pb Ξ^+ .

y	dN/dy	stat. error	sys. error
-0.75	1.0678	0.0784	0.1175
-0.25	1.4695	0.1171	0.1616
0.25	1.5002	0.1301	0.1650
0.75	1.1640	0.0801	0.1280
1.25	0.9796	0.1357	0.1078

Table E.19.: Numerical values for the 158 AGeV (256tb) (10% most central) central Pb+Pb Ξ^- y spectra.

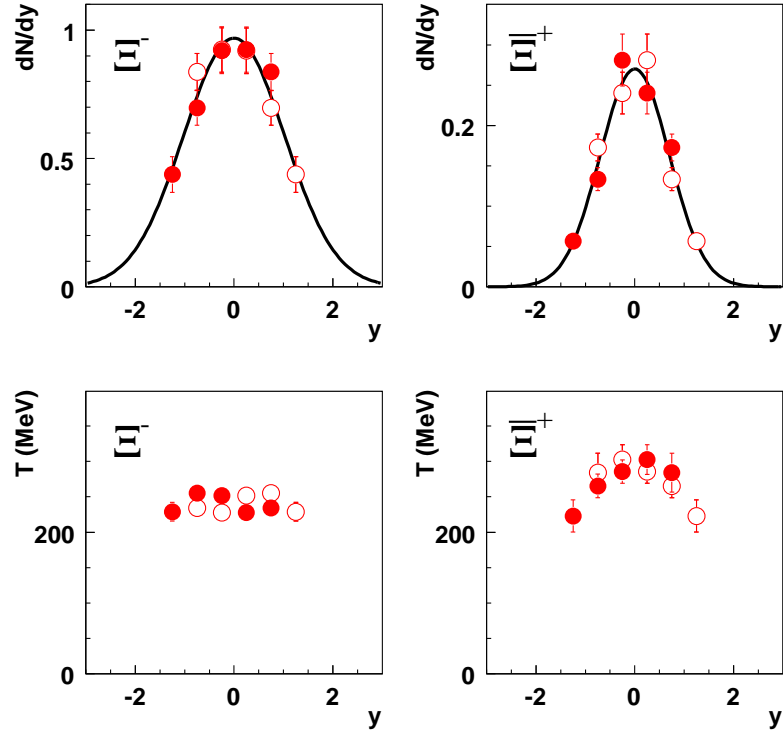


Figure E.1.: Rapidity distribution for Ξ^- (top left) and Ξ^+ (top right) corrected with the *bin-by-bin* method and the inverse slope parameter as a function of the rapidity for Ξ^- (bottom left) and Ξ^+ (bottom right) at 158 AGeV (256tb) (23% most central).

y	Slope (MeV)	stat. error (MeV)	sys. error (MeV)
-0.75	260	6	16
-0.25	291	6	17
0.25	261	12	16
0.75	253	7	15
1.25	241	15	14

Table E.20.: Numerical values for the inverse slope parameter as a function of rapidity for the 158 AGeV (256tb) (10% most central) central Pb+Pb Ξ^- .

E. Invariant Mass Distribution for y Spectra and Numerical Values

y	dN/dy	stat. error	sys. error
-0.75	0.1560	0.0179	0.0171
-0.25	0.3172	0.0353	0.0349
0.25	0.3159	0.0389	0.0347
0.75	0.2077	0.0212	0.0228
1.25	0.1070	0.0264	0.0118

Table E.21.: Numerical values for the 158 AGeV (256tb) (10% most central) central Pb+Pb Ξ^+ y spectra.

y	Slope (MeV)	stat. error (MeV)	sys. error (MeV)
-0.75	295	17	30
-0.25	389	54	39
0.25	438	81	44
0.75	304	32	30
1.25	296	73	30

Table E.22.: Numerical values for the inverse slope parameter as a function of rapidity for the 158 AGeV (256tb) (10% most central) central Pb+Pb Ξ^+ .

Energy (AGeV)		4π yield (Eq. 4.4)	C_y	RMS
20	Ξ^-	$1.50 \pm 0.13 \pm 0.10$	1.09	$0.64 \pm 0.08 \pm 0.07$
	Ξ^+	$0.12 \pm 0.02 \pm 0.03$	1.54	$0.76 \pm 0.35 \pm 0.17$
30	Ξ^-	$2.42 \pm 0.19 \pm 0.29$	1.14	$0.73 \pm 0.14 \pm 0.09$
	Ξ^+	$0.13 \pm 0.01 \pm 0.02$	1.39	$0.65 \pm 0.13 \pm 0.09$
40	Ξ^-	$2.96 \pm 0.20 \pm 0.36$	1.27	$0.94 \pm 0.13 \pm 0.11$
	Ξ^+	$0.58 \pm 0.06 \pm 0.13$	1.56	$0.87 \pm 0.29 \pm 0.20$
80	Ξ^-	$3.80 \pm 0.26 \pm 0.61$	1.26	$0.98 \pm 0.25 \pm 0.16$
	Ξ^+	$0.52 \pm 0.03 \pm 0.06$	1.18	$0.70 \pm 0.05 \pm 0.08$
158 (256) (23% most central)	Ξ^-	$4.04 \pm 0.16 \pm 0.57$	1.31	$1.18 \pm 0.18 \pm 0.17$
	Ξ^+	$0.66 \pm 0.04 \pm 0.08$	1.20	$0.73 \pm 0.08 \pm 0.09$
158 (from [59])	Ξ^-	$4.12 \pm 0.20 \pm 0.62$	—	0.99 ± 0.13
	Ξ^+	$0.77 \pm 0.04 \pm 0.12$	—	0.87 ± 0.07

Table E.23.: Summary of central Pb+Pb results showing energy, 4π yield calculated from 4.4, extrapolation factor C_y (from eq. 4.4) and RMS.

F. Systematic Errors

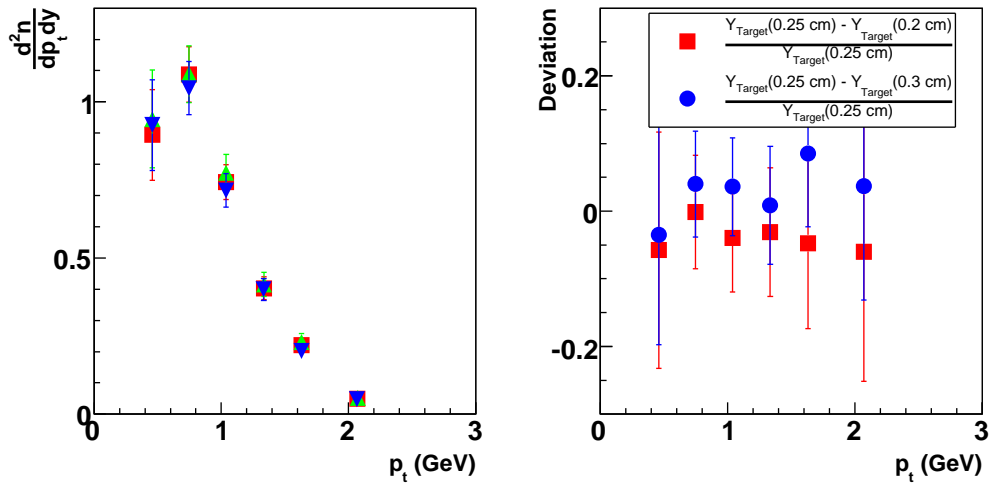


Figure F.1.: Stability with respect to changes of the cut Y_{Target} for Ξ^- at 30 AGeV illustrated at the transverse momentum spectra (top left) and $m_t - m_0$ spectra (top right) at midrapidity, respectively and the deviation due to the changes of the cut Y_{Target} of the Ξ^- (bottom left).

F. Systematic Errors

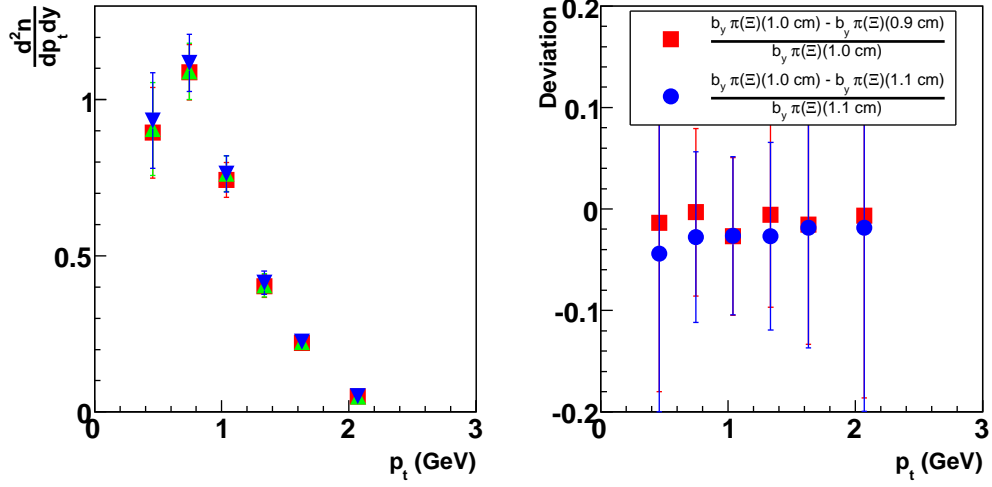


Figure F.2.: Stability with respect to changes of the cut b_y for daughter π^- of the mother Ξ^- at 30 AGeV illustrated at the transverse momentum spectra (top left) and $m_t - m_0$ spectra (top right) at midrapidity, respectively and the deviation due to the changes of the cut b_y of the daughter π^- of the mother Ξ^- (bottom left).

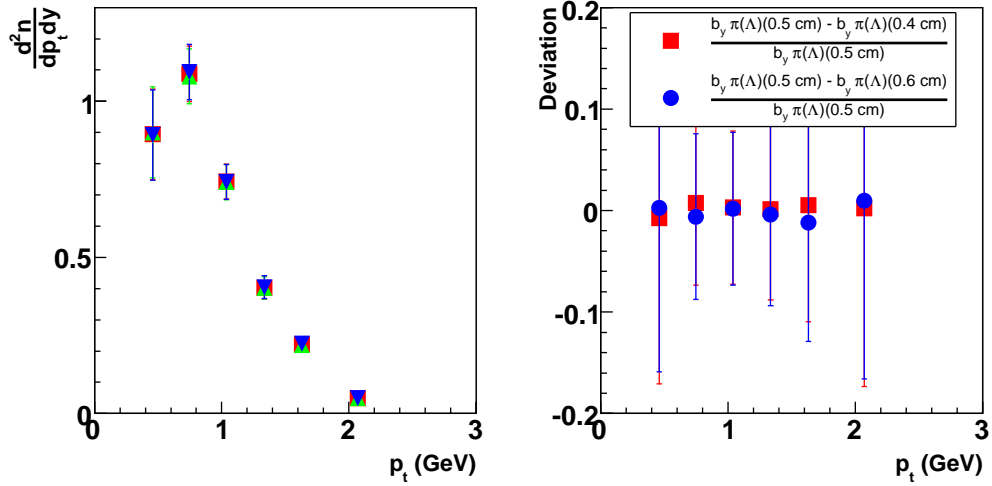


Figure F.3.: Stability with respect to changes of the cut b_y for daughter π^- of the daughter Λ at 30 AGeV illustrated at the transverse momentum spectra (top left) and $m_t - m_0$ spectra (top right) at midrapidity, respectively and the deviation due to the changes of the cut b_y of the daughter π^- of the daughter Λ (bottom left).

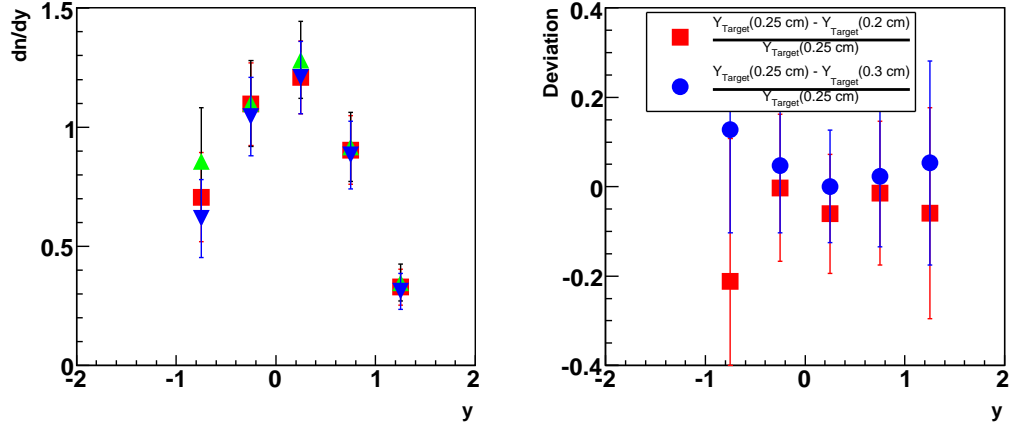


Figure F.4.: Stability with changes of the cut Y_{Target} of the Ξ^- at 30 AGeV illustrated at the rapidity spectra (left) and the deviation of the changes of the cut Y_{Target} of the Ξ^- (right).

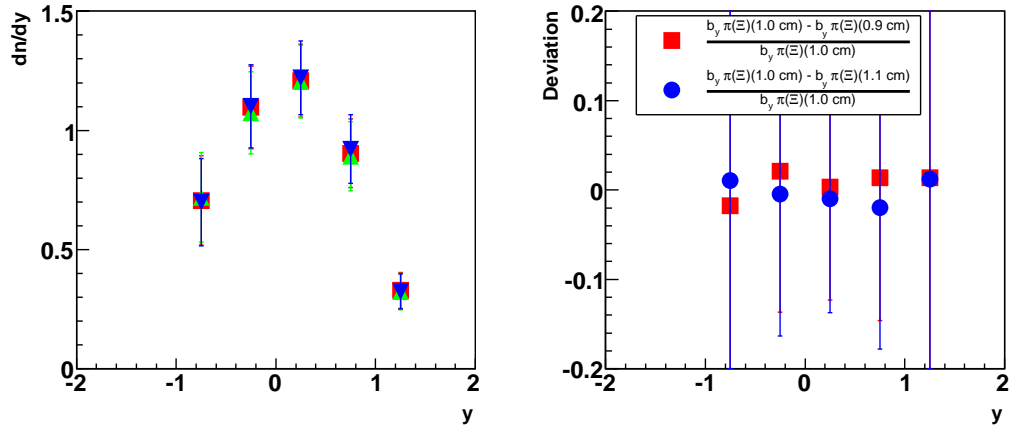


Figure F.5.: Compare of the stability with changes of the cut b_y of the daughter π^- of the mother Ξ^- at 30 AGeV illustrated at the rapidity spectra (left) and the deviation of the changes of the cut b_y of the daughter π^- of the mother Ξ^- (right).

F. Systematic Errors

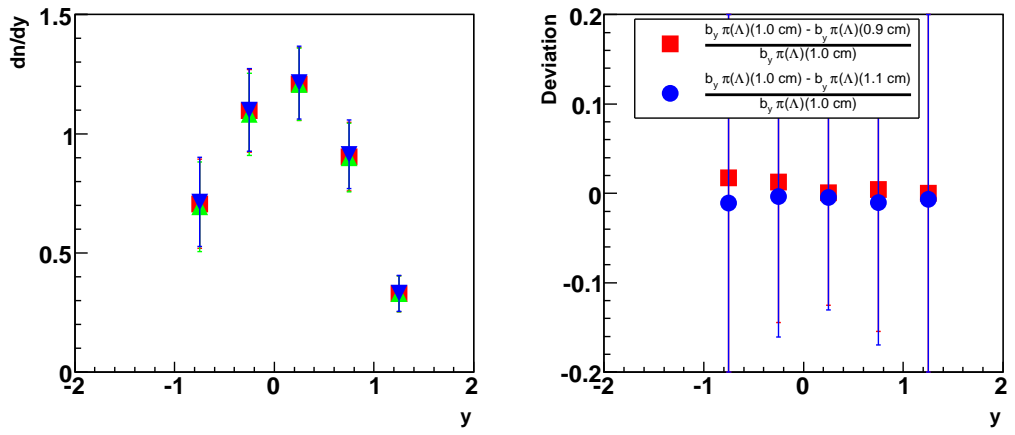


Figure F.6.: Compare of the stability with changes of the cut b_y of the daughter π^- of the daughter Λ at 30 AGeV illustrated at the rapidity spectra (left) and the deviation of the changes of the cut b_y of the daughter π^- of the daughter Λ (right).

G. Inverse Slope Parameter versus Particle Mass

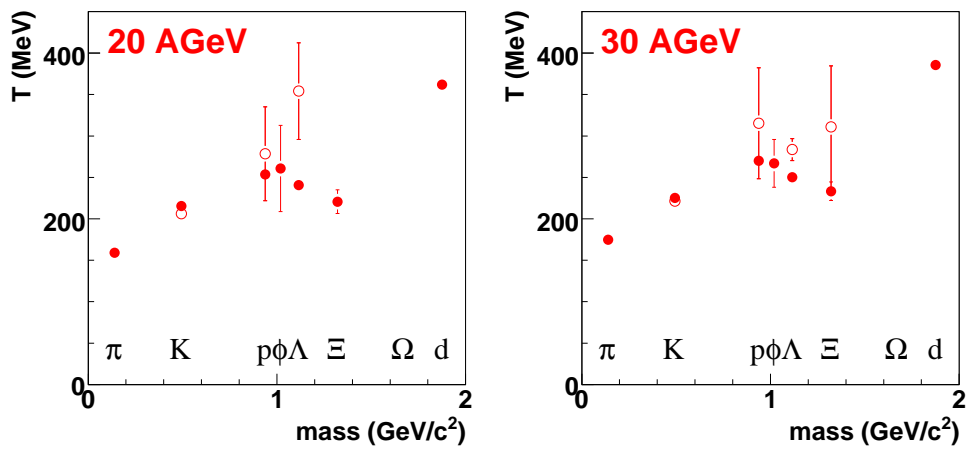


Figure G.1.: Midrapidity hadron slope parameter as a function of particle mass in central Pb+Pb collisions at 20 AGeV (left) and 30 AGeV (right). The open symbols represent the antiparticles.

G. Inverse Slope Parameter versus Particle Mass

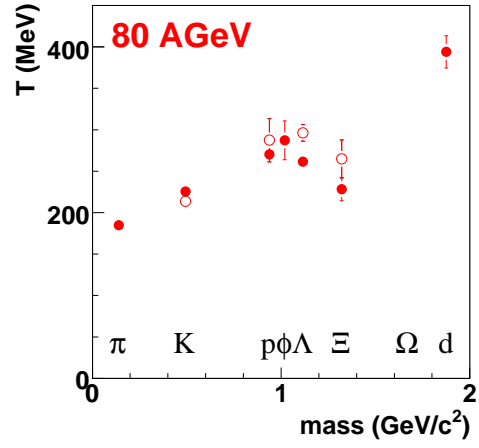


Figure G.2.: Midrapidity hadron slope parameter as a function of particle mass in central Pb+Pb collisions at 80 AGeV. The open symbols represent the antiparticles.

Bibliography

- [1] J. D. Bjorken, Phys. Rev. D **27** (1983) 140.
- [2] F. Weber, Acta Phys. Pol. **B30** (1999) 3149.
- [3] W. Bartel et al., Phys. Lett. B **28** (1968) 148.
- [4] M. Gell-Mann, Phys. Lett. **8** (1964) 214.
- [5] K. Hagiwara et al., Review of Particle Physics, Phys. Rev. D **66** (2002).
- [6] D. J. Gross and F. Wilczek, Phys. Rev. Lett. **30** (1973) 1343.
- [7] H. D. Politzer, Phys. Rev. Lett. **30** (1973) 1346.
- [8] F. Karsch, hep-lat/9903031 (1999).
- [9] K. Rajagopal and F. Wilczek, hep-ph/0011333.
- [10] M. A. Stephanov, Prog. Theor. Phys. Suppl. **153** (2004) 139.
- [11] Z. Fodor and S. D. Katz, J. High Energy Phys **0404** (2004) 050.
- [12] F. Becattini et al., Phys. Rev. C **73** (2006) 044905.
- [13] L. D. Landau, Izv. Akad. Naul. SSSR, Ser. Fiz. **17** (1953) 51.
- [14] J. Rafelski and B. Müller, Phys. Rev. Lett. **48** (1982) 1066.
- [15] J. Rafelski and B. Müller, Phys. Rev. Lett. **56** (1986) 2334.
- [16] P. Koch, B. Müller and J. Rafelski Phys. Rep. **142** (1986) 167.
- [17] A. Wroblewski, Acta Phys. Polon. **B16** (1985) 379.
- [18] M. Gaździcki for the NA35 collaboration, Nucl. Phys. **A698** (1989) 375c.
- [19] C. Bormann for the NA49 Collaboration, J. Phys. **G 23** (1997) 1817.
- [20] S. V. Afanasiev et al. (NA49 Collaboration), Nucl. Phys. A **610** (1996) 188.
- [21] T. Alber et al. (NA35 Collaboration), Z. Phys. C **64** (1994) 195.
- [22] M. Gaździcki and O. Hansen, Nucl. Phys. A **528** (1991) 754.

Bibliography

- [23] H. Bialkowska et al., *Z. Phys. C* **55** (1992) 491.
- [24] P. Vincent for the E802 collaboration, *Nucl. Phys.* **A698** (1989) 67c.
- [25] L. Ahle et al. (E866 Collaboration and E917 Collaboration), *Phys. Lett. B* **476** (2000) 1.
- [26] L. Ahle et al. (E802 Collaboration), *Phys. Rev. C* **57** (1998) 466.
- [27] L. Ahle et al. (E802 Collaboration), *Phys. Rev. C* **58** (1998) 3523.
- [28] L. Ahle et al. (E866 Collaboration and E917 Collaboration), *Phys. Lett. B* **490** (2000) 53.
- [29] M. Gaździcki for the NA49 collaboration, *J. Phys.* **G** **30** (2004) S701.
- [30] I. G. Bearden et al. (BRAHMS Collaboration), *Phys.Rev.Lett.* **94** (2005) 162301
- [31] J. H. Lee for the Brahms Collaboration, shown at the International Conference on Strangeness in Quark Matter in Los Angeles (2006).
- [32] M. Gaździcki and D. Röhrich, *Z. Phys. C* **65** (1995) 215.
- [33] M. Gaździcki and D. Röhrich, *Z. Phys. C* **71** (1996) 55.
- [34] M. Gaździcki , M. I. Gorenstein and D. Röhrich, hep-ph/0006236.
- [35] M. Gaździcki and M. I. Gorenstein, *Acta Phys. Polon.* **B30** (1999) 2705.
- [36] S. V. Afanasiev et al. (NA49 Collaboration), *Nucl. Instrum. Meth. A* **430** (1999) 210.
- [37] H. D. Haseroth, CERN preprint PS-95-026 (1995).
- [38] T. Kleinknecht, *Detectors for particle radiation*, Teubner, Stuttgart (1987).
- [39] C. Blyth, B. Lasiuk, H. Stroebele, S. Trentalange, C. Whitten, The NA49 Magnet Mapping Programme, Internal Report (1995).
- [40] C. DeMarzo et al., *Nucl. Instrum. Meth. A* **217** (1983) 405.
- [41] F. Bieser et al., *Nucl. Instrum. Meth. A* **385** (1997) 535.
- [42] T. Alber et al., *Nucl. Instrum. Meth. A* **349** (1994) 56.
- [43] The T49 Root miniDSTs, <http://na49info.cern.ch/na49>.
- [44] R. Brun and F. Rademakers, *Nucl. Instrum. Meth. A* **389** (1997) 81.
- [45] The ROOT System Homepage, <http://root.cern.ch>.
- [46] C. Roland, Ph.D. Thesis, Johann Wolfgang Goethe-Universität Frankfurt am Main (2001).

- [47] D. Irscher, Philosophy and parts of the global tracking chain, NA49 note (1997).
- [48] A. Mischke, Ph.D. Thesis, Johann Wolfgang Goethe-Universität, Frankfurt am Main (2003).
- [49] L. S. Barnby, Ph.D. Thesis, Birmingham University, Birmingham (1999).
- [50] W. Press, S. Teukolsky, W. Vetterling und B. Flannery, Numerical Recipes, Cambridge University Press, Cambridge (1986).
- [51] J. Podolanski and P. Armenteros, Phil. Mag. **45** (1945) 13.
- [52] A. Laszlo, Calculating mean values of collision parameters as function of centrality, Internal Report (2006).
- [53] H. A. Bethe, Annalen der Physik **5**, (1930) 325.
- [54] F. Bloch, Z. Physik **81**, (1933) 363.
- [55] Application Software Group. GEANT, Detector Description and Simulation Tool, CERN Program Library Long Writeup W1013, CERN, Genf (1994).
- [56] G. E. Cooper, Ph.D. Thesis, The University of California (2000).
- [57] M. Y. Toy, Ph.D. Thesis, The University of California (1999).
- [58] B. Lungwitz. NA49 Note number 315 (2005).
- [59] S. V. Afanasiev et al., Phys. Lett. B **538** (2002) 275.
- [60] E. Schnedermann, J. Sollfrank and U. Heinz, Phys. Lett. C **48** (1993) 2462 .
- [61] R. Barton, Ph.D. Thesis, Birmingham University, Birmingham (2001).
- [62] F. Antinori et al. (NA57 Collaboration), Phys. Lett. B **595** (2004) 68.
- [63] <http://wa97.web.cern.ch/WA97/yields.html>.
- [64] F. Antinori et al. (NA57 Collaboration), J. Phys. **G** 31 (2005) 1345.
- [65] F. Antinori et al. (NA57 Collaboration), J. Phys. **G** 32 (2006) 427.
- [66] F. Antinori et al. (NA57 Collaboration), J. Phys. **G** 30 (2004) 823.
- [67] F. Antinori et al. (NA57 Collaboration), nucl-ex/0607004.
- [68] F. Antinori et al. (NA57 Collaboration), Nucl. Inst. Meth. A **452** (2000) 323.
- [69] S. V. Afanasiev et al. (NA49 collaboration), Phys. Lett. B **538** (2002) 275.

Bibliography

- [70] P. Chung et al. (E895 Collaboration), Phys. Rev. Lett. **91** (2003) 202301.
- [71] J. Adams et al. (STAR Collaboration), Phys. Rev. Lett. **92** (2004) 182301.
- [72] J. Speltz for the STAR Collaboration, J. Phys. G **31** (2005) 1025.
- [73] C. Blume for the NA49 Collaboration, J. Phys. G **31** (2005) 685.
- [74] C. Alt et al. (NA49 Collaboration), Phys. Rev. C **69** (2004) 024902.
- [75] H. van Hecke et al., Phys. Rev. Lett. **81** (1998) 5764.
- [76] T. Susa for the NA49 collaboration, Nucl. Phys. **A698** (2002) 491.
- [77] M. Lamont for the STAR collaboration, nucl-ex/0608017.
- [78] B. I. Abelev et al. (STAR Collaboration), nucl-ex/0607033.
- [79] K. Redlich and A. Tounsi, Eur. Phys. J. C **24** (2002) 589.
- [80] C. Hoehne, F. Pühlhofer and R. Stock, Phys. Lett. **B640** (2006) 96.
- [81] J. Adams et al. (STAR collaboration), nucl-ex/0606014.
- [82] S. V. Afanasiev et al. (NA49 Collaboration), Phys. Rev. C **66** (2002) 054902.
- [83] M. Gaździcki for the NA49 Collaboration, J. Phys. **G 30** (2004) 701.
- [84] J. L. Klay (E895 collaboration), Phys. Rev. C **68** (2003) 054905.
- [85] J. Adams (STAR collaboration), nucl-ex/0311017.
- [86] C. Alt et al. (NA49 collaboration), Phys. Rev. Lett. **94** (2005) 192301.
- [87] M. Mitrovski, Diploma Thesis, University of Frankfurt, 2004.
- [88] C. Alt et al. (NA49 Collaboration), Phys. Rev. C **73** (2006) 044910.
- [89] T. Anticic et al. (NA49 collaboration), Phys. Rev. Lett. **93** (2004) 022302.
- [90] A. Richard, Diploma Thesis, University of Frankfurt, 2004.
- [91] M. Mitrovski for the NA49 Collaboration, J. Phys. **G 32** (2006) 43.
- [92] R. J. Glauber and G. Matthiae, Nucl. Phys. B **21** (1970) 135.
- [93] H. Sorge, Phys. Rev. C **52** (1995) 3291.
- [94] U. Heinz et al., Phys. Rev. C **59** (1999) 1637.
- [95] M. Bleicher et al., J. Phys. **G 25** (1999) 1859; private communication.
- [96] E. Fermi, Prog. Theor. Phys. **5** (1950) 570.
- [97] R. Hagedorn, Riv. Nuovo Cimento **6** (1983) 1.

Bibliography

- [98] R. Hagedorn et al., Phys. Lett. B **97** (1980) 136.
- [99] A. Andronic et al., Nucl.Phys. A **772** (2006) 167.
- [100] J. Cleymans et al., Phys. Rev. C **60** (1999) 054908.
- [101] R. Stock, Prog. Part. Nucl. Phys. **42** (1999) 295.
- [102] P. Braun-Munzinger et al., Phys.Lett. B **596** (2004) 61.
- [103] V. Koch, Nucl. Phys., Nucl. Phys. A **715** (2003) 108.
- [104] F. Becattini et al., Z. Phys. C **76** (1997) 269.

Bibliography

Danksagung

Zuerst möchte ich vor allem meinem Doktorvater **Prof. Dr. Christoph Blume** danken, der mich als Doktorand aufgenommen hat und mir ermöglicht hat für eineinhalb Jahre in den USA zu sein, obwohl er mich lieber in Frankfurt behalten hätte. Ausserdem bin ich sein erster Doktorand der bei Ihm promoviert. Desweiteren möchte ich ihm danken dass er mich für den Philipp Siedler-Wissenschaftspreis vorgeschlagen hat, den ich dann auch erhalten habe und noch für die nette Laudatio. Er war jeder zeit ansprechbar und hat mit Diskussionen, Vorschlägen und Ideen meine Arbeit vorangetrieben.

Danken möchte ich auch **Prof. Dr. Marek Gaździcki** und **Prof. Dr. Herbert Ströbele** die immer für Fragen jeglicher Art Zeit gefunden haben und immer die richtigen Antworten auf meine Fragen wussten. Auch bei der Vorbereitung verschiedener Vorträge nahmen sich beide Zeit. Ausserdem möchte ich Marek auch noch für das Korrekturlesen danken. **Prof. Dr. Marcus Bleicher** danke ich für die netten Diskussionen bei diversen Konferenzen und in Frankfurt über die Physik und für sein Interesse an meinen Resultaten. Für die Möglichkeit eineinhalb Jahre in Stony Brook zu verbringen, möchte ich **Prof. Dr. Roy Lacey** danken. Viel Dank gebührt auch meinem Diplomvater **Prof. Dr. Dr. hc. Reinhard Stock**, welcher endlich wieder aus dem Ruhestand zurückgekehrt ist und neues Leben ins IKF bringt. **Dr. Alexander Wetzler** danke ich für das Korrekturlesen meiner Arbeit, Hilfe bei Fragen zu Apple und Physik und für das nette Essen gehen. **Dr. Thorsten Kolleger** danke ich für zahlreiche interessante Diskussionen über Physik und menschliche Angelegenheiten. Bei **Stefan Kniege** möchte ich mich für seine Besuche in den USA bedanken, die netten Aufenthalte im CERN und dass er mich immer wieder auf dem Boden der Tatsachen zurückgebracht hat. **Peter Dinkelaker**, **Dr. Matthias Hartig**, **Dr. Matheusz Ploskon** und **Wolfgang Sommer** danke ich für die angenehme und witzige Zeit im IKF. Dank gebührt auch unserem Zwillingspärchen **Claudia Strabel** und **Frederick Kramer** für nette Unterhaltungen und die netten Zeiten im CERN. Meinem Zimmerkollegen **Tim Schuster** danke ich für meine schnelle Akklimatisierung im IKF und für viele hitzige, aber trotzdem produktive Diskussionen über Physik und Analyse, dem täglichen Essen gehen und dem Korrekturlesen meiner Arbeit. **Alexandra Argyrakis** danke ich das sie frischen Wind in unser Office gebracht hat. Dank geht auch an **Dr. Rainer Renfordt** der mir vor allem den Aufbau und die Funktionsweise einer TPC ausführlich erklärt hat. **Werner Amend** danke ich, dass er immer Zeit und Rat bei jeglichen Problemen im IKF hatte und

Bibliography

mir auch Software für meinen Apple besorgt hat. **Jutta Berschin** möchte ich danken, für das Wiedereinleben im IKF und die netten Unterhaltungen neben der Physik. Ein Dank geht auch an alle Kollegen und Kolleginnen am IKF und der GSI, wobei besonders **Prof. Dr. Harald Appelhäuser, Volker Friese, Dr. Claudia Hoehne, Michael Kliemant, Ulrich Köpf, Benjamin Lungwitz, Nora Pitz, Milica Utvic** und **Arnold Wiesenäcker** zu erwähnen sind.

Bei **Melanie Flowers** möchte ich mich für die schöne Zeit auf Manhattan, Long Island, Umgebung und dem Korrekturlesen danken. Ein sehr grossen Dank bekommen **Björn, Chris, Christian, Daniela, Falko, Julia, Lauren, Lisa, Mihaela, Murat, Rosali, Sara, Sebastian** und **Sylvia** die für diverse Ablenkung ausserhalb der Physik gesorgt haben und mich immer unterstützt haben. Am Ende möchte ich mich noch bei meinen **Eltern**, meinem **Bruder** und meiner **Tante** bedanken, die mich bei meinem Studium immer unterstützt haben.

Curriculum Vitae

MICHAEL KOSTA MITROVSKI

Odenwaldring 81
63069 Offenbach am Main
Germany

Phone: +49-69-15347096
Cell Phone: +49-176-23218497
E-Mail: Michael.Mitrovski@cern.ch



EDUCATION

05/2004-Present Ph.D. Student Johann Wolfgang Goethe-University
10/1999-05/2004 Diploma Physics Johann Wolfgang Goethe-University

PROFESSIONAL EXPERIENCE

2004-2006 Research stay at the State University of New York in Stony Brook
2004-2006 Research stay at the Brookhaven National Laboratory (BNL) working on the PHENIX experiment with a total time of 6 months
2001-2006 Research stay at the European Laboratory for Particle Physics (CERN) working on the NA49 experiment with a total time of 13 months
2004 Organization of the International Workshop “Exploring the Phase Diagram of Strongly Interacting Matter”, State University of New York in Stony Brook
2002-2004 Student assistant at the Institute for Nuclear Physics at the Johann Wolfgang Goethe-University

HONORS AND AWARDS

2007 Philipp Siedler Science award for the best Diploma thesis at the Department of Physics
2005-2006 Fellowship of the German Academic Exchange Service (DAAD) for Ph.D.-research studies

2004-2006 Scholarship from the Research Foundation of State University of New York

THESIS

2007 Energy and System Size Dependence of Ξ and $\bar{\Xi}$ Production in Relativistic Heavy-Ion Collisions at CERN SPS, Johann Wolfgang Goethe-University

2004 Ω production in ultrarelativistic Lead-Lead collisions at 40A GeV, Published diploma thesis in Phys. Rev. Lett. **94** (2005) 192301, Johann Wolfgang Goethe-University

PUBLICATIONS AND PRESENTATIONS

22 published articles, 2 articles in preparation, 4 conference proceedings, 8 oral presentations (*see list of publications and presentations for details*)

MEMBERSHIP IN PROFESSIONAL ORGANIZATIONS

German Physics Society (DPG)

Physikalischer Verein Frankfurt

ADDITIONAL SKILLS

Native language German and Macedonian

Business fluent English

OS MacOS9, MacOSX, Linux, Windows 98/2000/XP

Comp. Language Perl, HTML, C++

Comp. appl. Root, Adobe Illustrator, Adobe Photoshop, Adobe Acrobat, Adobe FinalCut, Shell-Scripts, LaTeX, XEmacs, Microsoft Word, Microsoft Excel, Microsoft PowerPoint, Keynote, Macromedia Flash, Cubase, Reason, LabView

VOLUNTEER

1999-2002 Volunteer work at the Children, Teenager and Cultural Center in Offenbach am Main :

- Organization of music workshops for teenagers
- Realization of a Hip Hop CD for young artists

INTEREST

Soccer, Basketball, Music, Literature, Photography

Publications and Presentations

SCIENTIFIC JOURNALS

1. C. Alt et al., Centrality and system size dependence of multiplicity fluctuations in nuclear collisions at 158 AGeV, nucl-ex/0612010.
2. A. Adare et al., J/psi production versus centrality, transverse momentum, and rapidity in Au+Au collisions at $\sqrt{s_{NN}} = 200$ -GeV, nucl-ex/0611020.
3. A. Adare et al., J/psi production versus transverse momentum and rapidity in p+p collisions at $\sqrt{s_{NN}} = 200$ -GeV, hep-ex/0611020.
4. A. Adare et al., System size and energy dependence of Jet-Induced hadron pair correlation shapes in Cu+Cu and Au+Au collisions at $\sqrt{s_{NN}} = 200$ and 62.4-GeV, nucl-ex/0611019.
5. A. Adare et al., Energy loss and flow of heavy quarks in Au+Au collisions at $\sqrt{s_{NN}} = 200$ -GeV, nucl-ex/0611018.
6. A. Adare et al., Measurement of high- p_T single electrons from heavy-flavor decays in p+p collisions at $\sqrt{s} = 200$ GeV, Phys. Rev. Lett. **97** (2006) 252002.
7. A. Adare et al., Scaling properties of azimuthal anisotropy in Au+Au and Cu+Cu collisions at $\sqrt{s_{NN}} = 200$ GeV, nucl-ex/0608033.
8. C. Alt et al., Elliptic flow of Lambda hyperons in Pb + Pb collisions at 158A GeV, nucl-ex/0606026.
9. C. Alt et al., Inclusive Production of Charged Pions in p+C Collisions at 158 GeV/c Beam Momentum, hep-ex/0606028.
10. C. Alt et al., Inclusive Production of Charged Pions in p+p Collisions at 158 GeV/c Beam Momentum, Eur. Phys. J. C **45** (2006) 343.
11. C. Alt et al., Energy and centrality dependence of \bar{p} and p production and the $\bar{\Lambda}/\bar{p}$ ratio in Pb+Pb collisions between 20A GeV and 158A GeV, Phys. Rev. C **73** (2006) 044910.
12. C. Alt et al., Upper limit of D0 production in central Pb+Pb collisions at 158 AGeV, Phys. Rev. C **73** (2006) 034910.

13. C. Alt et al., System size and centrality dependence of the balance function in A+A collisions at $\sqrt{s_{NN}} = 17.2$ GeV, Phys. Rev. C **71** (2005) 034903.
14. C. Alt et al., Ω and $\bar{\Omega}$ production in central Pb+Pb collisions at 40A GeV and 158A GeV, Phys. Rev. Lett. **94** (2005) 192301.
15. C. Alt et al., System-size dependence of strangeness production in nucleus-nucleus Collisions at $\sqrt{s_{NN}} = 17.3$ GeV, Phys. Rev. Lett. **94** (2005) 052301.
16. C. Alt et al., Electric charge fluctuations in central Pb+Pb collisions at 20A GeV, 30A GeV, 40A GeV, 80A GeV and 158A GeV, Phys. Rev. C **70** (2004) 064903.
17. T. Anticic et al., Λ and $\bar{\Lambda}$ production in central Pb+Pb collisions at 40A GeV, 80A GeV and 158A GeV, Phys. Rev. Lett. **93** (2004) 022302.
18. C. Alt et al., Observation of an exotic $S = -2$, $Q = -2$ baryon resonance in proton proton collisions at the CERN SPS, Phys. Rev. Lett. **92** (2004) 042003.
19. T. Anticic et al., Transverse momentum fluctuations in nuclear collisions at 158A GeV, Phys. Rev. C **70** (2004) 034902.
20. T. Anticic et al., Energy and centrality dependence of deuteron and proton production in Pb+Pb collisions at relativistic energies, Phys. Rev. C **69** (2004) 024902.
21. C. Alt et al., Directed and elliptic flow of charged π and protons in Pb+Pb collisions at 40A GeV and 158A GeV, Phys. Rev. C **68** (2003) 034903.
22. S. V. Afanasiev et al., Bose-Einstein correlations of charged kaons in central Pb+Pb collisions at $E(\text{Beam}) = 158A$ GeV per Nucleon, Phys. Lett. B **557** (2003) 157.

MANUSCRIPT IN PREPARATION

1. Energy dependence of Λ and Ξ production in central Pb+Pb collisions at the CERN SPS.
2. Centrality and system size dependence of Λ and Ξ production at the CERN SPS.

PUBLISHED CONFERENCE PROCEEDINGS

1. Strangeness production at SPS energies from NA49, J. Phys. **G 32** (2006) 43.
2. Hyperon production at CERN SPS energies, Acta Phys. Hung. **A 24** (2005) 157.

3. Multistrange hyperon production in Pb+Pb collisions at 30A GeV, 40A GeV, 80A GeV and 158A GeV, Prog. Part. Nucl. Phys. **53** (2004) 269.
4. Ω and $\bar{\Omega}$ production in Pb+Pb and p+p collisions at 30A GeV, 40A GeV and 158A GeV, J. Phys. **G** 30 (2004) 357.

TALKS

1. **Strangeness production at SPS energies from NA49**
Nuclear Physics Seminar at Yale University, USA (2006).
2. **Strangeness production at SPS energies from NA49**
Invited Plenary talk at the 9th International Conference on Strangeness in Quark Matter in Los Angeles, USA (2006).
3. **Multistrange hyperon production at CERN SPS**
Talk at the Nuclear Physics Spring Meeting of the German Physics Society in Berlin, Germany (2005).
4. **NA57 - NA49 discrepancies at SPS energies**
NA49-NA57 Workshop in Geneva, Switzerland (2004).
5. **Hyperon production at CERN SPS energies**
Talk at the 20th Winter Workshop on Nuclear Dynamics in Trelawny Beach, Jamaica (2004).
6. **Ω production in central Pb+Pb collisions at SPS energies**
Talk at the Nuclear Physics Spring Meeting of the German Physics Society in Cologne, Germany (2004).
7. **Multistrange hyperon production in Pb+Pb collisions at 30A GeV, 40A GeV, 80A GeV and 158A GeV**
Talk at the 25th International School of Nuclear Physics in Erice, Italy (2003).
8. **Ω and $\bar{\Omega}$ production in Pb+Pb and p+p collisions at 30A GeV, 40A GeV and 158A GeV**
Plenary talk at the 7th International Conference on Strangeness in Quark Matter in Atlantic Beach, USA (2003).